Ismail Gbadamosi

TDP-43-Metabolism Interplay in Neurodegenerative Disorders

PhD Thesis
Completed in the Laboratory for Translational Research in Neuropsychiatric Disorders, BRAINCITY - Center of Excellence for Neural Plasticity and Brain Disorders, Nencki Institute of Experimental Biology,
Polish Academy of Sciences.
Warsaw, 2025

SUPERVISOR:
Prof. Leszek Kaczmarek, Ph.D., D.Sc.
AUXILIARY SUPERVISOR
Dr. Ali Jawaid, M.D., Ph.D.

Table of Contents

Preface

A Tale of Two Patients: Rethinking Metabolism in ALS

Imagine two patients, seated side by side in the neurologist's office. Both are newly diagnosed with amyotrophic lateral sclerosis (ALS), a disease that robs its victims of movement, speech, and eventually life. They share striking similarities: same age, same gender, same socioeconomic background. Yet, there is one crucial difference. One patient lives a disciplined, athletic lifestyle—a marathon runner, the picture of fitness. The other is diabetic, a condition often painted in stark, ominous tones by public health campaigns.

Now, consider this: Which of these two patients, do you think, has the worse prognosis? Which is more likely to succumb to ALS first?

If you said the diabetic patient, you would be wrong. Understandably so. Conventional wisdom would suggest that the athlete stands the better chance against ALS, while the diabetic patient faces an accelerated disease course. But counterintuitively, epidemiological studies reveal the opposite. Patients with metabolic conditions such as T2DM and dyslipidemia—typically considered detrimental to overall health—often exhibit delayed ALS onset and prolonged survival. In contrast, individuals with physically active lifestyles appear more vulnerable to the rapid progression of the disease.

This puzzle is not just a quirk of epidemiology—it is a conundrum that lies at the intersection of metabolism and neurodegeneration, challenging our assumptions about health and disease. It was this paradox that captivated me as I stood at a crossroads in my academic journey 5 years ago. It was during the COVID-19 pandemic, amidst the stillness of lockdowns and the chaos of uncertainty, that I first encountered this anomaly. I was in Vienna, completing my predoctoral fellowship, when I stumbled upon an opening to pursue a project investigating TDP-43 proteinopathy and its role in ALS. The potential to explore such a fascinating intersection between cellular metabolism and neurodegeneration was irresistible.

Even now, years into this research, I find myself pausing to marvel at this paradox: how a risky metabolic profile like type 2 diabetes mellitus can improve the prognosis of one of the most devastating neurodegenerative diseases.

This doctoral thesis is, in essence, my journey into unraveling this enigma. It is a story of inquiry, of searching for answers to questions that defy easy explanations, and of illuminating the unseen connections between metabolism and disease. This thesis is not just an exploration of mechanisms or pathways. It is a testament to the mysteries that propel us as scientists and as humans—a pursuit not only of answers but of the questions that transform our thinking.

Welcome to the journey!!!

Acknowledgements

The completion of this work has been a journey of perseverance, learning, and collaboration, and I am deeply grateful to those who supported me along the way.

First and foremost, I extend my deepest gratitude to Dr. Ali Jawaid, whose belief in me has been nothing short of life-changing. In a world where opportunities are often scarce, Ali not only gave me a chance but took a remarkable leap of faith. He provided the space, trust, and guidance I needed to grow—not just as a researcher, but as a person. His unwavering support, intellectual generosity, and ability to challenge me in ways that fostered both independence and excellence have been instrumental in shaping my career. This journey would not have been possible without him, and for that, I am profoundly grateful. I would also like to thank Prof. Leszek Kaczmarek for his consistent support and invaluable insights throughout this project.

I also wish to acknowledge my colleagues—the TRENDlings, past and present—for their camaraderie, collaboration, and the vibrant, supportive environment they fostered in the lab. My sincere appreciation goes to Izabela Lepiarz-Raba, Magdalena Gomółka, Weronika Tomaszewska, Taufik Hidayat, Patrycja Rojek, Lena Majchrowicz, Joanna Przybyś, and Ilke Guntan. Working alongside you all has been both a privilege and a pleasure. I would also like to recognize the incredible interns who contributed to my project: Arogundade Tolulope, Natacha Adamus, Lesley Motherwell, and Jan Zakrzewski. Your enthusiasm, dedication, and hard work were deeply appreciated.

Beyond TREND, I had the privilege of collaborating with outstanding researchers at the Nencki Institute of Experimental Biology, whose expertise greatly enriched this work. My heartfelt thanks go to Dorota Dymkowska for metabolic flux analysis, Bartłomiej Gielniewski for RNA sequencing, Sandra Binias for transcriptomic analysis, Natalia Nowak and Artur Wolny for confocal microscopy, Debadeep Chaudhury for splicing analysis, and Łukasz Bijoch for image analysis. I am also grateful to my external collaborators—Blanca Aldana (Denmark), who provided valuable lab support and expertise in dynamic metabolic mapping, and Isabel Duarte and Ramiro Magno (Portugal), whose guidance in transcriptomic analysis strengthened this work immensely.

I am thankful to the organizations that provided financial and professional support, allowing me to attend conferences, advanced neuroscience schools, and symposiums where I presented my work. Special thanks to the European Society for Neurochemistry (ESN), the International Society for Neurochemistry (ISN), the International Brain Research Organization (IBRO), Black In Neuro (BIN), the European Molecular Biology Organization (EMBO), and the Federation of European Neuroscience Societies (FENS).

On a more personal note, I owe an immeasurable debt of gratitude to my wife, Rukayat—whom I fondly call Olori—and my son, Zane. They are my world, my greatest source of strength, and the reason I keep pushing forward. Being away from them has been unbearably difficult—a weight I've carried every single day of this journey. Yet despite the distance, their love remained my anchor. Olori's unwavering support, patience, and sacrifices have been the silent force that kept me going, while Zane's growth, laughter, and presence have been a constant reminder of why I strive for more. Every late night, every challenge, and every moment of doubt was met with the thought of them—and that alone gave me the courage to persevere. I could not have done this without them.

My heartfelt thanks also go to my parents and siblings, whose emotional support and encouragement have been a steady source of strength. I am deeply grateful to my mentors, Dr. Olajide Olayemi and Professor Gabriel Omotoso, whose guidance has shaped my academic path. My sincere thanks also go to my friends—Gabriel Michael, Lambe Ezra, Yawson Emmanuel, Ojiakor Vivian, John Oyem, and Bamisi Olawande—for their unwavering encouragement throughout this wild and demanding journey.

Finally, I take a moment to acknowledge myself—not just for staying the course, but for showing up every day with determination, pushing through setbacks, and refusing to let obstacles define my journey. This path has tested me in ways I never anticipated, demanding resilience, discipline, and unwavering commitment. Yet, despite it all, I adapted, I grew, and I endured. Reaching this milestone is not only a testament to perseverance but to the unshakable belief that hard work, faith, and purpose can turn aspiration into reality.

To all who have played a role, directly or indirectly, in shaping this journey—thank you. This accomplishment is as much yours as it is mine.

This work was supported by the EU Joint Programme–Neurodegenerative Disease Research (JPND) (TREMENDOS; UMO-2022/04/Y/NZ5/00122).

-Ismail Gbadamosi

List of abbreviations

Abbreviation	Full Term
ACACB	Acetyl-CoA Carboxylase Beta
ACC	Acetyl-CoA Carboxylase
AFM	Alpha-Ketoglutarate Dehydrogenase Complex
ALDO	Aldolase
ALS	Amyotrophic Lateral Sclerosis
AMP	Adenosine Monophosphate
AMPA	Alpha-Amino-3-Hydroxy-5-Methyl-4-Isoxazolepropionic Acid
AMPK	AMP-Activated Protein Kinase
ANOVA	Analysis of Variance
ATP	Adenosine Triphosphate
BCA	Bicinchoninic Acid (Protein Assay)
BCL	Base Call
BMI	Body Mass Index
BSA	Bovine Serum Albumin
CNS	Central Nervous System
CRAT	Carnitine Acetyltransferase
CS	Citrate Synthase
DAPI	4',6-Diamidino-2-Phenylindole
DEPC	Diethyl Pyrocarbonate
DG	Diacylglycerol
DGE	Differential Gene Expression
DM	Dorsomorphin
DMEM	Dulbecco's Modified Eagle Medium
DPBS	Dulbecco's Phosphate Buffered Saline
DSB	Double-Strand Break
ECAR	Extracellular Acidification Rate
EDTA	Ethylenediaminetetraacetic Acid
FASTQ	FASTQ Format
FASTQC	FASTQ Quality Control
FBS	Fetal Bovine Serum
FCCP	Carbonyl Cyanide-p-Trifluoromethoxyphenylhydrazone
FTD	Frontotemporal Dementia
FTLD	Frontotemporal Lobar Degeneration
FUS	Fused in Sarcoma
GAT	Glutamyl Aminotransferase (confirm exact usage in your context)
GFP	Green Fluorescent Protein
GLUT	Glucose Transporter
GO	Gene Ontology
GSH	Reduced Glutathione
GSSG	Oxidized Glutathione
GST	Glutathione S-Transferase
GYS	Glycogen Synthase
HDL	High-Density Lipoprotein
HFD	High-Fat Diet
HRP	Horseradish Peroxidase
IDH	Isocitrate Dehydrogenase
KD	Knockdown
LB	Luria-Bertani
LDH	Lactate Dehydrogenase
LDL	Low-Density Lipoprotein
MAPT	Microtubule-Associated Protein Tau
MCL	Molecular Carbon Labelling
MVT	Mutant TDP-43 M337V Expression
NAD	Nicotinamide Adenine Dinucleotide
NADH	Nicotinamide Adenine Dinucleotide (Reduced Form)
NADP	Nicotinamide Adenine Dinucleotide Phosphate
NADPH	Nicotinamide Adenine Dinucleotide Phosphate (Reduced Form)
NGM	NO Glucose Media
NGS	Next-Generation Sequencing
NHEJ	Non-Homologous End Joining
NLS	Nuclear Localization Signal
NMDA	N-Methyl-D-Aspartate
NS	Non-Targeting siRNA Control
NTD	N-Terminal Domain
OCR	Oxygen Consumption Rate
ORF	Open Reading Frame
OXPHOS	Oxidative Phosphorylation
PAGE	Polyacrylamide Gel Electrophoresis
PBS	Phosphate Buffered Saline
PCA	Principal Component Analysis
PCR	Polymerase Chain Reaction
PDC	Pyruvate Dehydrogenase Complex
PDH	Pyruvate Dehydrogenase
PFA	Paraformaldehyde
PFK	Phosphofructokinase
PKA	Protein Kinase A
PKR	Protein Kinase R
PPP	Pentose Phosphate Pathway

PYGB	Glycogen Phosphorylase B
RIPA	Radioimmunoprecipitation Assay (lysis buffer)
RNP	Ribonucleoprotein
ROS	Reactive Oxygen Species
ROUT	Robust Regression and Outlier Removal Test
RPM	Revolutions Per Minute
SDS	Sodium Dodecyl Sulfate

SEM	Standard Error of the Mean
SYBR	SYBR Green (fluorescent DNA dye for qPCR)
TARDBP	TAR DNA Binding Protein (gene encoding TDP-43)
TBS	Tris-Buffered Saline
TBST	Tris-Buffered Saline with Tween 20
TCA	Tricarboxylic Acid Cycle (Krebs Cycle)
WTT	Wild-Type TDP-43 Overexpression

Abstract

Cytoplasmic aggregation and nuclear depletion of TAR DNA-binding protein 43 (TDP-43) represent key pathological features in amyotrophic lateral sclerosis (ALS) and frontotemporal lobar degeneration (FTLD). Since TDP-43 is a critical regulator of RNA processing and metabolism, its dysfunction contributes to cellular stress through both loss- and gain-of-function mechanisms. Interestingly, metabolic conditions commonly linked to poor systemic health, including type 2 diabetes mellitus (T2DM), dyslipidemia, and elevated body mass index (BMI), are associated with prolonged survival in ALS. Conversely, high levels of physical activity have been linked to increased ALS risk, suggesting a complex interplay between metabolism and TDP-43-mediated neurodegeneration.

This study systematically investigates the impact of TDP-43 dysfunction—via knockdown or M337V mutation—on cellular energy metabolism and metabolic sensing, with a focus on motor neuron vulnerability. Using NSC34 motor neuron-like cells, TDP-43 knockdown induced a hypermetabolic state characterized by increased glycolysis, oxidative phosphorylation, and ATP production, accompanied by persistent activation of AMP-activated protein kinase (AMPK). In contrast, mutant TDP-43 disrupted AMPK regulation primarily under metabolic stress, leading to prolonged AMPK activation during recovery phases. Comparative analyses in BV2 microglia and N2A neuroblastoma cells highlighted distinct cell-specific metabolic responses to TDP-43 perturbation.

To explore how systemic metabolic status influences TDP-43–associated metabolic changes, we treated TDP-43–deficient NSC34 motor neuron–like cells with serum from mice subjected to voluntary exercise (VE) or a high-fat diet (HFD), revealing a sex-dependent modulation of those metabolic alterations. Female-derived serum more strongly regulated glycolytic and mitochondrial responses in both motor neurons and microglia. Finally, integration of patient-derived transcriptomic datasets from ALS and FTLD postmortem tissues with NSC34 RNA-seq data identified both common and disease-specific metabolic dysregulation. ALS transcriptomes were enriched for lipid metabolism and insulin signaling pathways, while FTLD transcriptomes showed predominant alterations in RNA processing and translation.

Collectively, these findings demonstrate that TDP-43 dysfunction disrupts cellular metabolism in a cell-type- and context-dependent manner, with motor neurons displaying heightened vulnerability. The data further suggest that systemic metabolic states modulate TDP-43-driven metabolic stress, providing insights into potential metabolic targets for therapeutic intervention in ALS and FTLD.

Keywords: TDP-43; amyotrophic lateral sclerosis; frontotemporal lobar degeneration; energy metabolism; AMPK; motor neurons; metabolic sensing; systemic metabolism.

Streszczenie

Agregacja cytoplazmatyczna oraz zmniejszenie obecności białka wiążącego DNA TAR (TDP-43) w jądrze komórkowym stanowią kluczowe cechy patologiczne stwardnienia zanikowego bocznego (ALS) oraz otępienia czołowo-skroniowego (FTLD). Ponieważ TDP-43 jest krytycznym regulatorem procesów RNA i metabolizmu, dysfunkcja TDP-43 przyczynia się do stresu komórkowego zarówno poprzez utratę funkcji, jak i toksyczne działanie nabytej funkcji. Co ciekawe, stany metaboliczne powszechnie związane z pogorszeniem zdrowia ogólnego, takie jak cukrzyca typu 2 (T2DM), dyslipidemia oraz podwyższony wskaźnik masy ciała (BMI), korelują z wydłużonym czasem przeżycia w ALS. Z kolei intensywna aktywność fizyczna została powiązana ze zwiększonym ryzykiem rozwoju ALS, co sugeruje złożoną interakcję pomiędzy metabolizmem a neurodegeneracją zależną od TDP-43.

Celem niniejszego projektu była systematyczna ocena wpływu dysfunkcji TDP-43 — poprzez wyciszenie ekspresji genu lub wprowadzenie mutacji M337V — na metabolizm energetyczny komórek oraz mechanizmy czujników metabolicznych, ze szczególnym uwzględnieniem wrażliwości motoneuronów. Wykorzystując komórki podobne do motoneuronów NSC34, wykazano, że wyciszenie TDP-43 indukuje stan hipermetaboliczny charakteryzujący się zwiększoną glikolizą, fosforylacją oksydacyjną i produkcją ATP, przy jednoczesnej trwałej aktywacji kinazy AMPK. W przeciwieństwie do tego, mutacja TDP-43 prowadziła do zakłócenia regulacji AMPK głównie w warunkach stresu metabolicznego, z utrzymującą się aktywacją AMPK w fazie regeneracji. Analizy porównawcze przeprowadzone w liniach komórkowych BV2 (mikroglej) i N2A (neuroblastoma) ujawniły odmienną, zależną od typu komórki odpowiedź metaboliczną na zaburzenia TDP-43.

W celu oceny wpływu systemowego stanu metabolicznego zastosowano surowicę pobraną od myszy poddanych dobrowolnej aktywności fizycznej (VE) lub żywionych dietą wysokotłuszczową (HFD). Wyniki wykazały zależną od płci modulację zmian metabolicznych związanych z TDP-43, przy czym surowica pochodząca od samic silniej regulowała odpowiedzi glikolityczne i mitochondrialne zarówno w motoneuronach, jak i mikrogleju. Następnie integracja zestawów danych transkryptomicznych pochodzących z tkanek pośmiertnych pacjentów z ALS i FTLD z danymi RNA-seq NSC34 ujawniła zarówno wspólne, jak i specyficzne dla choroby zaburzenia metaboliczne. Transkryptomy ALS były wzbogacone w szlaki związane z metabolizmem lipidów i sygnalizacją insulinową, natomiast transkryptomy FTLD charakteryzowały się głównie zmianami w procesach przetwarzania RNA i translacji.

Podsumowując, przedstawione wyniki wskazują, że dysfunkcja TDP-43 zaburza metabolizm komórkowy w sposób zależny od typu komórki i kontekstu, przy czym motoneurony wykazują szczególną podatność na stres metaboliczny wywołany przez TDP-43. Dane sugerują również, że stany metaboliczne organizmu mogą modulować ten stres, wskazując na metabolizm jako potencjalny cel terapeutyczny w ALS i FTLD.

Słowa kluczowe: TDP-43; stwardnienie zanikowe boczne; otępienie czołowo-skroniowe; metabolizm energetyczny; AMPK; motoneurony; czujniki metaboliczne; metabolizm systemowy.

The true journey of discovery is not only about exploring new landscapes, but also about gaining fresh perspectives."

Marcel Proust

Introduction

Disease-Modifying Effects of Metabolic Disorders in Neurodegenerative Disorders Characterized by TDP-43 Pathology

Amyotrophic lateral sclerosis (ALS) and frontotemporal lobar degeneration (FTLD) are two neurodegenerative disorders that, despite their distinct clinical symptoms, share a common pathological feature: the mislocalization and aggregation of TAR DNA-binding protein 43 (TDP-43). In ALS, TDP-43 pathology primarily affects motor neurons, leading to progressive paralysis, whereas in FTLD, it extends to the frontal and temporal cortices, contributing to cognitive and behavioral decline. While the mechanisms underlying TDP-43-driven neurodegeneration are not fully understood, increasing evidence suggests that metabolic factors play a role in disease progression. Observational studies indicate that conditions such as dyslipidemia, body weight alterations, and diabetes influence ALS and FTLD outcomes. However, the relationship between metabolism and neurodegeneration remains complex and context-dependent.

This Part provides an overview of ALS and FTLD as part of a pathological continuum, exploring their shared and distinct features. It then examines the potential role of metabolic factors in disease trajectory and discusses the broader implications for TDP-43-related neurodegeneration. The goal is to establish the foundation for investigating how metabolic alterations contribute to disease vulnerability and progression.

The Pathological Continuum Between ALS and FTLD

ALS and FTLD are increasingly recognized as part of a neurodegenerative continuum rather than entirely separate disorders. While ALS is primarily characterized by motor neuron degeneration and FTLD by progressive frontal and temporal lobe atrophy, both diseases share a critical molecular hallmark: the mislocalization and aggregation of TDP-43 in neurons and glial cells.

Although ALS typically presents with motor symptoms leading to paralysis and FTLD manifests with cognitive and behavioral impairments, there is substantial clinical overlap. Up to 50% of ALS patients exhibit cognitive and behavioral impairments similar to FTLD, while approximately 15% of FTLD cases develop motor dysfunction resembling ALS (Liscic et al., 2008). This overlap extends to their molecular pathology, with TDP-43 inclusions found in nearly all ALS cases and in about 45% of FTLD cases. Additionally, some forms of both diseases exhibit FUS protein aggregation, further reinforcing their shared pathophysiology (Dormann & Haass, 2011a; Tziortzouda et al., 2021a).

Based on the predominant aggregated protein, ALS and FTLD can be classified into distinct pathological subtypes. The ALS-TDP and FTLD-TDP subtypes are the most common, accounting for 98% of ALS and 45% of FTLD cases, respectively. In contrast, the ALS-FUS and FTLD-FUS subtypes involve FUS protein aggregation, a hallmark of a subset of cases that lack TDP-43 pathology but share similar neurodegenerative mechanisms. FTLD-Tau, a distinct FTLD subtype, is characterized by tau pathology, which sets it apart from TDP-43 and FUS-driven forms of ALS and FTLD (Jawaid et al., 2018a).

The recognition of ALS and FTLD as part of a pathophysiological spectrum rather than distinct entities provides a crucial framework for understanding neurodegeneration beyond the traditional division of motor and cognitive disorders. It underscores the need to identify both shared and disease-specific mechanisms underlying neuronal vulnerability. Increasing evidence suggests that systemic metabolic factors—including diabetes, dyslipidemia, and body weight variations—may influence disease risk and progression in ALS and FTLD, further shaping this neurodegenerative landscape. The following section explores the role of metabolic conditions in modifying disease trajectory and survival outcomes.

Metabolic Adaptations in TDP-43 Proteinopathies

Metabolic dysregulation is increasingly recognized as a critical modifier of disease progression in neurodegenerative disorders. In the context of TDP-43 proteinopathies such as ALS and FTLD, metabolic conditions—including dyslipidemia, type 2 diabetes mellitus (T2DM), and variations in body mass index (BMI)—have been paradoxically associated with favourable clinical outcomes. While these conditions are traditionally linked to systemic health risks, epidemiological and clinical studies suggest that certain metabolic states confer unexpected protective effects in ALS and, to a lesser extent, in FTLD. The mechanistic underpinnings of these associations remain poorly understood but likely involve metabolic adaptation at the cellular level. This section synthesizes clinical and epidemiological evidence to elucidate the impact of metabolic disorders on ALS and FTLD pathogenesis.

Diabetes Mellitus

T2DM has been associated with a reduced risk of ALS and an overall improvement in disease prognosis, suggesting that systemic metabolic perturbations may exert neuroprotective effects (Jawaid et al., 2018). Multiple lines of evidence, including meta-analyses, cohort studies, and genetic investigations, support this association. A meta-analysis encompassing three cohort studies and eight case-control studies found that individuals with T2DM had a significantly reduced risk of developing

ALS, with a pooled relative risk of 0.68 (Wannarong & Ungprasert, 2020). A separate meta-analysis confirmed this inverse relationship, further reinforcing the potential of T2DM as a disease-modifying factor (Zhu et al., 2023). In one of the largest cohort studies, which analyzed data from over 700,000 participants, T2DM was associated with a hazard ratio of 0.30 (95% CI: 0.19–0.45) for ALS risk. This protective effect was observed across sex, age, and ALS subtypes, suggesting a systemic influence of diabetes on ALS pathogenesis (D'Ovidio et al., 2018).

Beyond its association with reduced ALS risk, premorbid T2DM has been linked to delayed ALS onset. A comparative study found that ALS patients with T2DM exhibited a delayed disease onset of approximately four years (mean age: 60.3 years in ALS-DM vs. 56.3 years in ALS, $p < 0.05$) (Jawaid et al., 2010). This effect persisted after adjusting for confounders such as sex, ethnicity, and site of symptom onset, implying that metabolic dysfunctions associated with T2DM—such as insulin resistance and altered glucose utilization—may influence ALS progression. Although survival differences between ALS patients with and without T2DM have not been statistically significant, the protective effect of diabetes appears to be most pronounced during the preclinical and early stages of the disease (L. Zhang et al., 2022). A two-sample Mendelian randomization study further provided strong evidence for a causal relationship between genetically predicted T2DM and reduced ALS risk. This association was observed in both European (OR: 0.96, 95% CI: 0.92–0.996) and East Asian (OR: 0.83, 95% CI: 0.70–0.992) populations (L. Zhang et al., 2022).

Although direct evidence for a protective role of T2DM in FTLD is limited, emerging research points to potential mechanisms and overlaps with other neurodegenerative conditions. Neuroimaging studies have shown that FTLD is associated with reduced cerebral glucose uptake, particularly in the anterior temporal and frontal lobes, which is largely considered a proxy for neuronal loss rather than a direct reflection of impaired metabolism (Garrett & Niccoli, 2022). While systemic metabolic alterations in T2DM could theoretically influence neurodegenerative processes, there is currently limited direct evidence to suggest that T2DM adaptations mitigate glucose metabolism dysfunction in FTLD. Instead, broader metabolic factors, such as lipid metabolism, may have a more prominent role in shaping FTLD pathology (El-Wahsh et al., 2021). Studies of survival and disease heterogeneity in FTLD further support the complexity of its metabolic underpinnings. For instance, phenotypes like FTD-ALS exhibit the varied survival, while others, such as behavioral variant FTD, display survival rates comparable to Alzheimer's disease (Kansal et al., 2016). Additionally, FTLD exhibits marked transcriptomic and splicing heterogeneity, reflecting the involvement of diverse neuronal subtypes and molecular pathways (Ahmed, 2021). While these variations contribute to disease complexity, their connection to metabolic regulation remains underexplored. Identifying whether specific

metabolic pathways are differentially affected across FTLD subtypes could provide insights into potential mechanisms of metabolic vulnerability in TDP-43-related neurodegeneration.

Taken together, these findings highlight the paradoxical role of T2DM in ALS and FTLD. While diabetes is traditionally regarded as a systemic health risk, its association with reduced ALS risk and delayed disease onset suggests a more complex interplay between metabolic dysfunction and neurodegeneration. The potential protective effects of T2DM may be mediated through mechanisms such as altered insulin signaling, glucose metabolism, or lipid regulation—factors that warrant further investigation in both ALS and FTLD.

Dyslipidemia

Dyslipidemia, particularly elevated levels of total cholesterol and low-density lipoprotein (LDL), has been proposed as a potential modifier of ALS survival. A study involving 369 ALS patients found that LDL cholesterol and total cholesterol were elevated in ALS patients compared to controls and were associated with a 12-month survival benefits (Dupuis et al., 2008). Similarly, a cohort of 99 ALS patients found that higher levels of total cholesterol, LDL cholesterol, LDL/HDL ratios, and apolipoprotein B were significantly linked to lower mortality risk, with a dose-response relationship observed (Ingre et al., 2020). These findings suggest that lipid metabolism may play a role in ALS progression, though its precise contribution remains debated.

A clinical trial found that 73% of ALS patients exhibited hypercholesterolemia at baseline (Rafiq et al., 2015). However, after adjusting for confounders, cholesterol levels were no longer significant predictors of survival, suggesting that other prognostic factors, such as body weight or metabolic adaptations, may influence survival more directly (Rafiq et al., 2015). Supporting this, a study of 427 ALS patients identified a U-shaped relationship between BMI and survival, indicating that body weight itself—rather than lipid levels alone—may be a stronger predictor of prognosis (Paganoni et al., 2011a).

Despite the apparent survival advantage associated with higher LDL levels, genetic studies provide conflicting evidence regarding the role of lipid metabolism in ALS risk. Mendelian randomization analyses have implicated elevated LDL cholesterol as a potential risk factor for ALS, suggesting that higher cholesterol may contribute to disease onset rather than progression onset (Chalitsios et al., 2024). Additionally, some studies have reported lower lipid levels (hypolipidemia) in ALS patients, particularly males, indicating that disease-specific metabolic alterations may override the protective effects of dyslipidemia in some cases (Yang et al., 2013).

In contrast to ALS, where higher LDL and total cholesterol have been associated with improved survival, the role of lipid metabolism in FTLD remains uncertain. Some studies suggest that FTLD patients exhibit altered lipid profiles, including increased triglycerides, reduced HDL cholesterol, and elevated cholesterol/HDL ratios compared to controls (Ahmed, MacMillan, et al., 2014). However, it remains unclear whether these changes precede neurodegeneration or emerge as a consequence of disease progression. A study found no significant association between hyperlipidemia and FTLD, with prevalence rates of 42.9% in FTLD patients and 48.9% in non-FTD dementias ($P > 0.05$). This suggests that dyslipidemia may not be a major contributor to FTLD pathogenesis. Similarly, other vascular risk factors such as hypertension (65.1% vs. 68.2%), diabetes (31.7% vs. 26.9%), and tobacco use (7.9% vs. 8.8%) were not significantly different between the FTLD group and non-FTLD dementia patients (Kalkonde et al., 2012). Interestingly, the study also found that FTLD patients had a lower prevalence of heart disease (19.0% vs. 36.7%, $P < 0.05$) and cerebrovascular diseases (12.7% vs. 26.1%, $P < 0.05$), despite having similar rates of vascular risk factors (Kalkonde et al., 2012). These findings suggest that FTLD does not share the same metabolic risk factors as ALS, despite both disorders involving TDP-43 pathology. While some studies have reported altered lipid profiles in FTLD, including increased triglycerides, reduced HDL cholesterol, and elevated cholesterol/HDL ratios, the overall evidence remains inconclusive (Ahmed, MacMillan, et al., 2014; Kalkonde et al., 2012). Further research is needed to determine whether lipid imbalances play a causal role in FTLD or simply reflect disease-associated metabolic changes.

Overall, these findings highlight key differences in the metabolic profiles of ALS and FTLD. In ALS, higher cholesterol levels and BMI have been linked to improved survival, though the causal role of dyslipidemia remains debated. In contrast, FTLD does not exhibit a strong metabolic association. While some studies suggest altered lipid profiles, others, including Kalkonde et al. (2012), found no significant link between hyperlipidemia and FTLD risk. Additionally, FTLD patients had a lower prevalence of heart and cerebrovascular disease despite similar vascular risk factors. These findings suggest that metabolic factors are more relevant to ALS than FTLD, warranting distinct investigative approaches for each disorder.

Body Mass Index

Building on the relationship between metabolic disorders and TDP-43 proteinopathies, body mass index (BMI) emerges as a critical modifiable factor influencing both the risk and progression of ALS and FTLD. While traditionally associated with general health outcomes, variations in BMI have distinct implications across the ALS-FTLD spectrum, revealing shared and divergent metabolic

mechanisms. Here, I discuss the role of BMI as a factor modulating disease onset, survival, and progression, highlighting its potential as a target for intervention in these TDP-43-related neurodegeneration.

Numerous evidence links lower BMI with increased risk of developing ALS. Studies show that stable or decreasing BMI in early to midlife is associated with a 61% higher risk of ALS, while a 1-unit BMI increase at age 40 reduces risk by 5% (Mariosa et al., 2017). Large cohort studies reinforce this finding, revealing that for every 5-unit increase in BMI, ALS rates drop by 21%, with overweight and obese individuals exhibiting significantly lower risks compared to those with normal BMI (O'Reilly et al., 2013). These findings indicate that lower premorbid BMI and progressive weight loss may increase susceptibility to ALS, whereas higher BMI or obesity appears to confer a protective effect. The protective association between BMI and ALS extends beyond risk reduction, as higher BMI has also been consistently linked to improved survival outcomes. Meta-analyses show that each 1 kg/m^2 increase in BMI reduces mortality risk by 5% (Ning et al., 2019), and obesity is a strong predictor of favorable prognosis (HR = 0.73, 95% CI: 0.62–0.86). Similarly, systematic reviews indicate that underweight individuals face nearly double the mortality risk compared to those with normal BMI, while overweight and obese patients experience significant survival benefits (Dardiotis et al., 2018). This observation is particularly intriguing, as it challenges the conventional assumption that maintaining a healthy weight or pursuing weight loss, typically regarded as metabolically advantageous, would reduce the risk or improve the prognosis of a disease like ALS

The relationship between BMI and ALS prognosis becomes even more compelling when considering BMI dynamic changes over time. ALS patients with significant BMI loss in the five years preceding diagnosis show a 27.1% reduction in survival, while those maintaining higher BMI trajectories fare better (Goutman et al., 2023). The "U"-shaped relationship between BMI and survival, with optimal outcomes observed at 30–35 kg/m^2, reinforces the importance of weight management in ALS care (Paganoni et al., 2011b). Mechanistically, metabolomic studies reveal dysregulation in sphingomyelin, bile acid, and plasmalogen subpathways, providing insights into the metabolic underpinnings of BMI-related survival differences (Goutman et al., 2023).

In FTLD, BMI is intertwined with distinct metabolic profiles across clinical phenotypes. While ALS patients often exhibit low BMI, FTLD patients, particularly those with bvFTD, tend to have higher BMI and increased fat mass (Ahmed, Mioshi, et al., 2014). Behavioral-variant FTD is characterized by increased total fat mass, visceral adipose tissue, and altered fat distribution, correlating with eating behaviors, functional decline, and grey matter atrophy in regions governing reward and autonomic

control (Ahmed et al., 2019).These findings suggest that centrally mediated metabolic dysregulation extends beyond cognition and behavior in FTLD.

BMI-related changes in ALS and FTLD may converge through shared metabolic pathways. Systemic lipid metabolism alterations, evident years before ALS diagnosis, are less studied in FTLD but appear central to mixed ALS-FTD forms (Godoy-Corchuelo et al., 2022). Metabolic hormone dysregulation in regions affected by TDP-43 pathology, including leptin and insulin receptor alterations, further supports the role of metabolic changes in ALS and FTLD pathogenesis. A study examining metabolic hormone expression in ALS and FTD found distinct alterations in regions affected by TDP-43 pathology (Atkinson et al., 2024). Leptin receptor (LEPR) mRNA levels were increased in the superior frontal gyrus in FTD and in the primary motor cortex and lumbar spinal cord in ALS (Atkinson et al., 2024). Insulin receptor mRNA was elevated in the superior frontal gyrus and insular cortex in FTD, while neuropeptide Y protein levels were decreased in the primary motor cortex and lumbar spinal cord in ALS (Atkinson et al., 2024).

Taken together, BMI is a pivotal modifiable factor with significant implications for the risk, progression, and prognosis of ALS and FTLD. In ALS, maintaining higher BMI is consistently associated with reduced risk and improved survival, while in FTLD, BMI reflects broader metabolic disruptions tied to disease phenotype and progression. These findings underscore the broader role of systemic metabolic factors in TDP-43-related neurodegeneration, inviting further exploration of other lifestyle factors, such as physical activity, and their impact on ALS and FTLD risk and outcomes.

Physical Activity

Building on the role of systemic metabolic factors in ALS and FTLD, physical activity emerges as another lifestyle factor with complex implications for disease risk and progression. The relationship between physical activity and TDP-43 proteinopathies like ALS and FTLD. is both complex and contentious. While intense physical activity has been implicated in increased ALS risk, moderate exercise appears to confer therapeutic benefits, particularly in improving quality of life and slowing disease progression (Maugeri & D'Agata, 2020). This section explores the nuanced roles of physical activity in modulating the risk, progression, and prognosis of ALS and FTLD, highlighting both clinical observations and mechanistic insights.

Conflicting evidence underscores the complexity of the relationship between physical activity and ALS risk. A population-based case-control study of 174 ALS patients and 348 matched controls found no significant association between physical activity—whether at work, during leisure time, or both—and ALS risk (Longstreth et al., 1998). However, a slightly higher prevalence of organized high school

sports participation was observed among ALS patients (OR 1.52, 95% CI: 1.03–2.25) (Longstreth et al., 1998). This suggests that while routine physical activity may not directly influence ALS risk, certain high-intensity activities or associated factors could play a role. Conversely, another population-based study of 636 ALS patients and 2,166 controls reported an association between higher levels of lifetime leisure-time physical activity and increased sporadic ALS risk (OR 1.08, 95% CI: 1.02–1.14) (Huisman et al., 2013). Notably, no significant relationship was observed for vigorous activities, such as marathons, or occupational physical activity, and a dose-response relationship was absent (Huisman et al., 2013). These findings suggest that genetic predispositions or lifestyle factors promoting physical fitness, rather than physical activity itself, may increase ALS susceptibility.

In contrast, a large cohort study of 373,696 participants found that higher self-reported physical activity levels were associated with reduced ALS risk in men but not in women. Men engaging in moderate physical activity had a 29% reduced ALS risk (HR 0.71, 95% CI: 0.53–0.95), while those with high activity levels experienced a 41% risk reduction (HR 0.59, 95% CI: 0.42–0.84) compared to men with low activity levels. Additionally, men with resting heart rates in the lowest quartile exhibited a 32% lower ALS risk (HR 0.68, 95% CI: 0.49–0.94) (Vaage et al., 2024). These findings underscore the nuanced relationship between physical activity and ALS, with potential gender differences warranting further investigation.

Genetic predispositions further complicate this relationship. Mendelian randomization studies have provided evidence for a causal link between strenuous leisure-time exercise and ALS risk, particularly in individuals with genetic susceptibilities, such as *C9ORF72* expansions. Transcriptomic analyses revealed that genes upregulated during acute exercise, including *C9ORF72*, are enriched with known ALS risk genes (Julian et al., 2021). Additionally, *C9ORF72* ALS patients demonstrated an inverse relationship between age of onset and historical physical activity levels, suggesting that exercise may accelerate disease onset in genetically predisposed individuals (Julian et al., 2021).

While intense physical activity has been linked to increased ALS risk, moderate exercise shows promise as a therapeutic intervention. Evidence from human studies indicates that moderate exercise improves ALS functionality scores and alleviates symptoms. Similarly, research in transgenic mouse models of familial ALS demonstrates slowed disease progression, enhanced motor function, and extended survival (McCrate & Kaspar, 2008). Mechanistic studies suggest that these benefits may arise from exercise-induced changes in motor neuron morphology, improved muscle-nerve interactions, and the upregulation of neurotrophic factors and anti-apoptotic proteins. These findings

emphasize the importance of optimizing exercise regimens in ALS care, tailoring intensity and duration to maximize therapeutic benefits (McCrate & Kaspar, 2008).

Evidence suggests that physical activity may exert neuroprotective effects in FTLD. A cohort study of 160 individuals with autosomal dominant FTLD variants found that higher baseline physical activity was associated with significantly slower progression of neurofilament light chain (NfL), a marker of axonal degeneration, over four years (McCrate & Kaspar, 2008). Carriers of *C9ORF72* and *MAPT* variants with high physical activity levels exhibited 18%–21% slower NfL progression compared to their low-activity counterparts. Activities requiring higher cardiorespiratory and cognitive engagement, such as sports and yard work, demonstrated the strongest correlations with slower NfL trajectories (McCrate & Kaspar, 2008). A 48-week multimodal exercise program for FTLD patients demonstrated feasibility and some benefits across cognitive performance, psychological state, and physical function. Functional near-infrared spectroscopy (fNIRS) revealed increased frontal lobe activation, suggesting a possible link to executive function and attention. However, these effects were limited, and disease progression continued in several measures (Nemoto et al., 2024).

The relationship between physical activity and neurodegenerative diseases like ALS and FTLD is multifaceted, influenced by intensity, genetic predispositions, and disease stage. While intense physical activity may increase ALS risk in genetically predisposed individuals, moderate exercise emerges as a potentially protective factor, improving functionality and survival. In FTLD, physical activity has demonstrated potential benefits in slowing axonal degeneration and enhancing cognitive and behavioral outcomes. These findings underscore the importance of tailoring physical activity interventions to individual profiles, offering new avenues for therapeutic strategies in TDP-43-related neurodegeneration.

In summary, the evidence highlights the significant disease-modifying effects of metabolic factors, such as diabetes mellitus, dyslipidemia, BMI, and physical activity, on ALS and FTLD. Each metabolic factor discussed—whether the protective role of T2DM, the complex implications of dyslipidemia, the pivotal influence of BMI, or the nuanced effects of physical activity—converges on a central theme of metabolic maladaptation in TDP-43 proteinopathies. These findings underscore the complexity of metabolic contributions to neurodegenerative diseases, revealing both protective and deleterious roles depending on the context. Given that TDP-43 proteinopathy is a shared hallmark of ALS and FTLD, metabolic factors may contribute to disease mechanisms, though their precise role remains to be fully elucidated. Understanding the interplay between TDP-43 and metabolic pathways could unveil novel insights into the mechanisms driving these diseases and provide therapeutic

opportunities. Furthermore, exploring how TDP-43 influences and is influenced by metabolic alterations could clarify its broader role in cellular homeostasis and disease progression. The next section delves into the structure and canonical functions of TDP-43, building on the foundation for understanding the rationale for the research carried out in this thesis.

TDP-43: Structure, Function, and Proteinopathy

Structure of TDP-43

TAR DNA-binding protein 43 (TDP-43) is a ribonucleoprotein encoded by the TARDBP gene located on chromosome 1 (1p36.22) in humans (4|4 E2 in mice). TDP-43 is composed of 414 amino acids and features a modular structure with distinct functional domains, which contribute to its physiological and pathological roles (Conicella et al., 2020; Guenther et al., 2018; Mompeán et al., 2016a). Structurally, its consists of four main domains (figure 1.1): the N-terminal domain (NTD), two RNA recognition motifs (RRM1 and RRM2), and the C-terminal domain (CTD), each with specific roles in RNA binding, protein interactions, and pathology.(Jiang & Ngo, 2022a; Sharma et al., 2024).

- **N-Terminal Domain (NTD):** The NTD (residues 1–76) facilitates dimer and oligomer formation through a ubiquitin-like fold, stabilizing the protein and preventing aggregation under physiological conditions. It exhibits interactions with single-stranded DNA (ssDNA), contributing to TDP-43 conformational equilibrium and preventing aggregation under normal physiological conditions. This domain plays a critical role in maintaining TDP-43 structural stability and functional (Mompeán et al., 2016b).

- **RNA Recognition Motifs (RRM1 and RRM2):** The RRM1 (residues 106–176) is essential for RNA binding, particularly UG-rich motifs, with affinity increasing as the UG repeat length extends. The RRM2 (residues 191–259) enhances the specificity and stability of RNA-protein interactions. Together, these domains enable TDP-43 to regulate over 6,000 RNA targets, primarily binding to 3′ untranslated regions (UTRs) and introns of coding and non-coding RNAs (Tziortzouda et al., 2021b).

- **C-Terminal Domain (CTD):** The CTD (residues 274–414) is rich in glycine residues and functions as a prion-like domain, mediating protein-protein interactions, stress granule recruitment, and aggregation. It contains an amyloidogenic core (residues 311–360), which drives phase separation and liquid-liquid demixing during cellular stress. Post-translational modifications such as phosphorylation, ubiquitination, and cleavage within the CTD modulate its aggregation propensity, contributing to pathology (De Boer et al., 2021).

In the structure of TDP-43, there are two localization signals: The nuclear localization signal (NLS, residues 82–98) ensures nuclear import. The nuclear export signal (NES, residues 239–250) facilitates cytoplasmic shuttling. These dynamic signals are critical for physiological functions of TDP-43 in RNA metabolism and stress response. The precise organization of TDP-43 domains underscores its dual roles in RNA metabolism and pathological aggregation. The interplay between its structured and disordered regions makes TDP-43 uniquely susceptible to dysregulation, contributing to neurodegenerative diseases like ALS and FTLD.

Function of TDP-43

TDP-43 is a multifunctional ribonucleoprotein essential for RNA metabolism, DNA repair, mitochondrial function, and cellular stress responses. It primarily resides in the nucleus, where it regulates transcription, mRNA splicing, and miRNA biogenesis. Additionally, it maintains mRNA stability, facilitates mRNA transport, and modulates lncRNA processing. Beyond the nucleus, TDP-43 undergoes nucleo-cytoplasmic shuttling, integrating into stress granules during cellular stress and participating in transport granule formation, particularly in neurons. It also plays a role in translation regulation, ensuring proper protein synthesis (Jiang & Ngo, 2022b). Beyond RNA metabolism, TDP-43 contributes to DNA double-strand break (DSB) repair via the non-homologous end-joining (NHEJ) pathway. Loss of nuclear TDP-43 disrupts genomic stability, leading to DNA damage accumulation in ALS motor neurons (W. Wang et al., 2016). TDP-43 also regulates AMPA receptor splice-variant expression, thereby modulating synaptic plasticity and long-term potentiation (Koza et al., 2019). Additionally, it localizes to mitochondria under pathological conditions, where its accumulation is linked to oxidative phosphorylation deficits and neurodegeneration. Increased mitochondrial TDP-43 levels have been reported in ALS and FTLD, correlating with disrupted respiratory chain function and altered mitochondrial morphology. This C-terminal region is highly aggregation-prone and harbors disease-associated mutations linked to ALS and FTLD (Felemban et al., 2019). Post-translational modifications—including phosphorylation, ubiquitination, and proteolytic cleavage—modulate TDP-43's stability, localization, and aggregation propensity. For a comprehensive overview of TDP-43's structure and molecular functions, see Figure 1.1 (De Boer et al., 2021).

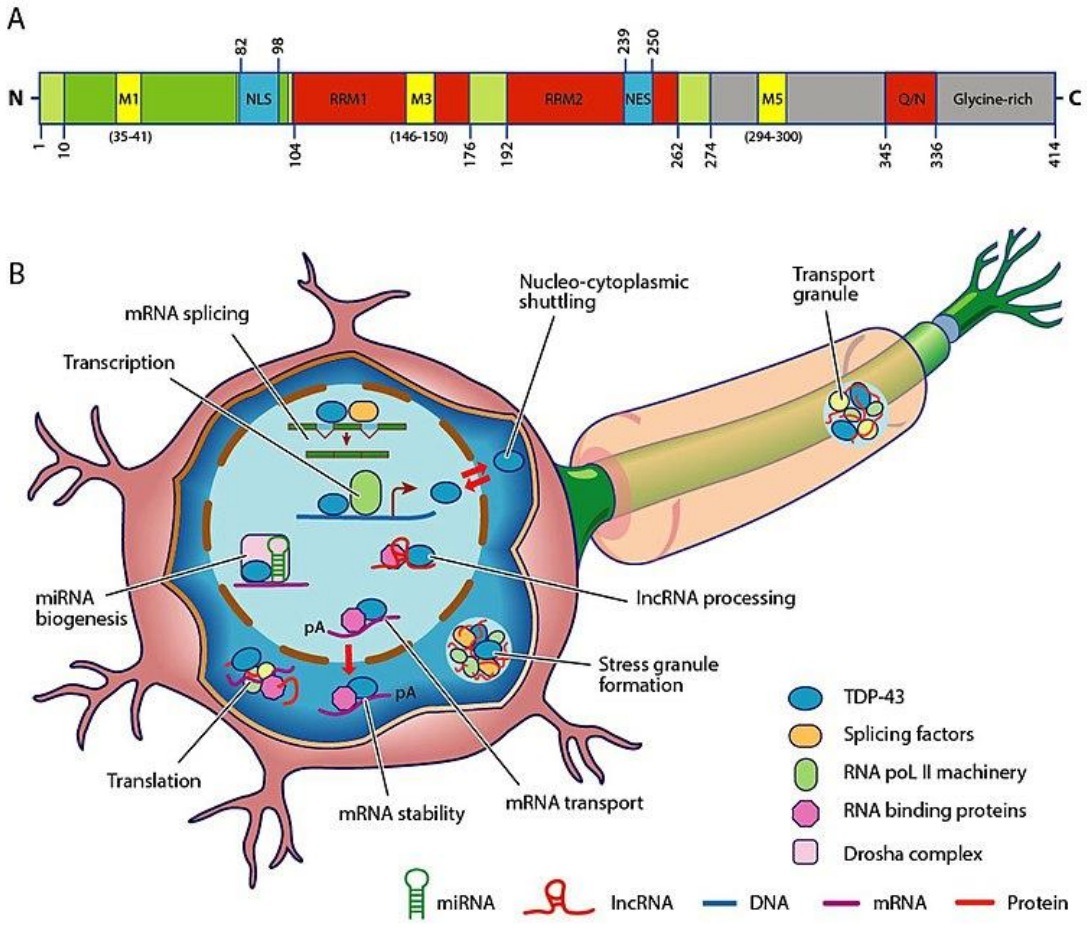

Figure 1.1. Structure and function of TDP-43. (A) The TAR DNA-binding protein 43 (TDP-43) is composed of 414 amino acids and exhibits a structured organization. It features an N-terminal segment housing a nuclear localization signal (NLS), essential for its targeting to the nucleus. Furthermore, the protein comprises two RNA recognition motifs (RRM1 and RRM2), a nuclear export signal (NES), and a C-terminal domain characterized by regions abundant in glutamine/asparagine (Q/N) and glycine residues. Additionally, motifs indicating mitochondrial localization (M1, M3, M5) are discernible. Notably, pathogenic mutations primarily cluster within the C-terminal region, which can demonstrate prion-like behavior. The numeric values denote the lengths of amino acid sequences. (B) TDP-43 plays a pivotal role in RNA metabolism. Within the nucleus, it governs the transcription and splicing of messenger RNA (mRNA), ensures RNA stability (pA), and facilitates RNA transport to the nucleus. Moreover, TDP-43 modulates the biogenesis of microRNA (miRNA) and the processing of long non-coding RNA (lncRNA). While predominantly residing in the nucleus, TDP-43 undergoes shuttling between the nucleus and cytoplasm. In the cytoplasmic compartment, it participates in mRNA stability, translation, and the formation of stress granules and ribonucleoprotein (RNP) transport granules. Adapted from (De Boer et al., 2021).

TDP-43 Proteinopathy: From Nuclear Loss of Function to Toxic Gain of Function

While TDP-43 mutations account for only a small subset of ALS and FTLD cases, TDP-43 proteinopathy is nearly ubiquitous in ALS and present in almost half of all FTLD cases, exhibiting TDP-43-positive inclusions in neurons and glia (Grossman et al., 2023; Hortobágyi & Cairns, 2018b; Masrori & Van Damme, 2020b). While TDP-43 pathology is most prominent in motor neurons in ALS, its distribution in FTLD extends to cortical neurons and glial cells. Moreover, its aggregates are also present in other neurodegenerative diseases, including Alzheimer's, Parkinson's, and Huntington's, indicating shared pathogenic mechanisms (De Boer et al., 2021; Huie et al., 2023). This pathological cascade, initiated by the mislocalization of TDP-43 from the nucleus to the cytoplasm, unfolds in a series of interlinked events, including nuclear loss of function, aberrant post-translational modifications, aggregation, and toxic gain of function. This mislocalization serves as the pivotal starting point, setting the stage for the disruption of cellular homeostasis.

TDP-43 mislocalization from the nucleus to the cytoplasm represents the cornerstone of its proteinopathy cascade (Gao et al., 2018). In fact, TDP-43 mislocalization is a defining characteristic of ALS and FTLD, marking the initiation of these pathological cascade (Dormann & Haass, 2011b). Under physiological conditions, TDP-43 dynamically shuttles between the nucleus and cytoplasm, with the majority residing in the nucleus to perform vital functions in RNA splicing, transcriptional regulation, and DNA repair. Mislocalization disrupts this delicate balance, depleting nuclear TDP-43 while promoting its pathological accumulation in the cytoplasm, and as a result, directly drives the nuclear loss of function that underpins the widespread dysregulation of essential cellular processes. TDP-43 transiently relocates to the cytoplasm during cellular stress responses, where it plays an adaptive role in maintaining homeostasis by forming stress granules (SGs) and halting non-essential translation. (Dewey et al., 2012). These non-membranous, ribonucleoprotein aggregates temporarily sequester untranslated mRNAs, halting non-essential translation and conserving cellular resources. This process is vital for promoting cytoprotective protein synthesis and enabling the cell to focus its machinery on addressing the stressor. TDP-43's interaction with SGs facilitates its role in RNA metabolism, including mRNA stabilization and translational repression, ensuring that the stress response is efficient and adaptive (Appleby-Mallinder et al., 2021). Once the stress resolves, TDP-43 dissociates from SGs, allowing them to disassemble and restore normal translational processes. This dynamic behavior underscores the essential cytoplasmic functions of TDP-43 in maintaining cellular homeostasis during transient stress conditions.

Loss of nuclear TDP-43 impairs RNA metabolism, resulting in dysregulation of alternative splicing, cryptic exon inclusion, and faulty polyadenylation (Keating et al., 2022; St. Martin et al., 2020; Suk & Rousseaux, 2020). Motor neurons of the spinal cord and cortex are particularly vulnerable to TDP-43 mislocalization, as the resulting loss of nuclear TDP-43 impairs STMN2 splicing, leading to premature polyadenylation of its transcripts, disruption of microtubule dynamics, and subsequent deficits in axon maintenance and regeneration—hallmarks of ALS-related neurodegeneration (Melamed et al., 2019). Moreover, nuclear TDP-43 plays an essential role in genomic stability by participating in the repair of double-strand DNA breaks (DSBs) via the non-homologous end-joining pathway. Depletion of nuclear TDP-43 leaves neurons particularly vulnerable to stress, as unrepaired DNA damage accumulates, leading to chromatin instability and transcriptional dysregulation (Fang et al., 2023; Mitra & Hegde, 2019). Although TARDBP mutations, such as M337V and A315T, impair TDP-43 NLS and promote mislocalization, the majority of ALS and FTLD cases lack these mutations (Wood et al., 2021). Instead, nuclear pore complex dysfunction and other extrinsic factors often drive TDP-43 mislocalization (Chou et al., 2018). For instance, in C9ORF72-associated ALS, toxic dipeptide repeats derived from the hexanucleotide repeat expansion disrupt nuclear transport, blocking TDP-43 re-entry into the nucleus (Ryan et al., 2022). Furthermore, TDP-43 can sequester nuclear pore proteins within cytoplasmic aggregates, compounding nuclear transport defects. The feedback loop between mislocalization and nuclear pore dysfunction amplifies TDP-43 pathology (Chou et al., 2018).

Once mislocalized to the cytoplasm, TDP-43 undergoes several post-translational modifications (PTMs), which, while typically physiological, can become pathological under disease conditions (Buratti, 2018). Physiologically, PTMs such as phosphorylation, acetylation, ubiquitination, and proteolytic cleavage regulate TDP-43 stability, localization, and interactions with other cellular components (Buratti, 2018). For instance, phosphorylation modulates its role in stress granule dynamics, while acetylation at lysine residues can affect RNA-binding capacity. However, under pathological conditions, these same modifications contribute to TDP-43 dysfunction. Phosphorylation at serine residues 409 and 410, commonly observed in ALS and FTLD, enhances TDP-43 aggregation propensity and stabilizes its cytoplasmic retention (Neumann et al., 2009). Proteolytic cleavage generates aggregation-prone C-terminal fragments (CTFs) that are enriched in pathological inclusions (Kumar et al., 2023; Li et al., 2015; Y. J. Zhang et al., 2009). Ubiquitination, a cellular mechanism typically used to mark proteins for degradation, paradoxically contributes to TDP-43 pathology when ubiquitinated forms accumulate within insoluble inclusions, overwhelming the proteostasis system (Tran & Lee, 2022; Q. Zhang et al., 2022).

TDP-43 aggregation is further driven by its ability to undergo liquid-liquid phase separation (LLPS), a process critical for forming functional ribonucleoprotein granules under normal conditions (Carey & Guo, 2022). Disease-associated mutations in TDP-43's prion-like C-terminal domain and aberrant PTMs disrupt LLPS dynamics, transforming TDP-43 into stable, pathological aggregates (Carey & Guo, 2022). These aggregates sequester RNAs and RNA-binding proteins, impairing RNA metabolism and exacerbating cellular dysfunction. SGs, transient cytoplasmic assemblies formed in response to stress, play a dual role in TDP-43 pathology. On one hand, SGs temporarily sequester TDP-43 during cellular stress, halting non-essential translation and conserving resources. On the other hand, persistent or aberrant SG formation caused by chronic stress or mutations in SG-associated proteins traps TDP-43 in a pathological state (Khalfallah et al., 2018; Streit et al., 2022). For example, ALS-associated mutations in TIA-1, an SG assembly factor, slow SG disassembly, enhancing the persistence of non-dynamic granules containing TDP-43 and promoting neurotoxicity (Kakihana et al., 2021).

Experimental evidence supports the role of SGs in TDP-43 aggregation. Inhibitors of SG formation have been shown to reduce TDP-43 aggregation, while SG-promoting proteins exacerbate its inclusion formation (Hayes & Kalab, 2022). Moreover, phosphorylation and cleavage of TDP-43 enhance its recruitment into SGs, disrupting granule dynamics and impairing cellular stress responses (Khalfallah et al., 2018). These disruptions not only promote TDP-43 aggregation but also impair protein homeostasis and mitochondrial function, amplifying neuronal vulnerability. Aggregated TDP-43 often exhibits prion-like properties, propagating its misfolding to neighboring cells (Harrison & Shorter, 2017). This intercellular spread amplifies neurodegeneration across neural networks, contributing to the progressive nature of ALS and FTLD.

In summary, the pathological cascade of TDP-43 proteinopathy begins with its mislocalization from the nucleus to the cytoplasm, initiating a sequence of events that includes nuclear loss of function, aberrant post-translational modifications, pathological aggregation, and ultimately a toxic gain of function. At the core of this cascade is the depletion of nuclear TDP-43, which impairs its critical roles in RNA metabolism, transcriptional regulation, and DNA repair, leaving neurons particularly vulnerable to stress and damage. Once in the cytoplasm, TDP-43 undergoes pathological post-translational modifications and aggregation, processes that not only amplify its toxicity but also propagate its dysfunction across cellular and intercellular networks. These interconnected mechanisms converge to create a vicious cycle of neuronal stress and degeneration, hallmarks of ALS and FTLD. By focusing on the early events of TDP-43 mislocalization and nuclear loss of function, as well as the impact of TARDBP mutations, this work underscores the pivotal role of these processes in driving disease pathogenesis and highlights them as critical targets for therapeutic intervention.

Scientific Rationale and Context

ALS presents a paradox that challenges conventional views of health and disease: individuals with systemic metabolic disorders such as T2DM, dyslipidemia, or elevated BMI—typically associated with poor health outcomes—often exhibit delayed ALS onset and slower disease progression. Conversely, highly active individuals may experience a more aggressive disease course. These epidemiological trends suggest a complex interplay between systemic metabolism and neuronal vulnerability in ALS.

Central to this phenomenon is the dysfunction of TDP-43, a defining pathological feature of ALS and a significant contributor to motor neuron degeneration. Motor neurons, with their exceptionally high energy demands and limited metabolic flexibility, may be particularly vulnerable to disruptions in bioenergetic homeostasis caused by TDP-43 pathology. While TDP-43 loss-of-function and mutation are known to disrupt RNA metabolism and cellular homeostasis, their influence on intrinsic metabolic programs and adaptation to external metabolic states remains poorly defined.

This study addresses these knowledge gaps by investigating how TDP-43 dysfunction affects cellular metabolism, with a focus on energy imbalance, metabolic sensing, and cell-type-specific vulnerability. It also explores how systemic metabolic cues—such as those associated with exercise or high-fat diet—modulate these effects. To do so, three murine cell lines were selected: NSC-34 motor neuron-like cells (to model motor neuron vulnerability), N2a neuroblastoma cells (as a non-motor neuronal comparator), and BV2 microglia (to assess neuroimmune-metabolic interactions). Together, these models provide a structured framework to dissect both intrinsic and extrinsic metabolic dynamics relevant to TDP-43-associated neurodegeneration.

Study Hypotheses

- **Hypothesis 1 – TDP-43 Dysfunction Disrupts Cellular Energy Metabolism**: TDP-43 loss of function and ALS-linked mutations disrupt glycolysis, oxidative phosphorylation, and mitochondrial function, leading to maladaptive metabolic responses that impair neuronal survival.

- **Hypothesis 2 – Cell-Type-Specific Metabolic Adaptations to TDP-43 Dysfunction**: Given their high energy demands and limited metabolic plasticity, motor neurons are hypothesized to exhibit distinct metabolic adaptations compared to non-motor neurons and microglia following TDP-43 dysfunction.

- **Hypothesis 3 – Dysregulation of Cellular Metabolic Sensing in TDP-43 Dysfunction:** TDP-43 depletion and mutation are hypothesized to disrupt metabolic sensing mechanisms,

leading to inappropriate activation or suppression of energy-regulating pathways. This disruption may contribute to increased metabolic stress, impaired adaptation to cellular energy demands, and heightened neuronal susceptibility to degeneration.

- **Hypothesis 4 – Systemic Metabolic Factors Modulate TDP-43-Induced Metabolic Stress in a Cell-Type- and Sex-Specific Manner**: Metabolic states induced by voluntary exercise and high-fat diet are hypothesized to differentially modulate TDP-43-associated metabolic stress across neural cell types.

General Objective of Study

The overarching objective of this study is to investigate how TDP-43 dysfunction, encompassing both loss of function and mutation, impacts cellular energy metabolism with a particular focus on motor neuron vulnerability. By integrating transcriptomic, metabolic, and functional analyses, this study aims to uncover the molecular mechanisms linking TDP-43 dysfunction to metabolic dysregulation, assess cell-type-specific metabolic responses, and explore the influence of systemic metabolic factors on TDP-43-associated adaptations.

Specific Aims of Study

- **Aim 1- To determine the impact of TDP-43 dysfunction on cellular energy metabolism in motor neurons:** This aim examines how TDP-43 loss of function and mutation affect metabolic pathways in NSC34 motor neuron-like cells. By integrating transcriptomic analysis with metabolic flux measurements, the study seeks to characterize alterations in glycolysis, mitochondrial function, ATP production, and redox balance, providing insight into how TDP-43 dysfunction disrupts cellular bioenergetics.

- **Aim 2 - To compare metabolic responses across motor neurons, microglia, and neuroblastoma cells following TDP-43 dysfunction:** Given the distinct functional phenotype of neural cell types, this aim investigates whether motor neurons exhibit a unique metabolic phenotype in response to TDP-43 loss and mutation, in contrast to microglia and neuroblastoma cells. By comparing glucose metabolism, oxidative phosphorylation, and ATP production across these cell types, the study aims to identify cell-type-specific metabolic adaptations to TDP-43 dysfunction.

- **Aim 3 - To investigate the role of cellular metabolic sensing in TDP-43-associated metabolic dysregulation:** This aim explores how TDP-43 loss of function and mutation influence metabolic sensing mechanisms in motor neurons. By evaluating changes in gene

and protein expression of key metabolic sensors and regulators, this study aims to determine whether TDP-43-induced metabolic alterations in motor neurons reflect adaptive cellular responses or dysregulated metabolic stress mechanisms.

- **Aim 4 - To assess the influence of systemic metabolic factors on TDP-43-driven metabolic adaptations:** Recognizing the role of systemic metabolism in neurodegeneration, this aim examines how metabolic conditions such as voluntary exercise and high-fat diet influence TDP-43-associated metabolic changes in motor neurons. Using serum from animals subjected to different metabolic states, the study evaluates how extrinsic metabolic cues modulate glycolysis and oxidative phosphorylation in TDP-43-deficient motor neurons.
- **Aim 5 - Evaluate the translational relevance of NSC-34 TDP-43 signatures by comparing them with RNA-seq profiles from ALS and FTLD post-mortem cortex**: This aim bridges the gap between cellular models and human disease by integrating RNA-seq data from ALS and FTLD cortical tissue with NSC-34 transcriptomes. By identifying shared and disease-specific differentially expressed genes (DEGs) and enriched pathways, the study will determine how closely NSC-34 motor-neuron-like cells recapitulate molecular alterations observed in human ALS and FTLD, while acknowledging the exploratory nature of these comparisons given the limited cohort size and regional heterogeneity.

The specific aims are addressed systematically across Parts I–VII of the Results section. Aim I is explored in Parts I and II, where transcriptomic profiling and metabolic flux analyses in NSC34 motor neuron-like cells following TDP-43 knockdown and mutant expression reveal distinct perturbations in energy metabolism. Aim II is examined in Part III by comparing metabolic responses across NSC34 motor neurons, BV2 microglia-like cells, and N2A neuroblastoma cells, highlighting cell-type–specific adaptations to both TDP-43 depletion and mutation. Aim III is investigated in Parts IV and V, which assess how TDP-43 dysfunction alters metabolic sensing pathways—through AMPK gene and protein expression, kinase activity assays, and post-translational analyses—under knockdown and mutant conditions. Aim IV is addressed in Part VI, where serum stimulation experiments and sex-specific systemic cues are applied to NSC34 cells to determine how extrinsic metabolic factors modulate TDP-43–associated metabolic adaptations. Finally, Aim V is covered in Part VII by performing transcriptomic comparisons between post-mortem ALS and FTLD cortex samples and NSC34 models to identify shared and disease-specific molecular signatures, thereby bridging cellular findings with human pathology.

Material and Methods

Cell Culture Media

For this study, various types of media formulations—complete media (CM), antibiotic-free media (AFM and no glucose media (NGM), reduced serum media (RSM)—were prepared and stored at 4°C, depending on the experimental setup. The 500 mL of reconstituted media was consistently aliquoted under the laminar hood into 50 mL tubes as a precautionary measure against contamination. Before use, the 50 mL aliquots were uniformly warmed to 37°C in a water bath. The compositions of the respective media are explicated below.

1. **Complete media (CM):** The complete media comprise Dulbecco's Modified Eagle's Medium (DMEM Sigma-Aldrich: D5796) with 4500 mg/L glucose, L-glutamine, and sodium bicarbonate—devoid of sodium pyruvate, liquid, and sterile-filtered. The media is enriched with 10% Fetal Bovine Serum (FBS, Gibco: 10500064) and 1% Penicillin-Streptomycin (Gibco: 15140122). This medium is used for the maintenance and growth of cells.

2. **Antibiotic-Free Media (AFM):** The antibiotic-free media consist of DMEM with 4500 mg/L glucose, L-glutamine, and sodium bicarbonate—without sodium pyruvate, liquid, and sterile-filtered. The media is supplemented solely with 1% Penicillin-Streptomycin. This medium is used for sustaining cells during experimental procedures.

3. **No Glucose Media (NGM):** The no glucose media is derived from DMEM (Sigma-Aldrich: D5030) without glucose, L-glutamine, phenol red, sodium pyruvate, and sodium bicarbonate. The media is supplemented solely with 1% Penicillin-Streptomycin. This medium is used for maintaining cells during experiments, particularly in studies involving varying glucose concentrations, and it is reconstituted to achieve the desired glucose concentration.

4. **Reduced Serum Media (RSM):** The reduced serum media used in this study is Opti-MEM (Gibco: 31985062) containing no fetal bovine serum (FBS) and antibiotic supplementation. This medium is used for preparing transfection complexes during RNA interference or plasmid transfection procedures.

Cell Lines Culture and Maintenance

This study employed three distinct mouse cell lines: the NSC34 motor neuron cell line (Tebubio: CLU140-A), BV2 microglial cell line, and N2A Neuroblastoma Cell line. The NSC34 motor neuron cell line, initially at passage 3 (p3), was provided by Tebubio; the BV2 Microglial cell line was a generous gift from Professor Emanuele Buratti at ICGEB in Italy, and the N2A neuroblastoma cell line was

generously donated by Professor Leszek Kaczmarek of the Nencki Institute. While the primary focus was on the NSC34 motor neuron-like cells, experiments were concurrently conducted on BV2 and N2A cells for comparative analysis. All cells were cultured and maintained in complete media in a T75 flask, and subculturing occurred when they reached 80-90% confluency. Subculturing procedures involved washing cells with Dulbecco's Phosphate-Buffered Saline (DPBS, Gibco: 14190-144) and dissociating cells using TrypLE™ Express Enzyme (Gibco: 12604013). Subsequently, the dissociated cells were harvested, centrifuged at room temperature at 120 revolutions per minute (rpm) for 5 minutes, the supernatant was discarded, and the cells were reconstituted with complete DMEM medium. These cells were subsequently maintained under standard cell culture conditions at 37°C in a humidified atmosphere with 5% CO_2, as previously described. All experiments conducted in this study were performed between passage 6 and 12 of the cultured cells. Upon reaching passage 13, the cells were discarded, and new frozen aliquots at passage 4 were retrieved and cultured to ensure continuity in experimentation

RNA Interference (RNAi)

RNA interference (RNAi) was employed to knock down TDP-43 in NSC 34 motor neurons and other cell lines. Lipofectamine™ RNAiMAX Transfection Reagent (Invitrogen: 13778075) was used for transfecting cells with two TDP-43-specific siRNAs: Mm_Tardp 1 siRNA (Qiagen: SI01441503|S2) with the sequence AACGATGAACCCATTGAAATA and Mm_Tardp 2 siRNA (Qiagen: SI01441510|S2) with the sequence CAGTAACATGGTAACATTAAA. As controls, non-silencing (NS) Qiagen AllStars Negative Control siRNA (Qiagen: 1027281) and AllStars Mm/Rn Cell Death Control siRNA (Qiagen: SI04939025) were employed. These controls served to establish a baseline for non-specific effects and cell viability, respectively.

Transfection protocol

Twenty-four hours before the scheduled transfection, cells were seeded in antibiotic-free media, reaching a confluency of 45-60% in a 12 or 6-well plate for RNA and protein-based assays, and a 96-well plate for high-throughput metabolic assays. On the day of transfection, Lipofectamine RNAiMAX Reagent and siRNA were separately diluted in Opti-MEM® Medium. The diluted components were then combined in a 1:1 ratio and incubated for 10 minutes to form the siRNA-lipid complex. This complex was added to fresh antibiotic-free media, resulting in a final siRNA concentration of 20nM. The cells were retrieved from the incubator, and the media was replaced with the constituted siRNA media. Subsequently, the cells were incubated under normal conditions for 6 hours, after which the media was changed again to fresh antibiotic-free media, and the cells were further incubated under

normal conditions for up to 24 hours. Transfection efficiency was assessed by the observation of cell death in cells transfected with Cell Death Control siRNA. Confirmation of TDP-43 knockdown was conducted using qPCR and western blot techniques.

TDP-43 RNAi rescue

To validate that the observed functional alterations following TDP-43 knockdown in NSC34 motor neuron-like cells were not due to off-target effects, an RNAi rescue experiment was performed. The open reading frame (ORF) of the mouse TDP-43 gene (sequence in the appendix), was cloned into a pcDNA3.1 vector bearing eGFP as a reporter gene, creating the Mouse TDP-43 ORF_pcDNA3.1(+)-C-eGFP (mTDP-43) plasmid. An empty vector without TDP-43 ORF (eGFP) served as the control.

RNAi Rescue protocol

Cells were seeded and transfected with either NS control or TDP-43 siRNAs, as described previously. After **12** hours, the NS control group was transfected with eGFP, while one part of the TDP-43 knockdown (KD) group was transfected with mTDP-43 and the other part with eGFP as an internal control, using Lipofectamine™ 3000 Transfection Reagent (Invitrogen: L3000001). The Lipofectamine™ 3000 Reagent was diluted in Opti-MEM Medium, and the plasmids DNA plus P300 reagents were also diluted in Opti-MEM. Diluted DNA and transfection reagent were mixed in a 1:1 ratio. This complex was then added to fresh antibiotic-free media. Cells were retrieved from the incubator, and the media was replaced with the constituted plasmid DNA media. Subsequently, the cells were incubated under normal conditions for up to 48 hours. Transfection efficiency was assessed by observing green fluorescence under the microscope. Confirmation of TDP-43 expression was conducted using qPCR and western blot techniques.

TDP-43 Wild-Type and Mutation Plasmid

The open reading frame (ORF) of human TDP-43, as outlined in appendix 1, was synthesized in the Express Cloning Vector pcDNA3.1+C-eGFP, featuring the enhanced Green Fluorescent Protein (eGFP). This resulted in the generation of the Cloning:TDP-43_WTT_pcDNA3.1(+)-C-eGFP plasmid (Genescript: SC1691), denoted as WTT in the experiment. Employing site-directed mutagenesis (Genescript: SC1441), three amyotrophic lateral sclerosis (ALS)-linked TDP-43 mutations were incorporated and cloned into the same pcDNA3.1+C-eGFP vector. These mutations include TDP-43 Q331K (QKT), where Glutamine 331 is replaced with Lysine; TDP-43 M337V (MVT), with Methionine 337 substituted by Valine; and TDP-43 G294A (GAT), involving a Glycine 294 to Alanine substitution. Genscript conducted the synthesis through sequence design, PCR amplification, ligation, bacterial screening, and sequencing for quality control. The synthetic sequence integrated into the vector

during sequence design, with PCR amplification generating appropriately sized products verified by electrophoresis. Ligation combined the target gene PCR product with the vector, followed by transformation into TOP10 competent cells and overnight culture. Bacterial screening and nucleic acid staining facilitated clone selection. Sanger sequencing and enzyme digestion verification, using sequencing primers AGCAGTTTTTCTGTCAGTAT and TGGGAGGTCTATATAAGCAGAG, confirmed the precision and reliability of the synthesized TDP-43 plasmids. Detailed vector maps for each plasmid are in the appendix, and all plasmids possess ampicillin resistance.

Expression vector and TDP-43 sequence confirmation

The plasmids WTT, QKT, MVT, and GAT underwent individual transformation into E. coli using heat transformation, followed by overnight growth on plates. Three single colonies for each plasmid were selected and cultured in LB media with ampicillin overnight at 37°C, constituting the mini-prep. Subsequently, plasmids were extracted from the mini-prep using the Zyppy™ Plasmid Miniprep Kit (Zymo Reasearch: D4036). The extracted vectors, carrying both wildtype and mutated TDP-43 sequences, underwent a quality check step using the Nanodrop Spectrophotometer instrument to assess DNA concentration and purity. The prepared plasmid samples were then sent to Genomed for long read Sanger sequencing. Upon receiving the sequencing results, alignment with the original sequences was performed using the SnapGene desktop application. The sequences were further analyzed the same tool. Colonies with verified sequencing were subsequently used to generate maxi-preps, ensuring high concentrations of the plasmid vector carrying the DNA of interest. Notably, the sequencing results were specifically checked for the presence of the introduced TDP-43 mutations (QKT, MVT, and GAT) to confirm the successful incorporation of modifications.

TDP-43 wildtype and mutant expression in cell

Twenty-four hours before transfection, cells were seeded in antibiotic-free media, achieving a confluency of 45-60% in 12 or 6-well plates for RNA and protein-based assays, and a 96-well plate for high-throughput metabolic assays. On the day of transfection, cells were grouped for transfection with WTT (control), QKT, MVT, GAT, and eGFP (transfection control), employing Lipofectamine™ 3000 Transfection Reagent (Invitrogen: L3000001). The reagent was diluted in Opti-MEM Medium, and plasmids DNA plus P300 reagents were also diluted in Opti-MEM. The diluted DNA and transfection reagent were mixed in a 1:1 ratio and added to fresh antibiotic-free media. After retrieval from the incubator, the media was replaced, and cells were incubated under normal conditions for up to 48 hours. Transfection efficiency was gauged by observing green fluorescence, and confirmation of TDP-43 wild-type and mutant expression was conducted using qPCR and western blot techniques.

RNA Extraction

The cell culture media was aspirated, and cells underwent a single wash with ice-cold PBS. Subsequently, after complete removal of PBS, 1 ml of Trizol per sample was added. The cells were allowed to shake for 5 minutes at room temperature on a rotary shaker at 300 RPM. Following this, the cell lysate was passed through a pipette multiple times and vigorously vortexed. The homogenized sample was incubated for 5 minutes at room temperature to facilitate the complete dissociation of nucleoprotein complexes. Next, 0.2 ml of chloroform per 1 ml of Trizol reagent (Life Technologies: 15596018) was added, vortexed vigorously until the lysate turned visibly white, and incubated at room temperature for 2 to 3 minutes. The samples were then centrifuged at 12,000g for 15 minutes at 2-8°C, and the upper aqueous phase was carefully transferred to a fresh tube without disturbing the interphase. A volume of 400 µl of the aqueous phase was collected, and an equal volume of chloroform was added. Following another centrifugation at 12,000g for 15 minutes at 2-8°C, 0.5 ml of isopropyl alcohol was added to the samples, mixed, and incubated at room temperature for 10 minutes. To aid visibility, 10 µl of glycogen was added. The samples were then centrifuged at 12,000g for 10 minutes at 2-4°C. After removing the supernatant, the RNA pellet underwent two washes with 1 ml of 70% ethanol, with vortexing and centrifugation at 7,500g for 5 minutes. The pellet was air-dried for 30 minutes, and the RNA was resuspended in 30 µl of DEPC-treated water. The quantification of RNA was performed using a Nanodrop Spectrophotometer.

qPCR

For gene expression analysis, 2 µg of RNA from each sample was used, and potential genomic DNA contamination was removed using the ezDNase™ Enzyme (Invitrogen: 11766051). The SuperScript™ IV Reverse Transcriptase (Invitrogen: 18090010) was employed for reverse transcription, converting RNA into cDNA, which was subsequently diluted to 5 ng/µl. For qPCR reactions, the 2x concentration SYBR™ Green PCR Master Mix, along with forward and reverse primers at a concentration of 3 mM, and 10 ng of cDNA template were used in a final volume of 10 µl on a PCR plate. All reactions for each sample were prepared in triplicate for reliability. The qPCR machine was programmed with initial denaturation at 95.0 °C for 10 minutes, followed by 40 cycles of denaturation at 95.0 °C for 15 seconds and annealing/extension at 60.0 °C for 60 seconds. A gradual temperature increase from 60 to 95 degrees generated a melting curve, analyzed for primer specificity. The cycle threshold (Ct) values were exported for subsequent quantitative analysis, providing insights into the target gene expression levels. The primer used for respective gene in this study are listed in the appendix.

RNA Sequencing

RNA samples from both RNAi experiments and TDP-43 mutation experiments in NSC34 motor neuron-like cells underwent a quality check. Samples with an RNA Integrity Number (RIN) value equal to or exceeding 8.5, determined through bioanalyzer analysis, were specifically chosen for further analysis. The subsequent step involved library preparation using the SEQuoia Complete Stranded RNA Library Prep Kit (Bio-Rad: 17005710). This kit, designed for capturing both long and short RNAs, facilitates a comprehensive profiling of the coding and noncoding transcriptome within a single library. Following library preparation, ribodepletion was carried out using the SEQuoia RiboDepletion Kit (Bio-Rad: 17006487) to eliminate fragments of ribosomal and mitochondrial RNA while retaining those rare transcripts that are often lost in conventional methods. For sequencing purposes, the samples were sent to the sequencing facility at the Nencki Institute of Experimental Biology, where the Illumina NovaSeq 6000 sequencer was employed for the sequencing process. Post-sequencing, normalization was implemented using the DESeq function within DESeq2, known as the median-of-ratios. This method involves dividing raw counts by a size factor, where the size factor for each sample is determined as the median of the ratio of its raw counts to the geometric mean of counts across all samples. Next, the obtained data underwent a predesigned and optimized analysis pipeline, including quality control, alignment, and identification of differentially expressed genes or transcripts. These bioinformatic analyses were conducted by experts at the sequencing facility, using specialized tools and protocols in the R programming language optimized for mouse genome research.

2.8 Protein Extraction

Following the completion of the experimental procedure with the cells in the dish, the media is removed, and the cells are washed with room temperature PBS. Subsequently, Tryple is used for cell dissociation at 37°C for 5 minutes, and the reaction is neutralized with an equal volume of PBS. The harvested cells are then spun at 1200rpm for 5 minutes at 4°C, and the supernatant is discarded. Ice-cold PBS is added for washing, and the cells are spun again under the same parameters. The supernatant is discarded, and 500 µl of RIPA lysis buffer (Sigma-Aldrich: R0278-50ML) reconstituted with protease inhibitor (Roche: 4693132001) and phosphatase inhibitor (Roche: 4906845001) is added to the cell pellet. The cells are vortexed every 5 minutes for 30 minutes to ensure complete lysis, followed by centrifugation at 12,000g for 15 minutes at 4°C. The resulting supernatant is collected into a fresh tube, and the protein concentration is measured using the Pierce™ BCA Protein Assay Kit (Thermo Scientific: 23225). Ten micrograms of protein samples are then reduced with Laemmli Sample Buffer (Bio-Rad: 1616747) containing 1x NuPAGE Sample Reducing Agent

(Invitrogen: NP0004) to make a total volume of 10 µl per sample. Subsequently, the samples are incubated at 95°C for 10 minutes before proceeding to SDS-PAGE for further analysis.

Western Blot

Reduced protein samples are resolved using sodium dodecyl polyacrylamide gel electrophoresis (SDS-PAGE) with mini-PROTEAN TGX stain-free gels (Bio-Rad: 4568126). Protein samples are loaded onto the gel alongside Novex™ Sharp Pre-stained Protein Standard (Invitrogen: LC5800). The gel is run at 80 volts for 10 minutes and 100 volts for one hour. Subsequently, the gel is transferred onto a nitrocellulose paper using the Bio-Rad Trans-Blot Turbo Transfer System with a preset system. The blot papers are incubated in Ponceau S solution (Abcam: ab270042) to confirm the effective transfer of protein from the gel to the blot. The blots are then washed with TBS tween (TBST) and blocked in the StartingBlock™ Blocking Buffer (Thermo Scientific: 37538) for 1 hour. After washing in TBST, the blots are incubated with rabbit anti-mouse antibodies diluted in 5% BSA in TBST overnight at 4°C. Following additional washes in TBST, the blots are incubated with Goat anti-rabbit IgG (H+L) Secondary Antibody, diluted in 5% BSA in TBST, for 120 minutes at room temperature. The blots are then washed three times in TBST for one hour. Detection is performed using the Immobilon Western Chemiluminescent HRP Substrate (Millipore: P90720), and the blot image is captured using the Bio-Rad ChemiDoc Imaging System. The list of antibodies and the dilutions are listed in the table below.

Table 2.1 | List of western blot antibodies

Target Name	**Company**	**Catalogue Number**
AMPKÎ± (D5A2) Rabbit mAb	Cell Signalling	#5831
Acetyl-CoA Carboxylase Antibody	Cell Signalling	#3662
Alpha Tubulin Recombinant Rabbit Monoclonal Antibody (3P2D9)	Invitrogen	MA5-38163
Beta Actin Recombinant Rabbit Monoclonal Antibody (RM112)	Invitrogen	MA5-33078
GAPDH Loading Control	Invitrogen	MA5-15738-HRP
IgG (H+L)	Invitrogen	A27036
LKB1 Polyclonal Antibody	Invitrogen	PA5-96062
Lamin A/C Recombinant Rabbit Monoclonal Antibody (2Q2)	Invitrogen	MA5-35284
PKA alpha Polyclonal Antibody	Invitrogen	PA5-17626
PP2A alpha Polyclonal Antibody	Invitrogen	PA5-17510
Phospho-AMPKÎ± (Thr172) (40H9) Rabbit mAb	Cell Signalling	#2535
Phospho-Acetyl-CoA Carboxylase (Ser79) (D7D11) Rabbit mAb	Cell Signalling	#11818
Phospho-LKB1 (Ser334) Polyclonal Antibody	Invitrogen	PA5-105896
Phospho-PKA alpha/beta (Thr197) Polyclonal Antibody	Invitrogen	PA5-105515
Phospho-PP2A alpha (Tyr307) Polyclonal Antibody	Invitrogen	PA5-36874
TDP-43 Polyclonal Antibody	Invitrogen	PA5-29949
Total OXPHOS Rodent WB Antibody Cocktail	Abcam	ab110413-300

Metabolic Assays

Energy substrate assay

The energy substrate levels, including glucose, lactate, and glutamine, in the consumed media of cells at various time points during the experiments were assessed using specific assay kits: Glucose-Glo™ (Promega: J6021), Lactate-Glo™ (Promega: J5021), and Glutamine/Glutamate-Glo™ (Promega: J8021), respectively. At designated intervals (0, 12, 24, 48, and 72 hours post-transfection), 5 µl of consumed media samples were collected and subsequently diluted in 95 µl of PBS for storage until further analysis. For the substrate analysis, the samples were further diluted to a final dilution of 1:400 (consumed media sample: PBS). Following sample preparation in a 96-well plate, in accordance with the assay kit instructions, the substrates were detected using a luciferase reporter to generate a luminescent signal directly proportional to the substrate levels in the sample. The luminescence was then quantified using the Tecan plate reader.

Glucose uptake assay

The rate of glucose uptake in cells was assessed using the Glucose Uptake Assay Kit (Promega: J6021). Upon completion of the experimental conditioning, the consumed media was aspirated, and cells were washed with PBS. Subsequently, cells were incubated in 2-deoxyglucose-6-phosphate (2DG6P), an analogue of glucose, dissolved in PBS. Upon addition to cells, 2DG is transported across the membrane and undergoes rapid phosphorylation, similar to glucose. However, enzymes that typically modify glucose-6-phosphate (G6P) cannot act on 2DG6P, leading to the accumulation of this membrane-impermeable analyte within the cell. After a 10-minute incubation period, the uptake process was halted, and the solution was neutralized. A Detection Reagent, comprising glucose-6-phosphate dehydrogenase (G6PDH), NADP+, Reductase, Ultra-Glo™ Recombinant Luciferase, and proluciferin substrate, was added to the sample wells. G6PDH oxidizes 2DG6P to 6-phosphodeoxygluconate while simultaneously reducing NADP+ to NADPH. The Reductase uses NADPH to convert proluciferin to luciferin, which is then acted upon by Ultra-Glo™ Recombinant Luciferase to produce a luminescent signal directly proportional to the concentration of 2DG6P.

Reactive Oxygen Species Detection

Following the completion of TDP-43 knockdown and mutation experiments in NSC34 motor neuron-like cells, a reactive oxygen species (ROS) H2O2 assay was conducted to detect the activities of reactive oxygen species. The ROS-Glo™ H2O2 Assay kit (Promega: G8820) was employed for this purpose. As hydrogen peroxide (H2O2) is the final reactive species in the reduction of triplet and singlet oxygen species, the H2O2 Substrate was introduced to the cells during the final 6 hours of the

experiment, reaching a final volume of 100 µl in a 96-well plate. Subsequently, 100 µl of ROS-Glo™ Detection Solution was added to the cells, and the mixture was incubated at room temperature for 20 minutes. Upon addition of ROS-Glo™ Detection Solution, the precursor is converted to luciferin, and Ultra-Glo™ Recombinant Luciferase produces a light signal proportional to the level of H_2O_2 present in the sample.

Reduced and Oxidized Glutathione assays

After completing the experimental procedures involving TDP-43 knockdown and mutation in NSC34 motor neuron-like cells, we used the GSH/GSSG-Glo™ Assay (Promega: V6611) to evaluate and quantify total glutathione (GSH + GSSG), GSSG, and the GSH-to-GSSG ratio in cultured cells. These assessments were carried out directly on cells in 96-well culture plates. To specifically measure total glutathione, we introduced a reducing agent, converting all glutathione (GSH and GSSG) in a cell lysate to the reduced form, GSH. Simultaneously, we employed a parallel reaction to exclusively measure the oxidized form, GSSG. In this configuration, a reagent was added to block all GSH while preserving GSSG. Subsequent reducing steps transformed the GSSG to GSH, facilitating quantification in the luminescent reaction generating a light signal proportional to the level GSH or GSSG

Nucleotide cofactors assay

For the assessment of unphosphorylated (NAD and NADH) and phosphorylated (NADP and NADPH) nucleotide cofactors in this study, the NAD/NADH-Glo™ (Promega: G9071) and NADP/NADPH-Glo™ (Promega: G9081) Assay kits were used. Upon the completion of the experiment, cells were processed in a 96-well plate. Removal of the media and subsequent washing with PBS preceded cell lysis, facilitating the detection of total cellular NAD+ and NADH or NADP+ and NADPH separately, as outlined in the provided accessory protocol. These assays enable the quantification and comparison of phosphorylated and unphosphorylated nucleotide cofactor levels, providing valuable insights into the redox state of the cells and contributing to a comprehensive understanding of cellular metabolic processes in the experimental context.

ATP assay

The assessment of ATP levels in the cells was conducted using the Colorimetric ATP Assay Kit (Abcam: ab83355). Following the completion of the experiment in a 6-well plate, cells were subjected to cold PBS washing to halt metabolism. Subsequently, cells were harvested and lysed with ATP Assay Buffer, followed by centrifugation at 4°C for 5 minutes at 13,000g. The resulting supernatant was collected, and the protein concentration was determined using the BCA assay kit. For deproteinization, 200 µg (in 50 µL) of protein lysates were processed using the Deproteinizing Sample Preparation Kit – TCA

(Abcam: ab204708) to prevent interference from enzymes during the assay. All standards, controls, and samples were assayed in duplicate. In each reaction well, 50 µL of ATP Reaction Mix and Background Control Mix were added, and a master mix was prepared for consistency. The Reaction Mix was added to standard and sample wells, while the Background Reaction Mix was added to the background control sample wells. The mixture was then incubated at room temperature for 30 minutes, protected from light. The output was measured on a microplate reader at OD 570 nm. The calculation of ATP concentrations in the test samples was performed using the standard curve generated during the assay. Average duplicate readings for each standard, control, and sample were obtained and corrected by subtracting the mean value of the blank (Standard #1) from all readings, taking into account the correction for the sample background control if significant. These corrected values were then plotted as a function of the final concentration of ATP, and a trendline equation was derived based on the standard curve data. The corrected sample absorbance/relative fluorescence was applied to this standard curve for each sample well to estimate the amount of ATP (B) present. The concentration of ATP (nmol/µL or µmol/mL or mM) in the test samples was subsequently calculated using the formula: ATP concentration = (B * V * D) * DDF. These calculations were estimated based on the standard curve as outlined in the user guide of the ATP Assay Kit (Abcam: ab83355).

AMPK assay

After conducting TDP-43 knockdown and mutation experiments in NSC34 motor neuron-like cells, the CycLex AMPK Kinase Assay Kit (MBL: CycLex AMPK Kinase Assay Kit) was used to measure the relative activity of AMPK in cell lysates. The cells were seeded and transfected in 6-well plates. Following this, they were washed with PBS and harvested in 1.5ml tubes, where they were lysed with RIPA buffer. After centrifugation at 15,000g at 4°C, the supernatant was collected. The BCA protein assay kit was employed to measure protein concentration, and 100µg of protein sample (in a 10µl volume) per sample was prepared. For control purposes, sample inhibitor controls were prepared using the AMPK-specific inhibitor Dorsomorphin (Geyer Polska: P5499-5MG). All samples and sample inhibitor controls were run in duplicate, and purified AMPK (α1, β1, γ1) Protein (Merck: 14-840) served as a standard positive control. The assay protocol initiating the reaction by adding 10 µL of the cell lysate sample to each well and mixing thoroughly at room temperature. The plate was then sealed and incubated at 30°C for 30 minutes. Following this, the reaction was stopped by flicking out the contents or by adding 150 µL of 0.1 M Na EDTA, pH 8.0 to each well. The wells were washed five times with Wash Buffer, and 100 µL of Anti-Phospho-mouse IRS-1 S789 Monoclonal Antibody was pipetted into each well. After incubating at room temperature for 30 minutes, the wells were washed

five times, and 100 µL of HRP-conjugated Anti-mouse IgG was added to each well, followed by another 30-minute incubation. The wells were washed again, and 100 µL of Substrate Reagent was added, incubating for 5–15 minutes at room temperature. The absorbance in each well was measured using a spectrophotometric plate reader at dual wavelengths of 450/540 nm within 30 minutes of adding the Stop Solution. The evaluation of results involved averaging the absorbance values for the AMPK sample duplicates and all experimental sample duplicate values. The calculations were based on the relative AMPK activity, defined as Compound C-sensitive protein kinase activity in cell lysate. This was calculated by subtracting A450 of the "Inhibitor control" from A450 of the Test Sample, where the level of A450 increases in the Test sample when AMPK enzyme activity is present, while the high level of A450 is not observed in the Inhibitor control, usually less than 0. The calculations were estimated based on the user guide of the CycLex AMPK Kinase Assay Kit (MBL: CycLex AMPK Kinase Assay Kit).

Metabolic Flux Analysis

To understand the intricacies of glycolysis and oxidative phosphorylation, glycolytic and mitochondrial stress tests were conducted using the Seahorse XF Glycolysis Stress Test Kit (Agilent: 103020-100) and Seahorse XF Cell Mito Stress Test Kit (Agilent: 103015-100), respectively. For the experiments, cells were seeded onto the dedicated XFe 96-well TC-treated plate for the required transfection duration. Twenty-four hours before the stress test, the oxygen consumption and extracellular acidification sensor cartridges were hydrated with distilled water overnight at 37°C. The Agilent Seahorse XF Pro analyzer, which measures and reports the oxygen consumption rate (OCR) and extracellular acidification rate (ECAR) of live cells in a 96-well format, was activated to stabilize the temperature at 37°C. On the test day, the hydrant in the sensor cartridge was replaced with a prewarmed calibrant and incubated at 37°C. The media for both tests were reconstituted based on the test requirements, with details of the media composition and test procedure explained below.

Glycolytic stress test

For this test, XF DMEM (Agilent: 10357-100) was reconstituted with glutamine (Agilent: 103579-100) to a final concentration of 1 mM glutamine solution with no glucose or pyruvate. The reconstituted media were used to reconstitute the drugs in the glycolytic stress test kit to their respective stock solutions. These stock solutions and the reconstituted media were then used to prepare 3 ml each of 10 mM glucose solution, 10 mM oligomycin, and 500 mM 2DG working solutions. These solutions were injected into port A, B, and C of each sensor in the 96-well sensor cartridge, after which the cartridge was loaded into the XF Pro analyzer for calibration. Cells in the 96-well plate

were washed once with the reconstituted XF media, and the media was replaced with 180 µl of the reconstituted XF media. The cells were incubated in a no CO2 incubator at 37°C for 60 minutes, after which they were loaded into the XF Pro analyzer. The XF Pro analyzer took baseline readings of ECAR and OCR three times at 3-minute intervals and repeated the same reading sequence following the serial injection of glucose, oligomycin, and 2DG, with three readings at 3-minute intervals after each injection. The data were then exported for further analysis using the Agilent Wave desktop application, where the data were normalized using the amount of protein per well.

Mitochondrial stress test

For this test, XF DMEM (Agilent: 10357-100) was reconstituted with glucose (Agilent: 10577-100) to a final concentration of 25 mM, pyruvate (Agilent: 103578-100) to a final concentration of 1 mM, and glutamine (Agilent: 103579-100) to a final concentration of 1 mM glutamine solution. The reconstituted media were used to reconstitute the drugs in the mitochondrial stress test kit to their respective stock solutions. These stock solutions and the reconstituted media were then used to prepare 3 ml each of 1.5 µM oligomycin solution, 1 µM FCCP, and 0.5 mM rotenone/antimycin A working solutions. These solutions were injected into port A, B, and C of each sensor in the 96-well sensor cartridge, after which the cartridge was loaded into the XF Pro analyzer for calibration. The cells in the 96-well plate were washed once with the reconstituted XF media, and the media was replaced with 180 µl of the reconstituted XF media. The cells were incubated in a no CO2 incubator at 37°C for 60 minutes, after which they were loaded into the XF Pro analyzer. The XF Pro analyzer took baseline readings of ECAR and OCR three times at 3-minute intervals and then repeated the same reading sequence following the serial injection of oligomycin, FCCP, and rotenone/antimycin A, with three readings at 3-minute intervals after each injection. The data were then exported for further analysis using the Agilent Wave desktop application, where the data were normalized using the amount of protein per well.

Flux analysis normalization

After completing the test readings, the cell plates were retrieved and observed under the microscope to ensure that the cells were still attached to the bottom of the plate. The media was removed from the cells, and a microscope examination confirmed their attachment. The media was then replaced with 0.5 mM sodium hydroxide to lyse the cells and quantify the protein concentration with the BCA assay kit. The amount of protein per well was estimated in micrograms and used to normalize the data. The associated parameters for each test were then estimated and exported for further analysis.

Glucose Metabolic Mapping

To investigate cellular glucose metabolism in NSC34 motor neuron-like cells, BV2 microglia, and N2A neuroblastoma cells, dynamic metabolic mapping techniques were employed following TDP-43 knockdown or mutation. The experimental design included the use of [U-13C] glucose to track metabolic flux through glycolysis and the TCA cycle. This approach enabled a detailed analysis of 13C incorporation into key metabolites, revealing the metabolic impact of TDP-43 dysregulation. Cells were incubated in 2.5 mM [U-13C] glucose (100 µL of 1M [U-13C] glucose in 40 mL DMEM), for 60 minutes at 37°C to allow for isotopic labeling. After incubation, the medium was collected for analysis, and cells were harvested using ice-cold PBS and 70% ethanol. Cell extracts and incubation media were stored at -80°C until further processing. To determine the 13C enrichment of TCA cycle intermediates and associated metabolites, GC-MS analysis was performed. Cell extracts and incubation media were reconstituted in water, acidified, and extracted with ethanol. Metabolites were derivatized using N-tert-butyldimethylsilyl-N-methyltrifluoroacetamide for enhanced stability and detection. Samples were analyzed using gas chromatography (Agilent Technologies, 7820A, J&W GC column HP-5 MS) coupled to mass spectrometry (Agilent Technologies, 5977E). Isotopic enrichment was corrected for the natural abundance of 13C by analyzing standards of unlabeled metabolites. Key metabolites analyzed included lactate, citrate, α-ketoglutarate, succinate, fumarate, and malate, with a focus on the most abundant isotopologues (e.g., M+2 or M+3). Data was reported as percent enrichment and molecular carbon labeling (MCL), providing insights into glycolytic and TCA cycle activity.

Immunofluorescence Staining

To assess mitochondrial integrity and TDP-43 localization, cells were stained sequentially with MitoTracker™ Red CMXRos, anti-TDP-43 antibody, and DAPI to visualize the nucleus. Cells were cultured on microscope slides. Fater TDP-43 RNAi or mtatnt expression, cells were incubated in full culture medium containing 100 nM MitoTracker™ Red CMXRos for 20 minutes at room temperature. The optimal concentration of MitoTracker™ Red was determined experimentally. Following incubation, cells were washed to remove unbound dye, first with culture medium (three 10-minute washes), then with PBS containing calcium and magnesium ions supplemented with 1% BSA (two 10-minute washes), and finally with cold PBS (without calcium and magnesium ions) for 5 minutes. Cells were then fixed with 4% paraformaldehyde (PFA) for 10 minutes at room temperature and washed three times with cold PBS for 5 minutes each. To allow antibody access, cells were permeabilized using 0.1% Triton™ X-100 in PBS containing 1% BSA for 5 minutes at room temperature. For nuclear protein analysis, a higher concentration of Triton™ X-100 (0.35%) was used.

After permeabilization, cells were washed twice with PBS for 5 minutes each. Primary staining for TDP-43 was performed by incubating the cells with a primary antibody against TDP-43 (details provided in the appendix) for 1 hour at room temperature in PBS containing 1% BSA. After three PBS washes, cells were incubated with the corresponding fluorescently labeled secondary antibody for 30 minutes at room temperature. Nuclei were stained with 2 µg/mL DAPI in PBS for 5 minutes, followed by three additional washes in PBS, each lasting 5 minutes. The stained cells were mounted using VECTASHIELD® Antifade Mounting Medium and sealed with a coverslip. Fluorescent signals were visualized using a Zeiss Spinning Disc confocal microscope equipped with a 63× oil immersion objective.

Data Analysis

Data analysis was performed using GraphPad Prism and R, with appropriate statistical and bioinformatics tools selected to ensure accuracy, reproducibility, and interpretability. For experimental data, outliers were identified and removed using the ROUT test (Q = 1%). Cleaned datasets were tested for normality using the Shapiro-Wilk test. Normally distributed data were analyzed using an unpaired parametric t-test, while non-normally distributed data were analyzed using the Mann-Whitney U test. Both tests were performed as two-tailed, unpaired analyses. For comparisons involving more than two groups, ordinary one-way ANOVA was applied to normally distributed data, followed by Tukey's post hoc test for pairwise comparisons. Non-parametric data were analyzed using the Kruskal-Wallis test, followed by Dunn's post hoc test. Where applicable, assumptions such as homogeneity of variances were verified. For repeated measures experiments, two-way ANOVA was used to account for within-subject variability, with post hoc Šidák's multiple comparisons test applied where appropriate. In all analyses, data are presented as mean ± SEM unless otherwise specified. Statistical significance between groups is denoted with *, **, *** and **** representing $p < 0.05$, $p < 0.01$, $p < 0.005$ and $p < 0.001$ respectively. Outcomes from qPCR were calculated using the ΔΔCt method, normalized to housekeeping genes, and expressed as fold changes relative to control groups. Western blot data were analyzed using densitometry in ImageJ, with band intensities normalized to loading controls such as Tubulin or β-actin. Metabolic flux data, including oxygen consumption rate (OCR), extracellular acidification rate (ECAR), and isotopologue enrichment, were normalized to protein concentration determined using the Pierce BCA assay.

For transcriptomic analysis, raw sequencing data from the Illumina NovaSeq 6000 platform were converted from BCL to FASTQ format using the Bcl2Fastq tool (v2.20.0.422). Quality control of raw reads was performed using FASTQC (v0.11.7) to assess metrics such as per-base sequence quality, GC

content, and adapter contamination. Low-quality bases and adapter sequences were trimmed using Cutadapt (v2.3), ensuring a minimum quality score of 0, a minimum read length of 15 bases, and removal of the first nucleotide. Trimmed reads were aligned to the mouse reference genome (GRCm38/mm10) using STAR (v2.7.0f) with default parameters. BAM files were sorted, indexed, and duplicate reads marked using Picard tools (v2.20.0). Gene-level quantification was performed using the featureCounts function in Subread (v1.6.4), generating raw counts, RPKMs, and TPMs. RNA-seq data quality and expression profiles were analyzed using R (v4.4.0) and the DESeq2 package (v1.44.0). Principal Component Analysis (PCA) and hierarchical clustering were conducted on log2-transformed normalized counts to evaluate sample similarity. A regularized log transformation (rlog) was applied to mitigate bias from low-count genes. Differential gene expression analysis was conducted using DESeq2, with results visualized as volcano plots, heatmaps, and PCA plots. Genes with adjusted p-values (Benjamini-Hochberg correction) below 0.05 were considered significantly differentially expressed. Visualizations were created using tidyverse (v2.0.0), pheatmap (v1.0.12), and patchwork (v1.2.0). All raw and processed data were integrated into a comprehensive dataset to evaluate differences between experimental group.

Results
Part I: Metabolic dynamics of NSC34 Motor Neurons upon TDP-43 Knockdown

This part of the results explores the implication of TDP-43 depletion on energy metabolism in NSC34 motor neuron-like cells. RNA-interference was employed to reduce TDP-43 levels, resulting in at least a 70% depletion at both RNA and protein levels. This experimental approach mimics TDP-43 loss-of-function, which is critical in the cascade of events underlying TDP-43 proteinopathies in ALS and FTLD. Under these conditions, various molecular and functional techniques were applied to comprehensively assess the metabolic status of the cells, focusing on key aspects such as glucose metabolism, mitochondrial function, and redox balance.

The investigation begins with a detailed validation of the RNAi approach, confirming the efficiency of TDP-43 depletion at both mRNA and protein levels. Subsequent analyses explore transcriptomic alterations and metabolic profiling to uncover significant changes in metabolic pathways. Functional assays further characterize the impact of TDP-43 knockdown on critical cellular processes, including glycolysis, oxidative phosphorylation, and the production of reactive oxygen species.

To ensure the rigor and completeness of the study, RNAi rescue experiments were performed to restore TDP-43 expression. This allowed us to assess the reversibility of the observed metabolic changes by conducting selected metabolic assays following rescue. Together, these approaches provide a robust framework for understanding the metabolic maladaptation induced by TDP-43 loss-of-function and its implications for motor neuron metabolic fitness and vulnerability to oxidative damage in the context of TDP-43 dysfunction.

Confirmation of TDP-43 knockdown in NSC34 motor neurons

One of the specific aims of this study is to investigate how alterations in TDP-43 physiology impact motor neuron energy metabolism. To mimic TDP-43 loss-of-function, RNA interference (RNAi) was employed to deplete TDP-43 levels in NSC34 motor neuron-like cells. The experimental workflow involved cell seeding, and transfection with TDP-43-specific siRNAs for 24 hours, followed by RNA or protein extraction for downstream analyses (Figure 3.1A).

qPCR analysis of extracted RNA revealed a significant reduction in TDP-43 gene expression, with transcript levels decreasing by over 75% (Figure 3.1B). This knockdown was further validated at the protein level, as Western blot analysis demonstrated a significant reduction in TDP-43 protein

expression (Figure 3.1C and D). Quantification of the Western blot bands confirmed over 80% decrease in TDP-43 protein levels.

The established protocol consistently validated TDP-43 knockdown at both mRNA and protein, providing a robust basis for all downstream analyses detailed in the following sections of this study.

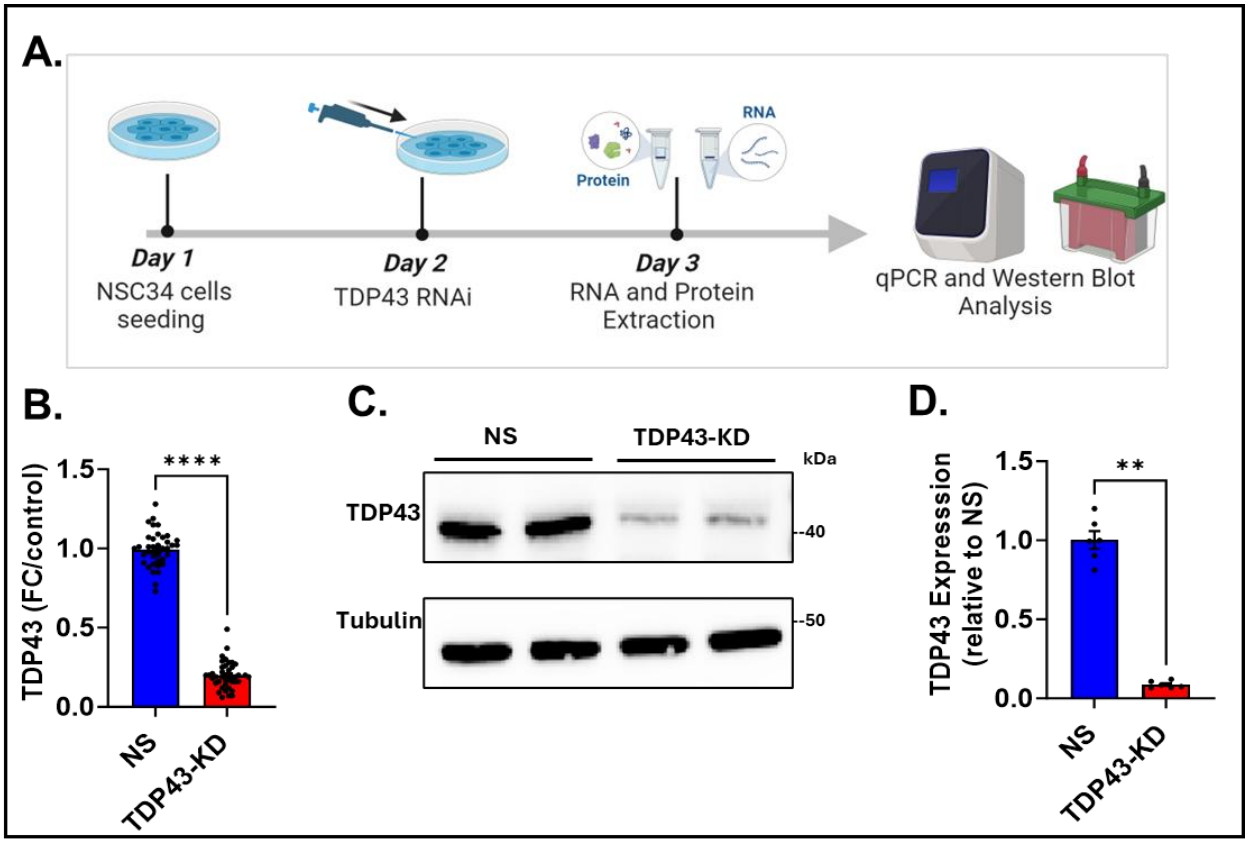

Figure 3.1 | TDP-43 RNAi Workflow and Validation. (A) Schematic representation of the experimental workflow: NSC34 motor neuron-like cells were seeded on Day 1, transfected with TDP-43-specific siRNAs on Day 2, and RNA and protein were extracted on Day 3 for downstream analysis. (B) qPCR analysis shows a significant reduction in TDP-43 transcript levels in the TDP-43 knockdown (TDP-43-KD) group compared to the non-silencing (NS) control. (C) Western blot analysis confirms a reduction in TDP-43 protein levels in TDP-43-KD samples. (D) Quantification of Western blot bands demonstrates over 80% decrease in TDP-43 protein expression. Bars and error bars represent mean ± SEM (n ≥ 3 biological replicates). Statistical tests: unpaired t-test (Welch correction) or Mann–Whitney U test. Statistical significance: **p < 0.01; ****p < 0.001.

Transcriptomic changes in NSC34 Motor Neurons upon TDP-43 Knockdown

To understand how TDP-43 knockdown impacts the transcriptome of NSC34 motor neuron-like cells, we employed next-generation sequencing (NGS) to analyze both coding and non-coding RNA transcripts. Following TDP-43 knockdown, RNA samples were collected from NSC34 motor neuron-like cells 24 hours post-knockdown. The integrity of these RNA samples was rigorously assessed to ensure high-quality input for sequencing. A ribo-depletion and library preparation strategy was employed to enrich for both small and large RNAs, enabling comprehensive profiling of transcriptomic changes induced by TDP-43 knockdown (Figure 3.2A).

Principal component analysis (PCA) of the RNA-seq data revealed distinct clustering patterns between the TDP-43 knockdown (TDP-43-KD) and non-silencing control (NS) groups (Figure 3.2B). This clear separation underscores the robust transcriptomic differences induced by TDP-43 knockdown.

Differential expression analysis identified significant transcriptomic changes across the 18,811 genes analyzed. Of these, 223 genes (1.19%) were significantly downregulated, while 142 genes (0.75%) were significantly upregulated, and the majority, 18,446 genes (98.06%), showed no significant change (Table 3.1). When categorized by gene type, the coding transcriptome revealed that 161 coding genes (1.27%) were downregulated, 90 coding genes (0.71%) were upregulated, and 12,396 (98.02%) remained unchanged. Similarly, for the noncoding transcriptome, 17 genes (0.83%) were downregulated, 8 genes (0.39%) were upregulated, and 2,034 (98.79%) showed no significant change. Additionally, among the unannotated transcripts, 45 genes (1.10%) were downregulated, 44 genes (1.07%) were upregulated, and 4,016 (97.83%) remained unchanged.

Volcano plots of the RNA-seq data (Figure 3.2C) visually represent these differentially expressed genes (DEGs). Significantly downregulated genes are highlighted in red, while significantly upregulated genes are marked in blue. Separate plots for coding and noncoding transcripts further illustrate the distinct differential expression patterns in these RNA subsets.

In summary, these findings reveal that TDP-43 knockdown in NSC34 motor neuron-like cells induces specific and measurable changes in the transcriptome, affecting both coding and noncoding RNA species. These results provide a strong foundation for further exploration of the biological pathways and processes influenced by TDP-43 loss-of-function, particularly those related to energy metabolism and cellular vulnerability in neurodegenerative diseases.

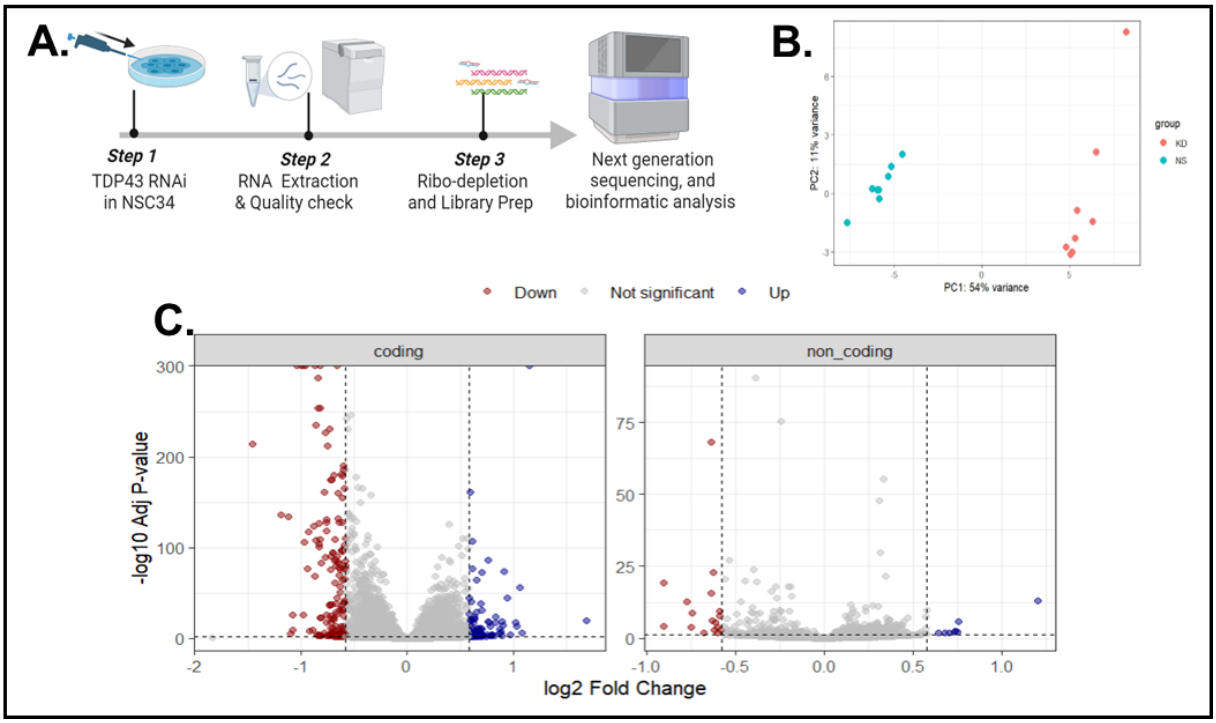

Figure 3.2 | Transcriptomic Analysis of NSC34 motor neuron-like cells Following TDP-43 Knockdown. (A) Schematic representation of the RNA sequencing workflow: NSC34 motor neuron-like cells were subjected to TDP-43 RNAi, followed by RNA isolation, quality checks, library preparation, and sequencing. (B) Principal component analysis (PCA) of transcriptomic profiles from control and TDP-43-KD groups shows distinct clustering, indicating separation of gene expression patterns between conditions. (C) Volcano plots display differentially expressed genes (DEGs) within the coding and noncoding RNA subsets, with significantly downregulated genes in red, upregulated genes in blue, and unchanged genes in gray. Statistical significance: adjusted p-value < 0.05, log2 fold change > ±0.58.

Table 3.1 | Differential Expression Analysis of TDP-43-KD vs NS Groups. Differentially expressed genes were identified with an adjusted p-value < 0.05 and log2 fold change > ±0.58.

Gene Category	Total Genes	Downregulated	No Change	Upregulated
All Genes	18,811	223 (1.19%)	18,446 (98.06%)	142 (0.75%)
Coding	12,647	161 (1.27%)	12,396 (98.02%)	90 (0.71%)
Noncoding	2,059	17 (0.83%)	2,034 (98.79%)	8 (0.39%)
Unannotated (NA)	4,105	45 (1.10%)	4,016 (97.83%)	44 (1.07%)

Validation of RNA Sequencing Results

To validate the findings from the RNA sequencing analysis, we performed qPCR on selected differentially expressed genes. This included assessing TDP-43 expression and the top five upregulated and downregulated genes identified from the RNA sequencing data. Genes were selected based on predefined thresholds for statistical significance (adjusted p-value < 0.01) and fold change (log2FC > 1 or log2FC < -1). As expected, TDP-43 expression was significantly downregulated, showing a reduction of over 75% at the transcript level (Figure 3.3A). Among the upregulated genes, AK7, Samsn1, Ceacam18, Arhgef18, and Isma1 exhibited significant increases in fold change, consistent with the RNA sequencing results (Figure 3.3B). Similarly, qPCR verification confirmed significant downregulation of Snx10, Jazf1, Tas2r137, and DPY1911 (Figure 3.3C). However, Tmem255b, one of the top five downregulated genes identified in the RNA sequencing data, did not show a significant reduction in transcript levels during qPCR analysis.

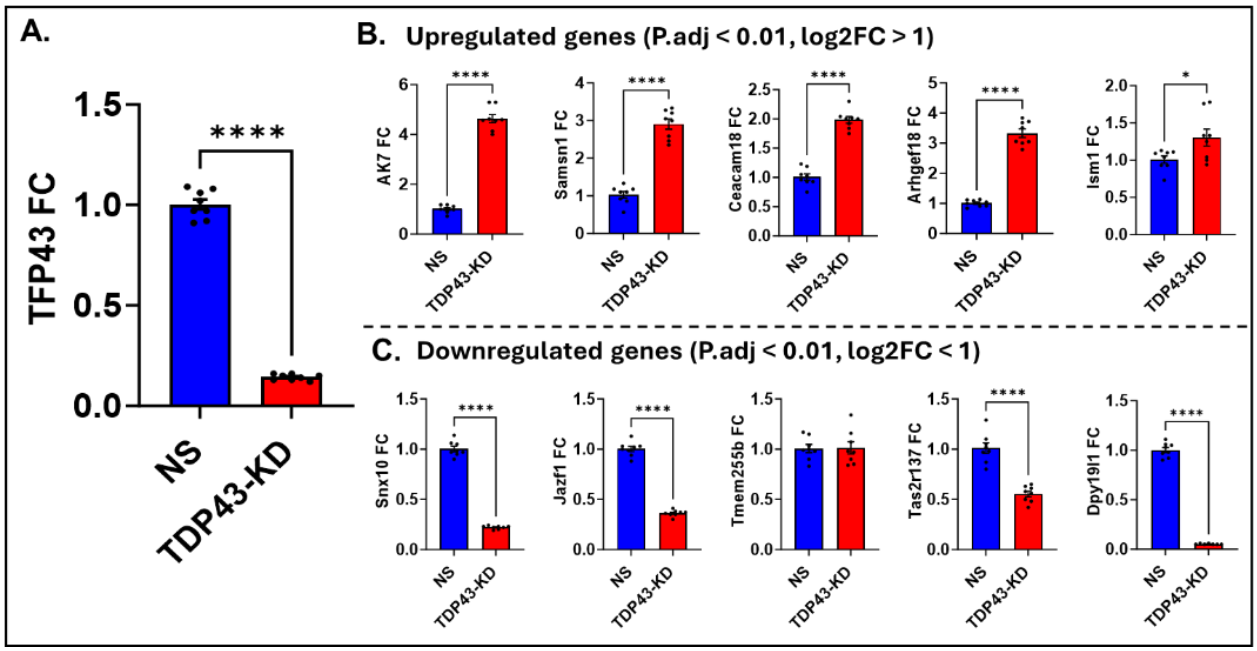

Figure 3.3 | Validation of RNA Sequencing Data via qPCR. (A) qPCR analysis confirms a significant reduction in TDP-43 transcript levels in the TDP-43-KD group compared to the NS control. (B) Fold changes in the expression of the top five upregulated genes identified from RNA sequencing. (C) Fold changes in the expression of the top five downregulated genes identified from RNA sequencing. Bars and error bars represent mean ± SEM (n = 8). Statistical tests: unpaired t-test with Welch correction (or Mann–Whitney U test for non-parametric data). Statistical significance: *p < 0.05; ****p < 0.001.

Pathway Analysis of Differentially Expressed Genes

The transcriptomic analysis of NSC34 motor neuron-like cells following TDP-43 knockdown revealed significant gene expression changes, necessitating further investigation into their biological impact. To identify key functional disruptions, differentially expressed genes (DEGs) were subjected to pathway enrichment analysis using established pathway databases. This analysis prioritized pathways related to metabolism, cellular stress responses, and neurodegenerative disease mechanisms.

Among the top 100 enriched pathways, upregulated genes were predominantly associated with metabolic processes, including carbohydrate metabolism, glycolysis, pyruvate metabolism, the citric acid cycle, and gluconeogenesis (Figure 3.4A). The overrepresentation of these pathways suggests a metabolic shift in TDP-43-deficient motor neurons, potentially reflecting a compensatory response to altered cellular energy demands. Additionally, upregulated genes mapped to pathways involved in cholesterol biosynthesis, oxidative stress responses, and mitochondrial function, further supporting the hypothesis that TDP-43 plays a central role in maintaining metabolic homeostasis.

In contrast, downregulated genes were enriched in pathways related to cell cycle regulation, mitotic processes, and RHO GTPase signaling (Figure 3.4B). The suppression of cell cycle-related pathways suggests potential impairments in neuronal maintenance and survival, although the relevance of these changes in post-mitotic motor neurons requires further investigation.

Overall, these findings highlight a strong link between TDP-43 dysfunction and metabolic dysregulation, reinforcing the hypothesis that ALS-related neurodegeneration may be driven, at least in part, by energy imbalance. To further characterize the metabolic adaptations triggered by TDP-43 depletion, the following sections will focus on targeted gene expression analysis of metabolic enzymes and transporters, functional metabolic assays, and dynamic metabolic flux measurements.

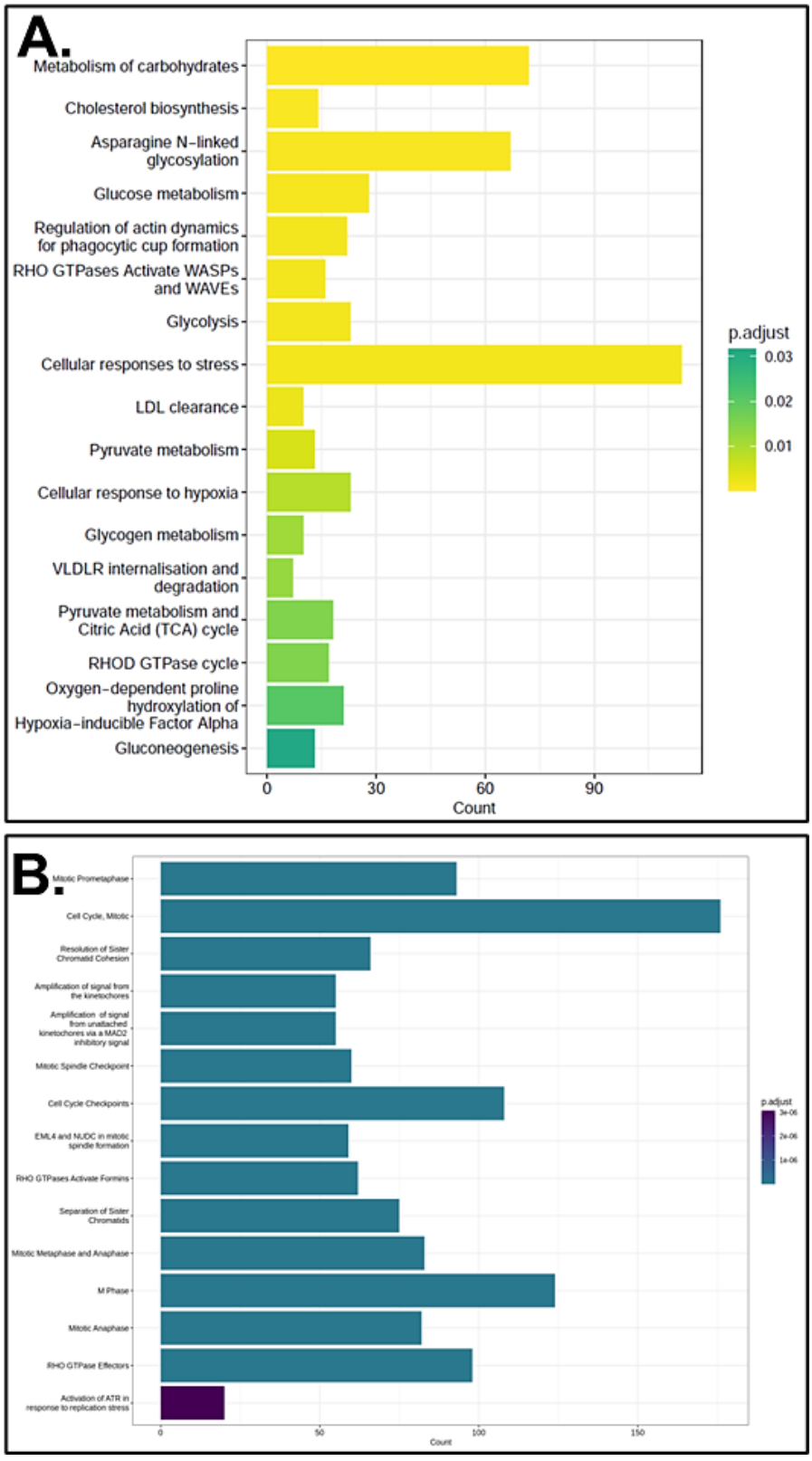

Figure 3.4 | Pathway Analysis of Differentially Expressed Genes in NSC34 motor neuron-like cells Following TDP-43 Knockdown. (A) Enrichment analysis of upregulated genes highlights pathways associated with energy metabolism, including glucose metabolism, glycolysis, pyruvate metabolism, and gluconeogenesis. (B) Enrichment analysis of downregulated genes shows pathways related to cell cycle regulation, mitotic processes, and RHO GTPase signaling. Statistical significance: p.adjust < 0.05.

Gene Expression Analysis of Metabolic Pathway Enzymes and Glucose Transporters in NSC34 motor neuron-like cells Following TDP-43 Knockdown

The enrichment analysis of differentially expressed genes in NSC34 motor neuron-like cells following TDP-43 knockdown revealed potential perturbations in energy metabolic pathways. To further characterize metabolic changes following TDP-43 knockdown, we assessed the expression of key metabolic enzymes and glucose transporters in NSC34 motor neuron-like cells. Gene expression analysis focused on enzymes involved in glucose metabolism, glycogen metabolism, and lipid metabolism, as well as glucose transporters and solute carriers.

Glucose Metabolism: For glucose metabolism, the gene expression of phosphofructokinase (PFK), isocitrate dehydrogenase (IDH), glucose-6-phosphate dehydrogenase (G6PD), and aldolase-B (ALDO-B) was analyzed (Figure 3.5A). qPCR results showed a significant increase in the expression of PFK and IDH suggestive of potentially enhanced glycolytic flux and citric acid cycle activity. However, no significant changes were observed in the expression of G6PD or ALDO-B.

Glycogen and Lipid Metabolism: In glycogen metabolism, we assessed the expression of glycogen synthase (GYS) and glycogen phosphorylase (PYGB) (Figure 3.5B). While GYS expression was significantly downregulated, PYGB showed no significant changes, indicating a shift away from glycogen synthesis and storage. For lipid metabolism, the expression of acetyl-CoA carboxylase (ACACB) and carnitine acetyltransferase (CRAT) was examined. ACACB exhibited a significant increase in expression, reflecting a potential upregulation of fatty acid biosynthesis, while CRAT expression remained unchanged.

Glucose Transporters and Solute Carriers: To further elucidate metabolic adaptations, we analyzed the expression of glucose transporters and solute carriers responsible for energy substrate uptake (Figure 3.5C). GLUT1 expression was significantly increased, suggesting enhanced glucose uptake to support the elevated energy demand. In contrast, GLUT3 and solute carriers SLC16A1 and SLC16A3 showed no significant changes in their expression levels.

These findings indicate a shift in metabolic enzyme expression following TDP-43 knockdown. The upregulation of PFK and IDH, key regulators of glycolysis and the TCA cycle, suggests an increase in glycolytic flux and mitochondrial metabolism. Simultaneously, the increase in GLUT1 expression is consistent with enhanced glucose uptake, potentially supporting the observed metabolic changes. The downregulation of glycogen synthase suggests a reduced emphasis on glycogen storage, possibly favoring immediate glucose utilization. Taken together, these expression changes provide molecular

evidence for a metabolic shift in NSC34 motor neuron-like cells, characterized by increased glucose uptake and utilization, with potential implications for cellular energy balance.

Pyruvate Metabolism in NSC34 motor neuron-like cells Following TDP-43 Knockdown

Given the observed upregulation of key glycolytic components, such as PFK and GLUT1, in NSC34 motor neuron-like cells following TDP-43 knockdown, we next investigated the fate of pyruvate, a critical end product of glycolysis. Pyruvate can be metabolized through two primary pathways: it may undergo reduction by lactate dehydrogenase (LDH) to produce lactate or oxidative decarboxylation by the pyruvate dehydrogenase complex (PDC) to generate acetyl-CoA. The metabolic route depends on the cellular metabolic state and energy demands. To assess these pathways, we analyzed the expression of genes encoding LDH and components of the PDC, including pyruvate dehydrogenase subunits a1 and a2 (PDHa1 and PDHa2). Our qPCR analysis revealed a significant increase in the expression of PDHa1, indicating a preference for the conversion of pyruvate to acetyl-CoA under TDP-43 knockdown conditions (Figure 3.6A). In parallel, we examined the expression of regulatory elements involved in PDC activity, such as pyruvate dehydrogenase phosphorylase (PDP1) and pyruvate dehydrogenase kinases (PDK1-4). Among these, PDK1 showed a notable increase in expression, further supporting the hypothesis of altered pyruvate metabolism.

The observed increase in PDHa1 expression suggests that pyruvate metabolism is directed toward oxidative decarboxylation rather than lactate fermentation in NSC34 motor neuron-like cells following TDP-43 knockdown. These findings, together with previous results indicating increased glycolytic enzyme expression, suggest that TDP-43 knockdown promotes enhanced glycolytic flux while favoring oxidative metabolism over anaerobic lactate production.

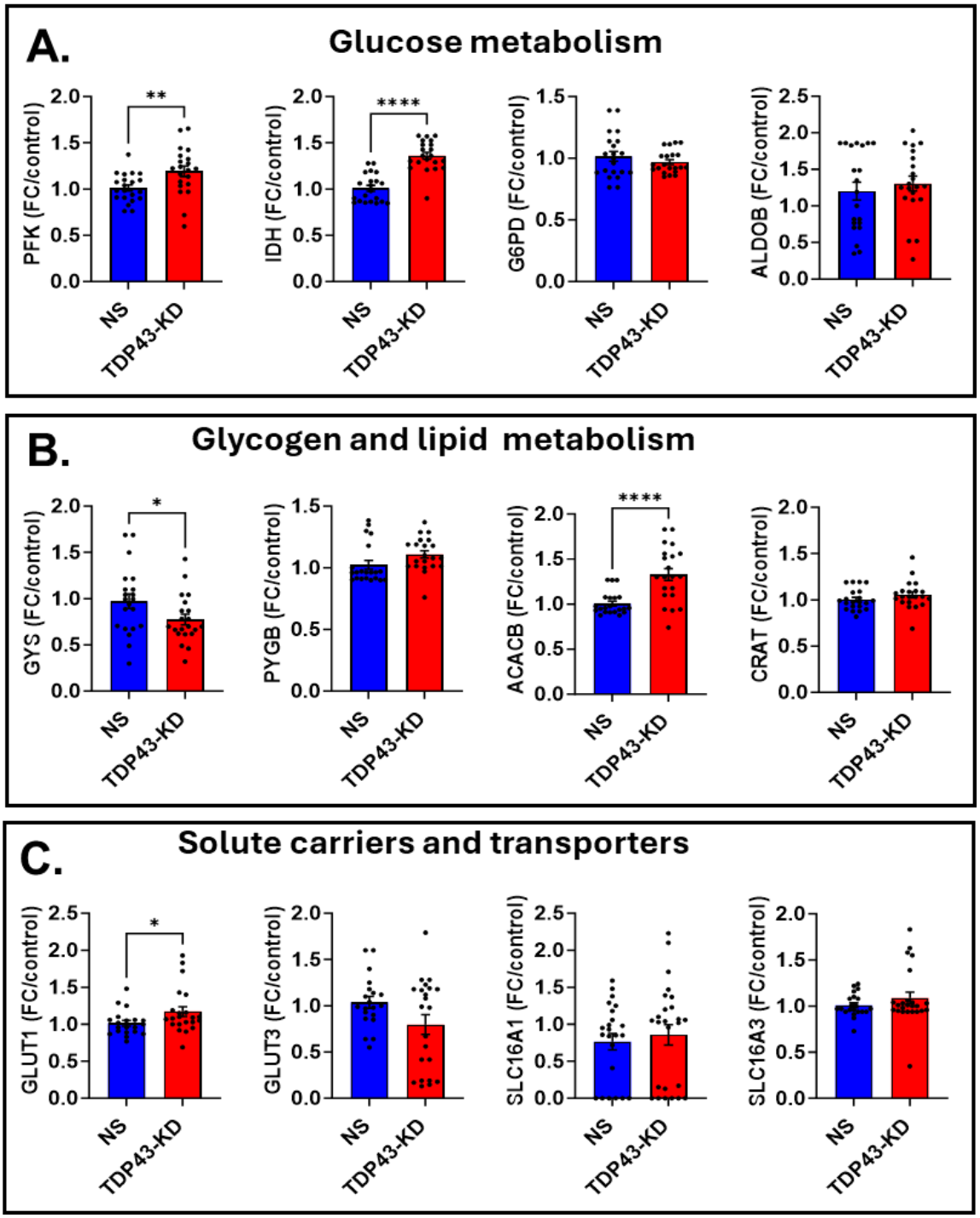

Figure 3.5 | Gene Expression Analysis of Metabolic Enzymes and Glucose Transporters in NSC34 motor neuron-like cells Following TDP-43 Knockdown. (A) qPCR analysis of glucose metabolism-related enzymes, including phosphofructokinase (PFK), isocitrate dehydrogenase (IDH), glucose-6-phosphate dehydrogenase (G6PD), and aldolase B (ALDO-B). (B) Expression levels of enzymes involved in glycogen and lipid metabolism, including glycogen synthase (GYS), glycogen phosphorylase (PYGB), acetyl-CoA carboxylase beta (ACACB), and carnitine acetyltransferase (CRAT). (C) Expression analysis of glucose transporters and solute carriers, including GLUT1, GLUT3, SLC16A1, and SLC16A3. Data are mean ± SEM (n = 3 biological replicates). Statistical tests: unpaired t-test (Welch's correction) or Mann–Whitney U test. Statistical significance: *$p < 0.05$; **$p < 0.01$; ****$p < 0.001$.

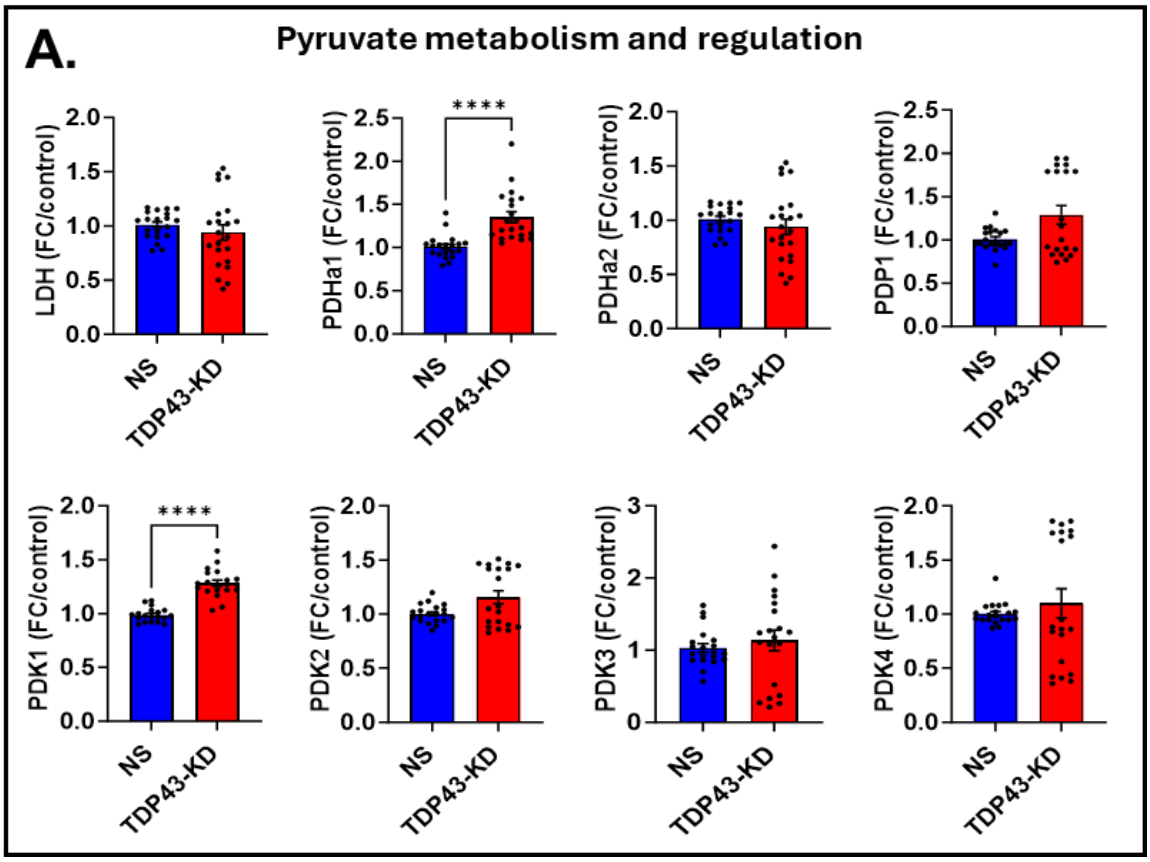

Figure 3.6 | Gene Expression Analysis of Pyruvate Metabolism Enzymes in NSC34 motor neuron-like cells Following TDP-43 Knockdown. qPCR analysis of genes involved in pyruvate metabolism, including lactate dehydrogenase (LDH), pyruvate dehydrogenase subunits alpha 1 (PDHA1) and alpha 2 (PDHA2), pyruvate dehydrogenase phosphatase 1 (PDP1), and pyruvate dehydrogenase kinases 1–4 (PDK1–PDK4)**.** Data are mean ± SEM (n ≥ 3 biological replicates). Statistical tests: unpaired t-test (Welch's correction) or Mann–Whitney U test. Statistical significance: ****p < 0.001.

Metabolic Cofactor Dynamics in NSC34 motor neuron-like cells Following TDP-43-KD

IDH catalyzes the conversion of isocitrate to α-ketoglutarate, a critical step in the TCA cycle that generates NADH, supporting ATP production and providing intermediates for biosynthesis. Given evidence suggesting a metabolic shift in NSC34 motor neuron-like cells toward acetyl-CoA, a key TCA precursor, we investigated changes in NAD, NADH, NADP, and NADPH at 24 and 48 hours post-TDP-43-KD (Figure 3.7A). Our analysis revealed a significant increase in NAD+ and a decrease in NADH at both time points, resulting in a marked elevation in the NAD+/NADH ratio in TDP-43-KD cells compared to controls (Figures 3.7B and 3.7C). This suggests a metabolic shift favoring oxidative metabolism, likely reflecting enhanced mitochondrial activity and cellular respiration. In contrast, NADP+ and NADPH levels were significantly reduced in the TDP-43-KD group at both time points, with a substantial increase in the NADP/NADPH ratio observed only at 48 hours (Figures 3.7D and

3.7E). The increase in NAD+ and the elevated NAD+/NADH ratio indicate a metabolic shift favoring oxidative metabolism, which aligns with previous observations of enhanced glycolytic enzyme expression and mitochondrial respiration. The concurrent decrease in NADPH suggests a potential reduction in anabolic and antioxidant capacity, as NADPH is a critical cofactor for biosynthetic reactions and redox homeostasis. These findings collectively indicate that TDP-43 knockdown alters metabolic cofactor balance, reinforcing a shift toward oxidative metabolism while potentially impacting cellular redox regulation.

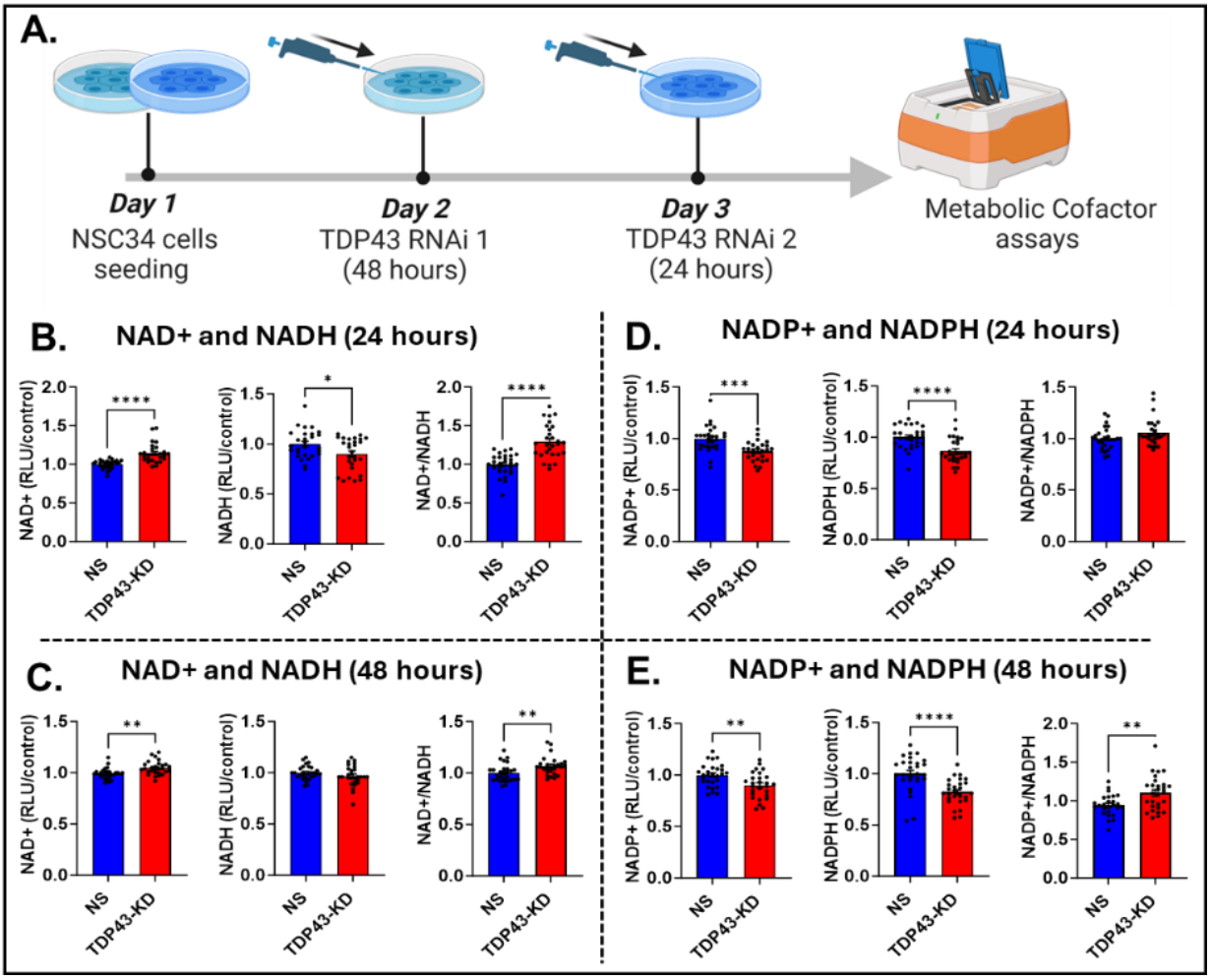

Figure 3.7 | Metabolic Cofactor Analysis in NSC34 motor neuron-like cells Following TDP-43 Knockdown. (A) Schematic representation of the workflow for metabolic cofactor assays at 24 and 48 hours post-TDP-43 RNAi. (B-C) Quantification of NAD+ and NADH levels and their ratio. (D-E) Quantification of NADP+ and NADPH levels and their ratio.**).** Data are mean ± SEM (n ≥ 3 biological replicates). Statistical tests: unpaired t-test (Welch's correction) or Mann–Whitney U test. Statistical significance: *p < 0.05; **p < 0.01; ***p < 0.005; ****p < 0.001.

Glucose Consumption in NSC34 Motor Neuron Following TDP-43-KD

The transcriptomic and metabolic cofactor analyses described earlier revealed significant perturbations in metabolic pathways following TDP-43 KD in NSC34 motor neuron-like cells, with a particular emphasis on glucose metabolism. To further investigate these findings, we conducted functional assessments to evaluate the cellular response to TDP-43-KD at the metabolic level. Substrate levels in the culture media were monitored at 6-, 24-, and 48-hours post-seeding and transfection with TDP-43-specific siRNA (Figure 3.8A). The consumed media analysis focused on glucose, lactate, and glutamine levels to understand the dynamic changes in metabolic substrate utilization. As shown in Figure 3.8B, lactate levels increased progressively over time in both the TDP-43-KD and NS groups, suggesting active glycolytic flux in both conditions. Glutamine levels, in contrast, decreased over time without significant differences between the groups, indicating that glutamine utilization was not significantly affected by TDP-43-KD. Importantly, glucose levels in the consumed media were markedly lower in TDP-43-KD cells at 24 and 48 hours compared to the NS controls, reflecting increased glucose consumption following TDP-43 loss-of-function.

To validate the enhanced glucose consumption observed in the media analysis, glucose uptake assays were performed at 24 and 48 hours (Figure 3.8C). The results confirmed a significant increase in glucose uptake in the TDP-43-KD cells relative to the NS controls at both time points. This increased glucose uptake aligns with the transcriptomic findings, which highlighted the upregulation of key glycolytic enzymes and glucose transporters and further supports the notion of metabolic adaptation to meet the heightened energy demands imposed by TDP-43 dysfunction. Given the increased glucose uptake and its likely utilization for energy production, we assessed intracellular ATP levels to determine how these metabolic changes impacted cellular energy status (Figure 3.8D). Intracellular ATP levels were significantly elevated in the TDP-43-KD cells at both 24 and 48 hours, with nearly a 50% increase observed compared to the NS controls. This substantial rise in ATP levels underscores a metabolic shift favoring energy production, likely driven by increased glycolysis and mitochondrial oxidative phosphorylation, as suggested by earlier analyses.

These findings indicate that TDP-43 knockdown enhances glucose consumption and uptake, which is accompanied by increased ATP production. The elevated ATP levels suggest a shift in metabolic activity that prioritizes energy generation, consistent with previous observations of upregulated glycolytic enzyme expression. The concurrent rise in lactate levels, alongside increased glucose uptake, supports the notion of augmented glycolytic flux, reinforcing a metabolic state characterized by increased energy turnover.

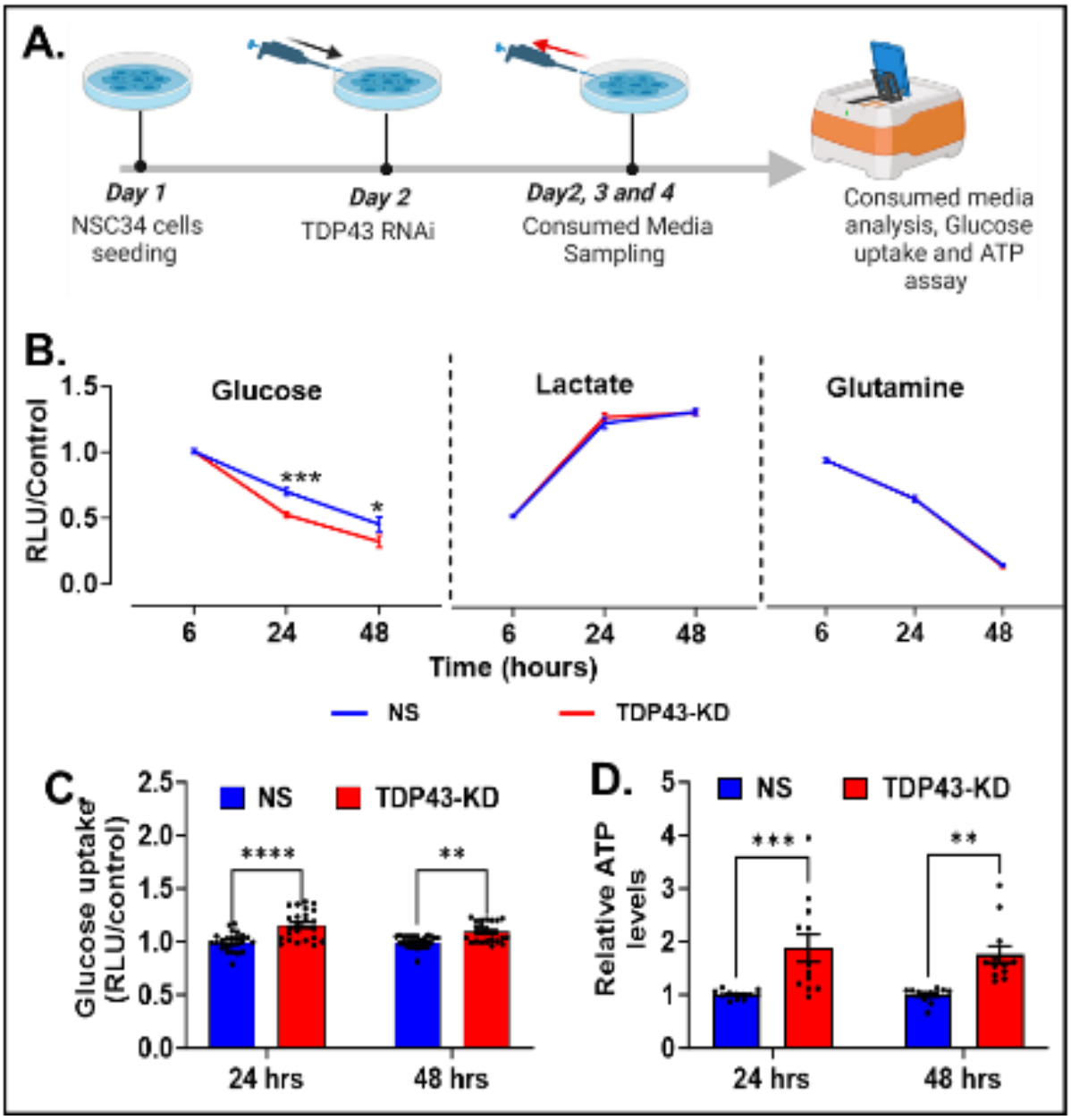

Figure 3.8 | Functional Assessments of Glucose Consumption, Uptake, and ATP Production in NSC34 motor neuron-like cells Following TDP-43 Knockdown. (A) Schematic representation of the experimental workflow for media analysis conducted at 6-, 24-, and 48-hours post-transfection. (B) Time-course plot depicting changes in glucose, lactate, and glutamine concentrations in the media. (C) Glucose uptake assay measurements at 24 and 48 hours post-transfection. (D) Intracellular ATP levels at 24- and 48-hours post-transfection. Statistical analysis: two-way repeated-measures ANOVA with Šidák's post hoc test for time courses (B); unpaired t-test (Welch's correction) or Mann-Whitney U test for bar graphs (C_D). Significance: *p < 0.05; **p < 0.01; ***p < 0.005; ****p < 0.001.

Dynamic Glucose Metabolic Mapping in NSC34 motor neuron-like cells following TDP-43 Knockdown

Building upon the increased glucose consumption observed in earlier experiments, we sought to gain deeper insights into how glucose is metabolized by NSC34 motor neuron-like cells under TDP-43 knockdown conditions. To achieve this, we performed dynamic glucose metabolic mapping by incubating the cells with U-13C-labeled glucose and employing GC-MS to track carbon-13 incorporation into key glycolytic and TCA cycle intermediates (Figure 3.9A). This approach allowed us to quantify isotopologues (e.g., M+2 or M+3) and molecular carbon labeling (MCL) for metabolites such as lactate, citrate, α-ketoglutarate, succinate, fumarate, and malate, providing a comprehensive view of altered glucose metabolism.

Analysis of the percentage of labeled carbon-13 in lactate isotopologues (M+3) and their MCL revealed no significant changes between TDP-43-KD and NS cells (Figure 3.9B). However, significant alterations were observed in TCA cycle intermediates, reflecting metabolic reprogramming induced by TDP-43 knockdown. Citrate exhibited a marked increase in both the percentage of labeled carbon-13 (M+2) and its MCL, indicating enhanced citrate synthesis (Figure 3.9C). Similarly, α-ketoglutarate showed a significant rise in labeled carbon-13 (M+2) and its MCL, suggesting increased production of this key metabolite (Figure 3.9D). Succinate demonstrated a significant increase in labeled carbon-13 (M+2) but a concomitant decrease in MCL, indicating potential disruptions in succinate metabolism (Figure 3.9E). In contrast, fumarate exhibited a significant reduction in labeled carbon-13 (M+2) with no changes in MCL, reflecting distinct metabolic perturbations (Figure 3.9F). Malate showed both a significant increase in labeled carbon-13 (M+2) and a corresponding rise in its MCL, suggesting heightened metabolic flux through this pathway (Figure 3.9G).

These results indicate that TDP-43 knockdown promotes a metabolic shift characterized by increased glucose-derived carbon flux into the TCA cycle rather than enhanced lactate production. The elevation of labeled carbon in citrate, α-ketoglutarate, and malate suggests that pyruvate is preferentially funneled into mitochondrial oxidative metabolism, supporting previous observations of increased oxidative phosphorylation and ATP production. This metabolic reorganization may reflect an adaptive response to increased energy demands following TDP-43 knockdown.

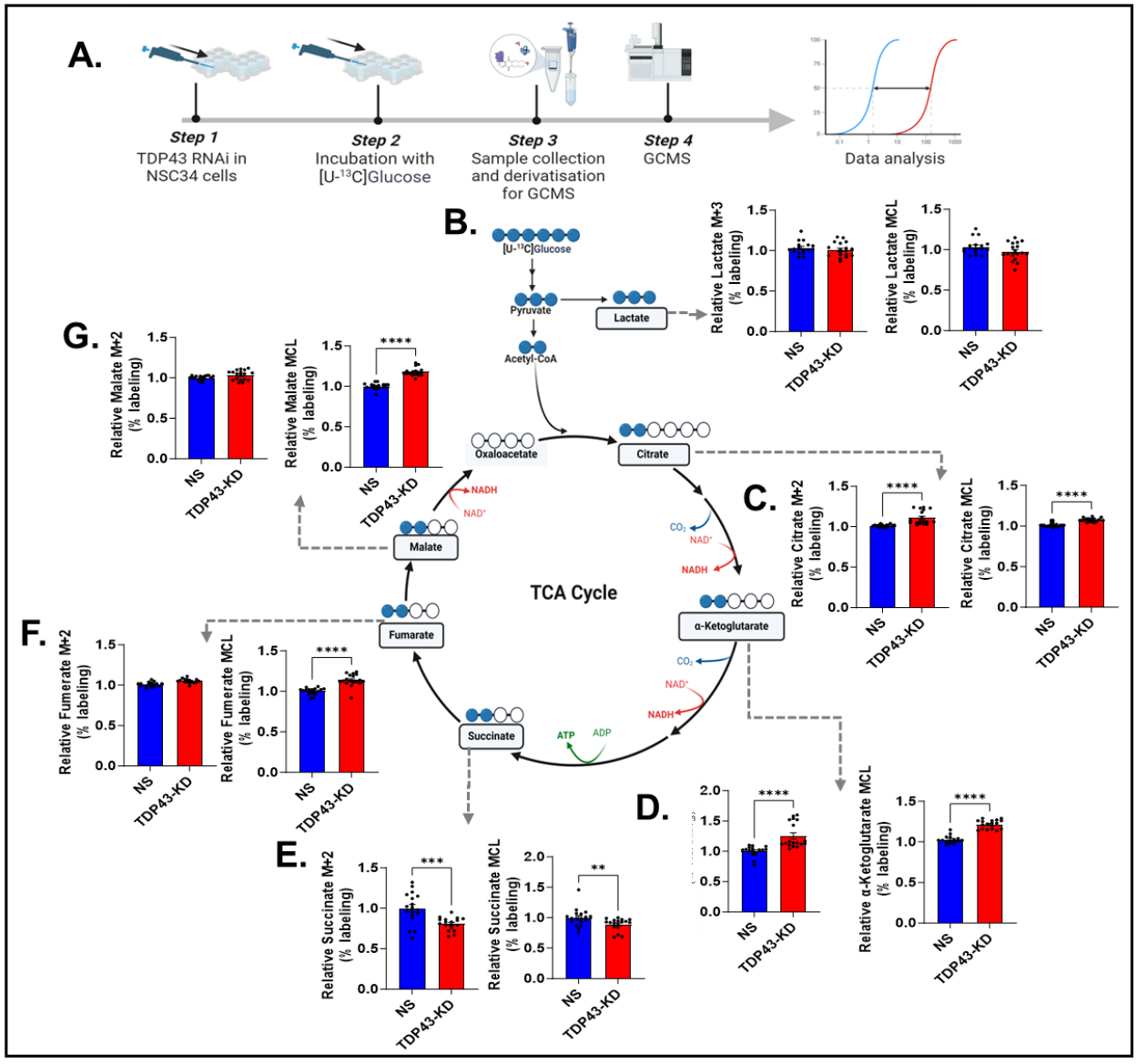

Figure 3.9 | Dynamic Glucose Metabolic Mapping in NSC34 motor neuron-like cells Following TDP-43 Knockdown. (A) Schematic representation of the experimental workflow: NSC34 motor neuron-like cells were subjected to TDP-43 RNAi, incubated with U-13C-labeled glucose, followed by sample collection, derivatization, and GC-MS analysis to track carbon-13 incorporation into glycolytic and TCA cycle intermediates. (B-G) Quantification of isotopologues (e.g., M+2 or M+3) and molecular carbon labeling (MCL) for key metabolic intermediates, including lactate, citrate, α-ketoglutarate, succinate, fumarate, and malate. TDP-43 knockdown significantly altered labeled carbon-13 incorporation in citrate, α-ketoglutarate, succinate, fumarate, and malate. Data are mean ± SEM (n ≥ 3 biological replicates). Statistical tests: unpaired t-test (Welch's correction) or Mann–Whitney U test. Statistical significance: **p < 0.01; ***p < 0.005; ****p < 0.001.

Metabolic flux analysis in NSC34 following TDP-43 knockdown.

Building on our findings that TDP-43 knockdown enhances glucose metabolism and elevates ATP production in NSC34 motor neuron-like cells, we explored the functional consequences of this metabolic shift by analyzing the respiratory status of the cells. ATP production in eukaryotic cells arises primarily from two sources: glycolysis, which generates modest amounts of ATP in the cytoplasm, and oxidative phosphorylation, which produces the majority of ATP through mitochondrial respiration. To comprehensively assess the metabolic reprogramming induced by TDP-43 knockdown, we performed metabolic flux analysis to analyze both glycolytic and mitochondrial contributions to ATP generation using the glycolytic stress test and mitochondrial stress test (Figure 3.10A).

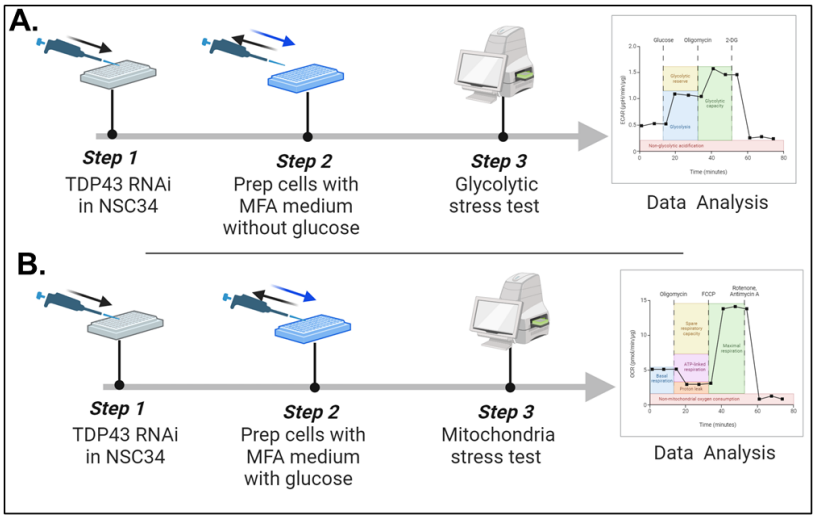

Figure 3.10 | Workflow for Metabolic Flux Analyses in NSC34 motor neuron-like cells Following TDP-43 Knockdown. (A) Glycolytic Stress Test (GST): Assesses ECAR at baseline and after sequential injections of glucose, oligomycin, and 2-DG. **(B)** Mitochondrial Stress Test (MST): Measures OCR at baseline and after sequential injections of oligomycin, FCCP, and rotenone/antimycin-A.

Glycolysis in NSC34 motor neuron-like cells following TDP-43-KD

To investigate the functional alterations in glycolytic activity induced by TDP-43 knockdown in NSC34 motor neuron-like cells, we performed a glycolytic stress test (GST), which measures the extracellular acidification rate (ECAR) as a proxy for glycolytic flux. Cells were first subjected to glucose deprivation for one hour to establish basal glycolytic activity under glucose-starved conditions. During this deprivation period, ECAR values in the TDP-43-KD group were comparable to those in the NS control group, indicating similar baseline glycolytic activity. Upon the addition of glucose, ECAR levels increased significantly in both groups, reflecting the activation of glycolysis. This increase was

markedly higher in the TDP-43-KD group, demonstrating an enhanced glycolytic response. Following oligomycin injection, which inhibits mitochondrial ATP production and forces cells to rely entirely on glycolysis, ECAR levels surged further in both groups. Once again, the TDP-43-KD group exhibited a significantly greater increase in ECAR compared to the NS control group, underscoring a heightened glycolytic capacity. Finally, 2-deoxyglucose (2-DG), a glycolysis inhibitor, reduced ECAR to baseline levels in both groups, confirming that the observed ECAR changes were glycolysis-dependent. Quantitative analysis revealed significant enhancements in glycolysis, glycolytic capacity, and glycolytic reserve in the TDP-43-KD group compared to NS controls.

Mitochondrial Respiration in NSC34 motor neuron-like cells following TDP-43-KD

To elucidate alterations in mitochondrial oxidative metabolism within NSC34 motor neuron-like cells following TDP-43 knockdown, we conducted a mitochondrial stress test (MST) to measure oxygen consumption rate (OCR) at baseline and after sequential injections of oligomycin (an ATP synthase inhibitor), FCCP (a mitochondrial membrane uncoupler), and a combination of rotenone and antimycin-A (inhibitors of mitochondrial complexes I and III). At baseline, the TDP-43-KD group exhibited a higher OCR compared to the NS control group, indicating an increase in oxidative metabolism as a result of TDP-43 knockdown (Figure 3.12A). Following the injection of oligomycin, OCR decreased significantly in both groups to comparable levels, reflecting oxygen consumption associated with proton leak. However, after mitochondrial membrane uncoupling with FCCP, OCR increased markedly in both groups, with the TDP-43-KD group demonstrating a significantly greater increase. This finding suggests enhanced oxidative capabilities in the motor neurons under TDP-43 knockdown conditions. Subsequent injection of rotenone and antimycin-A brought OCR levels below baseline to similar levels in both groups, representing non-mitochondrial oxygen consumption. Quantitative analysis further revealed significant enhancements in basal respiration, maximal respiration, ATP production, and spare respiratory capacity in the TDP-43-KD group compared to the NS controls (Figure 3.12B).

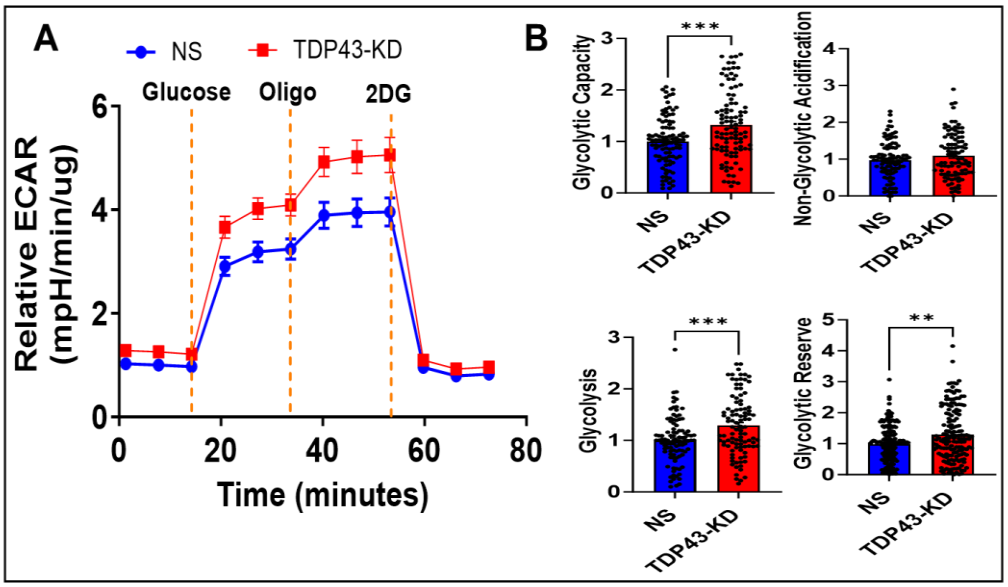

Figure 3.11 | Glycolytic Response in NSC34 motor neuron-like cells Following TDP-43 Knockdown. (A) Extracellular acidification rate (ECAR) measured at baseline and after sequential injections of glucose, oligomycin, and 2-deoxyglucose (2-DG). TDP-43-KD cells exhibit significantly elevated ECAR compared to NS controls, indicating enhanced glycolysis and glycolytic capacity. (B) Quantitative bar plots comparing glycolysis, glycolytic capacity, and glycolytic reserve between TDP-43-KD and NS cells. Data are mean ± SEM (n = 3 biological replicates). Statistical tests: unpaired t-test (Welch's correction) or Mann–Whitney U test. Statistical significance: **p < 0.01; ***p < 0.005.

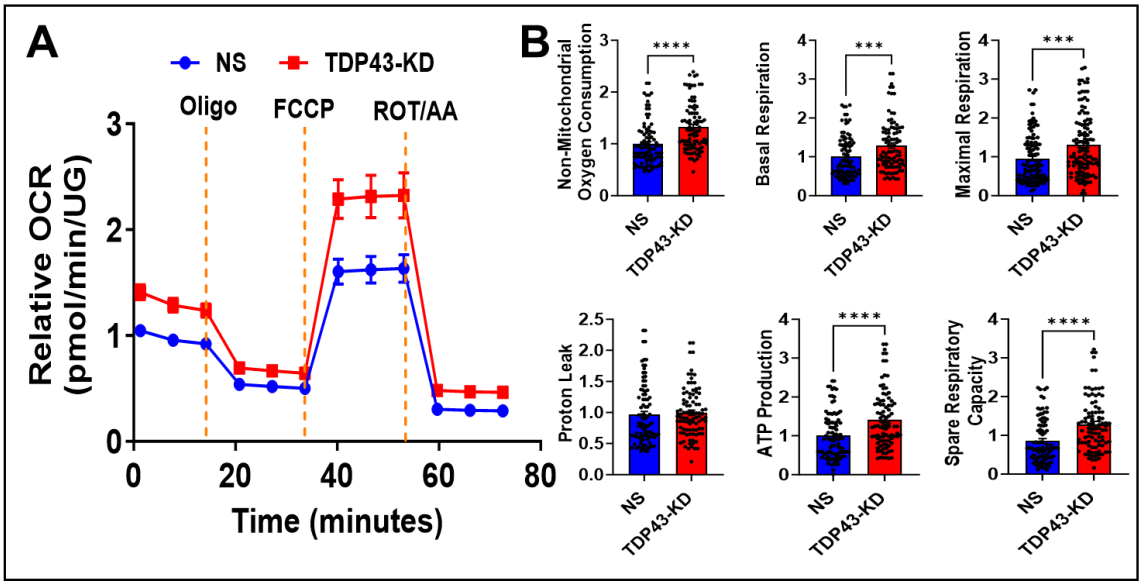

Figure 3.12 | Assessment of Oxidative Phosphorylation in NSC34 motor neuron-like cells Following TDP-43 Knockdown. (A) Oxygen consumption rate (OCR) measured at baseline and after sequential injections of oligomycin, FCCP, and rotenone/antimycin-A. The TDP-43-KD group shows elevated OCR at baseline and a marked increase in OCR after FCCP injection compared to the NS control group. (B) Quantitative analysis of basal respiration, maximal respiration, ATP production, and spare respiratory capacity, demonstrating significant enhancements in all parameters in the TDP-43-KD group relative to controls. Data are mean ± SEM (n = 3 biological replicates). Statistical tests: unpaired t-test (Welch's correction) or Mann–Whitney U test. Statistical significance: ***p < 0.005; ****p < 0.001.

Mitochondrial Respiratory Complexes and Structural Integrity in NSC34 motor neuron-like cells following TDP-43-KD

The mitochondrial stress test revealed a significant increase in the oxygen consumption rate (OCR) in TDP-43-KD NSC34 motor neuron-like cells, correlating with heightened basal respiration, maximal respiration, and ATP-linked OCR. However, no changes were observed in proton leak between the TDP-43-KD and control groups (Figure 3.12B). To investigate the underlying cause of this enhanced oxidative phosphorylation, we hypothesized that the increase in OCR might result from alterations in the expression levels of respiratory complexes or mitochondrial density.

Western blot analysis of mitochondrial respiratory complexes revealed no significant differences in protein expression between the TDP-43-KD and control groups (Figure 3.13A-B). Similarly, mitochondrial density assessed using MitoTracker staining showed no observable differences in staining intensity or mitochondrial localization between the groups (Figure 3.13C). These findings suggest that the enhanced oxidative phosphorylation observed in TDP-43-KD motor neurons is not driven by changes in the abundance of mitochondrial respiratory complexes or alterations in mitochondrial density. Instead, it highlights that the observed metabolic adaptation likely occurs without compromising the structural integrity of the mitochondria.

Together, these findings demonstrate that TDP-43 knockdown enhances both glycolysis and oxidative phosphorylation in NSC34 motor neuron-like cells, leading to a metabolic profile characterized by increased glycolytic capacity, mitochondrial respiration, and ATP production. This metabolic shift suggests that cells responds to TDP-43 loss by increasing energy metabolism, likely to sustain cellular function under altered physiological conditions. However, the concurrent upregulation of both glycolysis and oxidative phosphorylation indicates a state of heightened energy demand, which may impose additional metabolic stress on these cells.

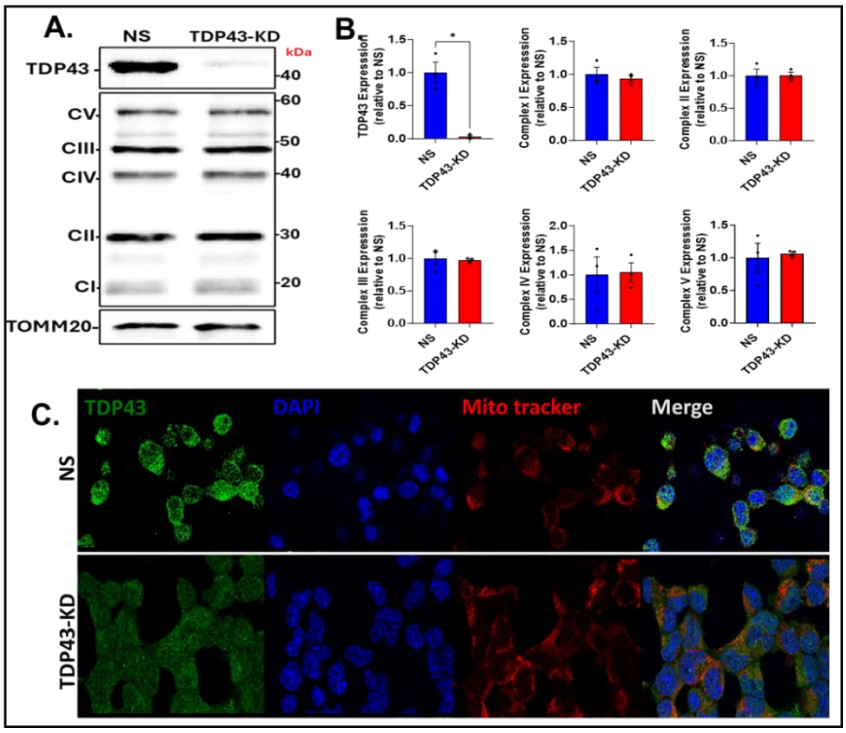

Figure 3.13 | Respiratory Complexes and Mitochondrial Density in NSC34 motor neuron-like cells Following TDP-43 Knockdown. (A) Western blot analysis of mitochondrial respiratory complexes. (B) Quantitative assessment of respiratory complex protein expression. (C) MitoTracker staining of NSC34 motor neuron-like cells showing mitochondrial localization.

NSC34 motor neuron redox status in TDP-43 Knockdown

In light of the observed alterations in glucose metabolism, glycolysis, and oxidative phosphorylation, we extended our investigation to examine the oxidative stress response and the intrinsic antioxidant defense system in NSC34 motor neuron-like cells following TDP-43 knockdown. Oxidative stress arises when reactive oxygen species (ROS) production exceeds the capacity of the antioxidant defense system, disrupting cellular redox homeostasis. This imbalance is a hallmark of many neurodegenerative diseases and may provide critical insights into the downstream effects of TDP-43 dysfunction.

Using the established transfection protocol, we assessed ROS levels and glutathione activity at 24 and 48 hours post-TDP-43 knockdown. At 24 hours, a significant increase in ROS levels was observed in the TDP-43 knockdown group compared to the NS control group, indicating heightened oxidative stress (Figure 3.14A). Concurrently, there was a marked reduction in total glutathione levels, a key cellular antioxidant. This reduction was coupled with a significant increase in the ratio of oxidized to reduced glutathione, reflecting a shift toward a more oxidized cellular environment and a compromised redox balance. By the 48-hour time point, ROS levels remained significantly elevated,

suggesting a sustained oxidative stress response (Figure 3.14B). Notably, while total glutathione levels did not show further depletion, the oxidized-to-reduced glutathione ratio continued to increase, indicating persistent redox imbalance. These changes highlight the inability of the glutathione system to adequately counteract the excessive ROS generated following TDP-43 knockdown.

These findings suggest that TDP-43 knockdown induces oxidative stress and disrupts redox homeostasis in NSC34 motor neuron-like cells, as evidenced by increased ROS accumulation and depletion of glutathione. The sustained rise in the oxidized-to-reduced glutathione ratio suggests an inability to counteract excessive ROS production, potentially exposing the cells to oxidative damage. This redox imbalance may contribute to cellular vulnerability, particularly under conditions of heightened metabolic activity.

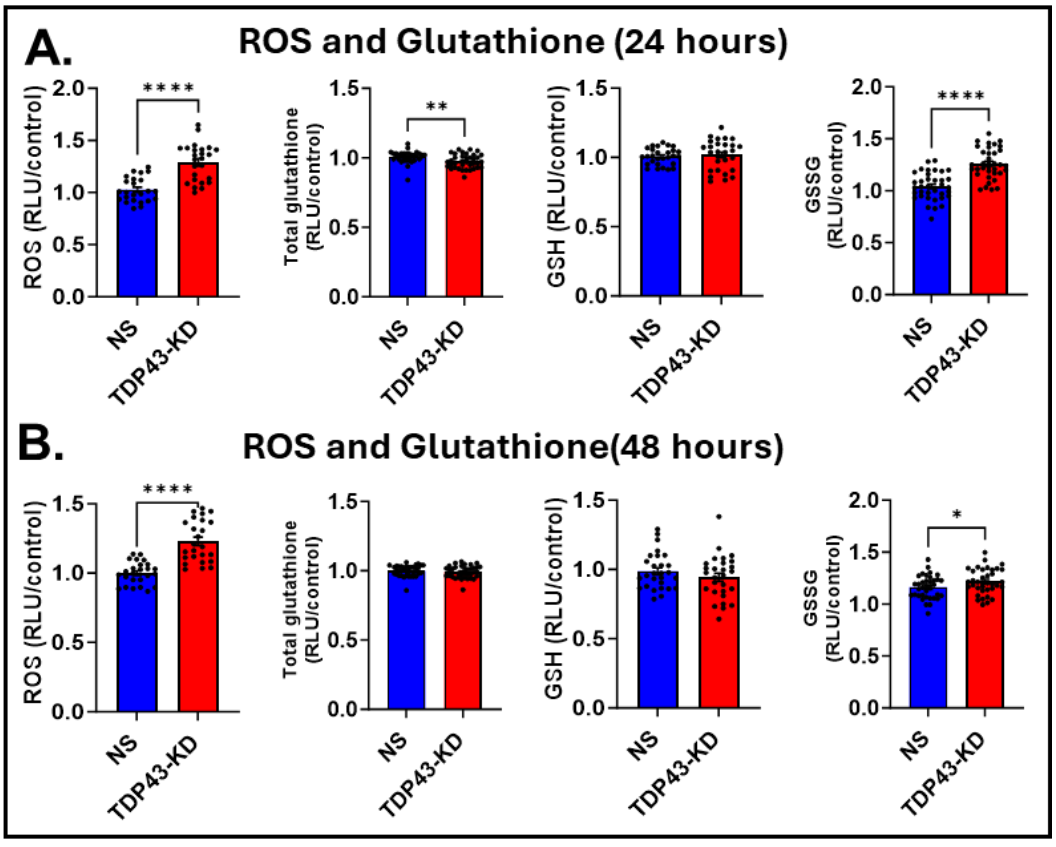

Figure 3.14 | Oxidative Stress Response in NSC34 motor neuron-like cells Following TDP-43 Knockdown. (A) ROS levels and glutathione activities at 24 hours post-TDP-43 knockdown. (B) ROS levels and glutathione activities at 48 hours post-TDP-43 knockdown. Data are mean ± SEM (n = 3 biological replicates). Statistical tests: unpaired t-test (Welch's correction) or Mann–Whitney U test. Statistical significance: *p < 0.05; **p < 0.01; ****p < 0.001.

TDP-43 RNAi Rescue

Restoring Glucose Metabolism and ROS Dynamics

The knockdown of TDP-43 in NSC34 motor neuron-like cells induces a profound metabolic reprogramming. To ensure that these effects are directly attributable to TDP-43 knockdown and not off-target RNAi effects, we conducted RNAi rescue experiments. The mouse TDP-43 open reading frame (mTDP-43) was cloned into a pcDNA3 plasmid vector containing a GFP tag (Figure 3.15A), with an empty vector expressing GFP serving as a control. Plasmid integrity and the presence of mTDP-43 were validated through restriction enzyme digestion and gel electrophoresis, which revealed distinct band patterns (Figure 3.15B). Successful transfection of these plasmids into NSC34 motor neuron-like cells was confirmed by GFP expression observed under confocal microscopy (Figure 3.15C).

Following transfection, qPCR and Western blot analyses confirmed the restoration of TDP-43 expression. At the transcriptional level, qPCR revealed a significant increase in TDP-43 mRNA levels in cells expressing mTDP-43 compared to GFP controls (Figure 3.15D). Similarly, Western blot analysis demonstrated a marked increase in TDP-43 protein levels, validating successful RNAi rescue at the protein level (Figure 3.15E-F).

Functional analyses assessed the impact of RNAi rescue on glucose metabolism and oxidative stress across three groups: NS+GFP, TDP-43-KD+GFP, and TDP-43-KD+mTDP. At 24 hours post-transfection, glucose consumption was significantly higher in TDP-43-KD+mTDP cells compared to TDP-43-KD+GFP cells, partially rescuing the glucose dysregulation observed in TDP-43 knockdown. By 48 hours, glucose consumption in the TDP-43-KD+mTDP group normalized to levels comparable to the NS control group (Figure 3.15G). Glucose uptake assays similarly demonstrated restoration in the TDP-43-KD+mTDP group compared to GFP controls, confirming the efficacy of TDP-43 rescue in mitigating glucose dysregulation (Figure 3.15H).

Notably, ROS levels were further elevated in TDP-43-KD cells expressing mTDP-43 compared to GFP controls (Figure 3.15I), suggesting a complex trade-off between restoring glucose metabolism and managing oxidative stress. These results underscore the central role of TDP-43 in balancing metabolic demands and redox homeostasis in motor neurons.

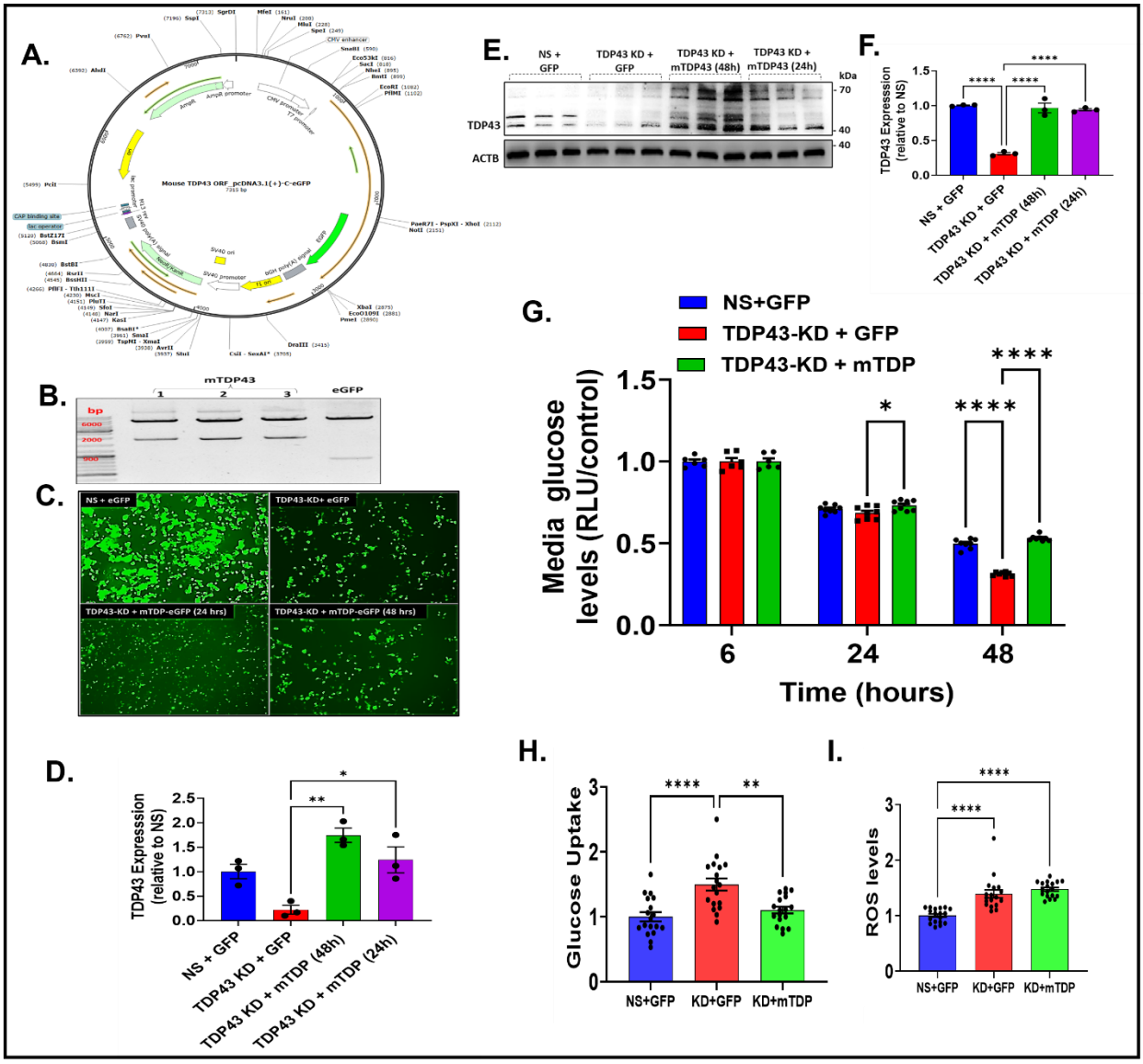

Figure 3.15 | TDP-43 RNAi Rescue in NSC34 motor neuron-like cells. (A) Schematic representation of the plasmid construct containing the mouse TDP-43 open reading frame (mTDP-43) with a GFP tag for RNAi rescue. (B) Gel electrophoresis analysis confirming plasmid integrity. (C) Confocal microscopy image showing GFP expression, verifying successful plasmid transfection. (D) qPCR analysis of TDP-43 transcript levels following RNAi rescue. (E-F) Western blot analysis of TDP-43 protein levels. (G) Glucose consumption measured at 6-, 24-, and 48-hours post-transfection. (H) Glucose uptake levels at 24- and 48-hours post-transfection. (I) Reactive oxygen species (ROS) levels at 24 hours post-transfection. Data are mean ± SEM (n ≥ 3 biological replicates). Statistical analysis: one-way ANOVA with Tukey's multiple comparisons test for multi-group bar graphs; two-way repeated-measures ANOVA with Šidák's post hoc test for time courses Statistical significance: *p < 0.05; **p < 0.01; ****p < 0.001.

Metabolic Flux Analysis Post-RNAi Rescue

To further evaluate the metabolic rescue, we performed metabolic flux analyses, including glycolytic and mitochondrial stress tests. In the glycolytic stress test (Figure 3.17A-B), TDP-43 knockdown led to a significant increase in glycolytic reserve, indicating a heightened reliance on glycolysis. However, mTDP-43 expression effectively reversed this increase, restoring glycolytic reserve to levels comparable to the NS control group. Similarly, the mitochondrial stress test (Figure 3.17C-D) demonstrated that TDP-43 knockdown elevated basal respiration, maximal respiration, and spare respiratory capacity, indicative of enhanced oxidative metabolism. mTDP-43 expression significantly reduced these parameters, normalizing them to levels observed in the NS control group.

These findings demonstrate the capacity of mTDP-43 to mitigate the metabolic maladaptation induced by TDP-43 knockdown, highlighting the reversibility of glycolytic and mitochondrial abnormalities upon TDP-43 restoration. This strongly supports the conclusion that the observed metabolic changes are specific to TDP-43 knockdown and validates RNAi as a reliable model for studying TDP-43 loss-of-function.

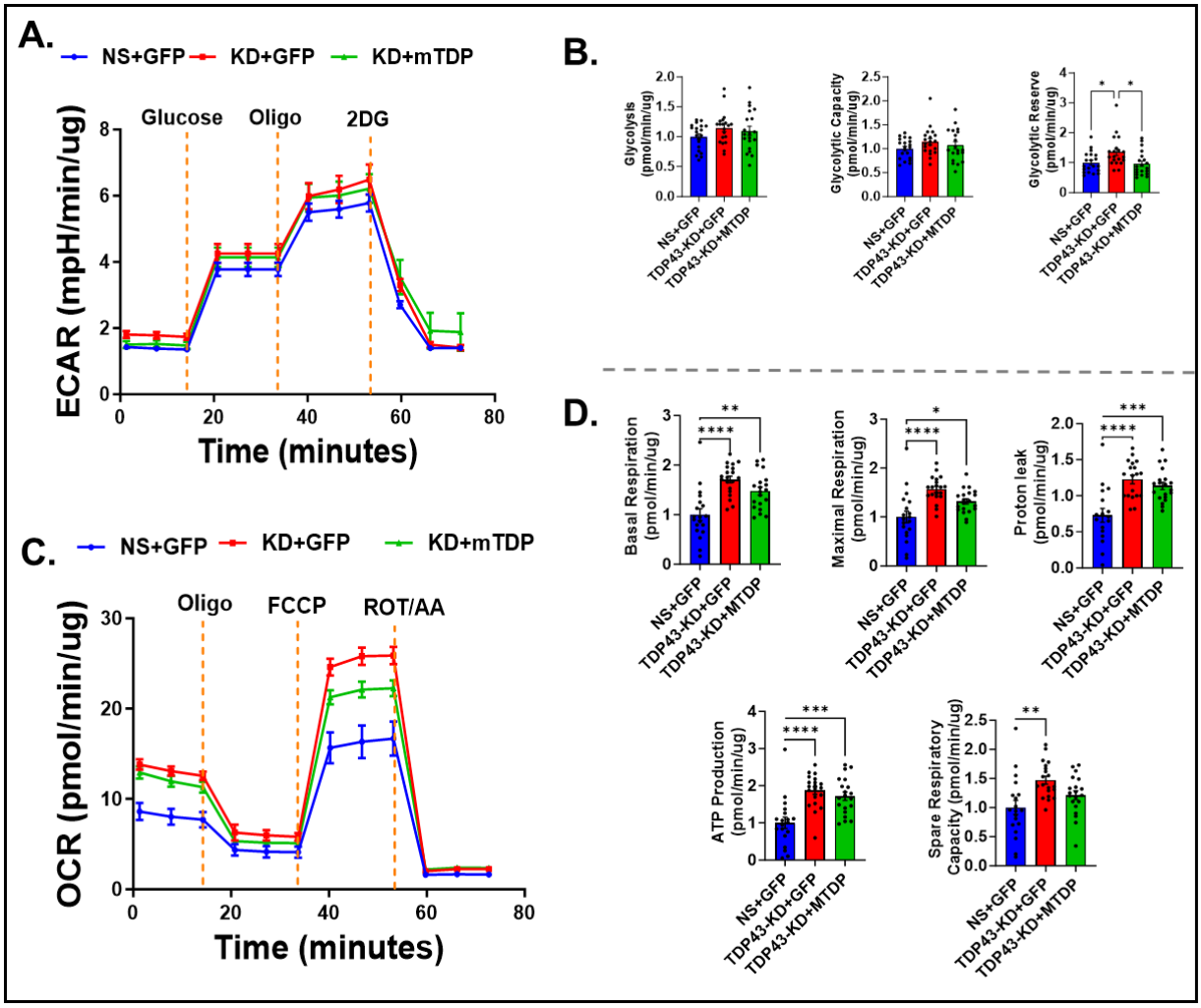

Figure 3.16 | Metabolic Flux Analysis Following TDP-43 Knockdown and Rescue in NSC34 motor neuron-like cells. (A-B) Glycolytic stress test showing mTDP-43-induced reduction in glycolytic reserve following TDP-43 knockdown. (C-D) Mitochondrial stress test showing mTDP-43-mediated reduction in basal respiration, maximal respiration, and spare respiratory capacity. Data are mean ± SEM . Statistical analysis was performed by one-way ANOVA with Tukey's multiple comparisons test. Statistical significance: *p < 0.05; **p < 0.01; ***p < 0.005; ****p < 0.001.

NSC34 metabolic phenotype following TDP-43 knockdown

Our findings collectively highlight a profound metabolic reprogramming in NSC34 motor neuron-like cells following TDP-43 knockdown, as summarized in Figure 3.17. These results can be logically interpreted in the following progression:

- **TDP-43 Knockdown Induces Transcriptomic Alterations:** TDP-43 knockdown leads to significant alterations in the transcriptome of NSC34 motor neuron-like cells, particularly affecting energy metabolic pathways such as glucose metabolism.

- **Increased Glucose Consumption:** Gene expression analysis reveals an increase in the expression of glucose transporters (GLUT1), indicating heightened glucose consumption following TDP-43 knockdown. Glucose uptake assays show a significant increase in glucose uptake by NSC34 motor neuron-like cells following TDP-43 knockdown.
- **Upregulation of Glycolysis:** Gene expression analysis demonstrates an increase in the expression of phosphofructokinase (PFK), suggesting enhanced glycolysis in NSC34 motor neuron-like cells after TDP-43 knockdown. Increased gene expression of pyruvate dehydrogenase (PDH) indicates a preference for metabolizing pyruvate into acetyl-CoA to fuel the Krebs cycle, supported by the rise in isocitrate dehydrogenase (IDH) expression.
- **Increase in TCA metabolic intermediates:** Dynamic metabolic mapping revealed there was a significant increase in key metabolic intermediates such as citrate, α-ketoglutarate, and malate, indicating a potential metabolic overdrive induced by TDP-43 knockdown
- **Alterations in Metabolic Cofactors and Elevated ATP Production**: Significant increases in NAD+ levels suggest heightened mitochondrial respiration following TDP-43 knockdown. Increased ATP levels indicate enhanced oxidative metabolism, further supported by the rise in reactive oxygen species (ROS), a byproduct of oxidative metabolism.
- **Functional Validation Through Metabolic Flux Analysis:** Metabolic flux analysis confirms a significant increase in both glycolysis and oxidative phosphorylation in NSC34 motor neuron-like cells following TDP-43 knockdown.

Together, these findings establish that TDP-43 knockdown drives a hypermetabolic phenotype in NSC34 motor neuron-like cells, characterized by increased glucose uptake, enhanced glycolysis, upregulated mitochondrial respiration, and elevated oxidative stress. This metabolic state reflects a shift in energy metabolism, with cells exhibiting heightened energy production and a concurrent increase in oxidative burden.

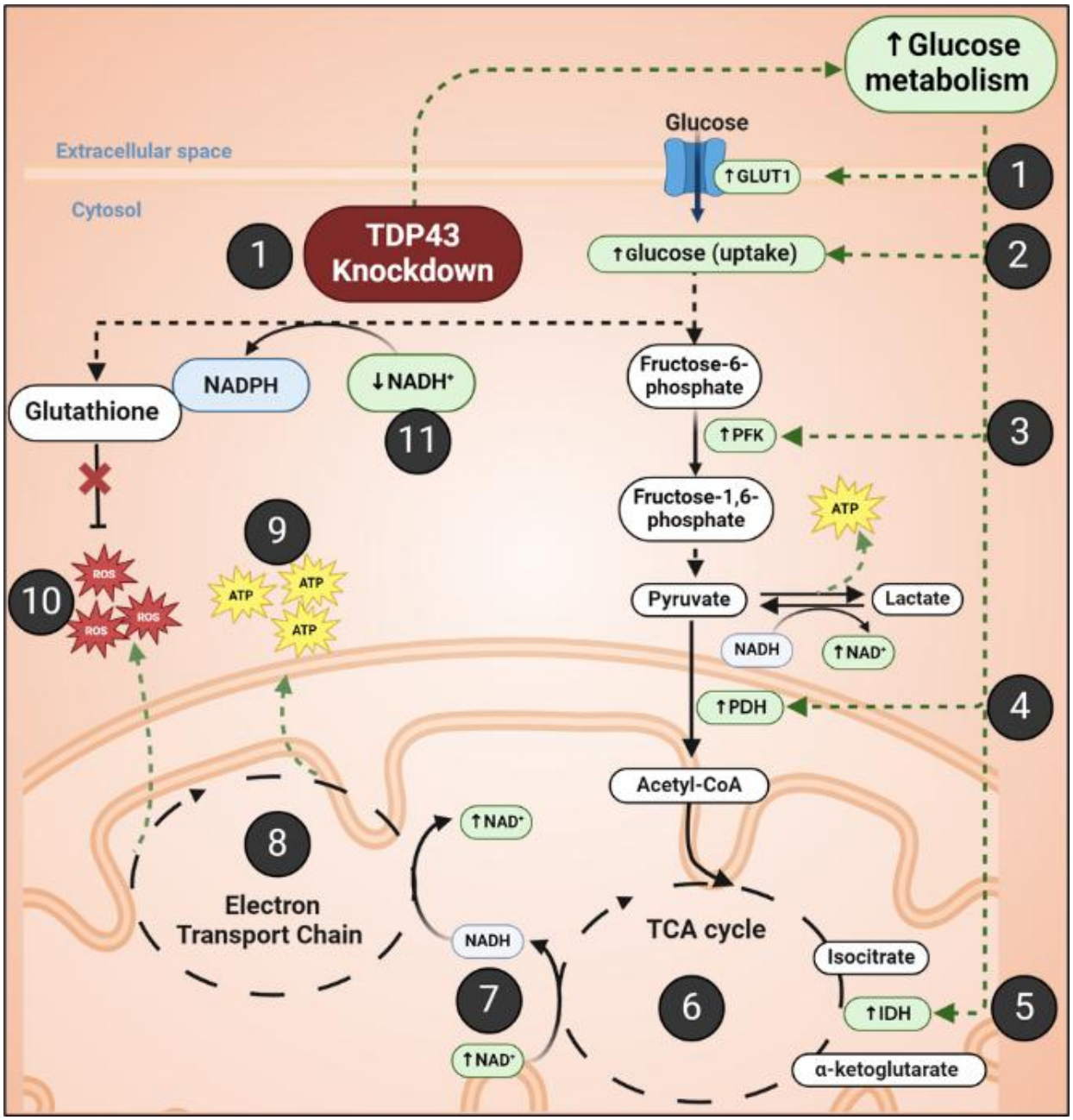

Figure 3.17 | TDP-43 knockdown cause metabolic shift in NSC34 motor neuron to a hypermetabolic phenotype. Following TDP-43 knockdown in NSC34 motor neuron-like cells, significant transcriptomic alterations are observed, particularly affecting energy metabolic pathways such as glucose metabolism. This is evidenced by increased expression of glucose transporters (1) and enhanced glucose uptake (2). Moreover, gene expression analysis reveals upregulation of phosphofructokinase (3), suggesting enhanced glycolysis, along with increased expression of pyruvate dehydrogenase (4), indicating a preference for metabolizing pyruvate into acetyl-CoA to fuel the Krebs cycle, as supported by the rise in isocitrate dehydrogenase (5&6) expression. Significant increases in NAD+ (7) levels suggest heightened mitochondrial respiration (8), leading to elevated ATP production (9) and an increase in reactive oxygen species (10), a byproduct of oxidative metabolism.

Part II: Metabolic dynamics of NSC34 Motor Neurons upon expression of TDP-43 disease-linked mutation

This part of the Results explores the impact of TDP-43 mutations on energy metabolism in NSC34 motor neuron-like cells. TDP-43 mutations, commonly identified in ALS and FTLD patients, represent a critical mechanisms contributing to disease pathogenesis. To investigate this, three ALS-associated single nucleotide TDP-43 mutations (Q331K, M337V, G294A) were selected for characterization, alongside wild-type TDP-43 as a control. These mutations were expressed in NSC34 motor neuron-like cells to assess their impact on key metabolic processes, including glucose metabolism, mitochondrial function, and redox balance.

TDP-43 Wildtype and Mutant Expression in NSC34

TDP-43 Mutations in NSC34 motor neuron-like cells

To assess the impact of TDP-43 mutations on energy metabolism in NSC34 motor neuron-like cells, three ALS-associated single nucleotide mutations in the C-terminal domain (CTD) of TDP-43—Q331K (QKT), M337V (MVT), and G294A (GAT)—were selected for analysis. Wild-type TDP-43 (WTT) was used as a control. GFP-tagged plasmid expression vectors (pCDNA3-GFP) were employed to express these variants in NSC34 motor neuron-like cells (Figure 4.1A). Fluorescence microscopy confirmed the expression of TDP-43 at 24- and 48-hours post-transfection, with optimal GFP signal observed at 48 hours (Figure 4.1B). Western blot analysis confirmed the expression of GFP-tagged TDP-43 at the expected 70 kDa molecular weight in both WTT and mutant groups (Figure 4.1C), consistent with the combined weights of TDP-43 (~43 kDa) and GFP (~27 kDa).

TDP-43 Mutant Selection Process

To identify the most suitable TDP-43 mutation for comprehensive metabolic characterization, three criteria were evaluated: localization, post-translational modification, and solubility. Localization analysis was conducted to determine which mutation exhibited the greatest cytoplasmic presence, as cytoplasmic mislocalization is a hallmark of TDP-43 pathology. Post-translational modification was assessed via phosphorylation of TDP-43, and solubility analyses aimed to identify the mutation with the highest proportion of insoluble TDP-43.

Fractionation analysis revealed that WTT was predominantly nuclear, while QKT and MVT exhibited both nuclear and cytoplasmic localization, and GAT remained mainly nuclear. Assessment of phosphorylated TDP-43 (pTDP-43) showed that phosphorylation was largely nuclear in WTT, whereas all mutants exhibited some degree of cytoplasmic phosphorylation. Under naïve conditions,

solubility analysis indicated that both wild-type and mutant TDP-43 were primarily present in the soluble fraction, with no substantial differences in pTDP-43 solubility.

To evaluate TDP-43 insolubility under stress conditions, sodium arsenite treatment was applied 48 hours post-transfection. Western blot analysis revealed that following stress induction, TDP-43 was primarily detected in the insoluble fraction across all groups. After one hour of recovery, WTT and QKT transitioned back to the soluble fraction, whereas MVT and GAT remained insoluble (Figure 4.1G). MVT exhibited the most pronounced cytoplasmic retention after recovery. Immunofluorescence analysis confirmed nuclear localization under normal conditions, transient cytoplasmic redistribution during stress, and partial nuclear recovery in WTT and QKT (Figure 4.1H).

MVT was selected for further metabolic characterization as it exhibited both nuclear and cytoplasmic localization, along with phosphorylation and increased insolubility under stress conditions—key features associated with TDP-43 pathology. These properties make MVT a relevant model for studying the metabolic consequences of TDP-43 mutations in motor neurons.

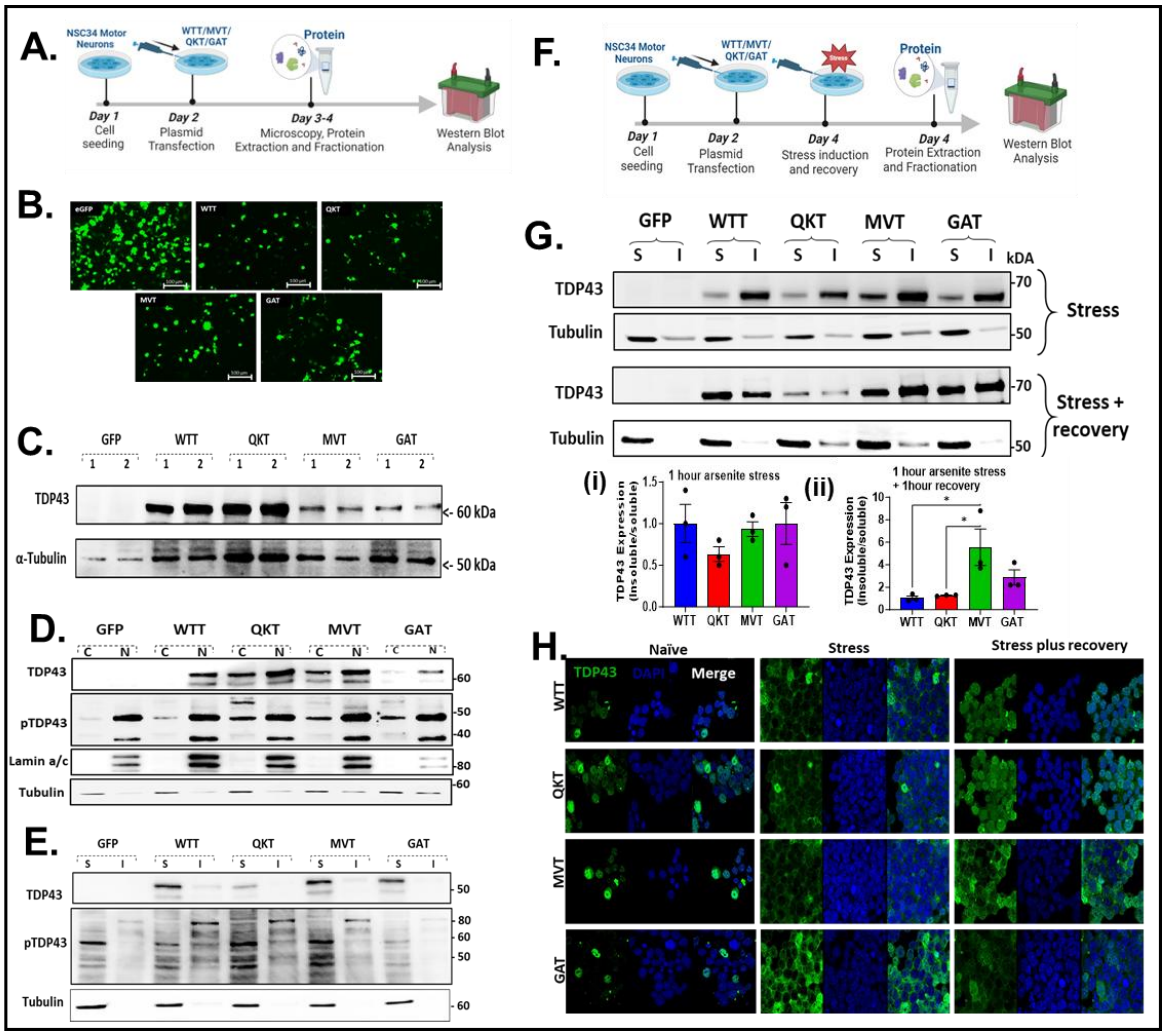

Figure 4.1 | Selection of TDP-43 Mutation for Subsequent Metabolic Characterization in NSC34 motor neuron-like cells. (A) Schematic representation of the experimental workflow illustrating GFP-tagged plasmid expression vectors used to express wild-type (WTT) and mutant (QKT, MVT, and GAT) TDP-43 in NSC34 motor neuron-like cells, followed by protein extraction and Western blot analysis. (B) Fluorescent microscopy images confirm the successful transfection and expression of TDP-43-GFP fusion proteins at 48 hours post-transfection, with optimal GFP expression in all groups. Scale bar = 50 µm. (C) Western blot analysis confirms the expression of TDP-43-GFP at the expected molecular weight of 70 kDa in all groups, validating plasmid expression. (D) Fractionation analysis demonstrates TDP-43 localization in nuclear and cytoplasmic compartments, with WTT predominantly localized in the nucleus, QKT and MVT showing dual nuclear-cytoplasmic localization, and GAT predominantly nuclear. (E) Solubility analysis of TDP-43 and phospho-TDP-43 (pTDP-43) shows that under naive conditions, both wild-type and mutant TDP-43 are predominantly expressed in the soluble fraction with no observable differences between groups. (F) Schematic illustrating stress induction with sodium arsenite at 48 hours post-transfection and subsequent recovery, followed by protein extraction for soluble and insoluble fraction analysis. (G) Western blot analysis of TDP-43 expression in soluble and insoluble fractions post-stress and recovery reveals that TDP-43 becomes predominantly insoluble in all groups during stress. Bar plots quantify the relative levels of TDP-43 in soluble and insoluble fractions during stress and recovery, showing significantly reduced solubility for MVT and GAT compared to WTT. Statistical significance is indicated as *$p < 0.05$. (H) Immunofluorescence analysis highlights the subcellular localization of TDP-43 under naive, stress, and recovery conditions.

NSC34 Transcriptomic Profile following TDP-43 mutation overexpression

To investigate the impact of TDP-43 mutation on the transcriptome of NSC34 motor neuron-like cells, we conducted next-generation sequencing and analysis of both coding and noncoding transcripts, following a similar approach to the TDP-43 knockdown experiment. RNA samples were collected from NSC34 motor neuron-like cells 48 hours post-transfection with wild-type (WTT) or mutant (MVT) TDP-43 constructs, ensuring their integrity prior to further analysis. Ribo-depletion and library preparation techniques were employed to enrich for both small and large RNAs, enabling comprehensive transcriptome profiling (Figure 4.2A).

Principal component analysis (PCA) of the sequencing data revealed clear clustering of samples into two distinct groups, corresponding to the WTT and MVT experimental conditions (Figure 4.2B). Differential expression analysis comparing MVT to WTT revealed significant alterations in gene expression. Out of a total of 18,811 genes analyzed, 384 genes were upregulated (2.04%), while 36 genes were downregulated (0.19%). The majority of genes (18,391; 97.77%) exhibited no significant changes in expression levels.

When focusing on coding genes, 12,647 genes were analyzed, of which 104 (0.82%) were upregulated and 15 (0.12%) were downregulated, while the remaining 12,528 genes (99.06%) showed no significant changes. Among noncoding genes, 2,059 were analyzed, revealing 38 (1.85%) upregulated and 10 (0.49%) downregulated genes, with the majority (2,011; 97.67%) showing no significant changes. Additionally, 4,105 genes were categorized as unannotated (NA); of these, 242 (5.90%) were upregulated, 11 (0.27%) were downregulated, and 3,852 (93.84%) exhibited no significant changes.

Overall, these findings highlight a distinct pattern of differential gene expression in response to TDP-43 mutation in NSC34 motor neuron-like cells. While a small subset of genes displayed significant upregulation or downregulation, the majority of genes remained unchanged, indicating that under naïve and unstressed conditions, the mutation induces targeted rather than widespread transcriptomic alterations.

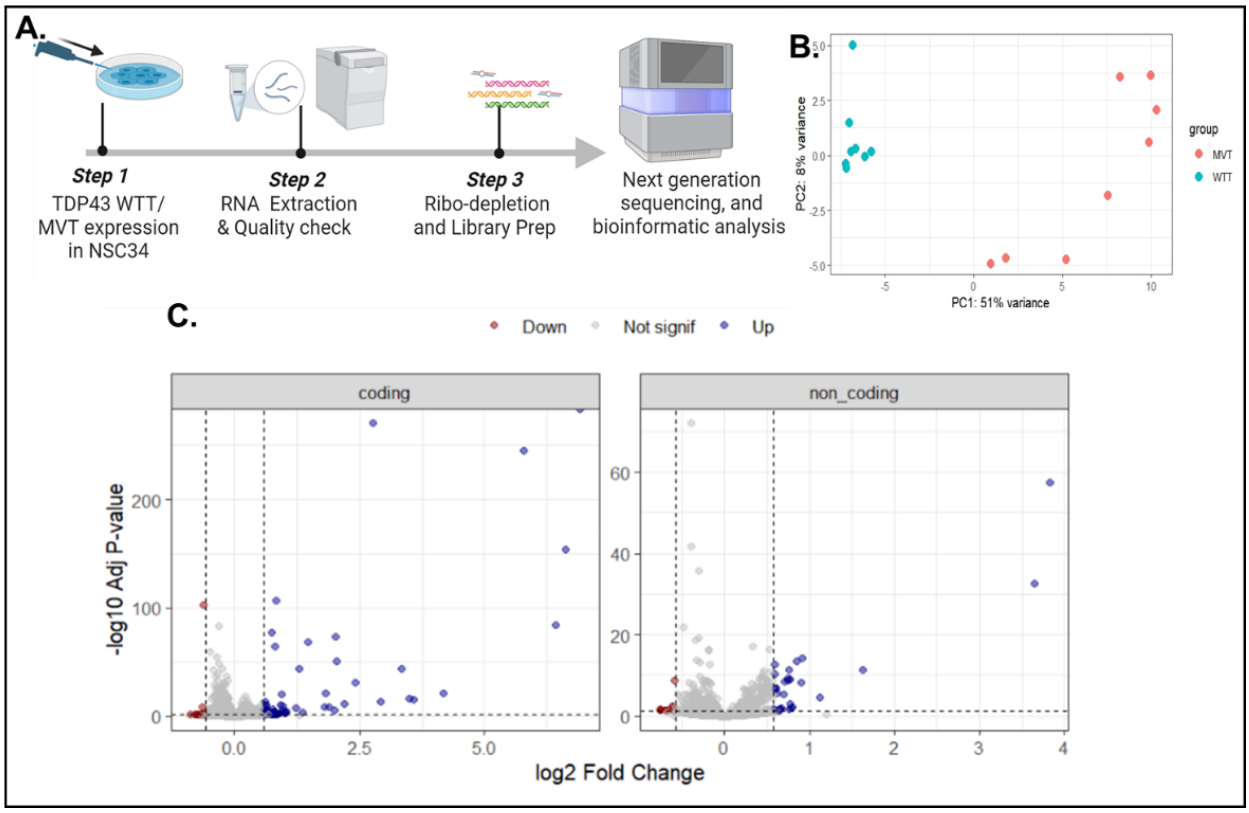

Figure 4.2 | Transcriptomic analysis of NSC34 motor neuron-like cells following TDP-43 mutation expression. (A) Schematic representation of the experimental workflow detailing the sequential steps: TDP-43 WTT/MVT transfection in NSC34 motor neuron-like cells, RNA extraction and quality check, ribo-depletion and library preparation, followed by next-generation sequencing and bioinformatic analysis to assess transcriptomic changes. (B) PCA reveals distinct clustering of samples into wild-type (WTT) and mutant (MVT) groups, with PC1 accounting for 51% of the variance, indicating clear separation of transcriptomic profiles between groups. (C) Volcano plots of coding (left) and noncoding (right) transcripts, illustrating significantly upregulated (blue) and downregulated (red) genes (adj. p-value < 0.05; |log2 fold change| > 0.58), while non-significant genes are in gray.

Table 4.1: Differential Expression Analysis of MVT vs WTT Groups. Differentially expressed genes were identified with an adjusted p-value < 0.05 and log2 fold change > ±0.58.

Gene Category	Total Genes	Downregulated	No Change	Upregulated
All Genes	18,811	36 (0.19%)	18,391 (97.77%)	384 (2.04%)
Coding	12,647	15 (0.12%)	12,528 (99.06%)	104 (0.82%)
Noncoding	2,059	10 (0.49%)	2,011 (97.67%)	38 (1.85%)
Unannotated (NA)	4,105	11 (0.27%)	3,852 (93.84%)	242 (5.90%)

Pathway Analysis of Differentially Expressed genes

Pathway analysis of the differentially expressed genes focused on the downregulated genes, as no significant pathways were enriched among the upregulated genes. This analysis was divided into two categories: the top 15 enriched pathways and pathways specifically related to energy metabolism (Figure 4.4).

In the first analysis (Figure 4.4A), the top 15 downregulated pathways highlighted broad cellular processes affected by TDP-43 mutation, including transcriptional regulation, cell cycle progression, and translation. Notable pathways included "TP53 Regulates Transcription of Cell Cycle Genes," "Cholesterol Biosynthesis," and several phases of the mitotic cycle, such as "Mitotic Metaphase and Anaphase" and "M Phase." These findings suggest that TDP-43 mutation may disrupt fundamental cellular regulatory mechanisms, particularly those involved in cell division and transcriptional control. The second analysis focused on energy metabolism-related pathways; isolating processes directly linked to cellular energetics (Figure 4.4B). This analysis identified key pathways such as "Fatty Acyl-CoA Biosynthesis," "Pentose Phosphate Pathway," "Citric Acid (TCA) Cycle," and "Glycolysis." Additional pathways included "Pyruvate Metabolism," "Glucose Metabolism," and "Gluconeogenesis," indicating a broad disruption in metabolic processes. These results suggest that the TDP-43 mutation affects the cellular metabolic landscape, with specific impacts on energy production and substrate utilization.

Together, these pathway analyses reveal that the downregulated genes in NSC34 motor neuron-like cells expressing mutant TDP-43 are predominantly associated with disruptions in critical regulatory and metabolic processes, providing insights into the cellular adaptations and vulnerabilities associated with TDP-43-related pathophysiology.

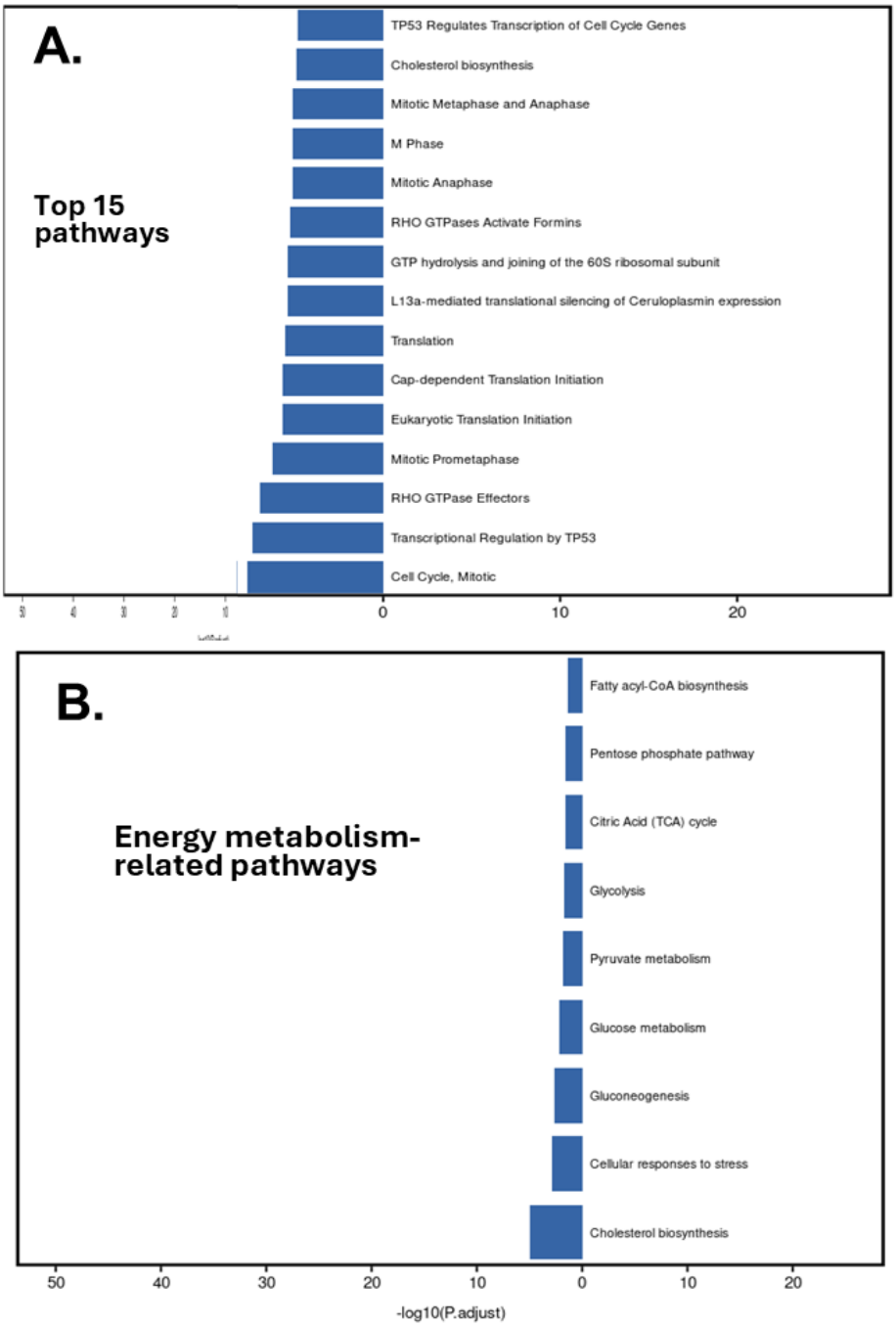

Figure 4.4 | Pathway enrichment analysis of downregulated genes in NSC34 motor neuron-like cells expressing mutant TDP-43. (A) Top 15 enriched pathways identified from the downregulated genes, highlighting disruptions in key cellular processes such as transcriptional regulation ("TP53 Regulates Transcription of Cell Cycle Genes"), cholesterol biosynthesis, mitotic cycle phases, and translation-related pathways. (B) Energy metabolism-related pathways filtered from the downregulated genes, showing significant enrichment in pathways such as "Fatty Acyl-CoA Biosynthesis," "Pentose Phosphate Pathway," "Citric Acid (TCA) Cycle," "Glycolysis," "Pyruvate Metabolism," and "Glucose Metabolism." These results indicate alterations in cellular regulatory mechanisms and metabolic processes in response to TDP-43 mutation.

NSC34 Glucose Metabolism following Mutant TDP-43 Expression

Building on the transcriptomic pathway analysis that suggested the potential impact of mutant TDP-43 expression on energy metabolism, we conducted a targeted gene expression analysis in NSC34 motor neuron-like cells. The analysis focused on key rate-limiting enzymes involved in glucose, lipid, and glycogen metabolism, adopting a similar approach to that used in the TDP-43 knockdown experiment. For glucose metabolism, we examined the expression of PFK, IDH, G6PD, and ALDO-B genes. For glycogen metabolism, we analyzed GYS and PYGB, while for lipid metabolism, we focused on ACACB and CRAT.

Comparison between NSC34 motor neuron-like cells expressing mutant TDP-43 (MVT) and those expressing wild-type TDP-43 (WTT) revealed significant gene expression changes. In the glucose metabolism pathway, PFK and IDH exhibited slight but non-significant increases in expression (Figure 4.5A). However, G6PD showed a significant increase, while ALDO-B displayed a significant decrease in expression following MVT expression. In the glycogen metabolism pathway, GYS and PYGB showed slight, non-significant increases in expression (Figure 4.5A). For lipid metabolism, CRAT was significantly upregulated, while ACACB expression remained unchanged (Figure 4.5B). To further explore downstream effects of glycolysis, we analyzed gene expression in the pyruvate and lactate metabolism pathway, specifically targeting PDHa1, PDHb2, and LDH (Figure 4.5C). No significant changes were observed in the expression of these genes when comparing MVT to WTT, suggesting that glycolytic outputs remain largely unaffected.

Together, these findings indicate that mutant TDP-43 expression in NSC34 motor neuron-like cells leads to selective changes in metabolic gene expression, particularly an upregulation of G6PD, a key enzyme in the pentose phosphate pathway (PPP), and CRAT, which plays a role in fatty acid metabolism. The increase in G6PD suggests a shift toward the PPP, which is critical for maintaining cellular redox balance and generating biosynthetic precursors, while the upregulation of CRAT points to enhanced lipid metabolism, possibly reflecting an increased reliance on fatty acid oxidation.

Metabolic Cofactors in NSC34 Following Mutant TDP-43 Expression

Expression of mutant TDP-43 in NSC34 motor neuron-like cells led to an upregulation of G6PD, a pivotal enzyme in the pentose phosphate pathway (PPP). Given that the PPP plays a key role in generating metabolic cofactors such as NADPH, which supports biosynthetic processes and antioxidant defense, we further investigated changes in the levels of NAD, NADH, NADP, and NADPH at 24 and 48 hours following mutant TDP-43 expression (Figure 4.6A). At 24 hours, there were no

significant changes in the absolute levels of NAD+ or NADH; however, the NAD+/NADH ratio was significantly reduced in mutant TDP-43-expressing cells compared to wild-type controls (Figure 4.6B). By 48 hours, this reduction was no longer observed, with the NAD+/NADH ratio returning to levels comparable to the wild-type group (Figure 4.6C). In contrast, NADP+ levels were significantly increased at 24 hours in the mutant TDP-43 group, while NADPH levels and the NADP+/NADPH ratio remained unchanged (Figure 4.6D). By 48 hours, NADP+ and NADPH levels showed no significant differences between groups (Figure 4.6E).

These findings suggest that mutant TDP-43 expression transiently affects redox homeostasis by reducing the NAD+/NADH ratio and increasing NADP+ levels at 24 hours. The drop in the NAD+/NADH ratio may indicate a temporary shift in cellular energy metabolism, favoring a more reduced intracellular environment, while the increase in NADP+ suggests an initial adaptation that could support anabolic metabolism or oxidative stress responses. However, the normalization of these metabolic cofactors by 48 hours implies that NSC34 motor neuron-like cells may compensate for these initial perturbations, restoring redox balance over time.

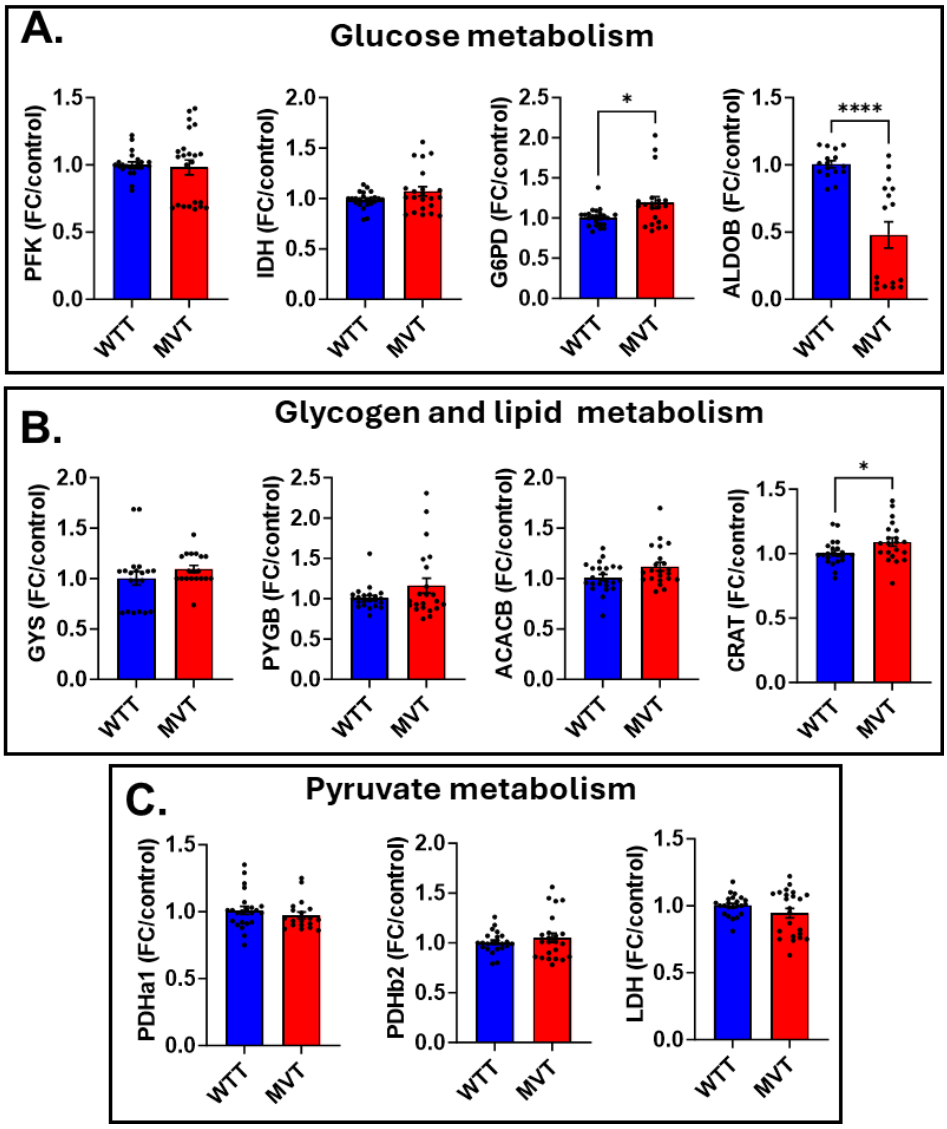

Figure 4.5 | Gene Expression Analysis of Glucose, Glycogen, and Lipid Metabolism Pathways in NSC34 motor neuron-like cells Expressing Mutant TDP-43. (A) Expression of key genes in the glucose metabolism pathway, including phosphofructokinase (PFK), glucose-6-phosphate dehydrogenase (G6PD), aldolase B (ALDO-B), and isocitrate dehydrogenase (IDH), showing a significant increase in G6PD and a significant decrease in ALDO-B expression in mutant TDP-43 (MVT)-expressing cells compared to wild-type TDP-43 (WTT). (B) Gene expression analysis of glycogen metabolism (GYS, PYGB) and lipid metabolism (ACACB, CRAT), highlighting a significant increase in CRAT expression in MVT-expressing cells. (C) Expression levels of pyruvate and lactate metabolism-related genes (PDHa1, PDHb2, and LDH) showing no significant changes between MVT- and WTT-expressing cells. Data are mean ± SEM (n = 3 biological replicates). Statistical tests: unpaired t-test (Welch's correction) or Mann–Whitney U test. Statistical significance: *p < 0.05; ****p < 0.001.

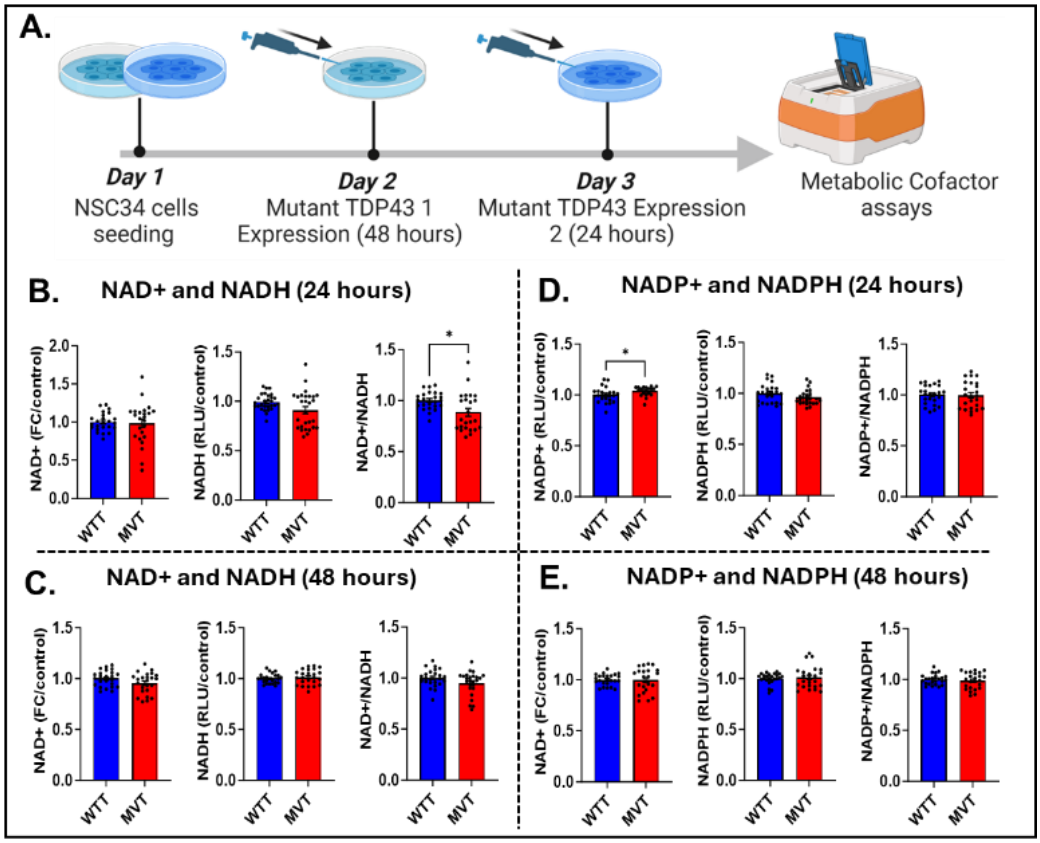

Figure 4.6 | NAD and NADP cofactor dynamics in NSC34 motor neuron-like cells following TDP-43 mutation expression. (A) Experimental timeline for NAD and NADP quantification at 24 and 48 hours post-TDP-43 mutation expression. (B) Levels of NAD+, NADH, and the NAD+/NADH ratio at 24 hours, showing a significant reduction in the NAD+/NADH ratio in MVT cells. (C) Levels of NAD+, NADH, and their ratio at 48 hours, showing no significant differences between WTT and MVT groups. (D) NADP+, NADPH, and their ratio at 24 hours, showing a significant increase in NADP+ in MVT cells. (E) Levels of NADP+, NADPH, and their ratio at 48 hours, showing no significant differences. Data are mean ± SEM (n = 3 biological replicates). Statistical tests: unpaired t-test (Welch's correction) or Mann–Whitney U test. Statistical significance: *p < 0.05

NSC34 Energy Substrate Metabolism Following Mutant TDP-43 Expression

To assess the impact of mutant TDP-43 expression on energy metabolism in NSC34 motor neuron-like cells, we measured glucose, lactate, and glutamine levels in the culture media at 24-, 48-, and 72-hours post-transfection (Figure 4.7A). Across all time points, glucose levels declined, while lactate levels increased, and glutamine levels decreased, reflecting normal cellular substrate utilization. However, no significant differences were observed between wild-type TDP-43 (WTT) and mutant TDP-43 (MVT) groups (Figure 4.7B). To further investigate glucose metabolism, glucose uptake and ATP production were quantified at 24 and 48 hours. A slight but non-significant increase in glucose uptake was observed at 24 hours in MVT-expressing cells compared to WTT controls (Figure 4.7C). However, by 48 hours, glucose uptake was significantly elevated in the MVT group, suggesting an increased cellular demand for glucose. Despite this rise in glucose uptake, intracellular ATP levels

remained unchanged between WTT and MVT groups at both time points (Figure 4.7D). These findings indicate that mutant TDP-43 expression may enhance glucose uptake in NSC34 motor neuron-like cells over time but does not significantly alter ATP production under the tested conditions. The observed increase in glucose uptake may represent an adaptive response to maintain energy balance in the face of mutant TDP-43-induced metabolic alterations. However, the absence of a corresponding ATP increase suggests glucose may be redirected to alternative pathways, supported by G6PD upregulation (Figure 4.5A) and increased PPP flux. These results provide a basis for further investigation into how mutant TDP-43 influences glycolytic flux and mitochondrial metabolism in NSC34 motor neuron-like cells.

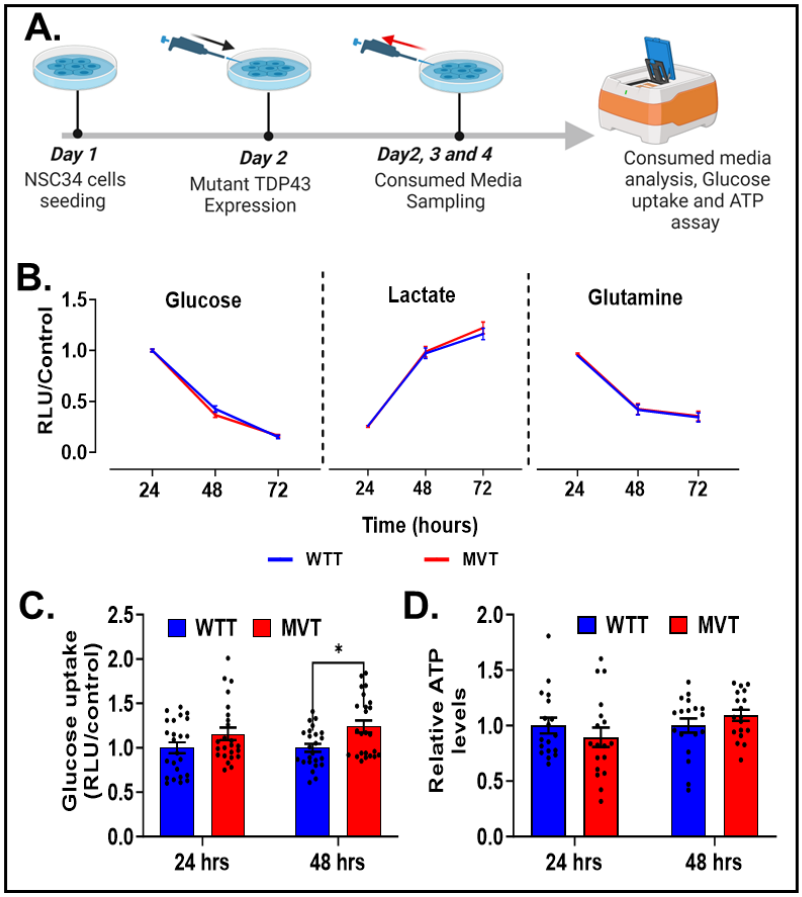

Figure 4.7 A-D | **Energy substrate utilization and ATP production in NSC34 motor neuron-like cells following TDP-43 mutation expression**. (A) Experimental workflow illustrating media collection at 24-, 48-, and 72-hours post-transfection. (B) Time-course analysis of glucose, lactate, and glutamine levels in consumed media, showing overall trends in substrate utilization without significant differences between WTT and MVT groups. (C) Glucose uptake quantification at 24 and 48 hours, showing a significant increase in MVT cells at 48 hours. (D) ATP production levels at 24 and 48 hours, showing no significant differences between WTT and MVT groups. Statistical analysis: two-way repeated-measures ANOVA with Šidák's post hoc test for time courses (B); unpaired t-test (Welch's correction) or Mann-Whitney U test for bar graphs (C_D). Significance: *p < 0.05.

Dynamic Glucose Metabolic Mapping in NSC34 motor neuron-like cells following mutant TDP-43 Expression

The findings thus far reveal notable alterations in gene expression and metabolic cofactor levels in NSC34 motor neuron-like cells following mutant TDP-43 expression. Despite these observations, the specific impact of mutant TDP-43 on glucose metabolism remains ambiguous. While increased glucose uptake and changes in metabolic cofactors, such as NADP+, suggest potential metabolic adaptations, the precise effects of TDP-43 mutation on glucose metabolism in NSC34 motor neuron-like cells have not been fully elucidated.

To address this gap, we conducted a complementary experiment using U-13C labeled glucose to map glucose metabolism dynamics in NSC34 motor neuron-like cells. By employing GC-MS-based metabolic mapping, we traced the incorporation of carbon-13 into glycolysis and TCA cycle intermediates (Figure 4.8A). This analysis focused on the relative abundance of labeled isotopologues (M+2 or M+3) and molecular carbon labeling (MCL) in key metabolites, including lactate, citrate, α-ketoglutarate, succinate, fumarate, and malate.

Our results revealed no significant changes in lactate labeling (M+3 or MCL) between the mutant (MVT) and wild-type (WTT) groups, indicating that glycolytic activity remained comparable (Figure 4.8B). However, a slight but significant increase in citrate M+2 was observed in the MVT group, though no corresponding changes were detected in citrate MCL (Figure 4.8C). In contrast, α-ketoglutarate labeling showed a significant reduction in M+2 in the MVT group, accompanied by a non-significant trend toward increased MCL (Figure 4.8D). Downstream analysis of TCA cycle intermediates, including succinate, fumarate, and malate, revealed no significant changes in their respective M+2 or MCL values between the two groups (Figures 4.8E-G).

These findings suggest that mutant TDP-43 expression induces subtle but specific changes in glucose metabolism, primarily affecting upstream TCA cycle intermediates such as citrate and α-ketoglutarate, while downstream TCA cycle flux appears to remain unaffected. Together with earlier observations of increased glucose uptake and altered cofactor dynamics, these results highlight complex metabolic adaptations in response to mutant TDP-43 expression. Such adaptations may represent early cellular responses to TDP-43 mutation, with implications for the broader understanding of energy metabolism dysregulation in TDP-43-associated neurodegenerative diseases.

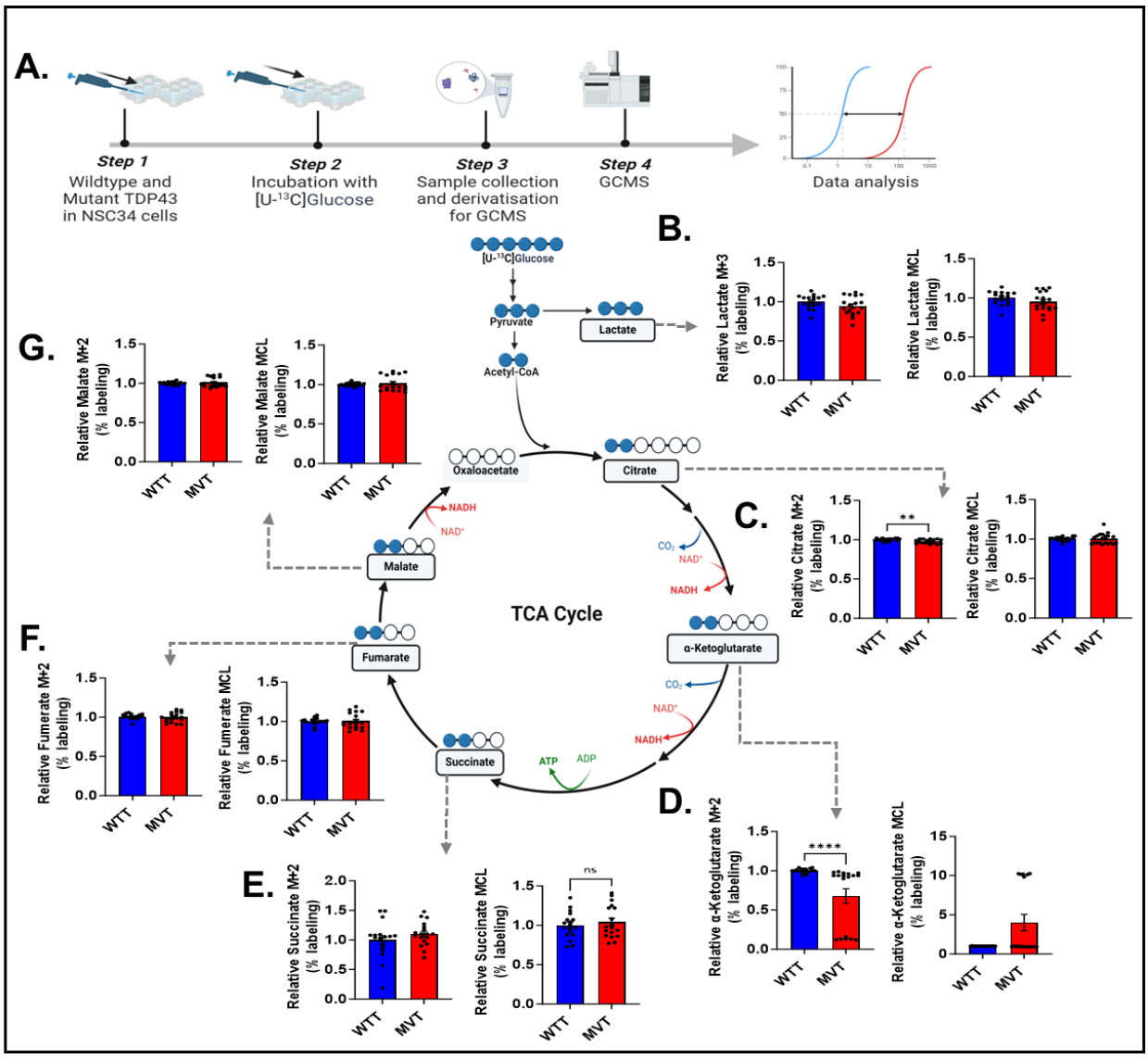

Figure 4.8 | Dynamic Metabolic Mapping of NSC34 motor neuron-like cells Following Mutant TDP-43 Expression. (A) Experimental setup illustrating the use of U-13C labeled glucose to track carbon-13 presence in glycolysis and TCA cycle intermediates. (B) Analysis of lactate labeled 13C showing no significant changes between mutant TDP-43 (MVT) and wild-type TDP-43 (WTT) groups. (C) Examination of citrate labeled 13C revealing a slight but significant increase in citrate M+2 in the MVT group compared to WTT. (D) Assessment of α-ketoglutarate labeled 13C indicating a significant decrease in α-ketoglutarate M+2 in the MVT group alongside a non-significant increase in molecular carbon labeling (MCL). (E-G) Analysis of succinate, fumarate, and malate labeled 13C showing no significant changes in their respective M+2 and MCL between MVT and WTT groups. Data are mean ± SEM (n = 3 biological replicates). Statistical tests: unpaired t-test (Welch correction) or Mann–Whitney U test. Statistical significance: **p < 0.01; ****p < 0.001.

Metabolic Flux Analysis in NSC34 motor neuron-like cells Following Mutant TDP-43 Expression

Next, to comprehensively assess the metabolic phenotype, we performed metabolic flux analysis using extracellular flux assays. Specifically, we conducted a glycolytic stress test (GST) to evaluate glycolytic function (Figure 4.9A) and a mitochondrial stress test (MST) to assess oxidative phosphorylation (Figure 4.9B). These assays provide dynamic insights into the metabolic adaptations driven by mutant TDP-43 expression. The results and implications of these analyses are detailed in the subsequent sections.

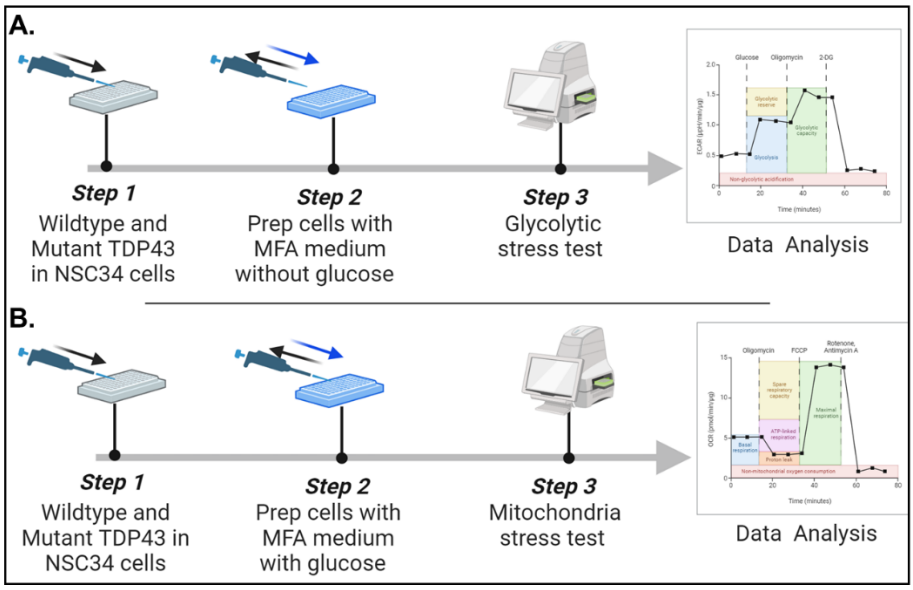

Figure 4.9 | Experimental workflow for glycolytic and mitochondrial stress tests in NSC34 motor neuron-like cells following TDP-43 mutation expression. (A) Schematic representation of the glycolytic stress test, showing sequential glucose-free incubation, assay execution, and data analysis. (B) Schematic representation of the mitochondrial stress test, illustrating transfection, incubation, metabolic perturbations, and data analysis.

NSC34 motor neuron-like cells Metabolic Flux following Mutant TDP-43 Expression

To investigate the functional metabolic phenotype of NSC34 motor neuron-like cells expressing mutant TDP-43, we conducted a glycolytic stress test by measuring extracellular acidification rate (ECAR) in response to sequential injections of glucose, oligomycin, and 2-deoxy-D-glucose (2DG) (Figure 4.10A). The data revealed a significant increase in glycolysis and glycolytic capacity, while non-glycolytic acidification was also elevated. However, there were no significant changes in glycolytic reserve (Figure 4.10B). These results suggest that mutant TDP-43 expression enhances glycolytic activity in NSC34 motor neuron-like cells.

In parallel, a mitochondrial stress test was performed to evaluate oxidative phosphorylation (OXPHOS) by measuring oxygen consumption rate (OCR) in response to metabolic perturbations (Figure 4.10C). Compared to wild-type TDP-43 (WTT), mutant TDP-43 (MVT) expression led to a slight increase in basal OCR before and after oligomycin injection, followed by a marked increase in OCR post-FCCP injection, indicative of heightened mitochondrial respiration. After rotenone and antimycin-A injection, OCR levels returned to baseline. Further quantitative analysis revealed a significant increase in basal respiration, proton leak, and ATP production in MVT-expressing cells, whereas maximal respiration and spare respiratory capacity remained unchanged (Figure 4.10D). These findings suggest that mutant TDP-43 expression enhances mitochondrial oxidative phosphorylation, potentially reflecting a maladaptive metabolic response in NSC34 motor neuron-like cells.

Mitochondrial Respiratory Complexes Integrity

The mitochondrial stress test revealed a significant increase in oxygen consumption rate following FCCP injection in NSC34 motor neuron-like cells expressing mutant TDP-43. This increase correlated with elevated OCR associated with ATP production, basal respiration, and maximal respiration, suggesting a possible alteration in mitochondrial respiratory activity. To investigate whether these changes were linked to differences in mitochondrial respiratory complex levels, we performed Western blot analysis of the five mitochondrial electron transport chain complexes in NSC34 motor neuron-like cells following mutant TDP-43 expression. Western blot analysis showed no change in the expression of mitochondrial complexes I–V between groups (Figure 4.11A & B). To assess whether mutant TDP-43 expression influenced mitochondrial quantity and localization, we conducted MitoTracker immunofluorescence staining, which revealed no observable differences in mitochondrial staining intensity or distribution between WTT and MVT groups (Figure 4.11C). Overall, these findings indicate that mutant TDP-43 expression does not compromise mitochondrial respiratory complex integrity or mitochondrial content, despite observed increases in OCR and ATP production.

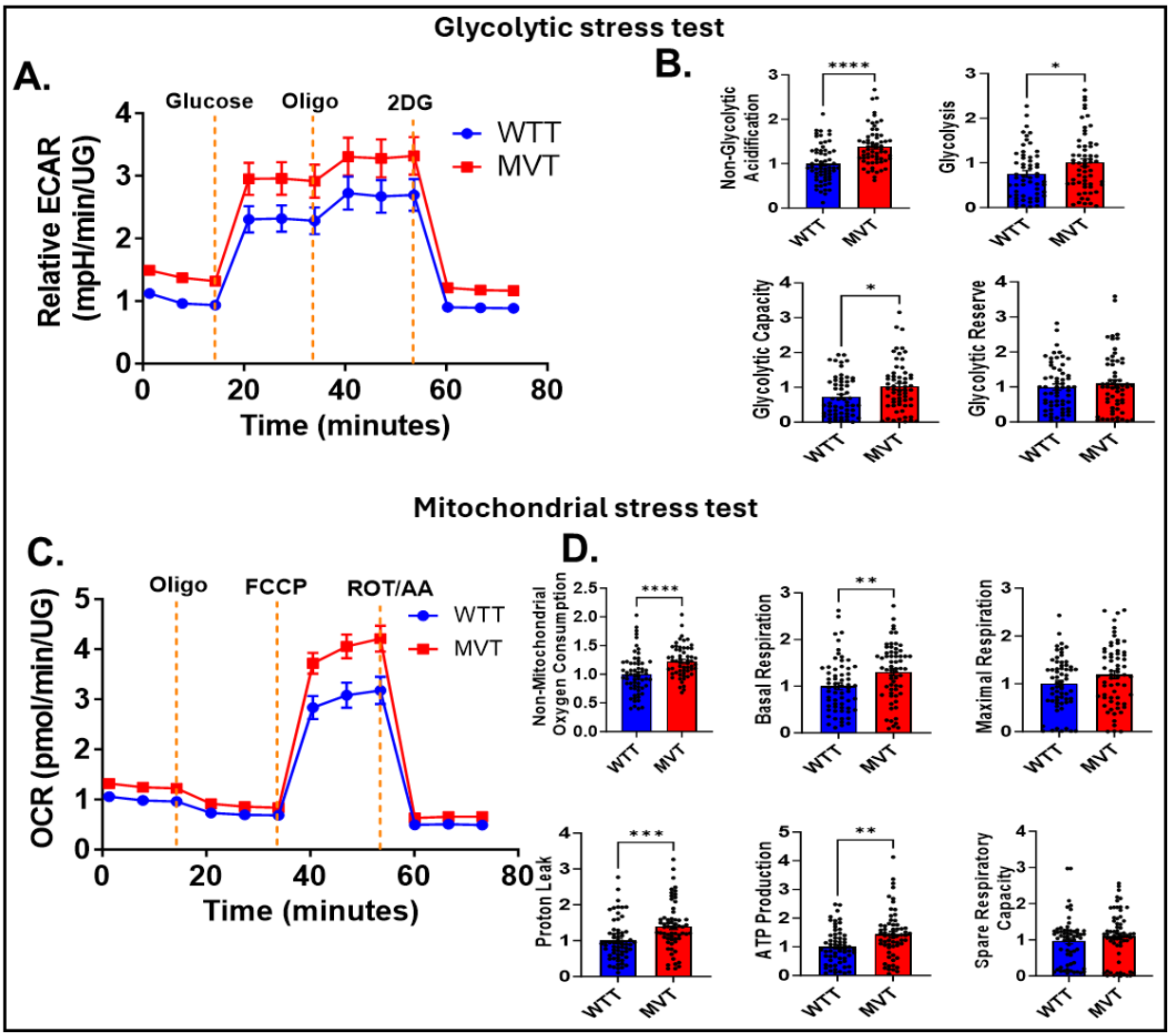

Figure 4.10 | Metabolic Flux Analysis in NSC34 motor neuron-like cells Following Mutant TDP-43 Expression. (A) Glycolytic stress test displaying extracellular acidification rate (ECAR) over time, illustrating metabolic responses to sequential injections of glucose, oligomycin, and 2-deoxy-D-glucose (2DG). (B) Quantification of non-glycolytic acidification, glycolysis, glycolytic reserve, and glycolytic capacity, showing significant increases in glycolysis and glycolytic capacity. (C) Mitochondrial stress test illustrating oxygen consumption rate (OCR) dynamics in response to injections of oligomycin, FCCP, and rotenone/antimycin-A, with a pronounced increase in OCR post-FCCP. (D) Quantification of mitochondrial parameters showing significant increases in basal respiration, proton leak, and ATP production, with no notable changes in maximal respiration and spare respiratory capacity. Statistical significance is denoted as follows. Data are mean ± SEM (n = 3 biological replicates). Statistical tests: unpaired t-test (Welch correction) or Mann–Whitney U test. *p < 0.05; **p < 0.01; ***p < 0.005; ****p < 0.001.

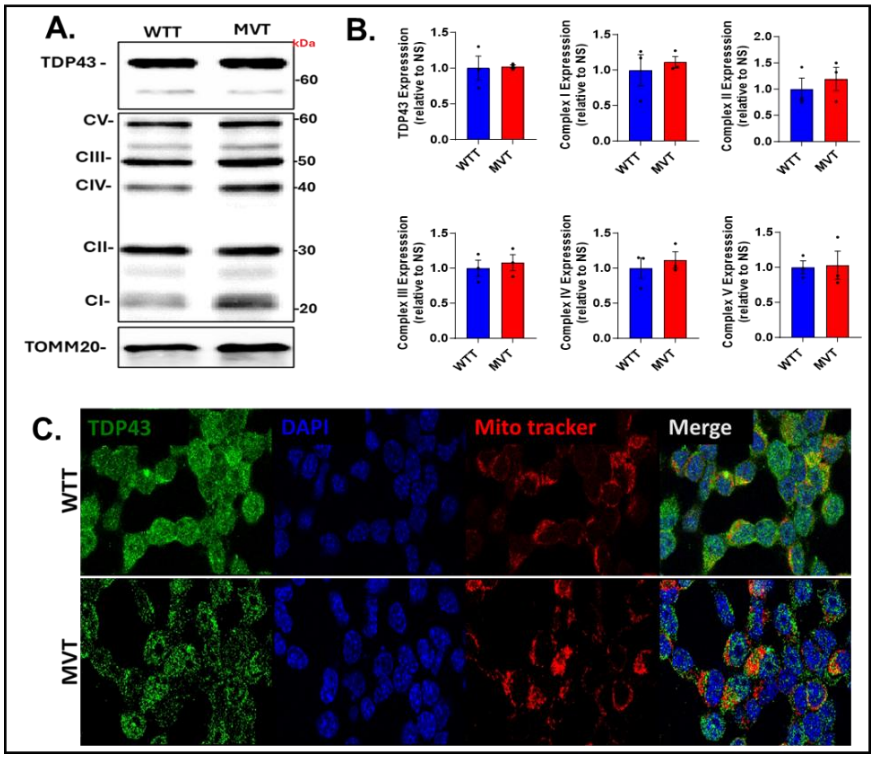

Figure 4.11 | Assessment of Mitochondrial Respiratory Complexes and Mitochondrial Density in NSC34 motor neuron-like cells Following Mutant TDP-43 Expression. (A-B) Western blot analysis and quantitative assessment of mitochondrial respiratory complexes (I-V) in NSC34 motor neuron-like cells, showing a non-significant increase in complex I and IV expression, with complexes II, III, and V remaining unchanged. (C) MitoTracker immunofluorescence staining illustrating mitochondrial localization and density, showing no observable differences between wild-type (WTT) and mutant (MVT) TDP-43-expressing NSC34 motor neuron-like cells.

Oxidative Stress and Glutathione Dynamics in NSC34 motor neuron-like cells Following Mutant TDP-43 Expression

Given the observed metabolic changes associated with mutant TDP-43 expression, we next investigated ROS dynamics and the levels of glutathione, a key antioxidant, in NSC34 motor neuron-like cells. Specifically, we assessed ROS levels along with the total glutathione pool and its oxidized (GSSG) and reduced (GSH) forms at 24 and 48 hours post-TDP-43 expression. At the 24-hour time point, no significant differences were observed between the MVT and WTT groups in ROS levels, total glutathione, GSH, or GSSG, indicating that mutant TDP-43 expression did not immediately perturb oxidative homeostasis. A similar trend was observed at the 48-hour time point, with ROS, total glutathione, and GSH levels remaining unchanged between the MVT and WTT groups. However, GSSG levels were significantly lower in the MVT group compared to WTT at 48 hours, suggesting a potential shift in the redox balance favoring glutathione reduction (Figure 4.12). These findings suggest that mutant TDP-43 expression does not induce overt oxidative stress in NSC34 motor neuron-like cells,

as indicated by stable ROS levels and glutathione content. However, the decrease in GSSG levels at 48 hours may reflect enhanced glutathione recycling or altered redox regulation in response to mutant TDP-43 expression.

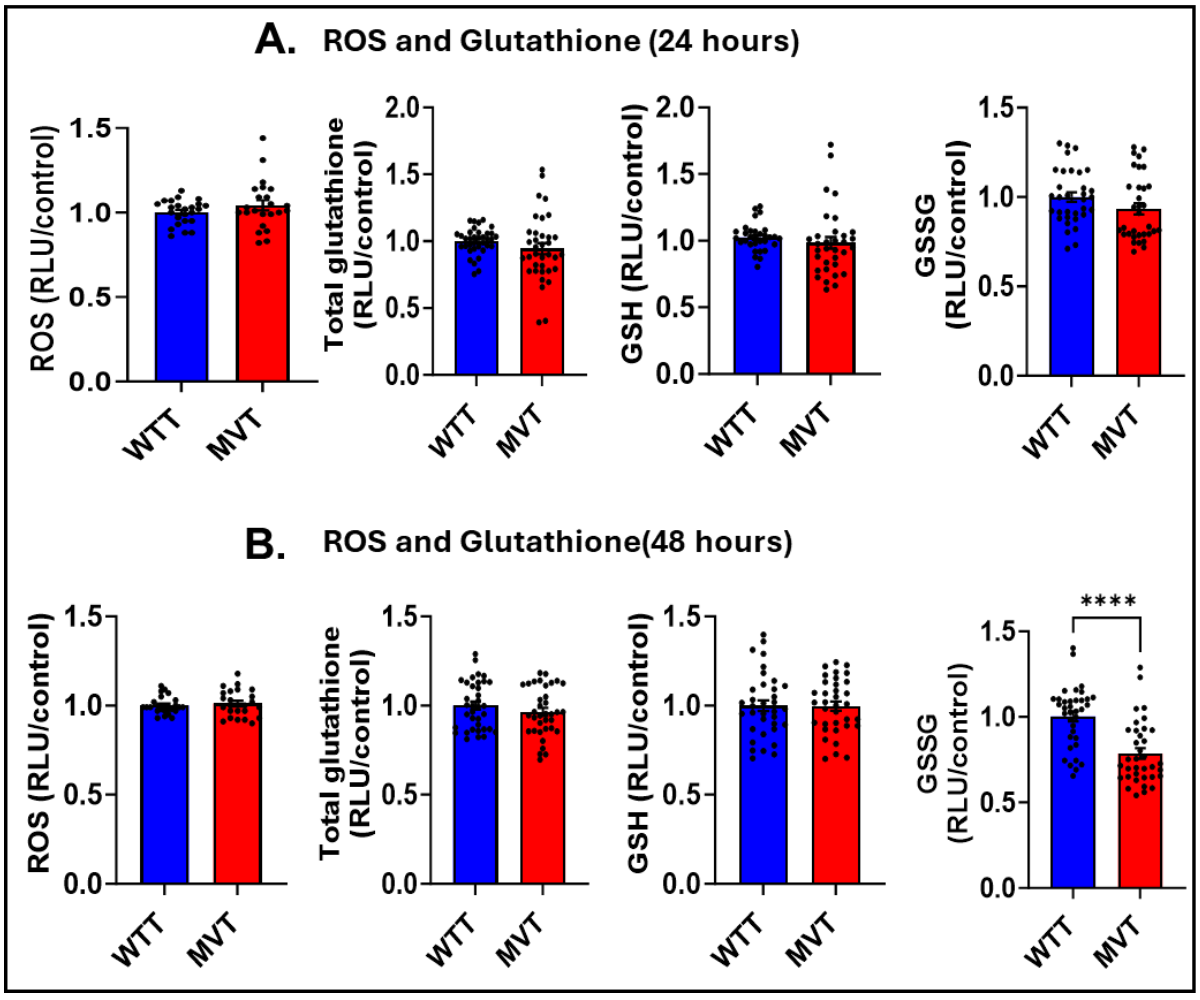

Figure 4.12 | Oxidative stress and glutathione levels in NSC34 motor neuron-like cells following TDP-43 mutation expression. (A-B) Quantification of ROS and total glutathione levels at 24 and 48-hour time points post-TDP-43 expression, showing no significant differences between the mutant (MVT) and wild-type (WTT) groups. (C-D) Assessment of oxidized (GSSG) and reduced (GSH) glutathione levels, revealing a significant decrease in GSSG levels at 48 hours in the MVT group, with no changes in GSH. Data are mean ± SEM (n = 3 biological replicates). Statistical tests: unpaired t-test (Welch correction) or Mann–Whitney U test. ****p < 0.001.

NSC34 Motor Neuron Energy Metabolic Phenotype Following TDP-43 Mutant Expression

The second part of the study aimed to investigate the metabolic implications of TDP-43 mutations in NSC34 motor neuron-like cells. Employing a rigorous selection process based on criteria such as localization, post-translational modification, and solubility, the M337V (MVT) mutation was identified as the most appropriate candidate for further analysis. Subsequently, we introduced wild-type TDP-43 (WTT) and the mutant TDP-43 (MVT) into NSC34 motor neuron-like cells. Following this, we conducted comprehensive metabolic phenotyping to assess the metabolic changes, summarized as follows:

- **Transcriptomic Profile Changes**: Following MVT expression in NSC34 motor neuron-like cells, the transcriptomic analysis revealed significant alterations in gene expression patterns. Out of 18,811 genes analyzed, 384 genes were upregulated, while only 36 genes were downregulated. Both coding and noncoding genes displayed similar patterns.

- **Metabolic Cofactor Dynamics:** Analysis of metabolic cofactors NAD and NADP revealed dynamic changes following MVT expression. While no significant alterations were observed in NAD+ and NADH levels, the NAD+/NADH ratio decreased at 24 hours post-expression. Additionally, NADP+ levels increased significantly at 24 hours, indicating potential metabolic adaptations in response to TDP-43 mutation.

- **Glucose Metabolism Alterations**. Gene expression analysis focusing on key enzymes involved in glucose, lipid, and glycogen metabolism revealed a significant increase in G6PD in the pentose phosphate pathway and CRAT in the beta-oxidation of fat.

- **Energy Substrate Utilization**: Investigation of glucose, lactate, and glutamine levels in the media revealed temporal changes in substrate utilization, with no significant differences between WTT and MVT groups. However, glucose uptake increased significantly at 48 hours post-expression, suggesting increased glucose demand in MVT-expressing cells.

- **Dynamic Glucose Metabolic Mapping**: Metabolic mapping experiments using U-13C labelled glucose provided insights into carbon utilization in glycolysis and the TCA cycle. While some metabolites showed slight alterations, overall metabolic flux remained largely unchanged between WTT and MVT groups, indicating complex metabolic adaptations in response to TDP-43 mutation.

- **Metabolic Flux Analysis**: Glycolytic and mitochondrial stress tests revealed increased glycolysis and mitochondrial oxidative phosphorylation in MVT-expressing cells. These findings suggest enhanced energy production pathways in response to TDP-43 mutation.
- **Redox Status Changes:** Analysis of ROS and glutathione dynamics revealed consistent levels of ROS, total glutathione, and GSH between WTT and MVT groups at both 24 and 48-hour time points. However, GSSG levels were significantly lower in the MVT group at the 48-hour time point, indicating potential alterations in cellular redox balance in response to TDP-43 mutation.

These findings highlight the complex molecular and metabolic changes induced by mutant TDP-43 expression in NSC34 motor neuron-like cells, underscoring the multifaceted nature of TDP-43-associated pathophysiology and its impact on metabolic homeostasis. While metabolic flux analysis suggests a hypermetabolic maladaptive phenotype, results from glucose dynamic metabolic mapping, gene expression, and energy substrate analysis revealed inconsistencies. Unlike TDP-43 knockdown, MVT does not result in a complete loss of function, which may account for the more subtle metabolic alterations observed. Furthermore, while MVT exhibits mild cytoplasmic mislocalization, its insolubility only increases under stress conditions, indicating that its baseline effect on metabolic homeostasis is limited. Additionally, exogenous expression of mutant TDP-43 may influence endogenous TDP-43 dynamics, potentially altering the broader metabolic landscape. These factors likely contribute to the observed inconsistencies across metabolic assessments. Nevertheless, even transient or mild metabolic perturbations in NSC34 cells have important implications for TDP-43-associated pathophysiology. In the next section, we extend this investigation to BV2 microglia and N2a neuroblastoma cells following TDP-43 mutant expression, further dissecting the relationship between proteinopathy and cellular energy metabolism.

Part III: Metabolic dynamics of N2A non-motor neuroblastoma and BV2 microglia-like cells upon TDP-43 perturbations

Previously, we demonstrated that TDP-43 perturbation disrupts metabolic homeostasis in NSC34 motor neuron-like cells, albeit with varying degrees of severity. TDP-43 knockdown induced a pronounced hypermetabolic state marked by elevated glucose uptake, increased ATP production, and heightened oxidative stress—features indicative of a maladaptive metabolic overdrive. In contrast, expression of mutant TDP-43 (M337V) produced subtler alterations, including increased glycolytic activity, disrupted NAD^+/NADH balance, and moderate oxidative stress, suggesting a more complex and potentially adaptive reprogramming of energy metabolism.

In ALS, over 95% of patients exhibit TDP-43 pathology, with progressive and selective degeneration of motor neurons in the central nervous system—despite the ubiquitous expression of TDP-43 across all brain cell types (Liscic et al., 2008). Conversely, in FTLD, approximately 45% of cases show TDP-43 inclusions, yet the degeneration is largely confined to neurons of the frontal and temporal cortices (Liscic et al., 2008). These contrasting patterns of selective vulnerability raise a fundamental question in neurodegeneration: how does dysfunction of a ubiquitously expressed protein like TDP-43 result in such distinct, cell-type- and region-specific patterns of pathology? These observations prompt a central question: Are motor neurons uniquely sensitive to TDP-43-induced metabolic disruption, or are such metabolic shifts a broader feature of TDP-43 dysfunction across neural cell types?

To address this, we extended our investigation to two additional brain-derived cell types with distinct lineage and physiological roles: N2A neuroblastoma cells and BV2 microglia. N2A cells, derived from the neural crest and often used to model autonomic neurons, represent a neuronal population that remains largely unaffected in TDP-43 proteinopathies, including ALS and FTLD (LePage et al., 2005; Tremblay et al., 2010). In contrast, BV2 microglia, the resident immune cells of the central nervous system, exhibit remarkable metabolic flexibility, enabling them to adapt their energy production pathways in response to environmental changes(Lepiarz-Raba et al., 2023). This adaptability allows microglia to switch between oxidative phosphorylation and glycolysis, depending on their activation state and functional demands (Lepiarz-Raba et al., 2023). Moreover, TDP-43 depletion in microglia has been shown to enhance phagocytic activity, indicating a direct role of TDP-43 in regulating microglial function (Paolicelli et al., 2017). By comparing these two models to motor neuron-like NSC34 cells, we aim to determine whether TDP-43-induced metabolic disruptions reflect selective

vulnerability in motor neurons, or whether such effects are shaped by broader cell-intrinsic features of metabolic resilience or susceptibility.

This part profiles the metabolic responses of BV2 microglia and N2A neuroblastoma cells following TDP-43 knockdown and mutant expression, with a focus on glucose metabolism (glucose uptake, lactate levels, metabolic flux), energy homeostasis (ATP production), oxidative stress (ROS levels), and mitochondrial and glycolytic function (stress tests). We hypothesize that TDP-43 perturbation elicits distinct metabolic responses across brain cell types, with motor neurons exhibiting the greatest susceptibility to maladaptive metabolic stress.

Metabolic Profiling of BV2 Microglia Following TDP-43 Perturbation

Western Blot Confirmation of TDP-43 Knockdown and Mutant Expression

To assess the metabolic consequences of TDP-43 perturbation in BV2 microglia and N2A neuroblastoma cells, we employed the same molecular approach previously applied to NSC34 motor neuron-like cells. TDP-43 knockdown (KD) was achieved via TDP-43-specific siRNA, while exogenous expression of human wildtype TDP-43 (WTT) and mutant TDP-43 (M337V, MVT) was accomplished through plasmid transfection. These experimental manipulations were subsequently validated by Western blot analysis.

Western blot analysis confirmed effective TDP-43 knockdown and overexpression in both BV2 and N2A cells. TDP-43 protein levels were assessed using an anti-TDP-43 antibody, with tubulin serving as the loading control. In BV2 cells, TDP-43 knockdown resulted in a substantial reduction of the endogenous TDP-43 band at approximately 43 kDa, confirming effective siRNA-mediated depletion. Densitometric quantification indicated over 80% reduction in TDP-43 protein levels relative to non-silencing (NS) controls (Figure 5.1A). Similarly, N2A cells exhibited a strong reduction in the endogenous TDP-43 band (~43 kDa), with knockdown efficiency comparable to BV2 (over 80%) (Figure 5.1B).

For TDP-43 overexpression studies, exogenously expressed WTT and MVT TDP-43 constructs carried a GFP tag, resulting in a molecular weight shift to ~70 kDa. In BV2 cells (Figure 5.1C), overexpression of both WTT and MVT resulted in a single, sharp band corresponding to the exogenous TDP-43-GFP fusion, while the endogenous TDP-43 band (~43 kDa) remained visible below. In contrast, N2A cells (Figure 5.1D) exhibited two distinct bands in the ~70 kDa range, suggesting the presence of multiple isoforms or post-translational variants of the exogenous TDP-43-GFP. Interestingly, the endogenous band (~43 kDa) was faint or undetectable in N2A cells under overexpression conditions, suggesting possible suppression or overshadowing by the exogenous

construct. These differences may reflect cell-type-specific processing or stability of exogenously expressed TDP-43.

Collectively, these findings confirm that TDP-43 expression was effectively manipulated in BV2 and N2A cells, establishing a robust experimental framework for subsequent metabolic assays aimed at elucidating the impact of TDP-43 dysregulation on cellular metabolism.

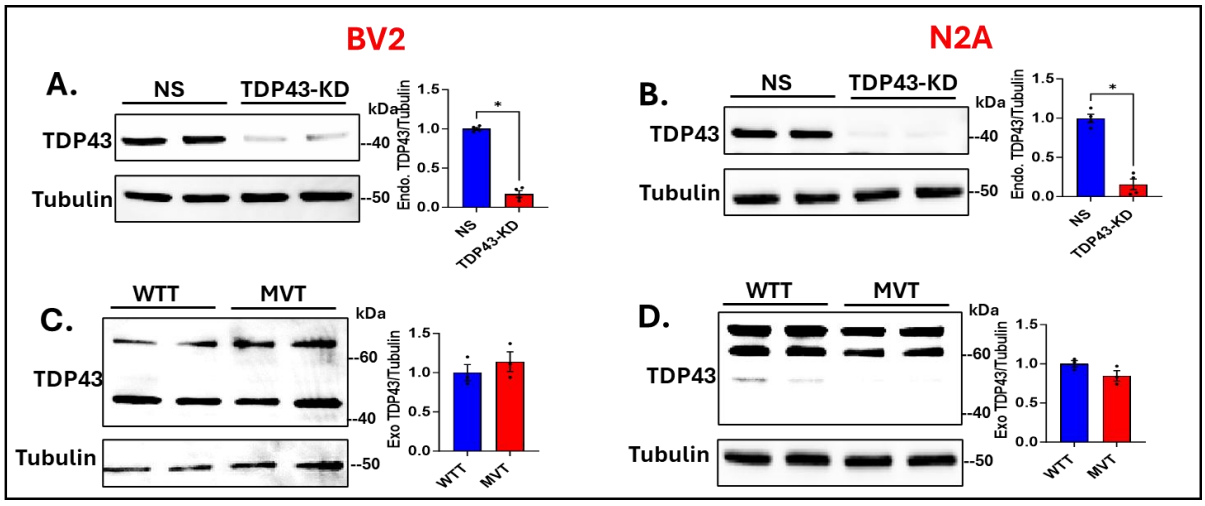

Figure 5.1 | Western blot validation of TDP-43 knockdown and overexpression in BV2 and N2A cells. (A, B) Representative Western blot images of endogenous TDP-43 expression in BV2 (A) and N2A (B) cells following transfection with non-silencing control siRNA (NS) or TDP-43-targeting siRNA (KD). Knockdown efficiency was confirmed by the substantial reduction of the endogenous TDP-43 band (~43 kDa) in KD conditions. Tubulin was used as a loading control. (C, D) Western blot analysis of exogenous TDP-43 overexpression in BV2 (C) and N2A (D) cells transfected with wild-type TDP-43 (WTT) or mutant TDP-43 (M337V, MVT). Exogenous constructs include a GFP tag, resulting in a molecular weight shift to ~70 kDa. In BV2 cells, a single exogenous band is visible at ~70 kDa for both WTT and MVT, along with a lower endogenous TDP-43 band (~43 kDa). In contrast, N2A cells display two distinct bands in the ~70 kDa range, likely representing differentially processed or modified forms of exogenous TDP-43-GFP. The endogenous TDP-43 band is faint or undetectable in N2A cells under these conditions, possibly due to suppression or overshadowing by the exogenous construct.

Glucose and Lactate Levels in BV2 Cells

To assess the impact of TDP-43 knockdown and mutant expression on glucose metabolism in BV2 microglia, glucose and lactate levels in the media were measured at 24- and 48-hours post-transfection. Additionally, glucose uptake was quantified at both 24 and 48 hours. Glucose levels in the media were significantly lower in the TDP-43 knockdown (KD) condition compared to non-silencing (NS) controls at both 24 and 48 hours (Figure 5.2A, $p < 0.01$, $p < 0.05$, respectively), indicating increased glucose consumption by BV2 cells following TDP-43 depletion. The reduction in glucose levels was more pronounced at 48 hours, suggesting that the metabolic shift persists over time. Lactate levels were significantly elevated in KD conditions compared to NS controls at both time points (Figure 5.2B, $p < 0.01$ at 24 hours, $p < 0.0001$ at 48 hours), with a greater increase observed at

48 hours, indicating a strong shift toward glycolytic metabolism. Glucose uptake was significantly higher in KD conditions compared to NS controls at both 24 and 48 hours (Figure 5.2C, $p < 0.001$), further supporting increased glucose metabolism following TDP-43 knockdown. The persistence of this increase across both time points suggests a sustained metabolic effect. In contrast to knockdown conditions, glucose levels in the media were comparable between wild-type TDP-43 (WTT) and mutant TDP-43 (MVT) conditions at both 24 and 48 hours (Figure 5.2D), indicating that mutant expression does not significantly alter glucose consumption in BV2 microglia. Similarly, lactate levels remained unchanged between WTT and MVT conditions at both time points (Figure 5.2E), suggesting that mutant expression does not induce a shift toward glycolysis in BV2 cells. Glucose uptake at both 24 and 48 hours showed no significant differences between WTT and MVT conditions (Figure 5.2F), further confirming that mutant expression does not enhance glucose metabolism in BV2 microglia.

These findings suggest that TDP-43 knockdown, but not mutant expression, drives metabolic reprogramming in BV2 microglia, leading to increased glucose consumption and glycolytic activity. The upregulation of glucose uptake and lactate production following knockdown suggests a shift toward a hyperglycolytic phenotype. In contrast, mutant TDP-43 expression did not significantly affect glucose metabolism, suggesting that BV2 microglia maintain metabolic stability under basal conditions when mutant TDP-43 is present.

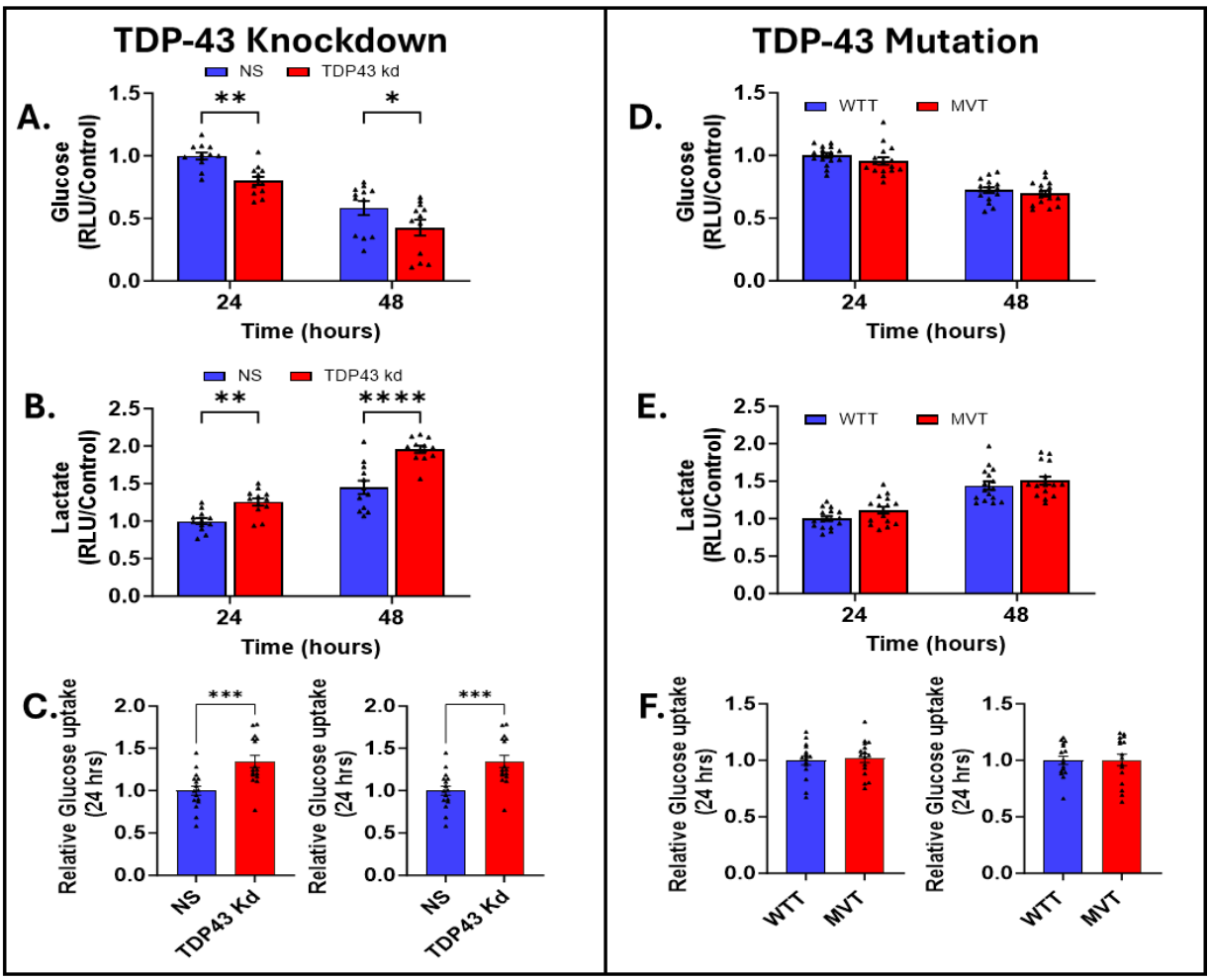

Figure 5.2 | Glucose consumption, lactate production, and glucose uptake in BV2 microglia following TDP-43 perturbation. (A–C) Measurements following TDP-43 knockdown (KD) in BV2 microglia. (A) Glucose levels in the media at 24 and 48 hours in non-silencing (NS) and KD conditions. (B) Lactate levels in the media at 24 and 48 hours in NS and KD conditions. (C) Glucose uptake in NS and KD conditions at 24 and 48 hours. (D–F) Measurements following wild-type (WTT) and mutant (MVT) TDP-43 overexpression in BV2 microglia. (D) Glucose levels in the media at 24 and 48 hours in WTT and MVT conditions. (E) Lactate levels in the media at 24 and 48 hours in WTT and MVT conditions. (F) Glucose uptake in WTT and MVT conditions at 24 and 48 hours. Data are mean ± SEM. *p < 0.05; **p < 0.01; ***p < 0.005; ****p < 0.001.

Glucose Metabolic Mapping in BV2 Microglia Following TDP-43 Perturbation

To assess how TDP-43 perturbation affects glucose metabolism in BV2 microglia, we performed [U-13C] glucose tracing, allowing us to track glucose incorporation into glycolysis and the TCA cycle. The isotopic enrichment of key metabolic intermediates was quantified by GC-MS, and the results are presented in Figure 5.3 (TDP-43 knockdown) and Figure 5.4 (mutant TDP-43 expression).

Following TDP-43 knockdown, lactate labeling (M+3) was significantly increased, suggesting a significant proportion of glucose was metabolized into lactate production (Figure 5.3A). This was accompanied by a marked increase in lactate molecular carbon labeling (MCL), indicating enhanced

retention of glucose-derived carbons in lactate. These findings suggest that knockdown of TDP-43 in BV2 microglia enhances glycolytic flux.

Glucose incorporation into the TCA cycle was also altered by TDP-43 knockdown, as evidenced by significant increases in citrate (Figure 5.3B), α-ketoglutarate (Figure 5.3C), and succinate (Figure 5.3D) MCL levels. Notably, succinate also showed a significant increase in M+2 labeling, reinforcing the idea that glucose-derived carbons continue to enter and contribute to oxidative metabolism in BV2 cells. However, no significant changes were observed in fumarate (Figure 5.3E) or malate (Figure 5.3F), suggesting that metabolic flux through the later stages of the TCA cycle remains stable.

In contrast, mutant TDP-43 expression (MVT) induced a much more limited metabolic shift (Figure 5.4). Among all measured metabolites, only lactate MCL was significantly increased (Figure 5.4A), while the M+3 fraction remained unchanged. This suggests that more glucose-derived carbon is retained in lactate, but the overall glycolytic flux remains stable. Importantly, there were no significant changes in M+2 labeling or MCL for citrate (Figure 5.4B), α-ketoglutarate (Figure 5.4C), succinate (Figure 5.4D), fumarate (Figure 5.4E), or malate (Figure 5.4F), indicating that mutant TDP-43 expression does not significantly impact glucose oxidation in BV2 microglia.

These findings indicate that TDP-43 knockdown strongly enhances glycolysis while also increasing glucose incorporation into the TCA cycle, suggesting a potential metabolic shift in BV2 microglia. In contrast, mutant TDP-43 expression does not induce major metabolic changes, apart from increased glucose retention in lactate.

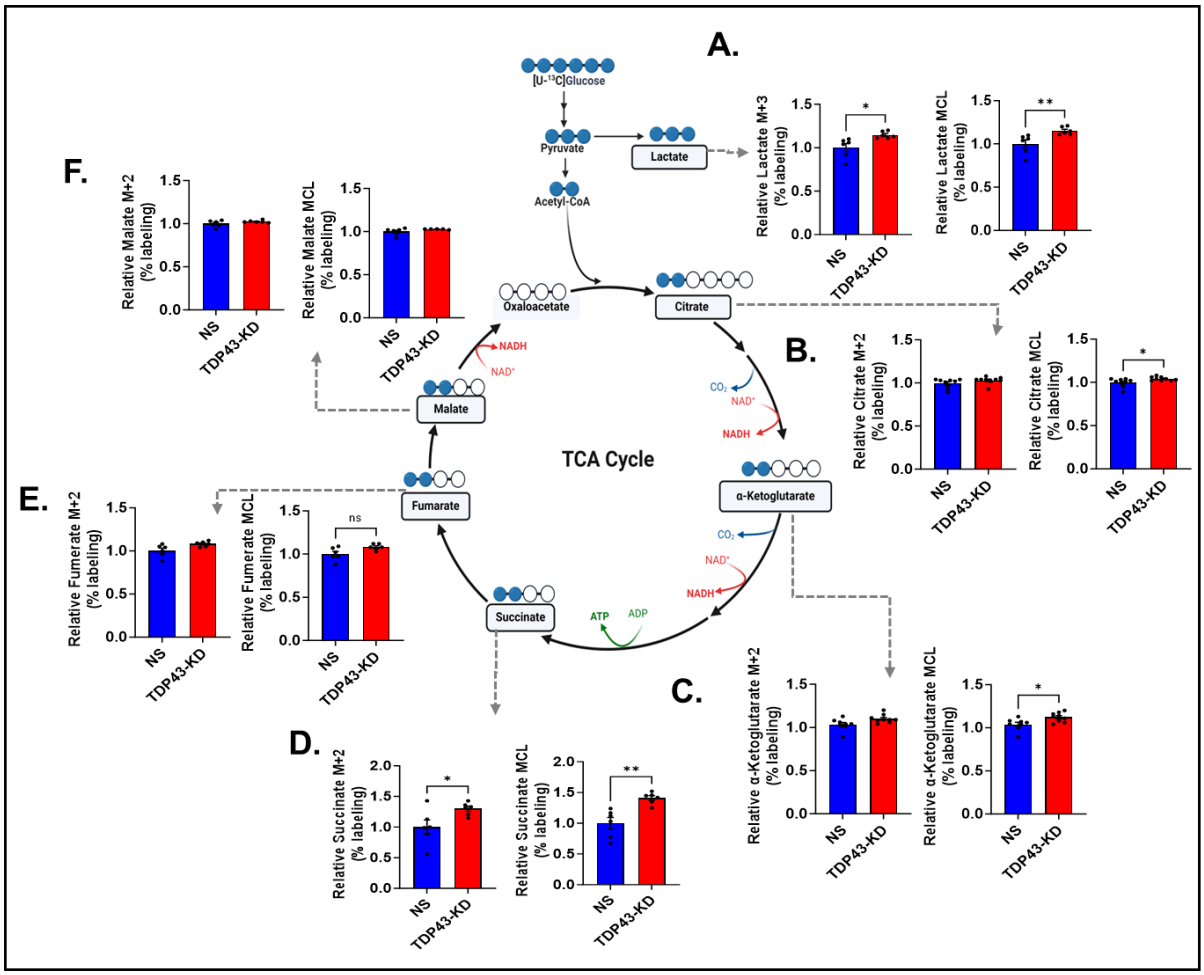

Figure 5.3 | Glucose metabolic mapping in BV2 microglia following TDP-43 knockdown. (A) Lactate labeling from [U-13C] glucose, showing the fractional incorporation of glucose-derived carbon (M+3) and molecular carbon labeling (MCL). (B–F) TCA cycle metabolite labeling, depicting fractional enrichment (M+2) and MCL for citrate (B), α-ketoglutarate (C), succinate (D), fumarate (E), and malate (F). The central schematic illustrates glucose entry into glycolysis and the TCA cycle, with dashed arrows indicating the corresponding metabolic pathways analyzed. Data are mean ± SEM. *p < 0.05; **p < 0.01.

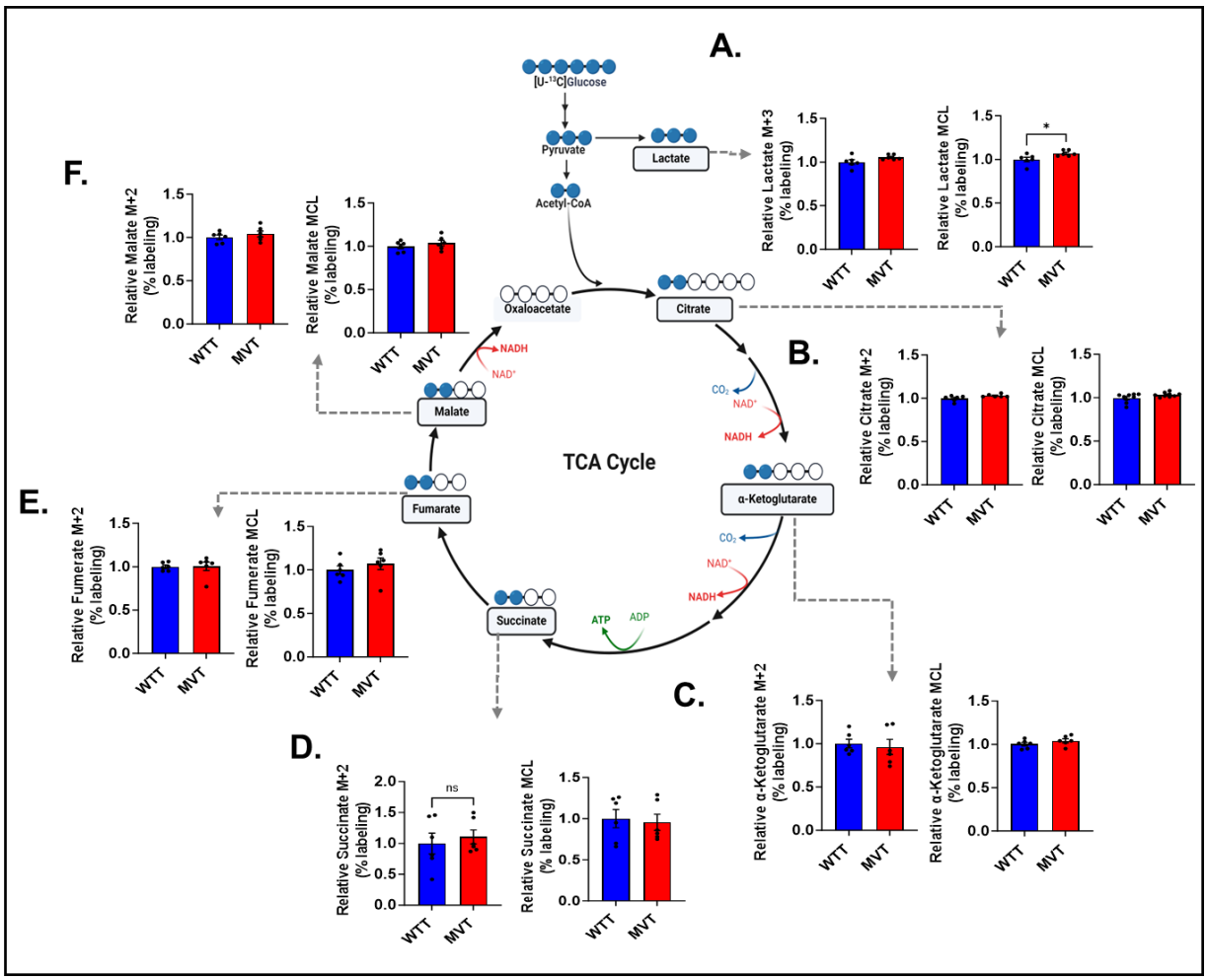

Figure 5.4 | Glucose metabolic mapping in BV2 microglia following mutant TDP-43 expression. (A) Lactate labeling from [U-13C] glucose, showing fractional incorporation (M+3) and molecular carbon labeling (MCL). (B–F) TCA cycle metabolite labeling, depicting fractional enrichment (M+2) and MCL for citrate (B), α-ketoglutarate (C), succinate (D), fumarate (E), and malate (F) in wild-type (WTT) and mutant (MVT) TDP-43 conditions. The central schematic illustrates glucose metabolism, with dashed arrows indicating the corresponding metabolic pathways analyzed. Data are mean ± SEM. *p < 0.05.

Metabolic Flux Analysis in BV2 Microglia Following TDP-43 Perturbation

To assess the functional impact of TDP-43 perturbation on cellular energy metabolism, we performed GST and MST in BV2 microglia following TDP-43 knockdown (KD) and mutant expression (MVT). As previously described in earlier parts, these assays measure extracellular acidification rate (ECAR) as an indicator of glycolytic flux and oxygen consumption rate (OCR) as a measure of mitochondrial respiration. The results are presented in Figure 5.5.

TDP-43 knockdown enhanced glycolytic function in BV2 microglia, while mitochondrial parameters remained unchanged. As shown in Figure 5.5A, GST analysis revealed a significant increase in ECAR-related glycolysis and glycolytic capacity in TDP-43 KD cells compared to non-silencing (NS) controls. Glycolytic reserve was unchanged, indicating that the cells were already operating near their maximal glycolytic capacity. In parallel, MST results (Figure 5.5B) showed no significant differences in basal respiration, maximal respiration, proton leak, ATP production, or spare respiratory capacity between KD and control cells.

In contrast, mutant TDP-43 expression (MVT) was associated with a distinct metabolic profile (Figure 5.5C–D). GST analysis showed significantly lower glycolysis and glycolytic capacity in MVT-expressing cells relative to wild-type TDP-43 (WTT), while glycolytic reserve remained unchanged (Figure 5.5C). MST analysis revealed a significant reduction in ATP production, whereas other mitochondrial parameters remained comparable between groups (Figure 5.5D). These findings suggest that mutant TDP-43 suppresses glycolytic output and reduces energy availability, without broadly impairing mitochondrial respiratory capacity.

Taken together, these findings indicate that TDP-43 knockdown and mutant expression induce distinct metabolic alterations in BV2 microglia. While TDP-43 KD enhances glycolysis without impacting mitochondrial respiration, mutant TDP-43 expression is associated with reduced glycolytic activity and lower ATP levels. Compared to NSC34 motor neuron-like cells—which exhibited both glycolytic and mitochondrial alterations—BV2 microglia show a more selective, glycolytic response, suggesting a degree of metabolic resilience potentially reflective of their intrinsic adaptability to cellular stress.

.

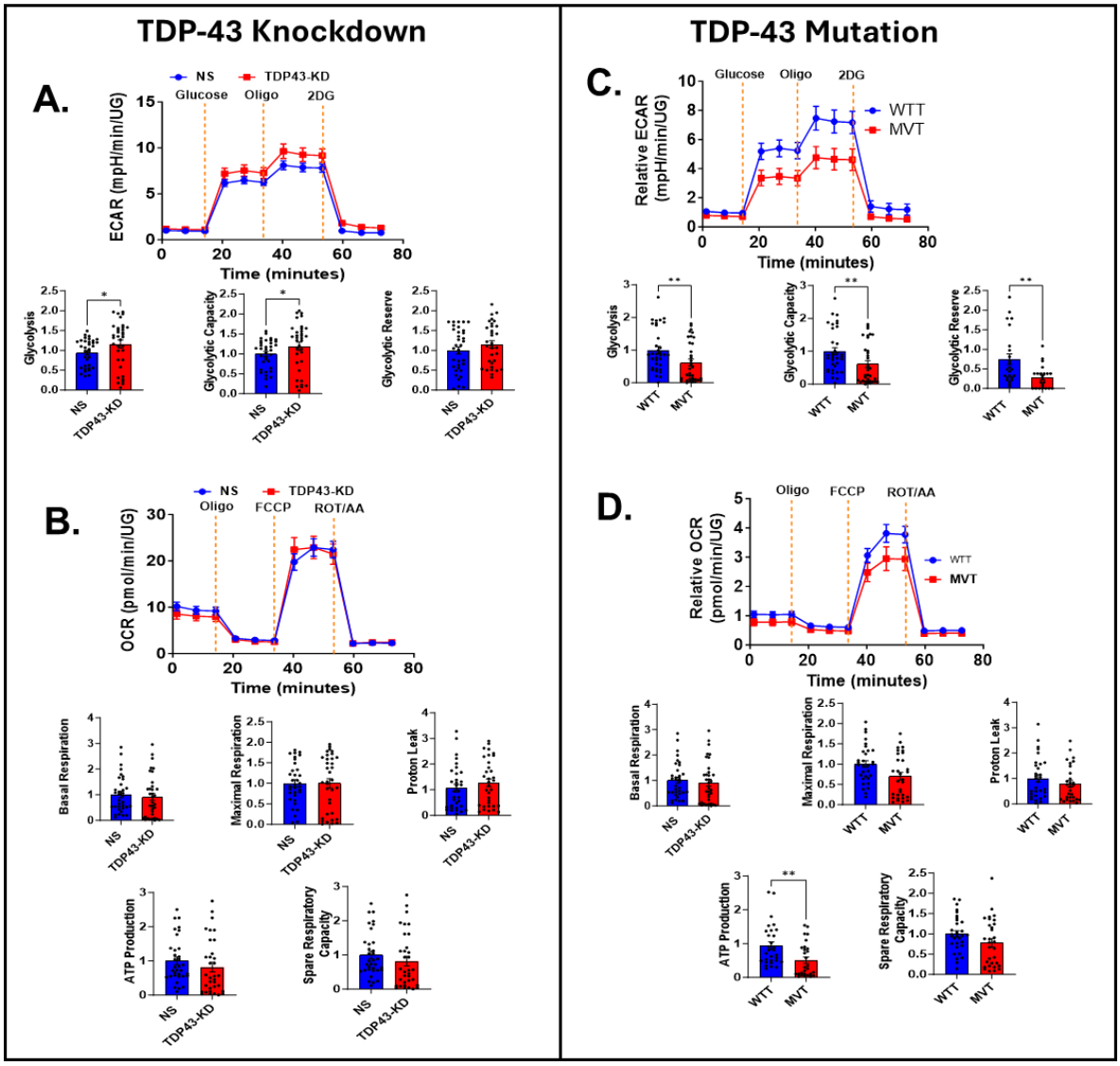

Figure 5.5 | Metabolic flux analysis in BV2 microglia following TDP-43 perturbation. (A) Glycolysis Stress Test (GST) response curve and quantification of glycolysis, glycolytic capacity, and glycolytic reserve in BV2 microglia following TDP-43 knockdown (KD). (B) Mitochondrial Stress Test (MST) response curve and quantification of basal respiration, maximal respiration, proton leak, ATP production, and spare respiratory capacity in TDP-43 KD BV2 cells. (C) GST response curve and quantification of glycolysis-related parameters in BV2 microglia expressing wild-type (WTT) or mutant (MVT) TDP-43. (D) MST response curve and quantification of mitochondrial parameters in WTT- and MVT-expressing BV2 cells. Data are mean ± SEM. *$p < 0.05$; **$p < 0.01$.

Oxidative Stress and ATP in BV2 Cells Following TDP-43 Perturbation

Having established that TDP-43 knockdown in BV2 microglia enhances glucose utilization and glycolytic activity, we next sought to determine whether these metabolic changes are accompanied by alterations in oxidative stress and ATP homeostasis. ROS levels were measured as an indicator of

oxidative stress, while ATP quantification provided insights into cellular energy balance at 24- and 48-hours post-transfection.

Following TDP-43 knockdown, ROS levels (Figure 5.6A) were significantly elevated at 24 hours compared to the NS control. By 48 hours, ROS levels remained elevated but were not statistically different from the control. Similarly, ATP levels (Figure 5.6B) showed a significant increase at 24 hours, while at 48 hours, ATP levels remained slightly elevated but without statistical significance. In the mutant TDP-43 (MVT) expression condition, ROS levels (Figure 5.6C) did not differ significantly between WTT and MVT groups at either 24 or 48 hours. Similarly, ATP levels (Figure 5.6D) remained unchanged across both time points, with no significant differences between the WTT and MVT groups.

These results indicate that TDP-43 knockdown in BV2 cells is associated with an initial rise in oxidative stress and ATP production at 24 hours, which stabilizes by 48 hours. However, mutant TDP-43 expression does not appear to induce notable changes in ROS or ATP levels within this timeframe. This temporal stabilization may reflect the inherent metabolic flexibility of microglia, enabling them to restore redox and energy homeostasis despite early perturbations.

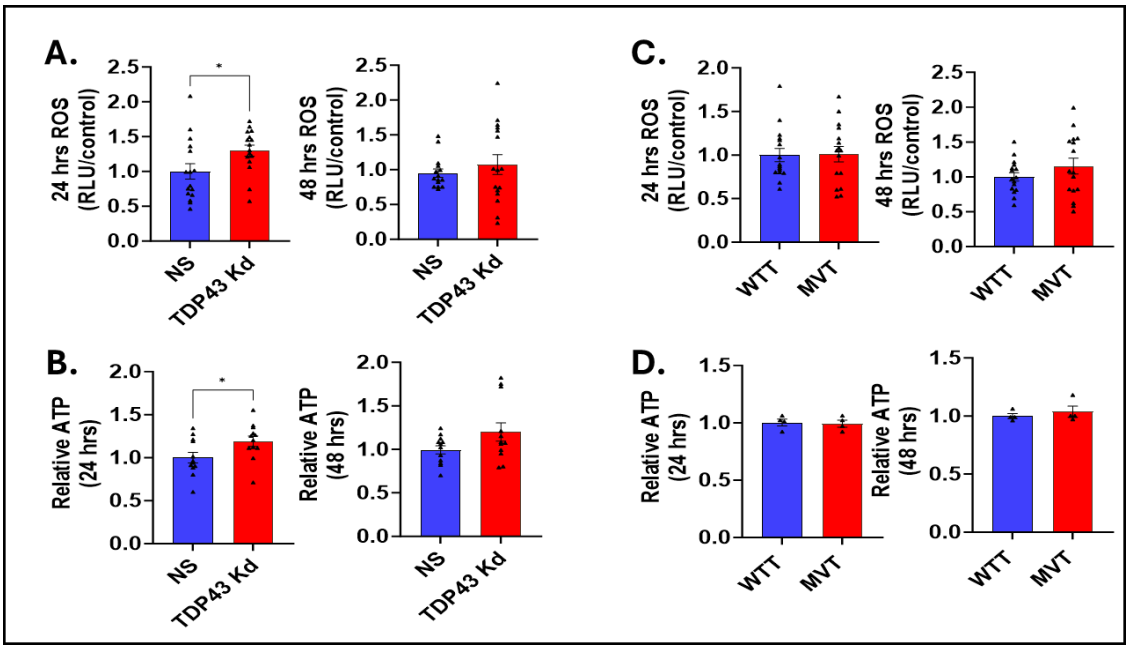

Figure 5.6 | Reactive oxygen species (ROS) and ATP levels in BV2 microglia following TDP-43 perturbation. (A) ROS levels measured at 24 and 48 hours post-TDP-43 knockdown (KD) in BV2 cells. (B) ATP levels measured at 24 and 48 hours post-TDP-43 KD. (C) ROS levels at 24 and 48 hours in BV2 cells expressing wild-type TDP-43 (WTT) or mutant TDP-43 (MVT). (D) ATP levels at 24 and 48 hours in BV2 cells expressing WTT or MVT. Data are mean ± SEM. *p < 0.05.

Metabolic Profiling of N2A Neuroblastoma Following TDP-43 Perturbation

We next examined whether a similar response occurs in N2A neuroblastoma cells. As a model for non-motor neuronal metabolism, N2A cells offer a useful comparator for assessing whether TDP-43-induced metabolic changes extend beyond motor neurons. These cells, which are derived from the neural crest and represent autonomic neurons not typically affected in TDP-43-related diseases, complement our comparison with NSC34 motor neuron-like cells and BV2 microglia. NSC34 cells exhibited pronounced metabolic maladaptation following TDP-43 depletion, whereas BV2 microglia responded with a glycolytic shift (Section 5.2). It remains unclear whether non-motor neurons such as N2A exhibit a metabolic response akin to motor neurons or glia. If neurons are inherently vulnerable to TDP-43-driven metabolic dysfunction, N2A cells would be expected to mirror the alterations observed in NSC34 cells. Conversely, a cell-type-dependent effect would support the presence of distinct metabolic programs shaped by developmental lineage or functional identity.

Glucose and Lactate Levels in N2A Cells

To determine whether TDP-43 knockdown or mutant expression influences glucose metabolism in N2A neuroblastoma cells, we measured glucose levels in the media, lactate production, and glucose uptake at 24- and 48-hours post-transfection (Figure 5.7 A–F). Unlike the metabolic adaptations observed in BV2 microglia, N2A cells did not exhibit significant changes in glucose metabolism under either TDP-43 knockdown (Figure 5.7A–C) or mutant expression (Figure 5.7D–F) conditions:

Glucose levels in the media remained unchanged between TDP-43 knockdown (KD) and non-silencing (NS) controls at both time points, indicating no increase in glucose consumption (Figure 5.7A). Similarly, glucose levels were comparable between wild-type (WTT) and mutant (MVT) TDP-43 conditions (Figure 5.7D). Lactate production, a key indicator of glycolytic activity, showed no significant differences at 24 or 48 hours, suggesting that neither TDP-43 knockdown nor mutant expression alters glycolytic flux in N2A cells (Figure 5.7B, E). Glucose uptake measurements further confirmed the absence of metabolic reprogramming, as no significant changes were detected across knockdown (Figure 5.7C) or mutant conditions (Figure 5.7F).

Taken together, these findings indicate that, unlike NSC34 motor-neuron like cells, N2A neuroblastoma cells may not exhibit metabolic shifts following TDP-43 perturbation.

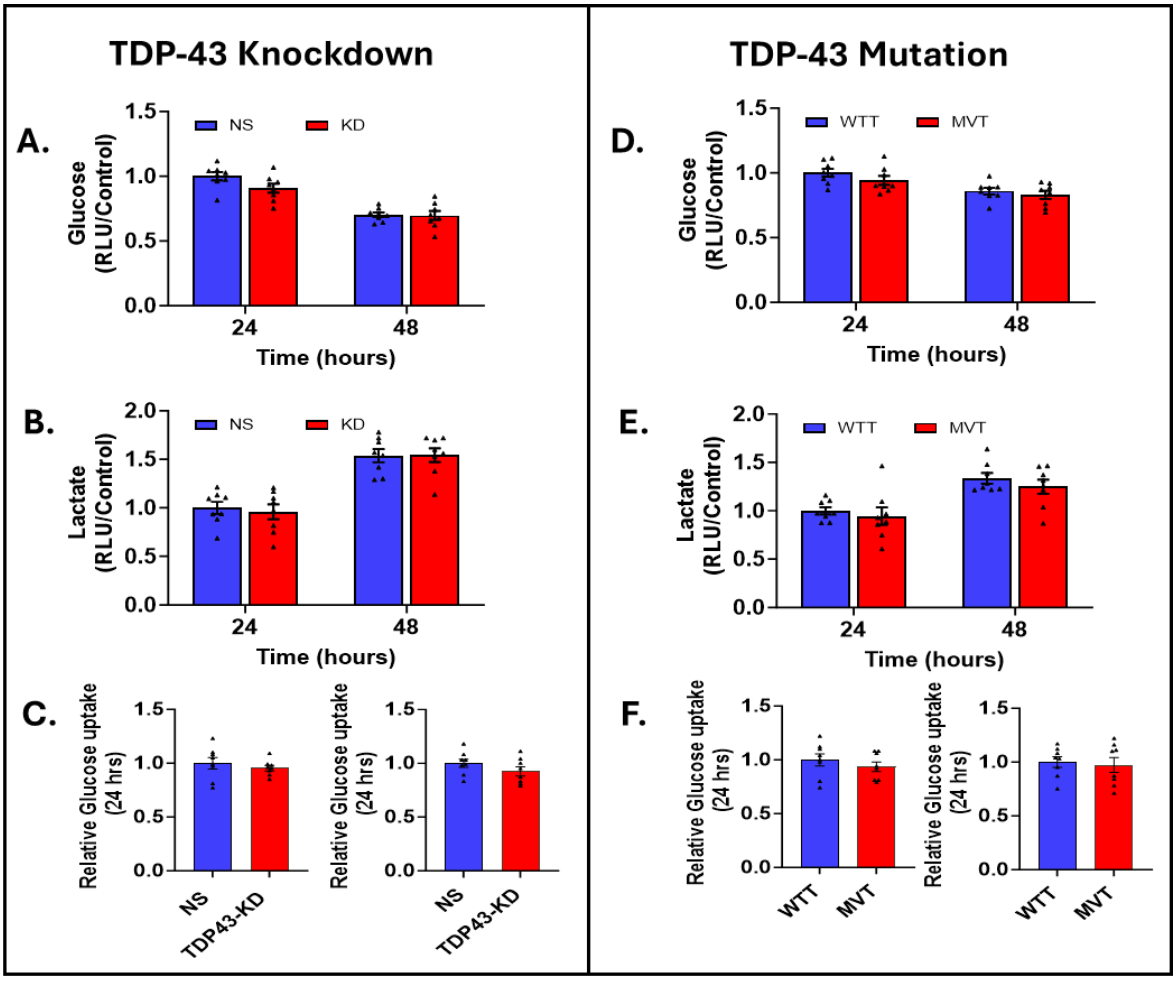

Figure 5.7 | Glucose consumption, lactate production, and glucose uptake in N2A neuroblastoma cells following TDP-43 perturbation. (A–C) TDP-43 knockdown (KD) does not significantly alter glucose levels in the media (A), lactate production (B), or glucose uptake (C) at 24 and 48 hours compared to non-silencing (NS) controls. (D–F) Similarly, mutant TDP-43 expression (MVT) does not significantly affect glucose metabolism, as glucose levels in the media (D), lactate production (E), and glucose uptake (F) remain unchanged compared to wild-type TDP-43 (WTT).

Glucose Metabolic Mapping in N2A Neuroblastoma Cells Following TDP-43 Perturbation

To examine how TDP-43 perturbation affects glucose metabolism in N2A neuroblastoma cells, [U-13C] glucose tracing was performed to track glucose incorporation into glycolysis and the TCA cycle. The isotopic enrichment of key metabolic intermediates was quantified by GC-MS, and the results are presented in Figure 5.8 (TDP-43 knockdown) and Figure 5.9 (mutant TDP-43 expression).

Following TDP-43 knockdown, lactate labeling (M+3) was significantly reduced (Figure 5.8A), accompanied by a decrease in lactate molecular carbon labeling (MCL). This suggests a lower retention of glucose-derived carbon in lactate. In addition, glucose incorporation into the TCA cycle

showed a reduction in citrate (Figure 5.8B), succinate (Figure 5.8C), and malate (Figure 5.8D) molecular carbon labeling (MCL). Notably, succinate also exhibited a significant decrease in M+2 labeling, indicating reduced entry of glucose-derived carbons into the TCA cycle. No significant changes were observed in α-ketoglutarate (Figure 5.8E) or fumarate (Figure 5.8F), suggesting that the later stages of the TCA cycle remain largely unaffected.

In contrast, mutant TDP-43 expression (MVT) resulted in minimal changes in glucose metabolism (Figure 5.9). Among all measured metabolites, only fumarate displayed significant alterations, with both M+2 labeling (Figure 5.9E) and MCL (Figure 5.9F) increasing. However, no significant changes were detected in lactate (Figure 5.9A), citrate (Figure 5.9B), α-ketoglutarate (Figure 5.9C), succinate (Figure 5.9D), or malate (Figure 5.9F), indicating that mutant TDP-43 expression does not induce widespread alterations in glucose metabolism in N2A cells.

These findings suggest that TDP-43 knockdown in N2A neuroblastoma cells may be associated with a subtle but reduced glucose incorporation into both glycolysis and the TCA cycle, whereas mutant TDP-43 expression results in only limited metabolic changes, primarily affecting fumarate labeling. To further explore the functional consequences of these findings, the next section assesses glycolytic and mitochondrial function using extracellular flux analysis.

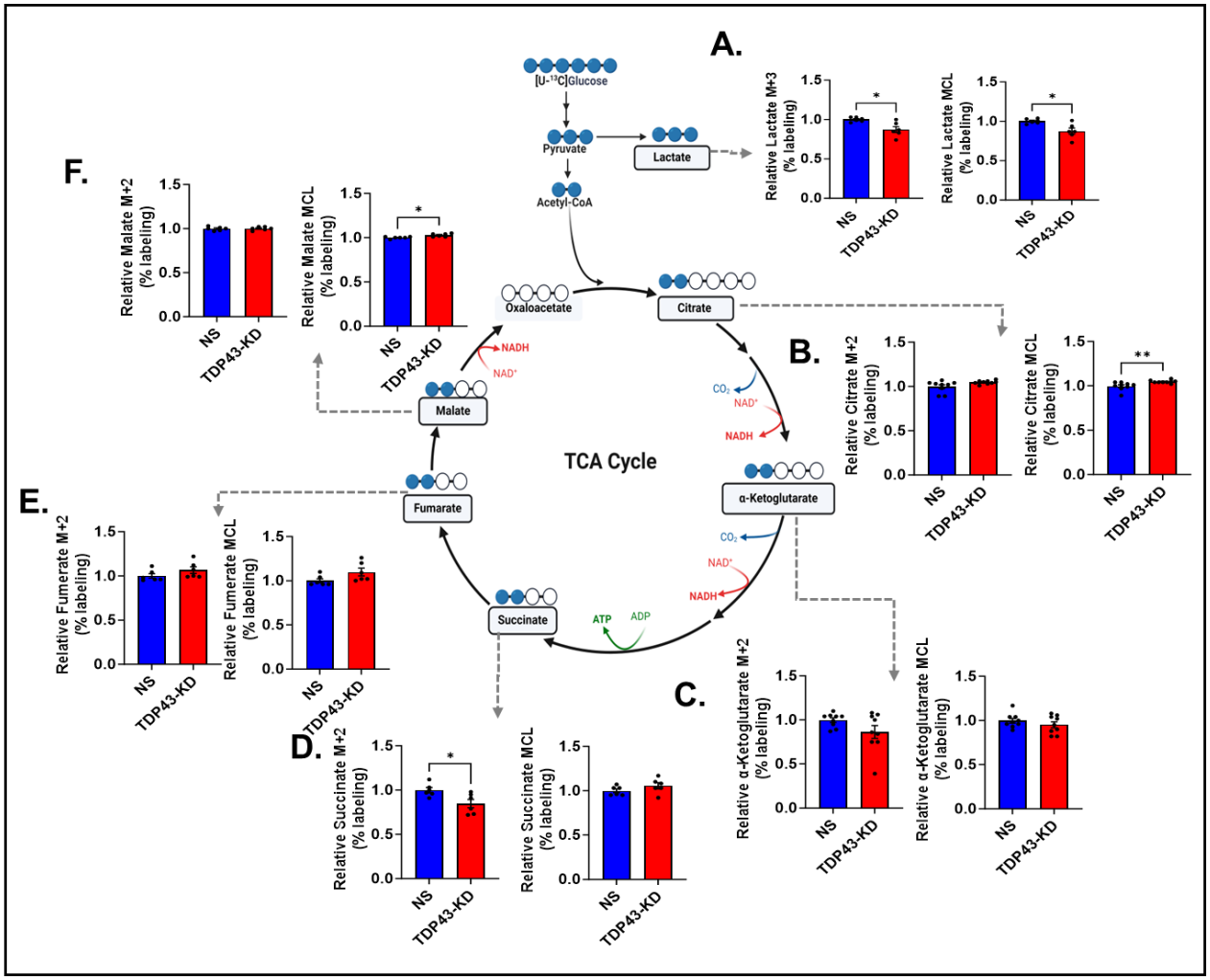

Figure 5.8 | Glucose metabolic mapping in N2A neuroblastoma cells following TDP-43 knockdown. (A) Lactate labeling from [U-13C] glucose, showing fractional incorporation of glucose-derived carbon (M+3) and molecular carbon labeling (MCL). (B–F) TCA cycle metabolite labeling, depicting fractional enrichment (M+2) and MCL for citrate (B), succinate (C), malate (D), α-ketoglutarate (E), and fumarate (F). The central schematic illustrates glucose entry into glycolysis and the TCA cycle, with dashed arrows indicating the corresponding metabolic pathways analyzed. Data are presented as mean ± SEM. Data are mean ± SEM. *p < 0.05; **p < 0.01.

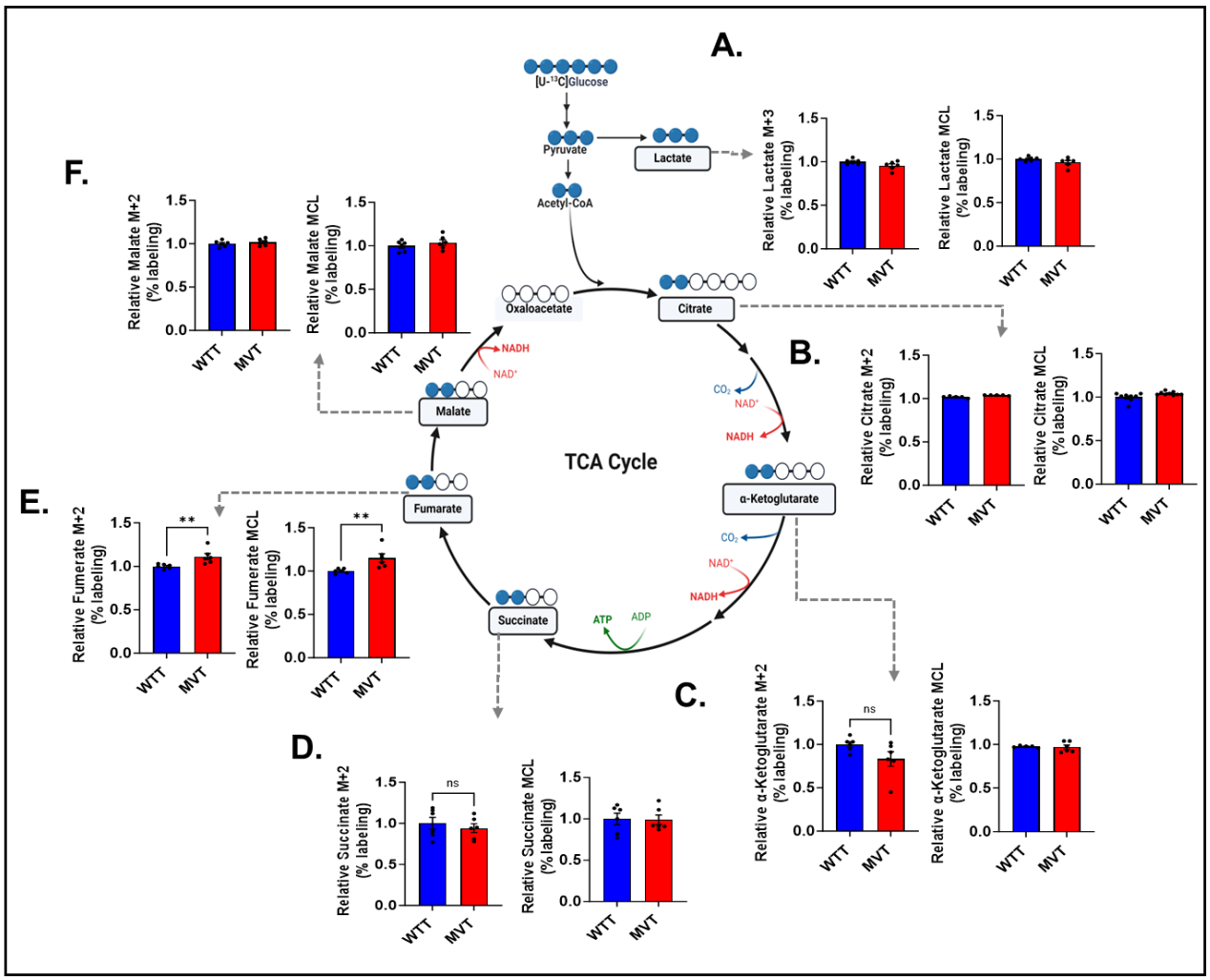

Figure 5.9 | Glucose metabolic mapping in N2A neuroblastoma cells following mutant TDP-43 expression. (A) Lactate labeling from [U-13C] glucose, showing fractional incorporation (M+3) and molecular carbon labeling (MCL). (B–F) TCA cycle metabolite labeling, depicting fractional enrichment (M+2) and MCL for citrate (B), succinate (C), malate (D), α-ketoglutarate (E), and fumarate (F) in wild-type (WTT) and mutant (MVT) TDP-43 conditions. The central schematic illustrates glucose metabolism, with dashed arrows indicating the corresponding metabolic pathways analyzed. Data are mean ± SEM. **p < 0.01.

Metabolic Flux Analysis in N2A Neuroblastoma Cells Following TDP-43 Perturbation

To evaluate the functional consequences of TDP-43 perturbation on energy metabolism in N2A neuroblastoma cells, we performed glycolysis stress tests (GST) and mitochondrial stress tests (MST), measuring extracellular acidification rate (ECAR) and oxygen consumption rate (OCR), respectively. These assays provide insights into glycolytic activity and mitochondrial respiration following TDP-43 knockdown (KD) and mutant expression (MVT). The results are presented in Figure 5.10.

TDP-43 knockdown led to a general reduction in ECAR and OCR parameters in N2A cells. As shown in Figure 5.10A, the GST response curve demonstrated that ECAR trended lower in the KD group compared to the non-silencing (NS) control. While all ECAR-related parameters were reduced, none reached statistical significance. In the MST assay (Figure 5.10B), OCR-related maximal respiration and ATP production were significantly reduced in the KD group, while basal respiration, proton leak, and spare respiratory capacity remained unchanged. These findings suggest that, unlike BV2 microglia, TDP-43 knockdown in N2A cells primarily affects mitochondrial function rather than glycolysis. In contrast, mutant TDP-43 expression (MVT) did not induce significant metabolic alterations (Figure 5.10C-D). The GST response curve showed a general downward trend in ECAR in MVT-expressing cells compared to wild-type TDP-43 (WTT), but this difference was not statistically significant (Figure 5.10C). Similarly, MST analysis (Figure 5.10D) revealed that while all OCR-related parameters trended lower in the MVT group, none of these changes reached statistical significance. This suggests that, in contrast to BV2 microglia, mutant TDP-43 expression does not significantly impair glycolytic or mitochondrial function in N2A cells.

Taken together, these findings indicate that TDP-43 knockdown, but not mutant expression, alters mitochondrial respiration in N2A cells, with significant reductions in maximal respiration and ATP production. Unlike BV2 microglia, where TDP-43 knockdown induced a hyperglycolytic phenotype, N2A cells do not exhibit glycolytic adaptations. Instead, the observed reductions in mitochondrial parameters suggest that N2A cells may be more susceptible to mitochondrial dysfunction following TDP-43 depletion.

In the next section (5.3.4), we examine oxidative stress (ROS levels) and ATP homeostasis in N2A cells following TDP-43 perturbation, providing further insights into the metabolic consequences of TDP-43 dysregulation in this neuronal model.

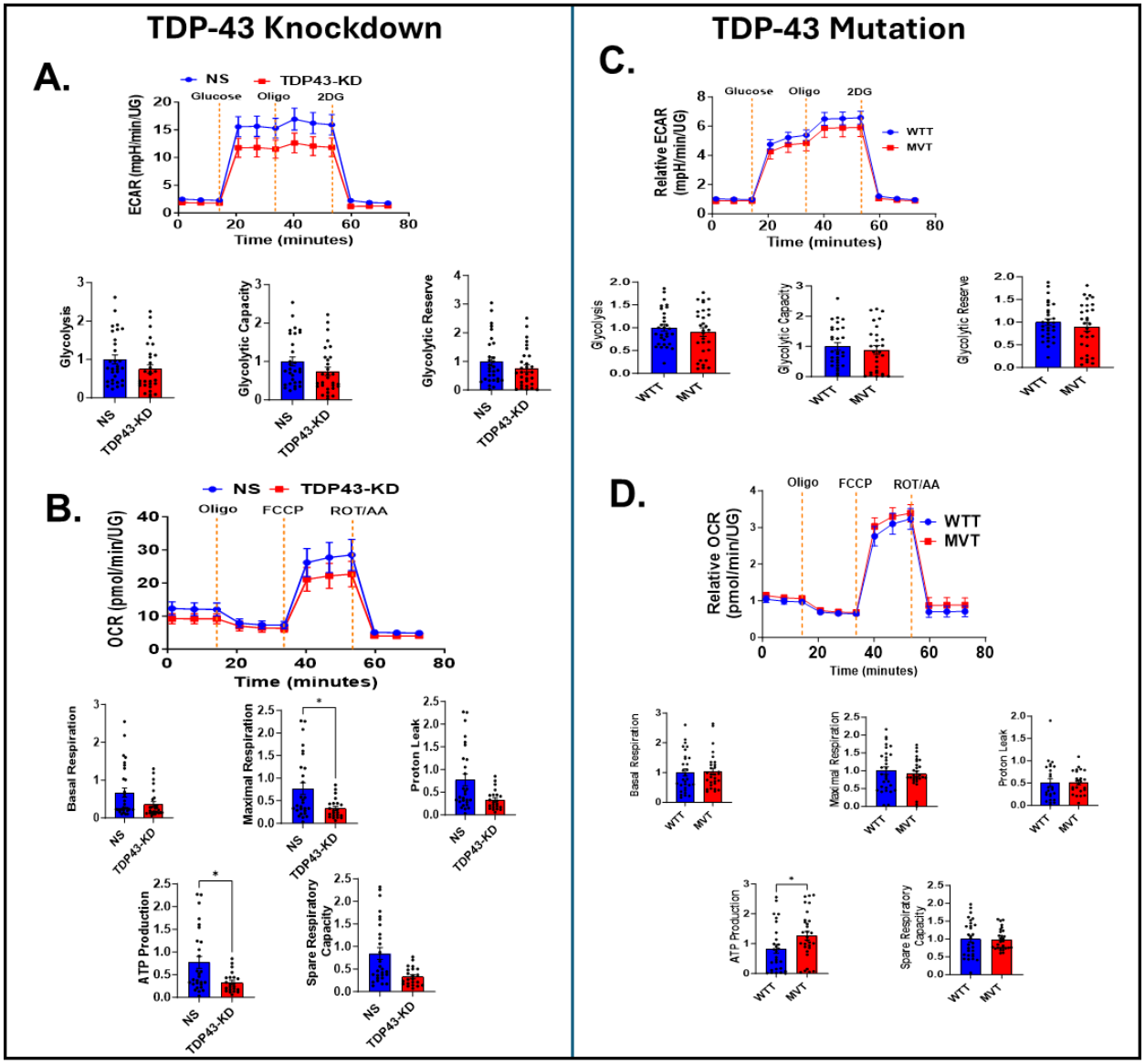

Figure 5.10 | Metabolic flux analysis in N2A neuroblastoma cells following TDP-43 perturbation. (A) Glycolysis Stress Test (GST) response curve and quantification of glycolysis, glycolytic capacity, and glycolytic reserve in N2A cells following TDP-43 knockdown (KD). (B) Mitochondrial Stress Test (MST) response curve and quantification of basal respiration, maximal respiration, proton leak, ATP production, and spare respiratory capacity in TDP-43 KD N2A cells. (C) GST response curve and quantification of glycolysis-related parameters in N2A cells expressing wild-type (WTT) or mutant (MVT) TDP-43. (D) MST response curve and quantification of mitochondrial parameters in WTT- and MVT-expressing N2A cells.

Oxidative Stress and ATP in N2A Cells Following TDP-43 Perturbation

To determine whether TDP-43 knockdown or mutant expression influences oxidative stress and energy homeostasis in N2A neuroblastoma cells, we measured reactive oxygen species (ROS) and ATP levels at 24- and 48-hours post-transfection. The results are presented in Figure 5.11.

Unlike BV2 microglia, where TDP-43 knockdown resulted in increased oxidative stress and ATP production at 24 hours, N2A cells did not exhibit significant changes in these parameters following TDP-43 perturbation. ROS levels (Figure 5.11A) remained comparable between TDP-43 knockdown (KD) and non-silencing (NS) controls at both 24 and 48 hours, indicating no measurable increase in oxidative stress. Similarly, ATP levels (Figure 5.11B) were stable across both time points, suggesting that cellular energy balance was not disrupted by TDP-43 depletion.

In the case of mutant TDP-43 expression (MVT), ROS levels (Figure 5.11C) were unchanged between wild-type TDP-43 (WTT) and MVT conditions at both 24 and 48 hours, further indicating that mutant expression does not induce oxidative stress in N2A cells. Likewise, ATP levels (Figure 5.11D) did not differ between WTT and MVT conditions at either time point, reinforcing the observation that N2A cells maintain metabolic stability regardless of TDP-43 perturbation.

These findings suggest that, unlike motor neurons and microglia, N2A neuroblastoma cells do not experience significant oxidative stress or ATP alterations in response to TDP-43 knockdown or mutant expression. This further supports the notion that metabolic reprogramming following TDP-43 perturbation is highly cell-type dependent, with N2A cells demonstrating greater metabolic stability compared to NSC34 motor neuron-like cells and BV2 microglia.

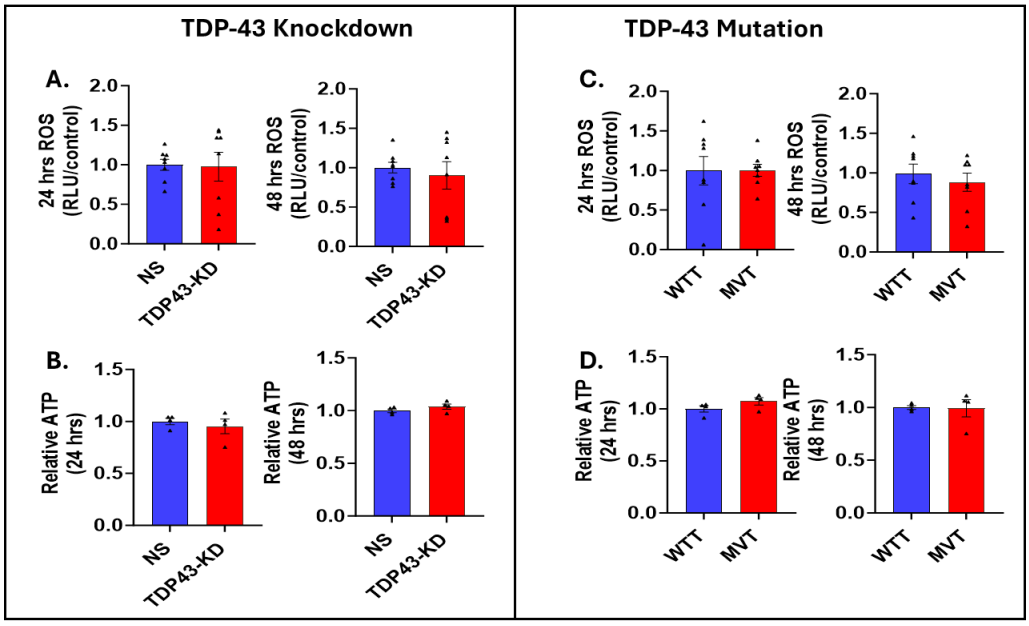

Figure 5.11 | Reactive oxygen species (ROS) and ATP levels in N2A neuroblastoma cells following TDP-43 perturbation. (A) ROS levels measured at 24 and 48 hours post-TDP-43 knockdown (KD) in N2A cells. (B) ATP levels measured at 24 and 48 hours post-TDP-43 KD. (C) ROS levels at 24 and 48 hours in N2A cells expressing wild-type TDP-43 (WTT) or mutant TDP-43 (MVT). (D) ATP levels at 24 and 48 hours in N2A cells expressing WTT or MVT. No significant changes were observed across conditions, indicating that TDP-43 perturbation does not induce oxidative stress or disrupt ATP homeostasis in N2A cells.

Comparative Analysis of Metabolic Responses Across Cell Types Following TDP-43 Perturbation

The metabolic consequences of TDP-43 knockdown and mutant expression exhibit striking cell-type-dependent differences, highlighting distinct susceptibilities and adaptive responses among NSC34 motor neuron-like cells, BV2 microglia, and N2A neuroblastoma cells. While all three cell types rely on glucose metabolism for energy production, their responses to TDP-43 perturbation diverge significantly in terms of glycolytic activity, mitochondrial function, and oxidative stress regulation.

TDP-43 Knockdown Induces Cell-Type-Specific Metabolic Adaptations

NSC34 motor neuron-like cells exhibit a hypermetabolic phenotype upon TDP-43 knockdown, characterized by increased glucose uptake, enhanced incorporation of glucose-derived carbons into TCA cycle intermediates, accentuated glycolytic flux, increased mitochondrial oxidative metabolism and elevated ATP production. This metabolic overdrive is accompanied by increased NAD+/NADH ratios, elevated oxidative stress, and a significant rise in both glycolysis and oxidative phosphorylation, suggesting that TDP-43 depletion pushes motor neurons into a state of heightened energy demand. The excessive metabolic activity in NSC34 motor neuron-like cells likely exacerbates oxidative damage, contributing to their vulnerability.

Furthermore, BV2 microglia responded to TDP-43 knockdown with a hyperglycolytic phenotype, displaying increased glucose consumption, enhanced lactate production, and elevated glycolytic capacity without significant changes in mitochondrial respiration. Notably, oxidative stress and ATP levels are transiently increased at 24 hours but stabilized by 48 hours, indicating a temporal adaptation mechanism in microglia.

However, N2A neuroblastoma cells exhibit a hypometabolic phenotype upon TDP-43 knockdown, characterized by reduced glucose incorporation into glycolysis and the TCA cycle, decreased lactate labeling, and diminished mitochondrial respiration. Unlike NSC34 or BV2 cells, exhibit significant reductions in maximal respiration and ATP production.

Mutant TDP-43 Expression Has Minimal Metabolic Impact Across Cell Types

Unlike the knockdown condition, the expression of mutant TDP-43 (M337V) elicits relatively minor metabolic alterations in all three cell types. In NSC34 motor neuron-like cells, mutant expression led to subtle increases in glucose uptake and slight alterations in metabolic cofactors but did not induce the same metabolic overdrive observed in the knockdown condition. While metabolic flux analysis indicated increased glycolysis and oxidative phosphorylation, these changes were inconsistent with

broader metabolic mapping, suggesting a subtle metabolic response to TDP-43 mutation. BV2 microglia exhibit minimal metabolic changes in response to mutant TDP-43 expression, with no significant alterations in glucose uptake, glycolysis, or oxidative metabolism. Similarly, N2A neuroblastoma cells displayed only minor metabolic changes in response to mutant TDP-43 expression, with isolated increases in fumarate labeling but no broader disruptions in glucose metabolism, glycolysis, or mitochondrial function.

Table 5.1 | Summary of Metabolic Changes in NSC34, BV2, and N2A Cells Following TDP-43 Perturbation. Arrows (↑/↓) indicate significant increases or decreases in metabolic parameters. A dash (—) indicates no significant changes.

	TDP-43 Knockdown			**TDP-43 mutation**		
Assay Type	NSC34	BV2	N2A	NSC34	BV2	N2A
Glucose Uptake	↑	↑	—	↑	—	—
Lactate Production	↑	↑	↓	—	—	—
Glucose Incorporation into TCA Cycle	↑	↑	↓	—	—	—
Metabolic Flux (GST - ECAR)	↑	↑	↓	↑	↓	↓
Metabolic Flux (MST - OCR)	↑	—	↓	↑	—	—
ATP Production	↑	↑	↓	—	—	—
ROS Levels	↑	↑	—	—	—	—

These findings indicate that TDP-43 depletion leads to cell-type-specific metabolic responses, with motor neurons exhibiting the most pronounced vulnerability. In NSC34 motor neuron-like cells, TDP-43 depletion triggers a state of metabolic overdrive, characterized by heightened glycolysis, increased mitochondrial respiration, and elevated oxidative stress—features that may contribute to their selective degeneration. In BV2 microglia, TDP-43 depletion results in a hyperglycolytic response, but oxidative stress and ATP production stabilize over time, likely reflecting the inherent metabolic flexibility of these cells. Nonetheless, sustained glycolytic activity may promote a pro-inflammatory state. In contrast, N2A neuroblastoma cells show relatively subtle metabolic changes, with reduced ATP production indicative of a hypometabolic phenotype. This reduction in energy metabolism may limit oxidative damage, suggesting a form of intrinsic resilience.

Mutant TDP-43 expression induces only modest metabolic changes across all three cell types, consistent with a pre-aggregation state in which the full pathological impact has yet to manifest. These observations collectively underscore the role of cell-intrinsic metabolic programs in shaping the vulnerability or adaptability of neural cells to TDP-43 dysfunction. However, it is important to note that the full metabolic impact of TDP-43 mutation may not be realized under naïve conditions. Since the pathological hallmark of ALS and FTLD is TDP-43 aggregation, more profound dysfunctions may emerge over time or in the presence of additional cellular stressors.

Part IV: Metabolic Sensing in NSC34 motor neuron-like cells upon TDP-43 Knockdown

The depletion of TDP-43 in motor neurons results in unique metabolic alterations warranting investigation into major regulators of cellular metabolism. Motor neurons, like other highly active cell types, regulate energy balance by sensing fluctuations in cellular ATP levels accompanied with corresponding adjustments of metabolic processes. These include, for instance, increasing glucose uptake or enhancing mitochondrial function to maintain energy homeostasis.

AMP-activated protein kinase (AMPK) is a critical sensor of cellular metabolism that regulates cellular energy balance by responding to fluctuations in ATP availability. Under normal conditions, AMPK activation is tightly linked to ATP depletion, triggering adaptive metabolic adjustments. This part of the results examines the role of AMPK in the distinct hypermetabolic phenotype observed in NSC34 motor-neuron like cells after TDP-43 depletion, as well as mutation.

AMPK Gene Expression Profiles Following TDP-43 Knockdown

To determine whether TDP-43 depletion alters metabolic sensing mechanisms in NSC34 motor neuron-like cells, we analyzed the transcriptional landscape of AMPK signaling components. AMPK consists of catalytic α subunits (PRKAA1, PRKAA2), regulatory β subunits (PRKAB1, PRKAB2), and γ subunits (PRKAG1, PRKAG3), which modulate AMP/ATP sensing. Additionally, we also examined the expression of key upstream regulators of AMPK, including calcium/calmodulin-dependent protein kinase kinase 1 and 2 (CAMKK1, CAMKK2), liver kinase β 1 (LKB1), citrate synthase (CS), protein kinase R (PKR), and protein phosphatase 2A (PP2A) (Figure 6.1).

Gene expression analysis revealed a selective upregulation of PRKAG1, encoding the γ1 subunit, suggesting a plausible increase in the sensitivity of AMPK to cellular energy fluctuations. Among upstream regulators, CAMKK1, CAMKK2, LKB1, and CS were significantly upregulated following TDP-43 knockdown, indicating potential enhancement of calcium-mediated AMPK activation. In contrast, PKR was downregulated, suggesting altered upstream regulation of AMPK activation, while PP2A expression remained unchanged. These findings indicate that TDP-43 knockdown modifies the transcriptional expression of AMPK regulators, potentially priming AMPK for enhanced activation through PRKAG1 and calcium-dependent signaling pathways. In the next section, we investigate whether these transcriptional changes translate into functional AMPK activation by assessing protein phosphorylation and kinase activity.

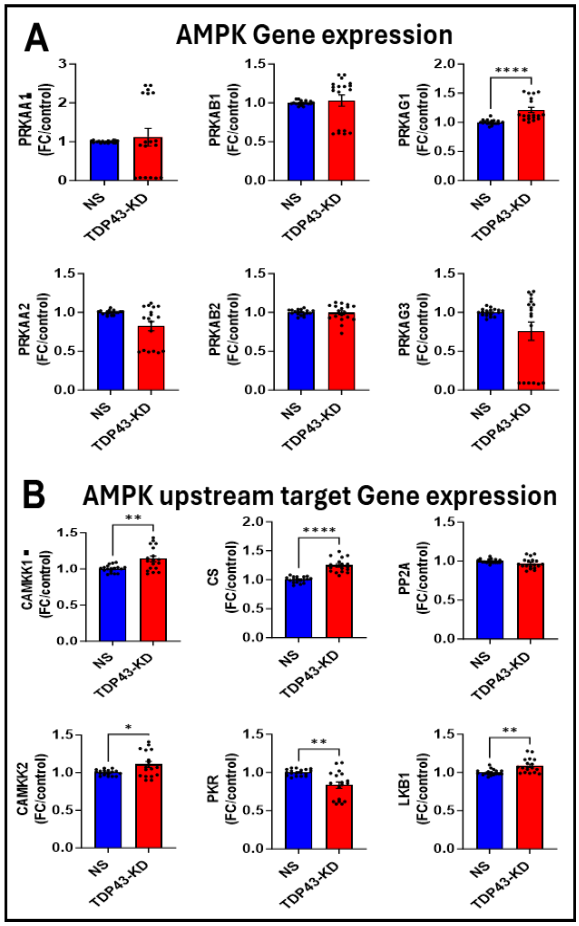

Figure 6.1 | Gene expression analysis of AMPK signaling components in NSC34 motor neuron-like cells following TDP-43 knockdown. Expression levels of AMPK subunits, including PRKAA1, PRKAA2 (α subunits), PRKAB1, PRKAB2 (β subunits), and PRKAG1, PRKAG3 (γ subunits), were assessed via qPCR. PRKAG1 expression was upregulated, whereas other subunits remained unchanged. Expression levels of AMPK upstream regulators, including CAMKK1, CAMKK2, citrate synthase (CS), protein kinase R (PKR), protein phosphatase 2A (PP2A), and liver kinase β 1 (LKB1), were also assessed. CAMKK1, CAMKK2, LKB1, and CS were upregulated, whereas PKR was downregulated. Data are mean ± SEM (n = 3 biological replicates). Statistical tests: unpaired t-test (Welch's correction) or Mann–Whitney U test. Statistical significance: *$p < 0.05$; **$p < 0.01$; ****$p < 0.001$.

AMPK Protein Expression and Kinase Activity Following TDP-43 Knockdown

To determine whether the transcriptional changes observed in AMPK signaling components translate into functional AMPK activation, we assessed total AMPK protein levels, phosphorylation status (pAMPK), and downstream kinase activity following TDP-43 knockdown.

Western blot analysis revealed that total AMPK protein levels remained unchanged following TDP-43 knockdown (Figure 6.2A). However, pAMPK levels were significantly increased suggesting an increase in AMPK activity. To evaluate whether this activation results in downstream metabolic signaling, we assessed phosphorylation of acetyl-CoA carboxylase (pACC), a direct AMPK substrate.

pACC levels were significantly elevated, indicating that AMPK activation translates into functional consequences. Furthermore, we quantified AMPK kinase activity assays at 12- and 24-hours post-TDP-43 knockdown (Figure 6.2B). AMPK activity was significantly increased at 12 hours, confirming functional engagement of AMPK in response to TDP-43 depletion. However, by 24 hours, AMPK activity returned to baseline, suggesting a transient rather than sustained response.

To further define the time course of AMPK activation, we examined AMPK and pAMPK levels across multiple time points (3-, 6-, 12-, and 24-hours) post-TDP-43 knockdown (Figure 6.2C). pAMPK levels progressively increased, peaking at 12 hours and remaining elevated at 24 hours, despite stable total AMPK expression. AMPK kinase activity followed a similar pattern, with a significant increase at 12 hours but a return to control levels by 24 hours (Figure 6.2D). To investigate whether AMPK activation upon TDP-43 depletion is influenced by upstream signaling pathways, we assessed the expression and phosphorylation status of LKB1, protein kinase A (PKA), and PP2A (Figure 6.3). No significant changes were observed in total or phosphorylated forms of these proteins following TDP-43 knockdown,

Collectively, these findings indicate that TDP-43 knockdown triggers AMPK activation via phosphorylation, peaking at 12 hours. The functional engagement of AMPK, as demonstrated by increased pACC, suggests that AMPK activation influences downstream metabolic pathways in motor neurons.

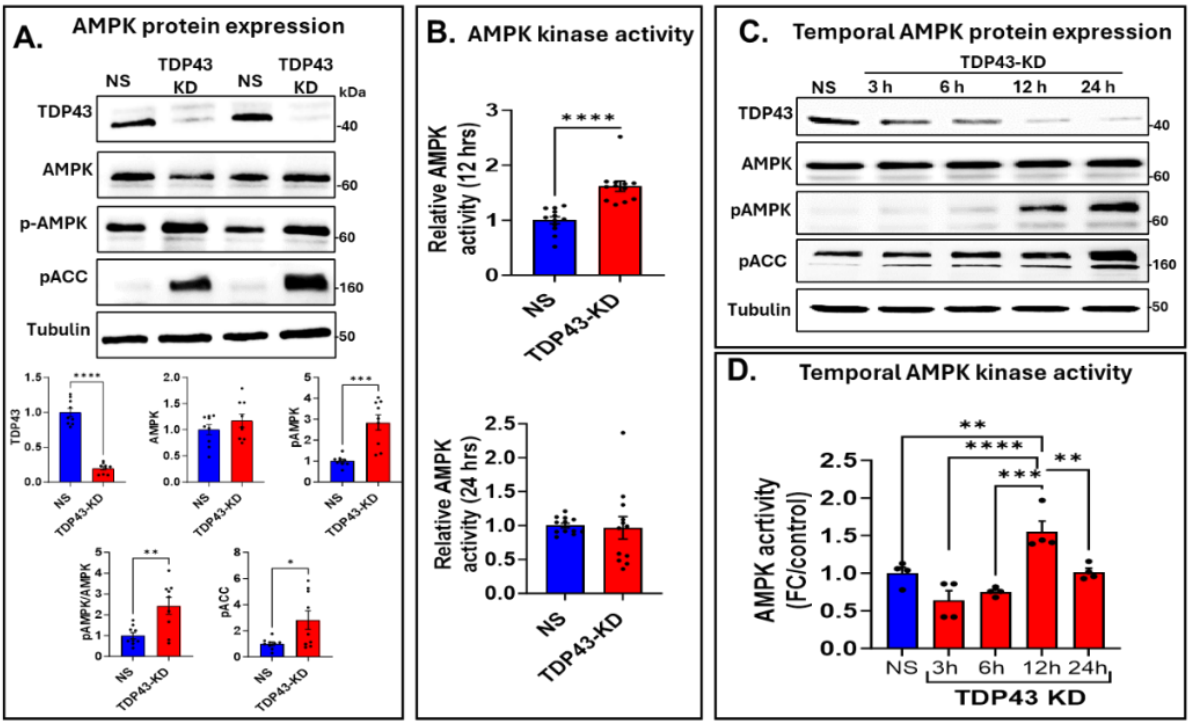

Figure 6.2 | AMPK protein expression, phosphorylation, and kinase activity in NSC34 motor neuron-like cells following TDP-43 knockdown. Western blot analysis was conducted for total AMPK and phosphorylated AMPK (pAMPK) in control and TDP-43 knockdown cells. pAMPK levels were elevated, while total AMPK levels remained unchanged. Phosphorylation of ACC (pACC), a downstream AMPK target, was also assessed. Kinase activity assays measured AMPK activity at 12- and 24-hours post-knockdown, showing changes over time. Temporal analysis of AMPK and pAMPK protein levels was performed at multiple time points (3, 6, 12, and 24 hours). Data are mean ± SEM (n = 3 biological replicates). Statistical tests: One-way ANOVA, unpaired t-test (Welch's correction) or Mann–Whitney U test. Statistical significance: *p < 0.05; **p < 0.01; ***p < 0.005; ****p < 0.001.

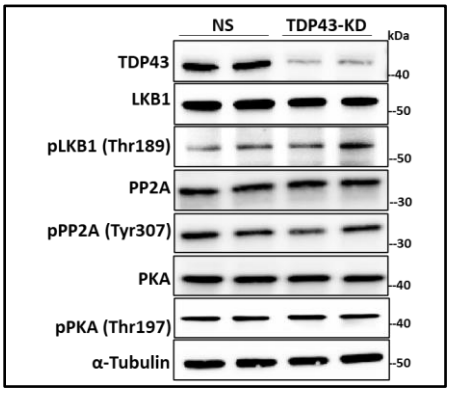

Figure 6.3 | Western blot analysis of AMPK upstream regulators in NSC34 motor neuron-like cells 24 hours following TDP-43 knockdown. Total and phosphorylated forms of key AMPK regulators, including liver kinase B1 (LKB1), protein kinase A (PKA), and protein phosphatase 2A (PP2A), were assessed 24 hour post following depletion of TDP43. No significant changes were observed in total or phosphorylated levels of LKB1, PKA, or PP2A.

Effects of Glucose Manipulation on AMPK Activation Following TDP-43 Knockdown

Given that AMPK is typically activated under conditions of low cellular energy availability, we next investigated whether AMPK activation in TDP-43 knockdown motor neurons reflects an adaptive response to energy stress or a dysregulated metabolic shift. To assess this, we manipulated glucose availability in the culture media and evaluated AMPK activation at 12- and 24-hours post-knockdown. NSC34 motor neuron-like cells were exposed to varying glucose concentrations (3.125 mM to 50 mM) following TDP-43 knockdown, and AMPK protein levels, phosphorylation status (pAMPK), and kinase activity were analyzed (Figure 6.4A).

Western blot analysis confirmed successful TDP-43 knockdown across all glucose concentrations (Figure 6.4B). At the 12-hour time point, total AMPK protein levels remained unchanged, suggesting that glucose availability does not influence AMPK translation or stability. However, phosphorylated AMPK (pAMPK) was significantly elevated in TDP-43 knockdown cells, irrespective of glucose concentration. Similarly, phosphorylation of ACC (pACC), a direct AMPK downstream target, was also consistently increased, reinforcing that AMPK activation remains functionally engaged across all glucose conditions.

To quantify AMPK enzymatic activity, we conducted kinase assays at 12 and 24 hours (Figure 6.4C). At 12 hours, AMPK activity was significantly higher in TDP-43 knockdown cells than in controls. Notably, AMPK activation was further enhanced at 25 mM and 50 mM glucose, suggesting that high glucose conditions amplify AMPK activation in TDP-43-depleted motor neurons. By 24 hours, AMPK activity remained elevated in TDP-43 knockdown cells, particularly at higher glucose concentrations, whereas control cells exhibited a decline in AMPK activity as glucose concentration increased.

These findings indicate that TDP-43 depletion induces sustained AMPK activation across all glucose conditions, disrupting the expected metabolic response. Under normal conditions, AMPK is activated in response to energy stress and suppressed under high-glucose conditions. However, TDP-43 knockdown cells maintain heightened AMPK activation, even in energy-rich environments, suggesting a failure to downregulate AMPK in response to increased glucose availability.

Overall, these findings highlight that TDP-43 depleted motor neuronlike cells are unable to regulate AMPK activity in response to glucose availability. Given AMPK's intricate involvement in regulation of cellular metabolism, enhanced and dysregulated AMPK activity could be the plausible link between TDP-43 depletion and hypermetabolism in NSC34 cells.

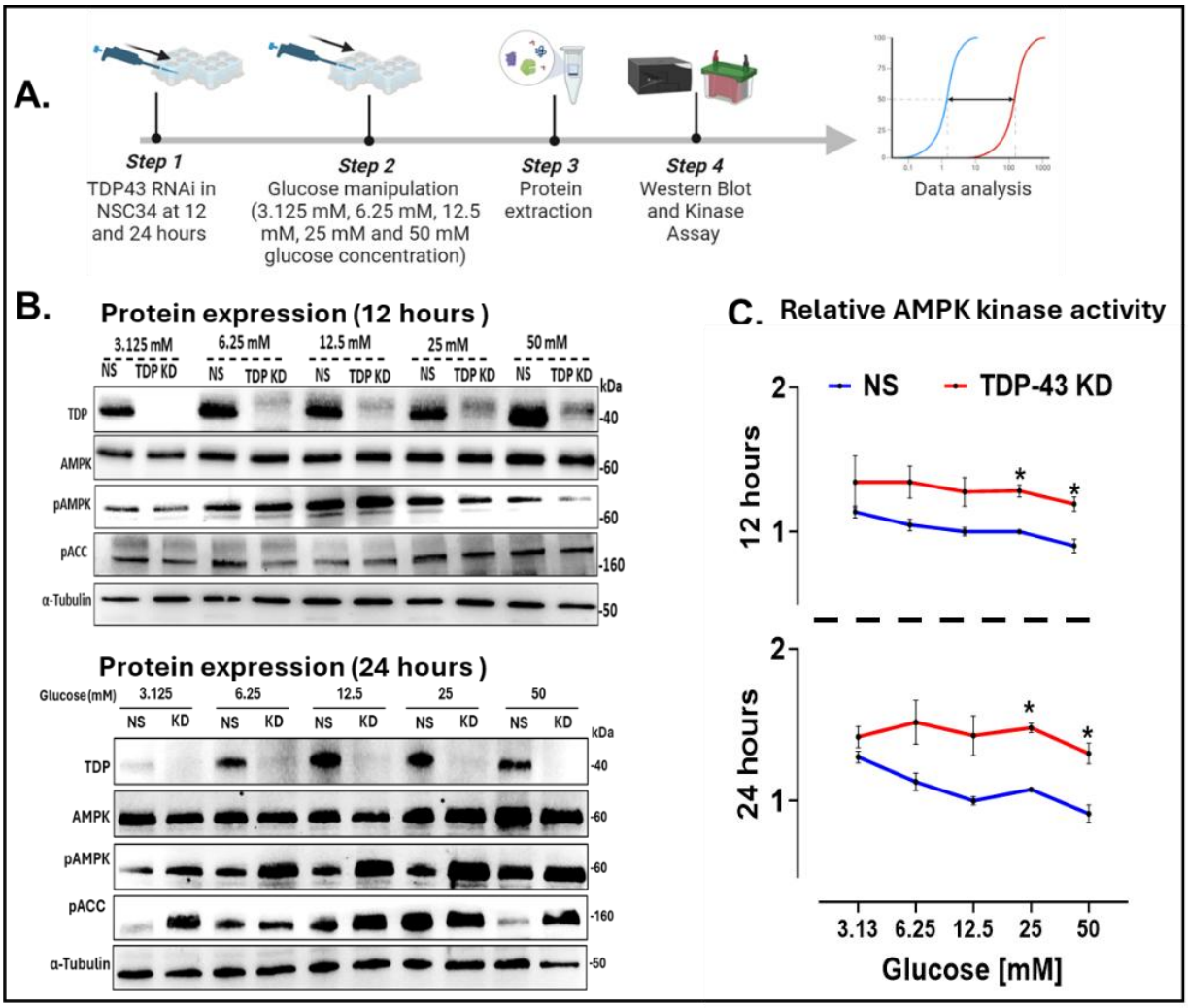

Figure 6.4 | Effects of glucose concentration on AMPK signaling following TDP-43 knockdown in NSC34 motor neuron-like cells. NSC34 motor neuron-like cells underwent TDP-43 RNAi treatment, followed by glucose concentration manipulation (3.125 mM to 50 mM). Western blot analysis was performed to assess total AMPK, phosphorylated AMPK (pAMPK), and phosphorylated ACC (pACC) at 12 and 24 hours across different glucose conditions. AMPK kinase activity was also measured to determine enzymatic function at varying glucose concentrations. Data are mean ± SEM (n ≥ 3 biological replicates). Statistical analysis: two-way ANOVA with Tukey's multiple comparisons test. Statistical significance: *p < 0.05.

Summary and Implications of AMPK Activation Following TDP-43 Knockdown

This Part of the results provides a comprehensive investigation into the metabolic sensing dynamics of NSC34 motor neuron-like cells following TDP-43 knockdown, with a particular focus on AMPK activation. The findings demonstrate that TDP-43 depletion induces persistent AMPK activation, despite the absence of classical energy deprivation cues. This suggests a deficit of metabolic sensing that may contribute to the hypermetabolic phenotype observed in motor neurons. At the transcriptional level, PRKAG1, encoding the gamma 1 subunit responsible for AMP/ATP sensing, was

significantly upregulated, alongside increased expression of LKB1, CAMKK1/2, and CS. These changes suggest that TDP-43 knockdown primes motor neurons for AMPK activation. However, Western blot analysis of key AMPK upstream regulators (LKB1, PKA, and PP2A) did not reveal significant changes in total or phosphorylated protein levels, indicating that AMPK activation is likely driven by posttranslational mechanisms.

At the protein level, AMPK phosphorylation (pAMPK) and its downstream target, phosphorylated ACC (pACC), were significantly increased, confirming functional relevance of AMPK activation following TDP-43 depletion. Kinase assays further demonstrated that AMPK activation peaks at 12 hours and normalizes by 24 hours, indicating a robust and transient metabolic response. Critically, manipulating glucose availability did not alter AMPK activity in NSC34 cells with TDP-43 knockdown, suggesting a disruption in the expected regulatory feedback. Under normal conditions, AMPK activation is a protective response that restores cellular energy balance by promoting glucose uptake, mitochondrial function, and autophagy. However, in TDP-43-depleted motor neurons, AMPK activation appears uncoupled from actual energy demand, raising critical questions about its role in TDP-43 related pathologies. The persistent AMPK activation in energy-rich conditions suggests a fundamental disruption in metabolic sensing mechanisms. Given this dysregulated AMPK activity upon TDP-43 knockdown, we next asked whether expression of mutant TDP-43 would elicit similar or divergent effects on metabolic sensing in motor neuron-like cells.

Part V: Metabolic Sensing in NSC34 motor neuron-like cells upon TDP-43 Mutant Expression

Investigating AMPK Dynamics in NSC34 motor neuron-like cells Following TDP-43 Mutant Expression

The findings presented so far demonstrate the plausibility that the TDP-43 knockdown-induced hypermetabolic state in NSC34 motor neuron-like cells is mediated via dysregulated AMPK activation. This raises an important question: How does AMPK signaling respond in the presence of mutant TDP-43? Unlike TDP-43 knockdown, which leads to a complete depletion of the protein, mutant TDP-43 (M337V) expression presents a different challenge—a gain-of-function or altered function that may impact metabolic regulation in distinct ways.

To address this, we investigated AMPK dynamics in NSC34 motor neuron-like cells expressing wild-type (WTT) and mutant (MVT) TDP-43 under different cellular conditions. First, we assessed basal AMPK activity and phosphorylation status to determine whether mutant TDP-43 expression alters AMPK signaling in the absence of external stressors. Next, we examined AMPK responses under stress conditions, particularly in the presence of insoluble mutant TDP-43 to evaluate whether AMPK activation is a general adaptive response to stress or specifically influenced by TDP-43 aggregation. Finally, we analyzed post-stress metabolic adaptations to investigate if the long-term impact of TDP-43 perturbation on metabolism are due to sustained changes in AMPK activity.

AMPK Dynamics in NSC34 motor neuron-like cells Following TDP-43 Mutant Expression Under Basal Conditions

To determine whether mutant TDP-43 disrupts AMPK signaling, we assessed its expression, phosphorylation, and activity under basal conditions. Western blot analysis confirmed successful exogenous TDP-43 expression in both WTT and MVT groups, with significantly higher expression levels of exogenous TDP-43 in the MVT group compared to WTT. Concurrently, endogenous TDP-43 expression was markedly reduced in both groups, with a more pronounced suppression in the MVT condition. This suggests that mutant TDP-43 may interfere with normal TDP-43 homeostasis, potentially disrupting cellular regulatory functions. Despite these changes, total AMPK protein levels remained unchanged between WTT and MVT groups, indicating that mutant TDP-43 does not affect AMPK translation or stability under basal conditions. Additionally, phosphorylation of AMPK (pAMPK) remained comparable between groups, suggesting that mutant TDP-43 does not induce AMPK hyperactivation under baseline conditions. Similarly, phosphorylation of ACC (pACC), a direct

downstream AMPK target, was unchanged, further supporting the notion that AMPK-dependent metabolic regulation is not significantly engaged under naïve conditions.

To determine whether AMPK function is impacted beyond its phosphorylation status, we assessed AMPK kinase activity at 24 and 48 hours post-TDP-43 expression. Interestingly, while total AMPK and pAMPK levels were unchanged, AMPK kinase activity was significantly reduced in the MVT group at 24 hours compared to WTT, suggesting a transient suppression of AMPK function. However, by 48 hours, AMPK kinase activity had normalized, reaching levels comparable to the WTT group. To further understand upstream regulatory changes, we assessed the expression and phosphorylation of key AMPK regulators, including LKB1, PKA, and PP2A. While total protein levels of these regulators remained unchanged between WTT and MVT groups, phosphorylation of LKB1 (pLKB1) was significantly reduced in the MVT group, suggesting a potential upstream dampening of AMPK activation under basal conditions. However, phosphorylation levels of PKA and PP2A remained comparable between WTT and MVT groups, indicating that these pathways were not significantly engaged in response to mutant TDP-43 expression.

These findings indicate that mutant TDP-43 does not substantially alter AMPK expression or phosphorylation under basal conditions but induces a temporary suppression of AMPK kinase activity, which is restored over time. The reduction in pLKB1 suggests a possible upstream dampening of AMPK activation, which may contribute to the transient suppression of AMPK function. This contrasts with the findings from Part IV of the results, where TDP-43 knockdown triggered AMPK activation as Part of a hypermetabolic response. Here, mutant TDP-43 induces only a transient suppression of AMPK function, potentially reflecting a more nuanced disruption in metabolic sensing. This effect may be driven not only by the gain-of-function properties of the mutant protein but also by the accompanying reduction in endogenous TDP-43, which itself plays a critical role in maintaining cellular homeostasis. Whether mutant TDP-43 more prominently engages AMPK signaling under metabolic stress—such as during protein aggregation or oxidative insult—will be explored in the next section.

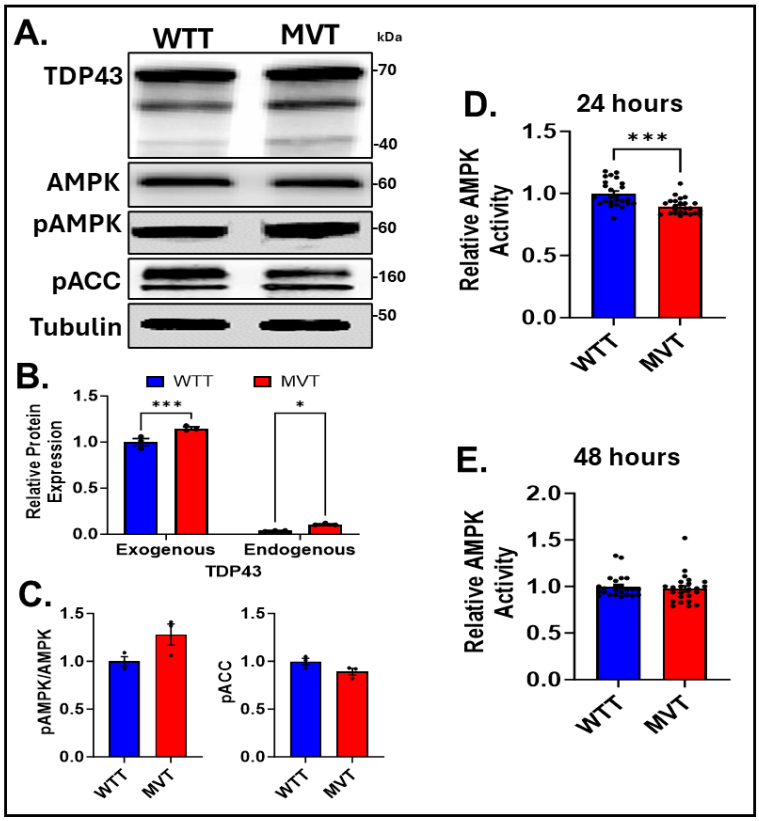

Figure 7.1 | AMPK dynamics in NSC34 motor neuron-like cells following TDP-43 mutant expression under basal conditions. Western blot analysis was conducted for TDP-43, AMPK, and phosphorylated ACC (pACC) in NSC34 motor neuron-like cells expressing wild-type (WTT) and mutant (MVT) TDP-43. Exogenous TDP-43 expression was higher in the MVT group, whereas endogenous TDP-43 levels were reduced. Quantification of total AMPK, pAMPK, and pACC expression was performed. AMPK kinase activity assays were conducted at 24- and 48-hours post-expression. Data are mean ± SEM (n = 3 biological replicates). Statistical tests: unpaired t-test (Welch's correction) or Mann–Whitney U test. Statistical significance: *p < 0.05; ***p < 0.05.

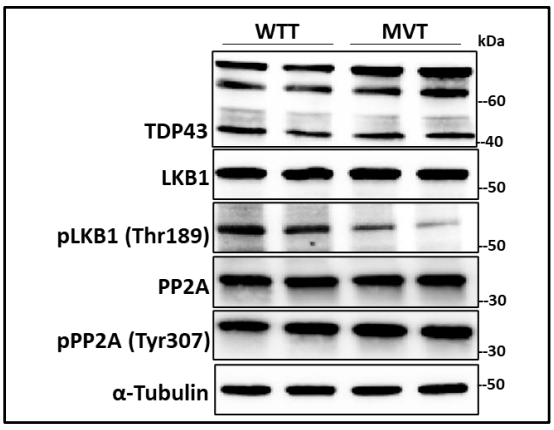

Figure 7.2 | Upstream regulators of AMPK in NSC34 motor neuron-like cells following TDP-43 mutant expression. Western blot analysis was conducted for total and phosphorylated forms of LKB1, PKA, and PP2A in NSC34 motor neuron-like cells expressing WTT or MVT TDP-43. Quantitative analysis was performed to assess changes in phosphorylation levels.

NSC34 MN AMPK dynamics under stress and recovery conditions following mutant TDP-43 expression

Since mutant TDP-43 becomes increasingly insoluble under stress conditions (as shown in Part II), we hypothesized that AMPK signaling might be more prominently engaged during this phase. Therefore, we assessed whether AMPK dynamics differ between wild-type (WTT) and mutant (MVT) TDP-43-expressing NSC34 cells under stress and subsequent recovery

To test this, NSC34 motor neuron-like cells were transfected with WTT or MVT for 48 hours, exposed to one hour of Sodium arsenite-induced oxidative stress, and allowed to recover for an additional hour before assessing AMPK expression, phosphorylation, and kinase activity. Under acute stress conditions, AMPK phosphorylation and kinase activity increased in both WTT and MVT groups, with no significant differences between them. This suggests that AMPK activation during stress is a general adaptive response, facilitating cellular efforts to cope with metabolic demands rather than a specific consequence of TDP-43 mutation. The lack of difference between groups further implies that mutant TDP-43 does not inherently impair AMPK's immediate response to oxidative stress.

However, a distinct divergence between WTT and MVT groups emerged during the recovery phase. In WTT-expressing cells, AMPK phosphorylation and kinase activity returned to baseline levels, consistent with a normal metabolic recovery process once the stressor was removed. In contrast, MVT-expressing cells exhibited sustained AMPK phosphorylation and significantly elevated kinase activity, despite the absence of continued stress. This persistent AMPK activation correlated with the retention of insoluble mutant TDP-43, suggesting that TDP-43 aggregation serves as a chronic stressor that prolongs AMPK engagement beyond its expected transient activation phase.

The persistence of AMPK activation in the post-stress phase suggests a maladaptive shift in metabolic regulation. Whereas transient AMPK activation during stress is a necessary protective response, its sustained activation in MVT-expressing cells following stress removal may reflect an ongoing attempt to compensate for the metabolic burden imposed by aggregated TDP-43. This aligns with the emerging idea that mutant TDP-43 drives a hypermetabolic state by continuously engaging AMPK-dependent catabolic pathways, potentially leading to metabolic exhaustion and neuronal vulnerability over time.These findings reinforce a key distinction between TDP-43 knockdown and TDP-43 mutant expression: whereas knockdown directly triggered AMPK activation as part of a hypermetabolic response, mutant TDP-43 altered AMPK regulation primarily during stress and recovery, with prolonged activation emerging because of persistent TDP-43 insolubility. This raises important questions about whether chronic AMPK activation contributes to neurodegeneration in

TDP-43 proteinopathies and whether targeting AMPK could mitigate metabolic dysregulation in these conditions.

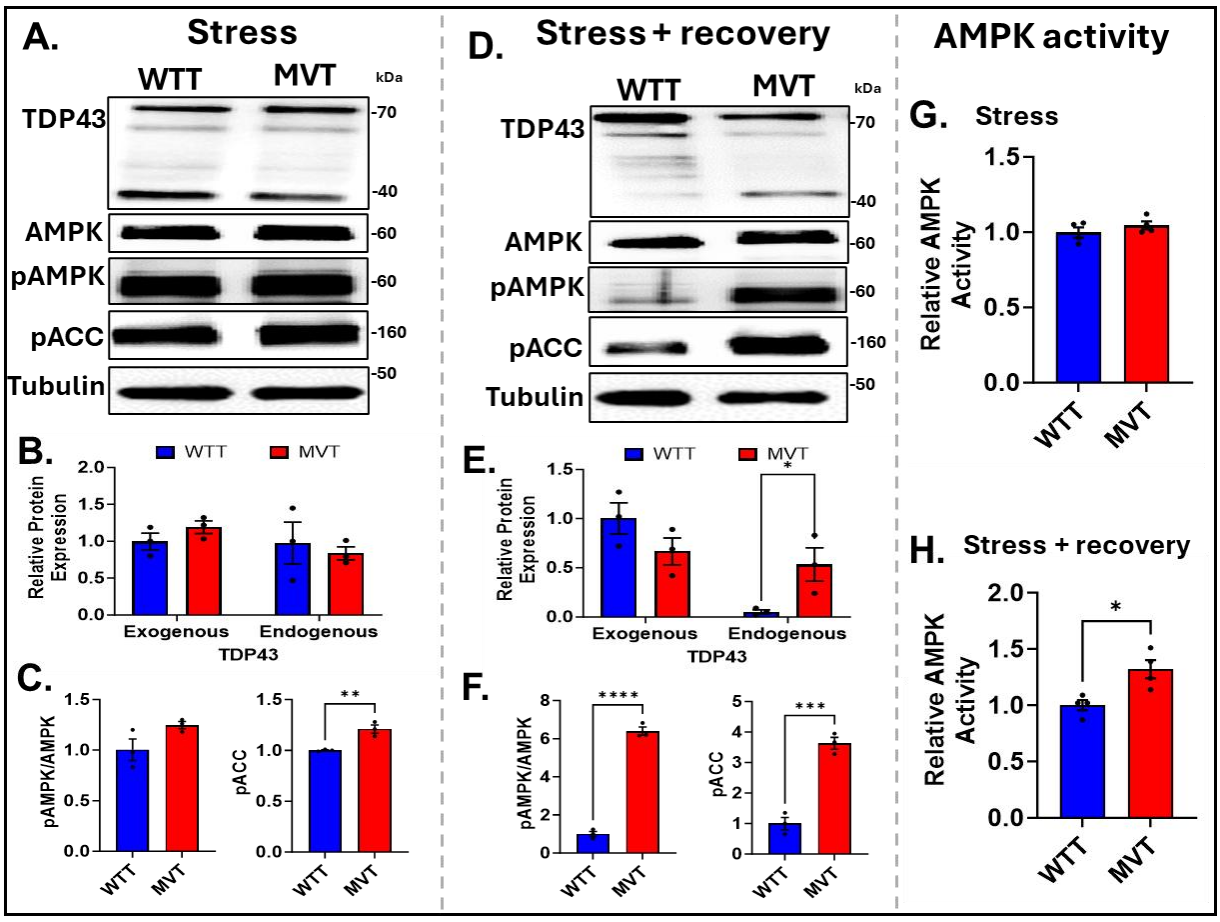

Figure 7.3 | AMPK response under stress and recovery conditions following TDP-43 mutant expression in NSC34 motor neuron-like cells. Western blot analysis and quantification were conducted for TDP-43, AMPK, phosphorylated AMPK (pAMPK), and phosphorylated ACC (pACC) in NSC34 motor neuron-like cells subjected to Sodium arsenite-induced oxidative stress following WTT and MVT TDP-43 expression. Protein levels were analyzed under both stress and recovery conditions. AMPK kinase activity assays were performed to assess functional changes in enzymatic activity across conditions. Data are mean ± SEM (n = 3 biological replicates). Statistical tests: unpaired t-test (Welch's correction) or Mann–Whitney U test. Statistical significance: *p < 0.05; ***p < 0.005; ****p < 0.001.

NSC34 AMPK signaling following TDP-43 mutation

This Part shows that AMPK signaling is only mildly affected by mutant TDP-43 under normal conditions but becomes more responsive during stress. Unlike TDP-43 knockdown, mutant TDP-43 did not change AMPK phosphorylation or activity at baseline, though a brief reduction in AMPK kinase activity and pLKB1 was observed at 24 hours. This suggests a subtle, short-term effect on metabolic signaling.

Under oxidative stress, AMPK activation occurred in both wild-type (WTT) and mutant (MVT) TDP-43-expressing cells, reflecting a general stress response. However, during recovery, only MVT cells showed sustained AMPK activation. This prolonged response coincided with persistent TDP-43 aggregation, suggesting that insoluble mutant TDP-43 may act as a chronic stressor, keeping AMPK active longer than expected.

Part VI: Influence of systemic metabolic factors on metabolic dynamics of motor neuron-like upon TDP-43 perturbation

As established previously, emerging evidence suggests that beyond its well-characterized nuclear roles, TDP-43 dysfunction has profound consequences on cellular metabolism. This thesis has systematically explored this metabolic link, demonstrating in earlier result parts that TDP-43 knockdown induces significant shifts in glycolytic and oxidative metabolism, particularly in motor neuron-like NSC34 motor neuron-like cells. One of the most intriguing paradoxes in ALS research, as highlighted in the introductory chapter, is the observation that metabolic conditions often deemed detrimental—such as obesity, dyslipidemia, and type 2 diabetes mellitus (T2DM)—are associated with prolonged survival and slower disease progression. This suggests that systemic metabolic factors may influence neurodegeneration in a manner that extends beyond cell-autonomous mechanisms. Given this, a critical question arises: Could external metabolic cues modulate the metabolic disturbances triggered by TDP-43 dysfunction?

To address this, herein it is investigated whether serum derived from different systemic metabolic states—control, high-fat diet (HFD), and voluntary exercise (VE) conditions—modifies the metabolic adaptations induced by TDP-43 depletion in NSC34 motor neuron-like cells. Using metabolic flux analysis as the primary functional readout, this section builds upon previous findings by integrating extrinsic metabolic influences into the discussion on TDP-43-related metabolic maladaptation. This approach bridges cellular pathology with broader physiological states, providing insights into the interplay between TDP-43 dysfunction and systemic metabolic factors—a perspective that may hold relevance for understanding metabolic resilience in ALS and FTLD..

Serum stimulation following TDP-43 knockdown

To examine the impact of systemic metabolic states on TDP-43-associated metabolic adaptations, serum was collected from three groups of B6 mice (n = 6 per group; 3 males and 3 females), all conditioned for ten weeks prior to sample collection. At the time of blood collection, the mice were 16 weeks old. The experimental groups included: Control (CTL) mice maintained on a standard chow diet; Voluntary Exercise (VE) mice with access to a running wheel; and High-Fat Diet (HFD) mice fed a 60% high-fat diet.

Whole blood was collected at the site of decapitation under terminal anesthesia, allowed to clot at room temperature, and centrifuged at 2,000 × g for 10 minutes at 4 degree to obtain serum. To

minimize biological variability, serum from animals of the same sex within each group was pooled, resulting in six pooled serum samples (one male and one female pool per group). The pooled serum was aliquoted and stored at −80°C until use.

Following siRNA-mediated TDP-43 knockdown (RNAi) in NSC34 motor neuron-like cells (24 hours post-transfection), cells were stimulated for an additional 24 hours with 10% pooled serum derived from either control, VE, or HFD-conditioned mice. This resulted in four experimental conditions per sex: NS Control (non-silencing siRNA + control serum), KD Control (TDP-43 knockdown + control serum), KD VE (TDP-43 knockdown + VE serum), and KD HFD (TDP-43 knockdown + HFD serum). Metabolic flux analysis was then performed using the Seahorse XF Analyzer to assess glycolytic and oxidative metabolism. Figure 8.1 illustrates the experimental workflow.

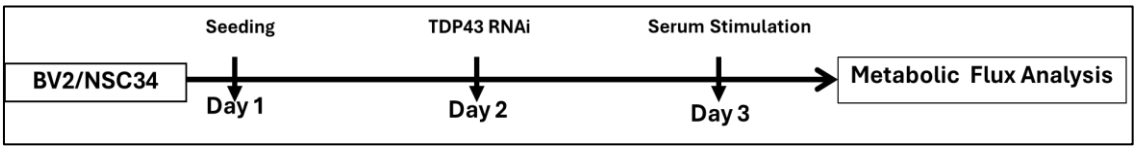

Figure 8.1 | Experimental workflow for metabolic flux analysis following TDP-43 knockdown and serum stimulation. NSC34 motor neuron-like cells were seeded under standard culture conditions. Following siRNA-mediated TDP-43 knockdown (RNAi, 24h), cells were stimulated with 10% pooled serum from control, voluntary exercise, or high-fat diet mice for an additional 24 hours. Metabolic flux analysis was subsequently performed to assess glycolytic and oxidative metabolism.

Glycolytic Response in NSC34 motor neuron-like cells Following Serum Stimulation

The extracellular acidification rate (ECAR) response curves following serum stimulation from male mice revealed that TDP-43 knockdown in NSC34 motor neuron-like cells led to an increase in glycolysis compared to non-silencing (NS) control cells, particularly after glucose and oligomycin injection. This pattern was observed in both control serum and voluntary exercise (VE) serum conditions, indicating that metabolic factors derived from voluntary exercise did not significantly alter glycolytic activation relative to standard metabolic conditions. However, stimulation with serum from high-fat diet (HFD)-conditioned mice resulted in a lower ECAR response compared to TDP-43 knockdown control (KD Control), suggesting that systemic metabolic factors associated with a high-fat diet partially mitigated glycolytic activation in TDP-43-depleted motor neurons.

Quantitative analysis of glycolytic parameters showed that while basal glycolysis remained elevated in TDP-43 knockdown cells compared to NS Control, glycolytic output was significantly reduced in the HFD-stimulated condition relative to KD Control. Glycolytic capacity, however, remained

unchanged across serum conditions, suggesting that the ability of NSC34 motor neuron-like cells to upregulate glycolysis in response to metabolic demand was not significantly influenced by systemic metabolic factors.

A distinct response was observed when NSC34 motor neuron-like cells were stimulated with serum from female mice. As seen with male-derived serum, TDP-43 knockdown cells stimulated with control serum exhibited a higher ECAR response compared to NS Control, confirming enhanced glycolysis following TDP-43 depletion. VE serum stimulation in TDP-43 knockdown cells resulted in a modestly lower ECAR trajectory compared to KD Control, suggesting a subtle modulation of glycolytic activation by systemic metabolic factors associated with voluntary exercise. In contrast, stimulation with female HFD serum resulted in an ECAR trajectory that closely resembled NS Control, indicating a clear reduction in glycolysis relative to KD Control. Quantification of glycolytic parameters further supported these observations: glycolysis was significantly reduced in the HFD condition, while the effect of VE serum was less pronounced. This pattern was consistent across both male- and female-derived serum conditions.

These findings demonstrate that while TDP-43 knockdown enhances glycolysis in NSC34 motor neuron-like cells, the response to systemic metabolic factors is dependent on both metabolic state and sex.

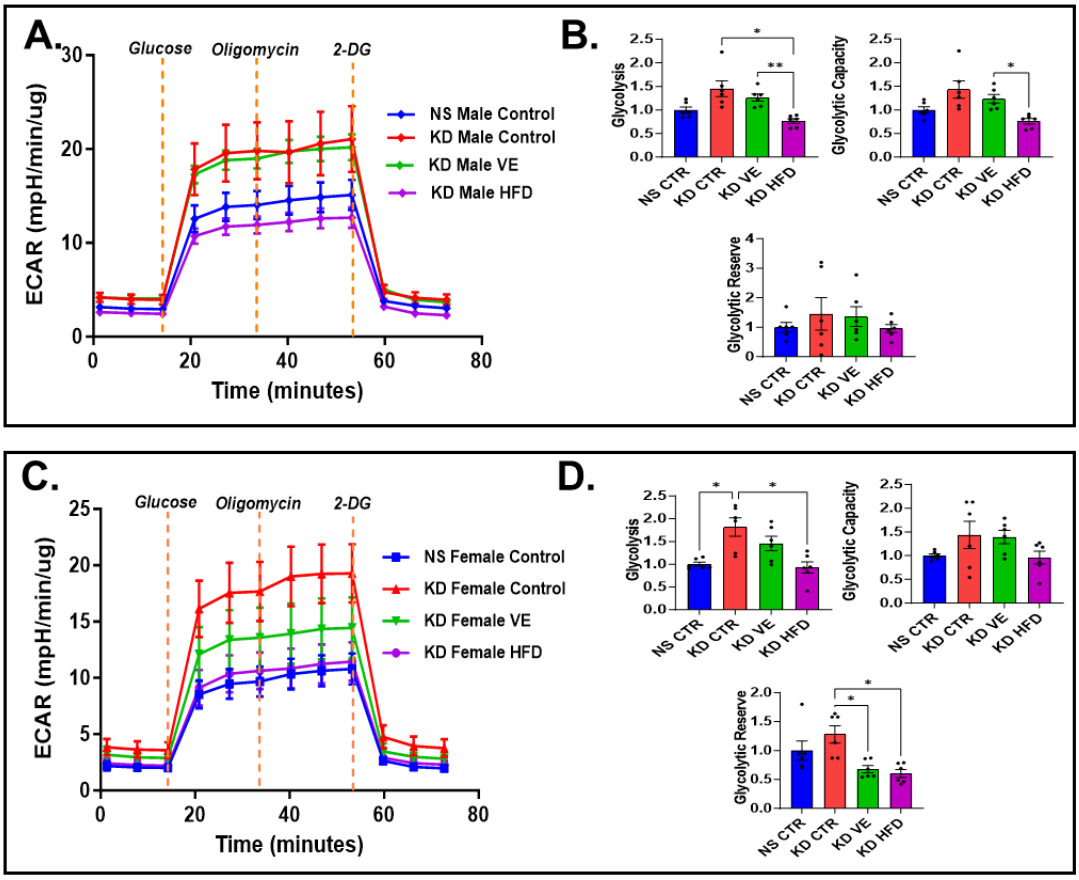

Figure 8.2 | Glycolytic Stress Test Following TDP-43 Knockdown and Serum Stimulation in NSC34 motor neuron-like cells. (A) ECAR response curves in NSC34 motor neuron-like cells following TDP-43 knockdown (KD) and stimulation with male serum under different conditions: non-silencing with control serum (NS Control), KD with control serum (KD Control), KD with voluntary exercise serum (KD VE), and KD with high-fat diet serum (KD HFD). Vertical dashed lines indicate sequential injections of glucose, oligomycin, and 2-deoxyglucose (2-DG). (B) Quantification of glycolytic parameters, including basal glycolysis, glycolytic capacity, and glycolytic reserve, in NSC34 motor neuron-like cells stimulated with male serum across conditions. (C) ECAR response curves following stimulation with female serum under the same experimental conditions as in (A). (D) Quantification of glycolytic parameters in NSC34 motor neuron-like cells stimulated with female serum across conditions. Data are mean ± SEM. Statistical analysis: one-way ANOVA with Tukey's multiple comparisons test. Statistical significance: *p < 0.05.

Mitochondrial Response in NSC34 motor neuron-like cells Following Serum Stimulation

The mitochondrial stress test following serum stimulation from male mice revealed that TDP-43 knockdown in NSC34 motor neuron-like cells resulted in a higher OCR compared to non-silencing (NS) control cells, suggesting an increase in mitochondrial activity. This increase was observed across all serum conditions, but notable differences emerged in response to voluntary exercise (VE) and high-fat diet (HFD) serum stimulation. The OCR trajectory of VE serum-stimulated TDP-43 knockdown neurons was comparable to that of KD Control, suggesting that VE-derived systemic

factors did not substantially alter mitochondrial respiration beyond the effects induced by TDP-43 knockdown alone. In contrast, HFD serum-stimulated TDP-43 knockdown neurons exhibited a lower OCR trajectory relative to KD Control, indicating that systemic metabolic factors derived from a high-fat diet exerted an inhibitory effect on mitochondrial function in TDP-43-depleted motor neurons. Quantitative analysis of mitochondrial respiration parameters showed that maximal respiration and spare respiratory capacity were significantly lower in HFD serum-stimulated TDP-43 knockdown neurons compared to KD Control, whereas basal respiration and ATP-linked respiration remained comparable across all conditions

A distinct mitochondrial response was observed when NSC34 motor neuron-like cells were stimulated with serum from female mice. As seen in male-derived serum conditions, KD Control exhibited a higher OCR response relative to NS Control, reinforcing the increase in mitochondrial function following TDP-43 depletion. However, in contrast to male serum conditions, both VE and HFD serum-stimulated TDP-43 knockdown neurons exhibited an OCR trajectory that was higher than KD Control, suggesting that systemic metabolic factors derived from female mice promoted rather than suppressed mitochondrial activity in NSC34 cells. Quantification of mitochondrial respiration parameters further revealed that maximal respiration and spare respiratory capacity were significantly increased in TDP-43 knockdown neurons following VE and HFD serum stimulation compared to KD Control. Notably, whereas HFD serum-stimulated conditions were associated with a reduction in mitochondrial respiration in male-derived serum conditions, the opposite effect was observed in female-derived serum conditions, reinforcing a sex-dependent influence of metabolic serum factors on mitochondrial function.

These findings underscore the importance of systemic metabolic cues in shaping mitochondrial function in TDP-43-depleted motor neurons and highlight sex-dependent differences in metabolic regulation. In male-derived serum conditions, HFD serum reduced maximal and spare respiratory capacity, whereas in female-derived conditions, HFD serum enhanced these parameters. Similarly, while VE serum had no apparent effect on mitochondrial function in male-derived conditions, it increased oxidative metabolism in female-derived conditions—potentially reflecting a metabolic shift from glycolysis to oxidative phosphorylation in TDP-43-depleted neurons. These results suggest that systemic metabolic factors modulate mitochondrial dynamics in NSC34 neurons following TDP-43 depletion in a sex-dependent manner, with female-derived metabolic factors promoting greater mitochondrial flexibility.

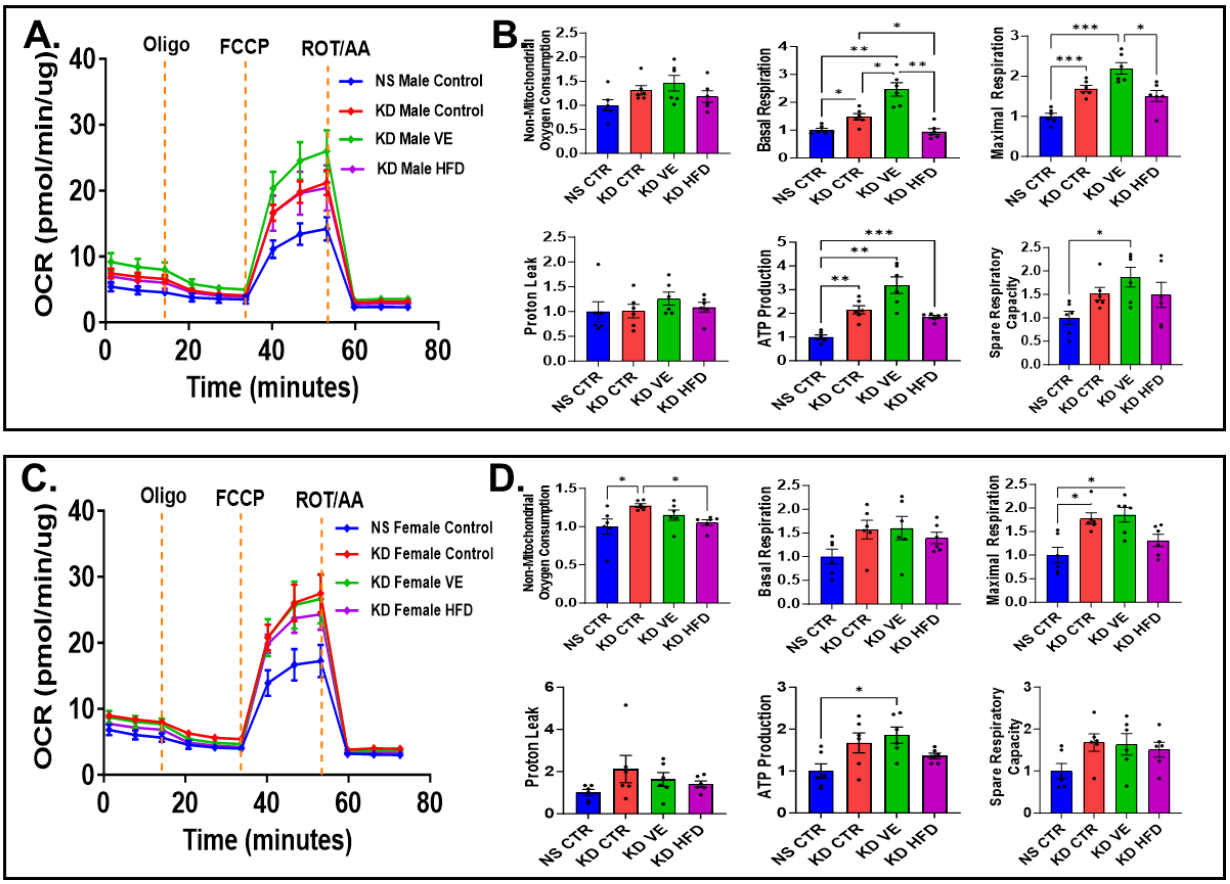

Figure 8.3 | Mitochondrial Stress Test (MST) Following TDP-43 Knockdown and Serum Stimulation in NSC34 motor neuron-like cells. (A) Oxygen consumption rate (OCR) response curve in NSC34 motor neuron-like cells following TDP-43 knockdown (KD) and stimulation with male serum under different conditions: non-silencing control with control serum (NS Control), KD with control serum (KD Control), KD with voluntary exercise serum (KD VE), and KD with high-fat diet serum (KD HFD). Sequential injections of oligomycin, FCCP, and rotenone/antimycin A were used to assess mitochondrial function. (B) Quantification of mitochondrial respiration parameters, including basal respiration, ATP-linked respiration, maximal respiratory capacity, and spare respiratory capacity, in NSC34 motor neuron-like cells stimulated with male serum across conditions. (C) OCR response curve following stimulation with female serum under the same experimental conditions as in (A). (D) Quantification of mitochondrial respiration parameters in NSC34 motor neuron-like cells stimulated with female serum across conditions. Data are mean ± SEM. Statistical analysis: one-way ANOVA with Tukey's multiple comparisons test. Statistical significance: *p < 0.05; **p < 0.01; ***p < 0.005; ****p < 0.001

Systemic Metabolic Cues Modulate TDP-43-Associated Metabolic Adaptations in Motor Neuron-like Cells in a Sex-Specific Manner

This Part systematically examined how systemic metabolic factors influence the metabolic response of NSC34 motor neuron-like cells following TDP-43 knockdown. Using serum derived from control, voluntary exercise (VE), and high-fat diet (HFD) conditions, we assessed the impact of systemic metabolic cues on glycolytic and oxidative metabolism in TDP-43-depleted motor neurons. The key findings are summarized in Table 8.2, illustrating distinct and sex-dependent effects.

TDP-43 knockdown in NSC34 motor neuron-like cells consistently led to increased glycolysis and oxidative phosphorylation, reinforcing the metabolic consequences of TDP-43 dysfunction. However, the magnitude and direction of these responses were modulated by systemic serum factors. HFD serum significantly reduced glycolysis across both sexes, while VE serum had little to no effect in males but slightly reduced glycolytic output in females. Notably, glycolytic reserve was reduced only in the female VE and HFD serum conditions, suggesting sex-specific regulation of glycolytic adaptability.

Mitochondrial respiration was also influenced in a sex-dependent manner. In male-derived serum conditions, HFD serum led to a reduction in maximal and spare respiratory capacity, while VE serum had no clear effect. In contrast, female-derived HFD and VE serum enhanced mitochondrial function, reflected by increased maximal respiration and spare respiratory capacity. This pattern suggests that female systemic factors promote greater mitochondrial flexibility in TDP-43-depleted motor neurons, potentially indicating a shift from glycolysis to oxidative phosphorylation under certain conditions.

Together, these findings underscore two major conclusions: (1) systemic metabolic factors modulate TDP-43-associated metabolic adaptations in motor neurons, and (2) this modulation is sex-specific. The results point to a nuanced interplay between intrinsic metabolic disturbances caused by TDP-43 dysfunction and extrinsic cues derived from systemic metabolic states.

Given the established link between metabolic disturbances and ALS progression, these observations provide new insight into how systemic metabolism may influence disease outcomes. The sex-specific effects observed here may help explain clinical differences in ALS and FTLD progression between males and females. Future studies should aim to identify the specific molecular components within serum that mediate these effects and explore their potential relevance for therapeutic strategies targeting neuronal energy metabolism in neurodegenerative diseases.

Table 8.1 | Summary of Metabolic Flux Responses in NSC34 motor neuron-like cells Following Serum Stimulation

(↑ = Increase, ↓ = Decrease, – = No Change, ↑↑ = Significant Increase, ↓↓ = Significant Decrease)

Sex	Condition	Glycolysis (ECAR)	Oxidative Phosphorylation (OCR)
Male	Control Serum	↑↑	↑↑
Male	VE Serum	↑↑	↑↑
Male	HFD Serum	↓↓	↓↓
Female	Control Serum	↑↑	↑↑
Female	VE Serum	↓	↑↑
Female	HFD Serum	↓↓	↑↑

Part VII: Transcriptomic Comparison Between Patient-Derived and NSC34 Models of TDP-43 Dysfunction

While the preceding results examined transcriptomic alterations caused by TDP-43 knock-down and expression of ALS-linked TDP-43 mutants in NSC-34 motor-neuron-like cells, this Part extends the analysis to patient-derived RNA-seq data. The aim is to determine how gene-expression changes in sporadic ALS and FTLD compare with those observed in NSC-34 models, highlighting potential overlaps as well as disease-specific signatures.

We analysed RNA-seq from post-mortem cortical tissue of two ALS patients, five FTLD patients and five neurologically normal controls. Differential-expression analyses were performed for ALS vs control and FTLD vs control, followed by pathway-enrichment analysis to identify biological processes perturbed in each condition. These transcriptomic profiles were then compared with the NSC-34 datasets to explore shared and unique molecular signatures.

A major limitation is the small cohort—particularly the ALS group (n = 2)—which reduces statistical power; additionally, the regional burden of TDP-43 pathology within the sampled cortex is unknown. Nevertheless, these patient data allow us to evaluate the extent to which cellular models capture molecular alterations present in human ALS and FTLD, providing a bridge from cell-based findings to human disease.

Differential Gene Expression and Pathway Analysis in ALS and FTLD Patients

Data Quality Assessment and Outlier Removal

Before proceeding with differential expression analysis, we first assessed sample clustering and quality control to ensure the integrity of the dataset. Given the relatively small number of patient samples, it was particularly important to identify potential outliers that could distort the results. Principal Component Analysis (PCA) and hierarchical clustering were used to evaluate transcriptomic variability across samples, helping to detect any samples that did not align with their expected disease group. Figure 9.1A shows a PCA plot of all samples, color-coded by condition (CTRL: red, FTLD: green, ALS: blue). While FTLD and ALS samples generally cluster separately, one control sample (CTRL_5) is positioned far from the main control cluster, suggesting it may be an outlier. To further investigate this, we performed hierarchical clustering analysis, which is visualized in the heatmap in Figure 9.1B. This heatmap represents sample-to-sample correlation, with warmer colors indicating a higher degree of similarity. Notably, CTRL_5 clusters separately from the other controls, showing weaker correlation, which strengthens the hypothesis that this sample may be biologically or technically different from the rest of the control group. Given that TDP-43 dysfunction is a defining

feature of ALS and FTLD, we next examined the expression levels of TARDBP, the gene encoding TDP-43, across all samples. Figure 9.1C presents TARDBP expression levels, revealing that while most control and FTLD samples exhibit relatively consistent TARDBP expression, CTRL_5 shows markedly reduced expression, an unexpected deviation from other control samples.

To avoid introducing confounding factors into the analysis, we removed CTRL_5 from the dataset before proceeding with differential expression analysis. Figure 9.1D presents an updated PCA plot after CTRL_5 was removed, demonstrating improved clustering of the control, FTLD, and ALS samples. Control samples now cluster more tightly together, while ALS and FTLD samples remain distinct from controls. This confirms that the removal of CTRL_5 eliminates noise and ensures that observed transcriptomic differences are driven by disease pathology rather than technical artifacts.

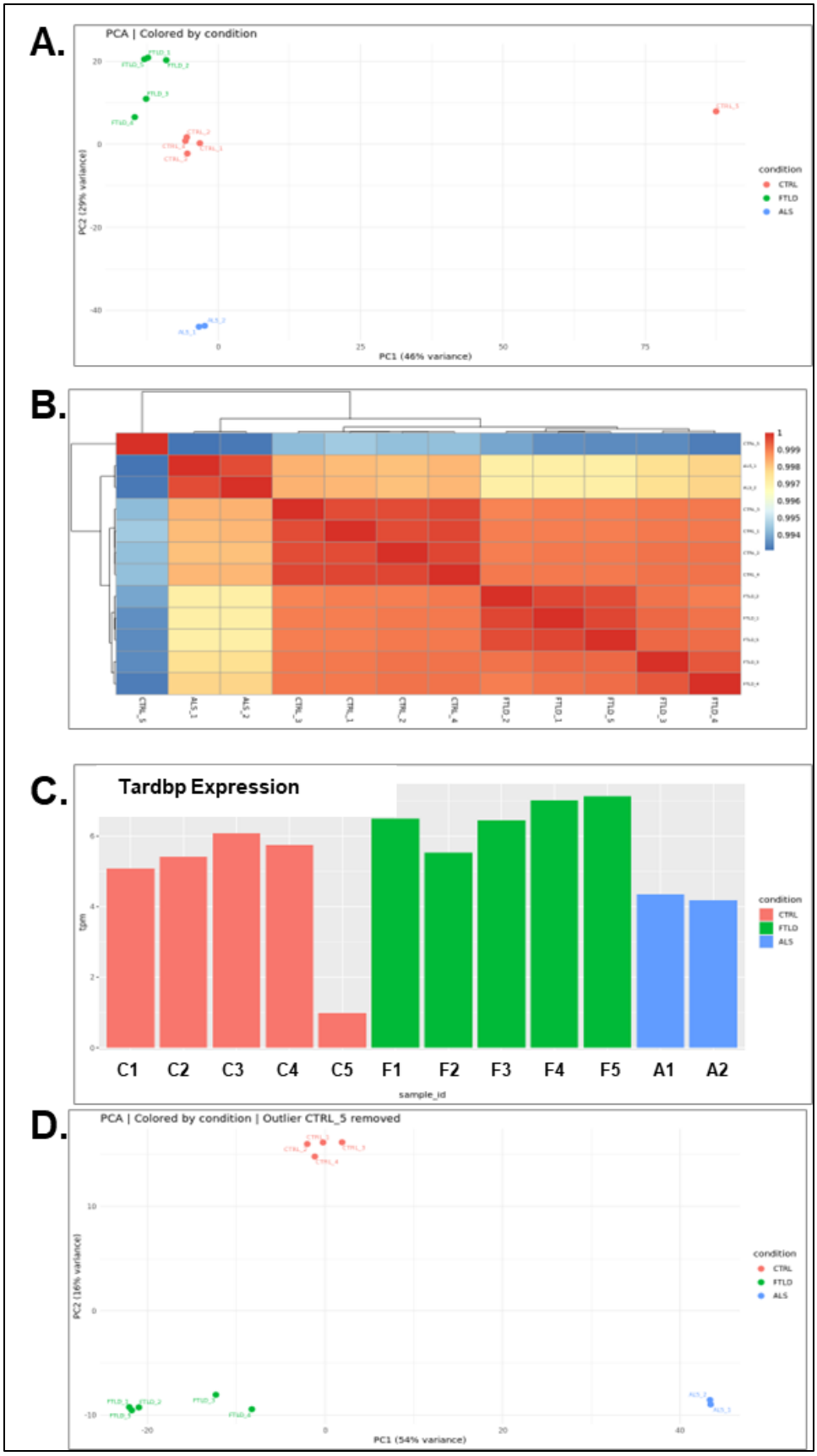

Figure 9.1: Principal Component Analysis, Sample Clustering, and Outlier Removal: (A) PCA plot of all samples colored by condition (CTRL: red, FTLD: green, ALS: blue). One control sample (CTRL_5) appears as an outlier, clustering away from the other control samples. (B) Hierarchical clustering heatmap showing sample-to-sample correlation. CTRL_5 exhibits lower correlation with other controls, supporting its identification as an outlier. (C) TARDBP expression levels across samples. CTRL_5 shows markedly reduced TARDBP expression, further supporting its exclusion from downstream analysis. (D) PCA plot after removing CTRL_5, showing improved clustering of control, FTLD, and ALS samples, ensuring more reliable differential expression analysis.

Differential Gene Expression Analysis

Following quality control and outlier removal, we performed differential gene expression (DGE) analysis to identify genes that were significantly upregulated or downregulated in ALS and FTLD patients relative to controls. The results are summarized in Figure 9.2 and Table 9.1, detailing the number of differentially expressed coding and non-coding genes across the three major comparisons: ALS vs. Control, FTLD vs. Control, and ALS vs. FTLD.

Volcano plots (Figure 9.2A–C) illustrate the global transcriptomic changes in each comparison. Genes that met the statistical significance threshold (padj < 0.05, log2 fold-change > 1) were classified as differentially expressed. Overall, ALS vs. control exhibited substantial transcriptomic alterations, with a large number of both upregulated (1,292 coding genes) and downregulated (1,051 coding genes) DEGs. In contrast, FTLD vs. control showed fewer DEGs, with 139 coding genes upregulated and 449 downregulated, suggesting more subtle transcriptomic shifts in FTLD. The direct ALS vs. FTLD comparison revealed 1,870 upregulated and 1,614 downregulated coding genes, highlighting distinct molecular differences between these two diseases.

A heatmap of significantly differentially expressed coding genes (padj < 0.01, log2 fold-change > 1) (Figure 9.2D) reveals distinct clustering patterns across ALS, FTLD, and control samples. ALS and FTLD samples exhibit transcriptomic profiles distinct from controls, supporting the idea that both conditions involve significant alterations in gene expression. Some genes are consistently dysregulated in both ALS and FTLD, while others display disease-specific expression patterns, indicating potentially distinct molecular mechanisms, although sample-size differences may also contribute to these patterns.

Table 9.1 | Summary of Differential Gene Expression in ALS and FTLD Patients. Number of upregulated, downregulated, and unchanged genes in ALS vs. control, FTLD vs. control, and ALS vs. FTLD comparisons. The numbers are categorized into coding, non-coding, and unannotated (NA) genes, reflecting the extent of transcriptomic alterations in each condition

Comparison	Expression Change	Coding Genes	Non-Coding Genes	NA
	Upregulated	139	28	41
	Downregulated	449	121	149
FTLD vs CTRL	Unchanged	14596	2767	3904
	Upregulated	1292	364	280
	Downregulated	1051	138	188
ALS vs CTRL	Unchanged	13020	2587	3976
	Upregulated	1870	487	436
	Downregulated	1614	175	296
ALS vs FTLD	Unchanged	12532	3155	5137

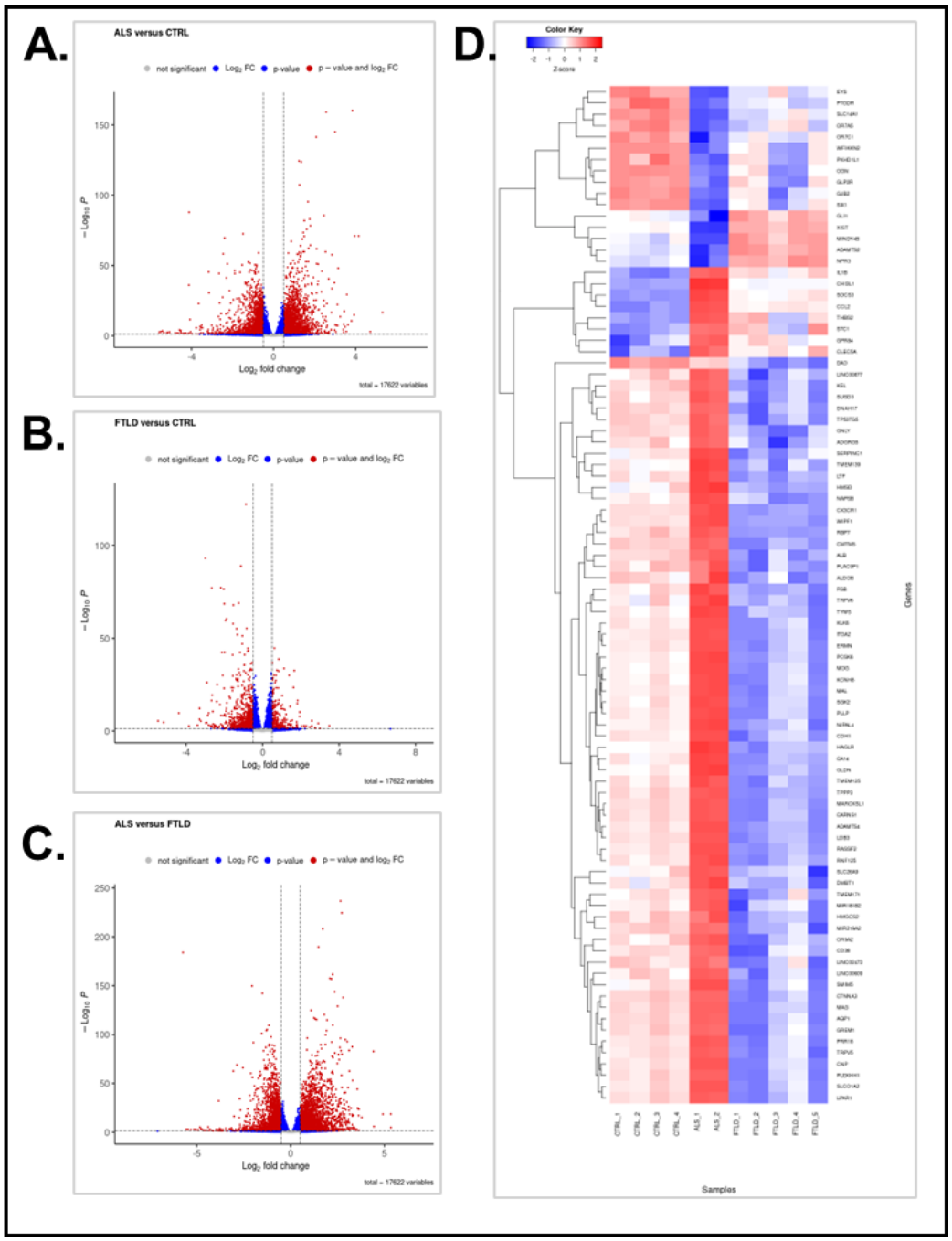

Figure 9.2: Differential Gene Expression in ALS and FTLD Patients. Volcano plots illustrate differentially expressed genes (DEGs) in ALS vs. control (A), FTLD vs. control (B), and ALS vs. FTLD (C). Each dot represents a gene, with significantly upregulated (red) and downregulated (blue) genes identified based on an adjusted p-value (**padj < 0.05**) and log2 fold-change threshold. ALS vs. control shows the highest number of DEGs, while FTLD vs. control exhibits fewer significant changes. The ALS vs. FTLD comparison highlights genes that are differentially expressed between the two diseases, allowing identification of disease-specific transcriptomic alterations. (D) A heatmap of significantly differentially expressed coding genes (**padj < 0.05, |log2 fold-change| > 1**) across all comparisons shows distinct gene expression patterns among ALS, FTLD, and control samples. Hierarchical clustering reveals condition-specific and shared gene expression changes, providing insight into the molecular differences and commonalities between ALS and FTLD.

ALS vs. FTLD Transcriptomic Comparison

To further investigate the relationship between ALS and FTLD at the transcriptomic level, we compared differentially expressed genes (DEGs) between both conditions. Although ALS and FTLD are distinct clinical syndromes, they share TDP-43 proteinopathy as a common pathological hallmark. Given this overlap, it is important to determine the extent to which gene expression changes are shared between the two diseases and where they diverge. This comparison provides insight into common and disease-specific transcriptional alterations, which may underlie the differing disease phenotypes.

Figure 9.3A presents a scatter plot comparing the log2 fold-change values of genes in FTLD vs. control and ALS vs. control. Each dot represents a gene, with those significantly differentially expressed in both comparisons (padj < 0.01) highlighted in green. Genes in the top-right and bottom-left quadrants are those that are consistently upregulated or downregulated in both ALS and FTLD, respectively. In contrast, genes in the top-left and bottom-right quadrants exhibit opposite regulation between ALS and FTLD, indicating disease-specific transcriptional changes. This scatter plot provides a direct visualization of the extent to which gene expression changes in ALS align with or diverge from those in FTLD.

To further explore transcriptomic similarities and differences, we examined how DEGs in one condition behave in the other using ranked gene plots (Figures 9.3B and 9.3C). In these plots, genes are ordered based on their log2 fold-change in one condition, and their corresponding expression changes in the other condition are plotted on the y-axis. The top-ranked genes in ALS vs. control or FTLD vs. control were examined to determine whether they followed similar trends in the other disease. In Figure 9.3B, genes significantly differentially expressed in FTLD vs. control are ranked, and their log2 fold-change values in ALS vs. control are plotted. Similarly, Figure 9.3C ranks ALS DEGs and plots their log2 fold-change in FTLD vs. control. This approach allows for a broader assessment of whether genes significantly altered in one disease exhibit corresponding changes in the other.

A key observation from these ranked gene plots is that ALS DEGs display larger fold-changes than FTLD DEGs in this dataset, although this pattern may partly reflect the smaller FTLD cohort and cortex-only sampling. This may indicate transcriptional disruption in ALS is more pronounced than in FTLD. While some FTLD DEGs show strong agreement with ALS DEGs, others remain largely unchanged in ALS, reflecting the presence of disease-specific transcriptomic alterations. The distribution of points in these plots further supports the finding that ALS exhibits more extensive

gene expression changes compared to FTLD, which may simply indicate broader transcriptional disruption in these two ALS samples.

Together, these analyses reinforce that while ALS and FTLD share a subset of differentially expressed genes, each disease also exhibits a distinct transcriptomic profile. The presence of shared DEGs suggests common molecular pathways affected in both diseases, possibly related to TDP-43 dysfunction. However, the subset of genes exhibiting opposite regulation or remaining unchanged in one disease highlights important disease-specific mechanisms. This distinction is critical for understanding the unique aspects of ALS and FTLD pathogenesis, as well as identifying potential targets for disease-specific therapeutic interventions.

By integrating scatter plot analysis with ranked gene plots, we provide a comprehensive overview of transcriptomic convergence and divergence between ALS and FTLD. The scatter plot quantifies the number of genes that show consistent or opposing regulation across diseases, while the ranked gene plots provide additional context regarding the extent to which expression changes align across conditions. These findings justify further investigation into the biological functions of these differentially expressed genes, as well as the molecular pathways they regulate.

To better understand the functional consequences of these transcriptomic differences, we next performed pathway enrichment analysis. This analysis identifies biological pathways that are significantly altered in ALS and FTLD and provides insights into the molecular mechanisms underlying these gene expression changes.

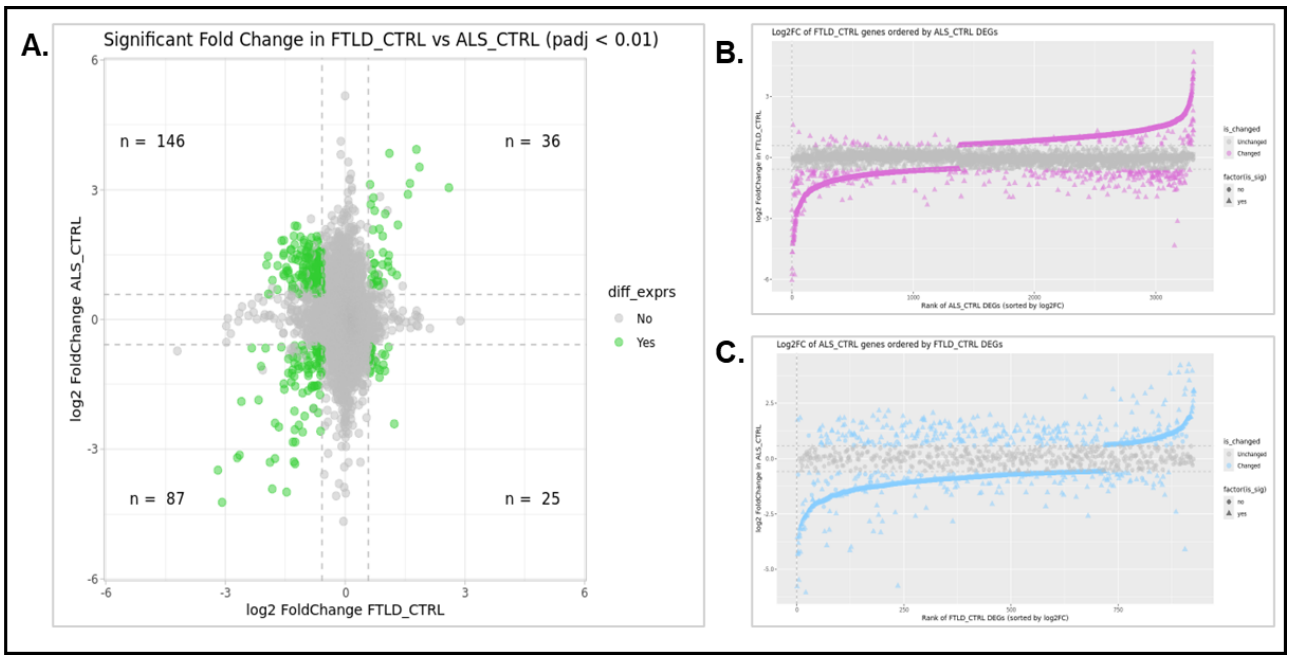

Figure 9.3 | Comparative Transcriptomic Analysis of ALS and FTLD: The figure presents a comparison of differentially expressed genes (DEGs) between ALS and FTLD. (A) A scatter plot comparing log2 fold-change values of genes in FTLD vs. Control (x-axis) and ALS vs. Control (y-axis). Significantly differentially expressed genes (padj < 0.01) in both comparisons are highlighted in green. Genes in the top-right (n = 36) and bottom-left (n = 87) quadrants are upregulated or downregulated in both ALS and FTLD, respectively. Genes in the top-left (n = 146) and bottom-right (n = 25) quadrants exhibit opposite regulation between ALS and FTLD. (B, C) Ranked gene plots showing the log2 fold-change of DEGs in one condition relative to the other. (B) FTLD DEGs ranked by their log2 fold-change in ALS vs. Control, and (C) ALS DEGs ranked by their log2 fold-change in FTLD vs. Control.

Pathway Enrichment Analysis

To understand the transcriptomic alterations identified in ALS and FTLD, we performed pathway-enrichment analysis on the respective DEG sets. This contextualises gene-expression changes in functional terms and highlights biological processes that may be relevant to pathogenesis. Because the cohort is small and restricted to cortical tissue, pathway rankings should be viewed as exploratory. The top fifteen up- and down-regulated pathways for FTLD vs Control (Figure 9.4A) and ALS vs Control (Figure 9.4B) are summarised below.

FTLD. Down-regulated pathways are dominated by synaptic and neuronal-signalling terms—e.g., transmission across chemical synapses, voltage-gated potassium channels and AMPA/NMDA receptor activation—consistent with reports that synaptic dysfunction contributes to FTLD pathophysiology. Up-regulated pathways centre on RNA metabolism and ribosomal function, including nonsense-mediated decay, translation elongation and ribosomal-subunit biogenesis, suggesting disrupted protein homeostasis and compensatory responses to deficits in RNA processing.

ALS. Down-regulated pathways involve immune response, lipid metabolism and intracellular signalling (e.g., Toll-like-receptor and Rho-GTPase pathways, cholesterol biosynthesis, antigen processing), implying altered neuro-immune interactions and metabolic stress. Up-regulated pathways are enriched for synaptic transmission, ion-channel activity and neurotransmitter signalling—including voltage-gated potassium channels, glutamate-receptor activation and neurotransmitter-release cycles—features that have been reported in ALS but require confirmation in larger cohorts.

Comparison. Both diseases share neuronal-signalling pathways, hinting that synaptic disturbance is a common theme. FTLD shows comparatively stronger enrichment in RNA-processing and translation pathways, whereas ALS leans towards ion-channel regulation and immune signalling. These patterns tentatively suggest differential mechanistic emphases, but cohort size and regional sampling limit firm inference.

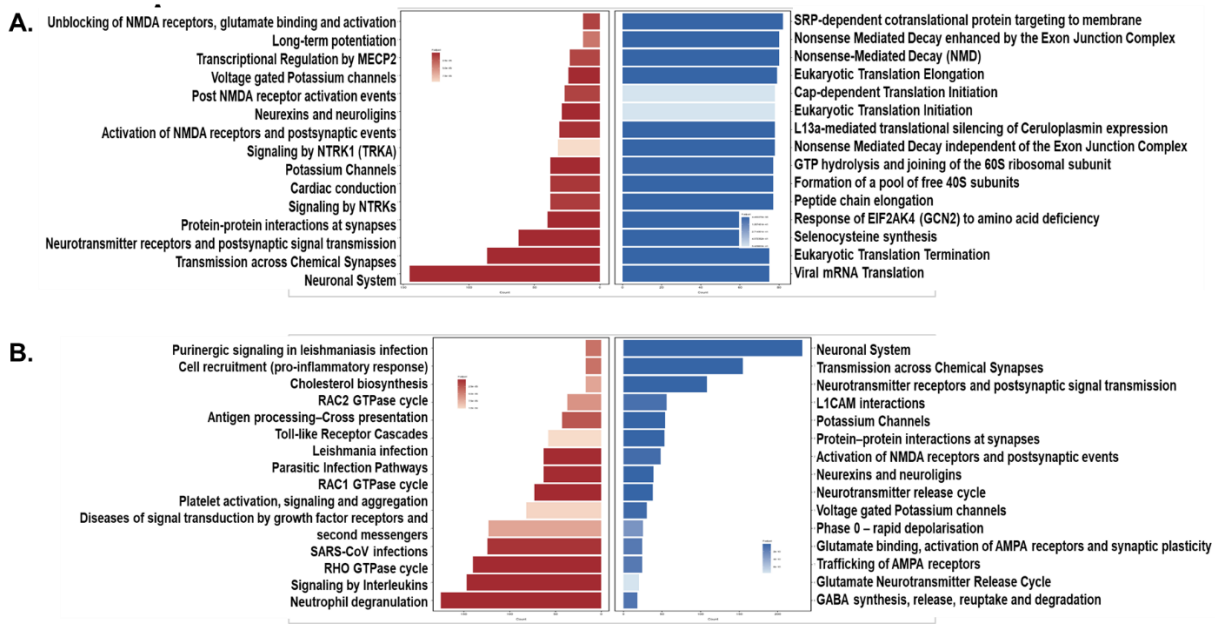

Figure 9.4 | Pathway Enrichment Analysis of Differentially Expressed Genes in FTLD and ALS. The pathway enrichment results for differentially expressed genes (DEGs) in FTLD vs. Control (A) and ALS vs. Control (B). In each panel, the left side (red) represents pathways enriched among downregulated genes, while the right side (blue) represents pathways enriched among upregulated genes. The top 15 enriched pathways are shown for each category based on statistical significance. (A) FTLD vs. Control: Downregulated pathways include synaptic transmission, potassium channels, cardiac conduction, and neurodevelopment-related signaling, while upregulated pathways are enriched for RNA metabolism, translation regulation, and protein synthesis processes, including nonsense-mediated decay, eukaryotic translation elongation, and ribosomal assembly. (B) ALS vs. Control: Downregulated pathways involve immune-related processes, lipid metabolism, and cell signaling cascades, while upregulated pathways are predominantly associated with synaptic transmission, ion channel activity, neurotransmitter regulation, and neuronal system processes.

Metabolic Pathway Analysis in ALS and FTLD

Building on the global pathway results, we asked whether metabolic processes were among the significantly altered pathways in each disease. Because metabolic dysfunction emerged in our NSC-34 TDP-43 models, we performed a focused enrichment search using terms related to glucose metabolism (glycolysis, gluconeogenesis, insulin signalling), energy metabolism (ATP production, oxidative phosphorylation, AMPK signalling), lipid metabolism (fatty-acid oxidation, cholesterol biosynthesis, lipid signalling) and mitochondrial function (TCA cycle, electron transport).

ALS. The targeted search revealed enrichment of lipid-metabolism pathways alongside suppression of glucose- and insulin-related pathways (Table 9.2). Up-regulated terms included cholesterol biosynthesis, sphingolipid metabolism and SREBF-mediated lipid regulation, indicating increased transcriptional activity in lipid processes. Conversely, insulin secretion, insulin-receptor signalling and GLP-1–mediated regulation were down-regulated, suggesting reduced expression of genes linked to glucose homeostasis. Together, these findings point to a transcriptional shift toward lipid metabolism in ALS, with a concomitant decrease in glucose/insulin signalling genes.

FTLD. Under the same criteria, no metabolic pathways passed the significance threshold in this dataset. Given the small FTLD cohort and cortex-only sampling, this absence indicates that metabolic terms were not among the most significantly enriched pathways detected here. FTLD continued to show strong enrichment of RNA-processing and translation pathways, consistent with earlier sections.

The presence of lipid- and insulin-related pathway enrichment in ALS but not in the current FTLD dataset tentatively suggests a stronger metabolic transcriptional signal in ALS. However, cohort size, regional sampling and statistical power preclude firm conclusions about relative "prominence." Within this dataset, RNA and protein-homeostasis pathways appear more conspicuous in FTLD, whereas ALS exhibits a detectable metabolic shift. Metabolic contributions to FTLD pathogenesis cannot be ruled out and warrant investigation in larger, region-matched cohorts.

Table 9.2 | Differentially Enriched Metabolic Pathways in ALS: Summary of metabolic pathways enriched in ALS upregulated and downregulated gene sets based on pathway enrichment analysis. Upregulated pathways include cholesterol biosynthesis and sphingolipid metabolism, while downregulated pathways involve insulin signaling and glucose homeostasis, reflecting alterations in lipid metabolism and energy regulation. No metabolic pathways were significantly enriched in FTLD under the same search criteria.

Comparison	Description	p.adjust	Gene Count
ALS Upregulated	Cholesterol biosynthesis	0.000133	16
	Regulation of cholesterol biosynthesis by SREBP (SREBF)	0.001097	24
	Sphingolipid de novo biosynthesis	0.002083	20
	Sphingolipid metabolism	0.004722	32
	Translation of Structural Proteins	0.019175	19
	Regulation of insulin secretion	0.000225	31
ALS Downregulated	Ion transport by P-type ATPases	0.001727	23
	Signaling by Insulin receptor	0.00725	27
	Insulin receptor recycling	0.014481	12
	Glucagon-like Peptide-1 (GLP1) regulates insulin secretion	0.026463	16
	Adrenaline,noradrenaline inhibits insulin secretion	0.029389	12
	Phospholipid metabolism	0.039568	55
	Glucagon signaling in metabolic regulation	0.041813	13

Intersection of Patient-Derived Transcriptomic Changes with NSC34 TDP-43 Perturbation Data

By identifying metabolic pathway alterations in ALS but not in FTLD, this analysis further delineates the transcriptomic differences between these two disorders and highlights the distinct roles of lipid and glucose metabolism in ALS pathology within this dataset. However, to further contextualize these findings, it is essential to determine whether the differentially expressed genes (DEGs) identified in ALS and FTLD patient-derived samples overlap with the transcriptomic changes observed in NSC34 motor neuron-like cells following TDP-43 knockdown and mutation expression.

To evaluate the overlap between DEGs from NSC34 motor neuron-like cells and human-derived transcriptomic datasets, an intersection analysis was performed, as shown in Figure 9.5. The first panel (Figure 9.5A) presents an UpSet plot that visualizes the intersections of DEGs across different experimental conditions. The bar heights represent the number of DEGs within each unique or overlapping category, while the dot matrix below indicates the DEG groups contributing to each intersection. The largest sets of DEGs are observed in the human-derived transcriptomes, followed

by NSC34-specific DEGs. Multiple overlapping groups are present, reflecting subsets of genes differentially expressed in both datasets.

Due to the complexity of the multiple intersecting sets in Figure 9.5A, a simplified version of the UpSet plot was generated (Figure 9.5B). This representation merges all DEGs from the human dataset and all DEGs from NSC34 into broader categories, thereby reducing the number of distinct groups while preserving information about shared and unique transcriptomic changes. The plot displays three primary DEG categories: those unique to human datasets, those unique to NSC34 datasets, and those found in both datasets. The human-derived dataset contains the largest number of unique DEGs, while a subset of genes is common to both datasets, suggesting potential shared transcriptomic alterations.

Following this intersection analysis, a GO enrichment analysis was performed on the shared DEGs to identify biological processes that may be commonly dysregulated in both NSC34 motor neuron-like cells and human patient-derived transcriptomes (Figure 9.5C). The analysis reveals enrichment in pathways related to ion transport, maintenance of location, vascular development, and signaling processes, including the regulation of G protein-coupled receptor signaling.

These findings outline the intersection between DEGs in NSC34 motor neuron-like cells and human ALS/FTLD transcriptomes, revealing both overlapping and distinct gene expression changes. While shared pathways are identified, this does not indicate that all NSC34 transcriptomic changes are directly representative of ALS or FTLD pathology. Instead, the overlap highlights conserved biological processes that may be relevant to TDP-43-driven neurodegeneration, although validation in larger, region-matched cohorts remains essential.

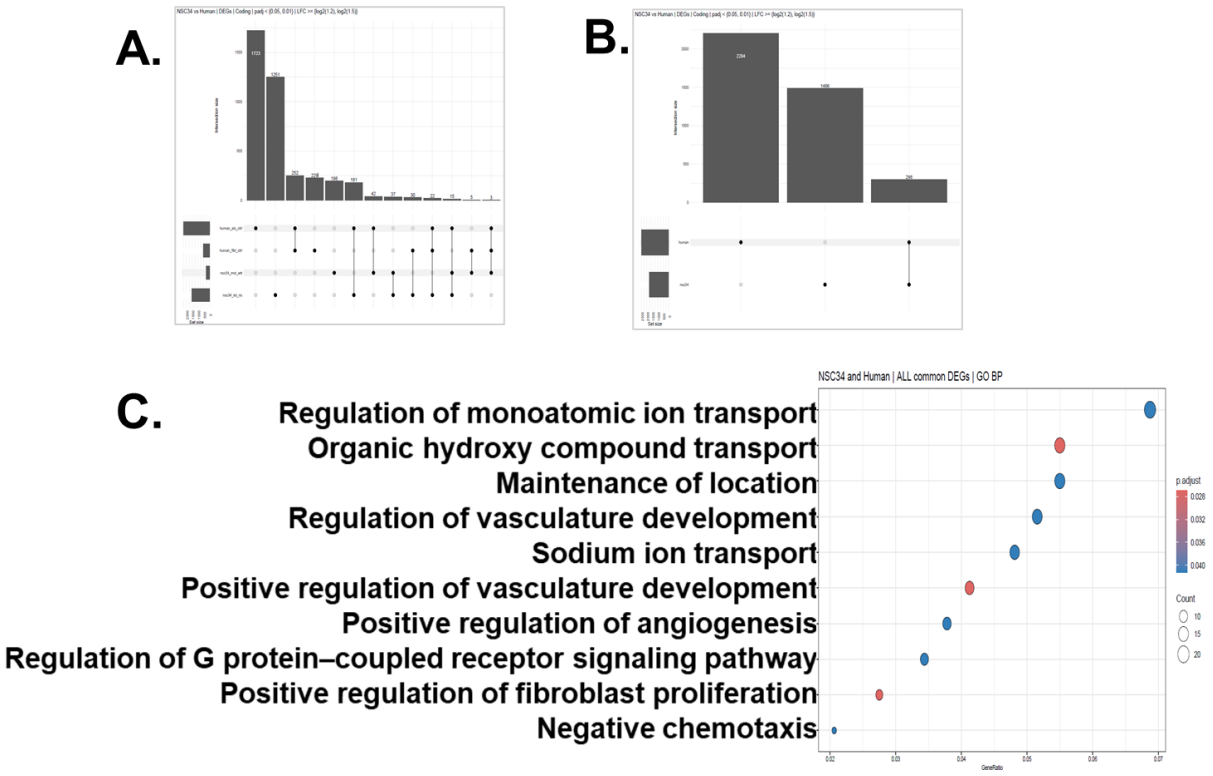

Figure 9.5 | Intersection and enrichment analysis of differentially expressed genes (DEGs) in human ALS/FTLD transcriptomes and NSC34 motor neuron-like cells following TDP-43 perturbation. (A) UpSet plot showing the number of DEGs shared across experimental conditions in human and NSC34 datasets. (B) Simplified intersection analysis merging all human DEGs and all NSC34 DEGs, highlighting common and unique gene sets. (C) Gene Ontology (GO) enrichment analysis of biological processes associated with common DEGs, with dot size reflecting gene count and color indicating adjusted p-value significance.

Discussion

General Discussion

As introduced before, metabolic dysfunction has emerged as a key disease-modifying factor in ALS and, to a lesser extent, FTLD. Epidemiological observations reveal that metabolic conditions such as type 2 diabetes and hyperlipidemia—traditionally considered detrimental to health—are paradoxically associated with slower ALS progression (Jawaid et al., 2018b). Conversely, lifestyle factors like intense physical activity, generally deemed beneficial, have been linked to increased ALS risk. These contradictory observations complicate our understanding of whether metabolic alterations contribute directly to neurodegeneration or reflect compensatory adaptations. To address this complexity, I focused on investigating how TDP-43 dysfunction alters cellular energy metabolism in motor neurons, with the aim of defining mechanisms of metabolic dysregulation, exploring cell-type-specific metabolic responses, examining the role of metabolic sensing pathways, and evaluating how systemic metabolic states modulate these responses.

The findings presented in Parts I-VII confirm that TDP-43 loss and mutation profoundly disrupt metabolism, though with distinct mechanisms across cell types and conditions. In this part, I revisit each hypothesis in light of these findings, integrating them into the broader framework of ALS and FTLD pathogenesis and considering their implications for future research and potential therapeutic strategies.

TDP-43 Perturbation Disrupts Cellular Energy Metabolism *(Hypothesis 1)*

As highlighted in the first part of the Results, TDP-43 is a key regulator of RNA metabolism, and its dysfunction has been implicated in neurodegenerative diseases such as ALS and FTLD. This study hypothesizes that TDP-43 perturbation disrupts cellular energy metabolism by altering glycolysis, oxidative phosphorylation, and mitochondrial function, ultimately leading to metabolic maladaptation. In line with Aim 1, the experiments detailed in Parts I and II of the results sought to determine how TDP-43 depletion and mutation impact motor neuron metabolism. The findings indicate a hypermetabolic shift in NSC34 motor neurons upon TDP-43 depletion, whereas expression of mutant TDP-43 indicated similar albeit less prominent effects.

In Part I, RNAi-mediated knockdown of TDP-43 in NSC34 motor neuron-like cells resulted in significant metabolic reprogramming. Transcriptomic analysis revealed widespread changes in genes involved in glycolysis, oxidative phosphorylation, and pyruvate metabolism. Functionally, NSC34 motor neuron-like cells exhibited increased glucose uptake with increased carbon flux through the TCA cycle, with notable elevations in citrate, α-ketoglutarate, and malate confirmed by dynamic

metabolic mapping reinforcing the notion of metabolic overdrive. Furthermore, glycolytic stress tests demonstrated an increase in both glycolytic capacity and glucose reliance, while mitochondrial stress tests indicated heightened oxidative phosphorylation, with increased basal and maximal respiration. Importantly, this metabolic acceleration was accompanied by a marked increase in ATP production, suggesting that TDP-43 loss-of-function induces a state of heightened energy demand. However, this hypermetabolic phenotype was not without consequence—elevated ATP synthesis coincided with excessive ROS production and depletion of glutathione, highlighting a vulnerability to oxidative stress. The RNAi rescue experiment provided conclusive evidence that these metabolic changes were directly attributable to TDP-43 depletion, as restoring TDP-43 expression normalized glucose metabolism, mitochondrial respiration, and redox homeostasis. Taken together, these findings strongly indicate that TDP-43 knockdown drives a metabolic shift, characterized by excessive glucose metabolism, mitochondrial overactivation, and oxidative imbalance.

In contrast, Part II investigated the metabolic consequences of TDP-43 mutation, focusing on the ALS-associated M337V variant. Unlike TDP-43 knockdown, which led to an immediate metabolic shift, TDP-43 mutation resulted in more subtle yet progressive changes. Transcriptomic profiling revealed downregulation of key energy metabolism pathways, particularly those governing glycolysis, fatty acid metabolism, and the TCA cycle. Notably, glucose-6-phosphate dehydrogenase (G6PD) expression was significantly upregulated, suggesting a shift toward the pentose phosphate pathway, which may serve as a compensatory mechanism to counteract oxidative stress.

At the functional level, NSC34 motor neuron-like cells expressing mutant TDP-43 exhibited increased glucose uptake at 48 hours post-transfection. Metabolic mapping experiments revealed altered carbon flux through the TCA cycle, with significant changes in citrate and α-ketoglutarate labeling, while downstream TCA intermediates remained unaffected. Glycolytic and mitochondrial stress tests further confirmed a shift in metabolic strategy—mutant TDP-43-expressing cells exhibited increased glycolytic capacity and oxidative phosphorylation, with elevated basal respiration and ATP production. Interestingly, despite these metabolic alterations, no significant increase in ROS levels was detected. However, a decrease in oxidized glutathione (GSSG) suggested that subtle redox changes were occurring, potentially reflecting an early-stage adaptation to mitochondrial stress.

Taken together, these findings support the hypothesis that TDP-43 dysfunction disrupts cellular energy metabolism, albeit through distinct mechanisms. TDP-43 knockdown induces a hypermetabolic state, overwhelming mitochondrial function and leading to oxidative stress, whereas TDP-43 mutation subtly alters metabolic flux. These insights suggest that metabolic dysfunction is a

core feature of TDP-43 proteinopathy and may play a pivotal role in motor neuron vulnerability in ALS and FTLD.

Cell-Type-Specific Metabolic Adaptations to TDP-43 Dysfunction *(Hypothesis 2)*

The metabolic consequences of TDP-43 dysfunction in motor neurons suggest that these cells undergo a hypermetabolic maladaptation. Given the central role of TDP-43 in RNA metabolism and cellular homeostasis, a critical question arises: Is this metabolic vulnerability unique to motor neurons, or do other neural cell types exhibit similar or distinct metabolic adaptations in response to TDP-43 perturbation? Addressing this question is essential to determining whether the metabolic dysregulation seen in ALS is neuron-specific or a broader feature of TDP-43 proteinopathy affecting multiple neural cell types. To explore this, Hypothesis 2 posited that TDP-43 depletion and mutation would induce metabolic dysfunction across different neural cell types, with motor neurons exhibiting the most pronounced metabolic vulnerability. This aligns with Aim 2 of this thesis, which investigated how BV2 microglia and N2A neuroblastoma cells respond to TDP-43 perturbation, providing a comparative framework to determine whether metabolic stress is selectively exacerbated in motor neurons or represents a more generalizable phenomenon across the CNS.

The findings reveal that while TDP-43 knockdown induces metabolic perturbations in all three cell types, the nature of these adaptations differs significantly. BV2 microglia respond to TDP-43 loss by increasing glucose uptake, lactate production, and glycolytic capacity, suggesting a Warburg-like shift toward glycolysis. Unlike NSC34 motor neuron-like cells, which exhibited a hypermetabolic maladaptation affecting both glycolysis and mitochondrial respiration upon TDP-43 knockdown, BV2 cells primarily relied on glycolytic upregulation without significant changes in oxidative phosphorylation. This metabolic shift was accompanied by a transient increase in oxidative stress and ATP levels. These results could be explained by the inherent metabolic plasticity of microglia and their ability to switch between oxidative and glycolytic metabolism in response to environmental stressors.

In contrast, N2A neuroblastoma cells exhibited a marginally hypometabolic response to TDP-43 knockdown, characterized by moderately reduced glucose incorporation into both glycolysis and the TCA cycle and lower ATP production. Notably, TDP-43 knockdown did not result in exaggerated ROS production in N2a cells.

A key distinction between knockdown and mutant TDP-43 expression was also observed across cell types. While TDP-43 depletion induced significant metabolic reprogramming in all three models, the expression of mutant TDP-43 (M337V) elicited far subtler metabolic effects. In BV2 microglia and

N2A cells, mutant expression did not significantly alter glucose metabolism, glycolysis, or mitochondrial function, suggesting that TDP-43 mutation alone is insufficient to drive immediate metabolic dysfunction in these cell types. Similarly, in NSC34 motor neuron-like cells, mutant expression resulted in less pronounced metabolic changes, such as altered glucose uptake and moderate shifts in metabolic flux, without the extreme metabolic overdrive observed upon TDP-43 knockdown. These findings imply that the complete loss of TDP-43 function disrupts fundamental metabolic regulatory mechanisms, whereas mutant TDP-43 may exert its effects more gradually or require additional stressors to unmask metabolic dysfunction.

Taken together, these findings highlight that while TDP-43 dysfunction induces metabolic alterations across different neural cell types, motor neurons exhibit the most profound maladaptive response. In NSC34 motor neuron-like cells, TDP-43 depletion triggered a hypermetabolic state characterized by excessive energy demand, mitochondrial overactivation, and oxidative stress, underscoring their heightened metabolic fragility in ALS. In contrast, BV2 microglia responded by increasing glycolysis, a shift that, while sustaining energy production, may also promote a pro-inflammatory phenotype and contribute to neuroinflammation. N2A neuroblastoma cells exhibited only modest reductions in glycolysis and mitochondrial respiration, with limited changes in oxidative stress markers. These insights reinforce the hypothesis that TDP-43 dysfunction disrupts metabolism in a cell-type-dependent manner, with motor neurons being the most metabolically vulnerable.

Dysregulation of Cellular Metabolic Sensing in TDP-43 Dysfunction *(Hypothesis 3)*

The findings in Part I-III establish that TDP-43 dysfunction disrupts cellular metabolism, with motor neurons exhibiting a hypermetabolic maladaptation. Given these cell-type-specific responses, a critical question emerges: How do motor neurons sense and regulate metabolic stress in response to TDP-43 perturbation? Metabolic homeostasis is tightly regulated by energy-sensing pathways that respond to cellular ATP levels, oxidative stress, and nutrient availability. A central player in this regulatory network is AMP-activated protein kinase (AMPK), a key metabolic checkpoint that coordinates energy balance by modulating glycolysis, mitochondrial respiration, and anabolic suppression. Thus, hypothesis 3 posited that TDP-43 dysfunction disrupts cellular metabolic sensing mechanisms, leading to altered AMPK signaling dynamics in motor neurons. In line with Aim 3, Parts IV and V investigated how AMPK signaling responds to TDP-43 depletion and mutant TDP-43 expression, providing mechanistic insights into metabolic stress adaptation in motor neurons.

Notably, the active form of AMPK, phosphorylated AMPK (pAMPK), as well as one of its downstream effectors pACC were significantly elevated upon TDP-43 knockdown. This was confirmed via

functional kinase activity assays, which revealed that AMPK activation peaked at 12 hours post-knockdown before returning to baseline at 24 hours, indicating a transient response. Additionally, AMPK activation persisted across varying glucose availability conditions, failing to suppress even in high-glucose environments. This disrupted regulatory feedback suggests that TDP-43 knockdown may impair the metabolic sensing of neurons leading to sustained AMPK activation despite an energy-rich state.

In contrast to the transient AMPK activation observed in TDP-43 knockdown, Part V of the results demonstrated that mutant TDP-43 (M337V) engages AMPK differently, primarily affecting its response to metabolic stress. Under basal conditions, total AMPK levels, phosphorylation status, and kinase activity remained largely unchanged between wild-type TDP-43 (WTT) and mutant TDP-43 (MVT), suggesting that mutant TDP-43 alone does not immediately perturb AMPK signaling. However, a divergence between WTT and MVT became evident under oxidative stress conditions. Both groups exhibited AMPK activation during arsenite-induced stress. However, a key distinction emerged during the recovery phase. WTT-expressing cells restored AMPK phosphorylation and kinase activity to baseline. In contrast, MVT-expressing cells maintained elevated AMPK phosphorylation and activity, even after stress removal. This persistent AMPK activation was associated with ongoing TDP-43 aggregation, suggesting that insoluble mutant TDP-43 prolongs metabolic stress signaling. This raises the question of whether sustained AMPK activation is protective or contributes to metabolic dysfunction in ALS. While transient AMPK activation supports cellular adaptation to stress, prolonged activation can drive catabolic depletion, mitochondrial strain, and metabolic exhaustion. This may increase neuronal vulnerability. Overall, these findings suggest that mutant TDP-43 disrupts normal AMPK signaling resolution, maintaining an energy-demanding state that could accelerate neurodegeneration.

Together, these findings highlight key differences in AMPK regulation between TDP-43 knockdown and mutant expression. TDP-43 knockdown induces a hypermetabolic shift, triggering transient AMPK activation that fails to downregulate despite energy abundance, suggesting a dysregulated metabolic feedback loop. In contrast, mutant TDP-43 does not activate AMPK under basal conditions but sustains its engagement following stress that correlates with persistent TDP-43 mislocalization and insolubility.

Systemic Metabolic Factors Modulate TDP-43-Induced Metabolic Stress in Motor Neurons in a Sex-Specific Manner *(Hypothesis 4)*

The findings discussed in Parts I - V establish that TDP-43 dysfunction disrupts cellular metabolism, with motor neurons exhibiting a hypermetabolic maladaptation. Additionally, Parts IV and V revealed that AMPK, a key metabolic sensor, is dysregulated in motor neurons following TDP-43 depletion and mutation, further highlighting the metabolic breakdown induced by TDP-43 dysfunction. However, the intrinsic metabolic changes described so far do not account for the potential influence of systemic metabolic factors on TDP-43-induced metabolic breakdown in motor neurons. Given that metabolic disorders such as obesity, dyslipidemia, and T2DM have been paradoxically associated with better outcomes in ALS, a critical question arises: how do systemic metabolic factors influence the metabolic breakdown induced in motor neurons by TDP-43 depletion? Addressing this question is essential to understand whether systemic metabolic states can modify the severity of TDP-43-driven metabolic dysfunction, either exacerbating or mitigating its effects.

To explore this, Hypothesis 4 posited that systemic metabolic cues influence TDP-43-associated metabolic reprogramming in a sex-dependent manner. In line with Aim 4, Part VI investigated the effects of serum stimulation from mice exposed to different systemic metabolic conditions—control (CTL), high-fat diet (HFD), and voluntary exercise (VE)—on NSC34 motor neuron-like cells following TDP-43 knockdown. A central finding from Part VI was that systemic metabolic cues significantly modulated glycolytic adaptations following TDP-43 knockdown, and these effects were sex-dependent. Consistent with observations in Parts I-III, TDP-43 depletion enhanced glycolysis in NSC34 motor neuron-like cells, as evidenced by increased extracellular acidification rate (ECAR). However, when exposed to serum from different metabolic conditions, NSC34 cells showed divergent responses based on serum donor sex. In male-derived serum conditions, glycolytic output remained elevated in both CTL and VE groups, whereas HFD serum suppressed glycolysis relative to TDP-43 knockdown alone—suggesting that systemic factors associated with high-fat feeding may counteract the glycolytic upregulation induced by TDP-43 depletion. In contrast, in female-derived serum conditions, both VE and HFD serum reduced glycolytic reserve, indicating that metabolic factors from female mice limit the glycolytic adaptability of TDP-43-deficient neurons.

Beyond glycolysis, Part VI also demonstrated that systemic metabolic factors significantly altered mitochondrial function following TDP-43 knockdown. Consistent with earlier findings, TDP-43 depletion alone increased mitochondrial respiration in NSC34 cells, reflecting a shift toward enhanced oxidative metabolism. However, when exposed to serum from different metabolic states, distinct patterns emerged. In male-derived serum conditions, HFD serum suppressed mitochondrial

function in NSC34 neurons, reducing both maximal and spare respiratory capacity, whereas VE serum had no significant effect. Conversely, in female-derived serum conditions, both VE and HFD serum increased mitochondrial activity, suggesting that systemic metabolic factors from female mice enhance mitochondrial function in TDP-43-deficient motor neurons. These results highlight the complexity of systemic metabolic regulation, with clear sex-dependent differences in mitochondrial responses.

Taken together, these findings establish that systemic metabolic factors influence the metabolic adaptations induced by TDP-43 dysfunction in motor neurons, with effects that are sex-specific. Metabolic serum conditions modulated both glycolysis and oxidative phosphorylation in NSC34 cells, but sex-based differences were particularly evident in the regulation of glycolytic reserve and mitochondrial adaptability. These findings align with clinical observations that sex-based differences exist in ALS progression, where female patients often present with a different metabolic profile and disease trajectory compared to males.

The observation that HFD serum suppresses glycolysis and mitochondrial function in TDP-43-deficient motor neurons provides a potential mechanistic link to the paradoxical association between metabolic disorders and ALS survival. While chronic metabolic dysfunction is generally detrimental, the metabolic constraints imposed by high-fat feeding may counteract the hypermetabolic overdrive observed in ALS motor neurons, potentially slowing disease progression.

These findings from Part VI reinforce Hypothesis 4, confirming that systemic metabolic cues modulate TDP-43-driven metabolic dysfunction in a sex-dependent manner. These results highlight the interplay between intrinsic cellular metabolic changes and extrinsic systemic influences, suggesting that metabolic resilience or vulnerability in ALS may be shaped by systemic metabolic states. The observed sex differences in metabolic responses may also have broader implications for understanding sex-specific disease mechanisms in ALS, particularly in relation to energy metabolism. Future research should focus on identifying the specific metabolic components within systemic circulation that mediate these effects, as well as evaluating whether metabolic interventions—such as dietary modifications—could selectively mitigate TDP-43-associated metabolic dysfunction in ALS.

Translational Relevance of NSC34 Findings: Comparison to Patient-Derived ALS and FTLD Transcriptomes *(Aim 5)*

The findings presented in Parts I–VI demonstrate that TDP-43 dysfunction disrupts cellular metabolism and metabolic sensing in motor neurons. Additionally, systemic metabolic factors

modulate these alterations, providing insight into how both intrinsic and extrinsic factors contribute to metabolic stress in ALS. However, while these models offer important mechanistic insights, it remains essential to assess how well they reflect the transcriptomic alterations observed in human ALS and FTLD. In line with Aim 5, Part VII explored the translational relevance of the NSC34 motor neuron-like cell models by comparing the transcriptomic changes following TDP-43 depletion and mutation with those identified in ALS and FTLD postmortem brain samples.

Differential gene expression analysis identified extensive transcriptional alterations in both ALS and FTLD samples compared to controls. ALS samples displayed a larger number of differentially expressed genes (DEGs) relative to FTLD. Enrichment analyses indicated that ALS samples exhibited alterations in lipid metabolism and insulin signaling pathways, with upregulation of cholesterol biosynthesis and sphingolipid metabolism, alongside downregulation of glucose homeostasis and insulin receptor signaling. In contrast, FTLD samples showed changes primarily involving RNA metabolism, translation regulation, and synaptic function, including pathways related to AMPA/NMDA receptor signaling, neurotransmission, and protein synthesis.

Part VII also performed intersection analyses to identify overlapping transcriptomic changes between NSC34 models and patient-derived samples. These analyses revealed that while ALS and FTLD exhibit largely distinct transcriptional landscapes, a subset of DEGs overlapped with those observed in NSC34 motor neuron-like cells following TDP-43 perturbation. This overlap included genes involved in RNA metabolism, translation regulation, ion transport, and synaptic function, reflecting pathways known to be affected by TDP-43 dysfunction. Additionally, some pathways associated with lipid metabolism and mitochondrial function were identified in both ALS patient samples and NSC34 models, suggesting that certain aspects of metabolic dysregulation observed in vitro may also be relevant to ALS pathology.

Overall, the transcriptomic overlap between NSC34 models and ALS samples appeared more prominent than with FTLD samples, particularly in pathways related to cellular metabolism, oxidative phosphorylation, and mitochondrial stress responses. However, it is important to interpret these findings cautiously. The NSC34 model represents a simplified system that captures selected features of motor neuron biology and does not fully recapitulate the complexity of human ALS or FTLD. Moreover, the ALS patient cohort analyzed included only two cases, limiting the generalizability of these findings.

These observations suggest that while the NSC34 model may provide a useful platform to explore aspects of metabolic dysfunction associated with ALS, particularly those involving lipid and energy

metabolism, additional models are likely needed to capture the broader transcriptomic alterations seen in FTLD, including RNA metabolism and synaptic pathways. These findings support the complementary use of diverse cellular models to study disease-specific transcriptomic alterations and to evaluate therapeutic strategies targeting metabolism and RNA homeostasis in ALS and FTLD.

From TDP-43 Dysregulation to Clinical Signatures: A Metabolic Perspective

Metabolic dysregulation is now recognized as a key modifier in TDP-43 proteinopathies, particularly ALS (Bouteloup et al., 2009; Scotter et al., 2015). Clinically, a hypermetabolic state is frequently observed in ALS patients and correlates with disease severity, while paradoxically, metabolic conditions such as T2DM and dyslipidemia are associated with delayed onset and slower progression (Jawaid et al., 2018b; Jésus et al., 2018). The findings from this thesis provide a mechanistic explanation for this paradox by demonstrating how TDP-43 dysfunction induces cell-intrinsic hypermetabolism in motor neurons—a state that, while initially adaptive, ultimately renders them vulnerable to energetic collapse and oxidative damage. In the sections that follow, I will examine four interconnected themes. First, I consider motor neuron hypermetabolism and oxidative stress, highlighting how TDP-43 loss and mutation drive simultaneous upregulation of glycolysis and oxidative phosphorylation at the cost of redox balance. Next, I compare cell-type–specific metabolic responses, contrasting the marked hypermetabolic maladaptation of NSC34 motor neuron–like cells with the resilience of BV2 microglia and the muted hypometabolism of N2A neuroblastoma cells. Then, I turn to dysregulated energy sensing via AMPK, exploring how persistent AMPK activation—even under nutrient-replete conditions—reflects a breakdown in metabolic feedback that may accelerate neuronal vulnerability. Finally, I integrate these cellular insights with systemic metabolic modulation, showing how high-fat diet and exercise-derived serum—in a sex-dependent manner—can buffer or exacerbate TDP-43–induced metabolic stress, thereby providing a mechanistic bridge to the paradoxical clinical observations that metabolic comorbidities can slow ALS progression. Together, these themes frame a metabolic perspective that links TDP-43 dysfunction at the molecular level to clinical signatures of disease.

Motor Neuron Hypermetabolism and Oxidative Stress

TDP-43 knockdown in NSC34 cells induced robust overactivation of glycolysis and oxidative phosphorylation, resulting in increased ATP production but also excessive ROS accumulation and disrupted NAD^+/NADH and GSH/GSSG ratios—even in the presence of normal glucose levels. Intriguingly, this metabolic amplification occurred despite normal glucose availability. These observations are consistent with prior reports showing that TDP-43 depletion elevates metabolic flux

and disrupts mitochondrial function(Jiang & Ngo, 2022b; Loganathan et al., 2022; P. Wang et al., 2019). By comparison, M337V mutation produced a subtler shift—less glycolytic/mitochondrial overdrive but greater PPP flux. This divergence supports emerging views that TDP-43 loss-of-function and toxic gain-of-function mutations may impact metabolism through distinct yet converging routes (Feneberg et al., 2020; Schweingruber et al., 2025). The findings from my thesis suggest that TDP-43 knockdown leads to an energetically costly overdrive state, where metabolic demand and output increases while redox balance becomes progressively compromised. This phenotype aligns with evidence that TDP-43 dysfunction can perturb glycolytic metabolism in neurons. In cellular and animal models of ALS, glycolytic intermediates such as pyruvate are elevated in response to TDP-43 overexpression, and upregulation of phosphofructokinase and glucose transporters has been reported (Manzo et al., 2019). Moreover, enhanced glycolysis has been shown to partially rescue survival and locomotor performance in Drosophila expressing human TDP-43, particularly when glucose supplementation or GLUT3 overexpression is employed (Manzo et al., 2019). These findings suggest that neurons attempt to respond to TDP-43–induced stress by increasing glucose utilization. However, unlike models that emphasize glycolytic compensation under aggregation stress, my findings demonstrate that TDP-43 knockdown alone is sufficient to initiate this metabolic shift. Importantly, these results indicate that this shift is maladaptive over time, as it coincides with elevated reactive oxygen species and does not restore redox equilibrium.

In classic overexpression/mutation models, TDP-43 aggregates disrupt mitochondrial cristae, reduce ATP output, and elevate ROS (Wang et al., 2016). In those models, mitochondrial cristae become disorganized and membrane potential is lost, leading to energy failure and enhanced vulnerability to cell death. By contrast, our knockdown cells maintain mitochondrial structure even while activating metabolism, implying that loss-of-function triggers a transient hypermetabolic phase prior to the collapse seen in late-stage aggregation. Thus, the metabolic response to TDP-43 dysregulation appears context-dependent—determined by whether the insult is acute aggregation or progressive nuclear depletion.

Another finding from my thesis is the uncoupling of metabolic activation from redox imbalance. This mirrors observations that TDP-43 dysfunction impairs the antioxidant system. For instance, in mutant TDP-43–expressing cells, transcription of Nrf2-responsive genes is elevated, yet protein levels of key antioxidant enzymes remain low, resulting in glutathione depletion and increased oxidative stress (Moujalled et al., 2017). A proposed mechanism is that TDP-43 mutations interfere with RNA binding proteins such as hnRNP K, thereby impairing translation of antioxidant transcripts despite increased mRNA levels (Moujalled et al., 2017). Similarly, my data show that TDP-43 knockdown

leads to increased GSSG and increased reactive oxygen species. This suggests that nuclear TDP-43 may play a role in coordinating transcription–translation coupling for antioxidant defense. When TDP-43 is lost, the cell mounts an inadequate antioxidant response, allowing reactive oxygen species to accumulate even as metabolism accelerates. The implications of this imbalance are significant. Early redox imbalance—preceding mitochondrial collapse—supports the hypothesis that hypermetabolism itself (rather than late-stage aggregation) drives oxidative damage. Sustained glycolytic and oxidative activation thus places neurons in an energetically costly 'overdrive,' hastening degeneration. This concept is further reinforced by clinical observations. ALS patients often present with elevated resting energy expenditure and progressive weight loss, correlating with faster disease progression (Steyn et al., 2022). In contrast, patients with higher BMI or metabolic comorbidities, such as type 2 diabetes mellitus or dyslipidemia, tend to have slower disease trajectories (D'Ovidio et al., 2018; Wannarong & Ungprasert, 2020).

Cell-Type–Specific Metabolic Responses to TDP-43 Loss

Importantly, our comparative analysis across cell types demonstrated that motor neurons are uniquely susceptible to this metabolic overload. While BV2 microglia shifted toward glycolysis and N2A neuroblastoma cells exhibited a muted hypometabolic response, only NSC34 motor neuron-like cells displayed the full spectrum of metabolic overactivation and oxidative stress. This cell-type specificity mirrors the clinical reality of selective motor neuron degeneration in ALS and reinforces the hypothesis that energy imbalance contributes to neuronal vulnerability (Nijssen et al., 2017; Vandoorne et al., 2018). TDP-43 deletion in microglia has been reported to alter immune gene expression and boosts phagocytic activity without disrupting mitochondrial ATP production or overall metabolic balance (Paolicelli et al., 2017; Zhao et al., 2010) Likewise, undifferentiated neuronal lines such as N2A neuroblastoma cells show only slight reductions in mitochondrial respiration and no change in glycolysis when TDP-43 is knocked down, reflecting their lower reliance on oxidative metabolism (Di Rita & Strappazzon, 2020). Thus, only motor-like cells mount a full hypermetabolic and oxidative-stress response to TDP-43 loss, whereas microglia and N2A lines exhibit much more modest shifts.

This divergence offers a compelling explanation for ALS's selective vulnerability: motor neurons, by virtue of high basal energy requirements and limited metabolic flexibility, may be intrinsically less capable of coping with TDP-43–induced stress. Although TDP-43 is ubiquitous in the CNS, other cell types avoid catastrophic overactivation, reinforcing the idea that motor neurons inherently lack the buffering capacity to handle this metabolic insult. The exaggerated energy demand observed in

NSC34 cells following TDP-43 knockdown likely pushes them beyond a threshold of failure. Therefore, cell-type–specific metabolic responses may underlie the clinical and pathological specificity of ALS, despite the systemic presence of TDP-43 pathology. This hypothesis aligns with recent proposals that neurodegeneration arises not only from toxic protein aggregates but from the failure of vulnerable cells to adapt to proteostatic and metabolic insults (van Es et al., 2017).

Dysregulated Energy Sensing via AMPK

The profound hypermetabolic reprogramming observed in NSC34 motor neuron–like cells following TDP-43 knockdown raised a critical question: are these cells failing to appropriately sense their energy status? This prompted an investigation into AMPK, a canonical energy sensor activated by rising AMP/ATP ratios. Under normal conditions, transient AMPK activation couples energy demand to supply by inhibiting ATP-consuming anabolic processes and promoting ATP-generating catabolic pathways. In the context of TDP-43 knockdown, however, NSC34 cells exhibited persistent AMPK activation despite elevated intracellular ATP levels, indicating a decoupling of AMPK from its classical regulatory mechanism. This suggests that motor neuron–like cells with TDP-43 dysfunction may misinterpret their energetic state, leading to maladaptive stress responses. Moreover, cells expressing the ALS-linked M337V TDP-43 mutation exhibited prolonged AMPK activation during metabolic recovery from stress, further supporting the notion that TDP-43 modulates AMPK feedback resolution.

These findings align partially with previous studies, though key differences reveal the novelty of my observations. For example, one study reported increased AMPK activity in the spinal cords of SOD1G93A ALS mice and postmortem ALS tissue, which was interpreted as a compensatory response to energetic failure (Lim et al., 2012). However, these data demonstrate that AMPK activation in TDP-43–deficient motor neurons occurs independently of energy depletion. This contrasts with the classical SOD1 model and suggests a more nuanced role for AMPK in TDP-43–mediated pathology. Another study showed that overexpression of TDP-43 in SH-SY5Y cells activated AMPK and led to mitochondrial fragmentation, but the mechanism was again presumed to involve ATP loss (Shi et al., 2010). My data challenge that interpretation, highlighting that AMPK dysregulation may occur even under energy-replete conditions. Also, a study using TDP-43 Q331K knock-in mice reported altered AMPK-mTOR signaling in spinal cord neurons, implicating AMPK in synaptic degeneration and autophagic stress (Perera et al., 2014). This complements my findings by extending the downstream consequences of AMPK dysregulation to protein turnover and neuronal integrity. Notably, persistent

AMPK—despite ample energy substrates—may prime neurons for chronic catabolism, atrophy, and impaired axonal growth (Perera et al., 2014; Perera & Turner, 2016).

These insights carry translational implications. Because AMPK is a druggable target, modulating its activity in a cell-type–specific manner may help restore metabolic homeostasis without triggering detrimental catabolic cascades in already stressed neurons. While systemic AMPK activators such as metformin have shown mixed results in ALS models, their lack of specificity could blunt their efficacy or even exacerbate pathology in motor neurons. A more targeted approach—perhaps using neuron-selective AMPK inhibitors or allosteric modulators that restore feedback sensitivity—may be required.

Systemic Metabolic Modulation and the ALS Paradox

The metabolic paradox in ALS is as clinically striking as it is counterintuitive: conditions traditionally linked to poor systemic health—T2DM, dyslipidemia, and elevated BMI—are associated with delayed ALS onset and longer survival, while high physical activity, typically seen as health-promoting, correlates with increased ALS risk (Jawaid et al., 2018). This contradiction prompted a core inquiry in this thesis: could systemic metabolic factors modulate the cellular consequences of TDP-43 dysfunction in a way that helps explain this paradox?

To test this, I exposed TDP-43–depleted NSC34 cells to serum from mice fed a high-fat diet or undergoing voluntary exercise. Female high-fat diet serum attenuated glycolytic overactivation and partially normalized mitochondrial respiration in TDP-43 KD NSC34 cells, whereas male exercise serum exacerbated oxidative stress and redox imbalance. These results align with $SOD1^{G93A}$ mice on ketogenic/high-fat diets that show improved motor performance and lifespan—suggesting elevated lipid availability buffers mitochondrial dysfunction (Dupuis et al., 2004; Mariosa et al., 2015). These studies imply that elevated lipid availability may serve as an alternative energy source or mitigate mitochondrial dysfunction during neurodegeneration. By contrast, exercise exacerbates TDP-43 pathology in preclinical models and, in human cohorts, high physical activity correlates with earlier ALS onset, whereas T2DM, obesity, and hyperlipidemia predict slower progression and longer survival(Jawaid et al., 2018; Mariosa et al., 2015). Exposing TDP-43–perturbed NSC34 cells to metabolically distinct sera offers a mechanistic bridge—under controlled KD or mutant expression—between cellular pathology and epidemiological observations. This approach provides a translational window into the ALS paradox.

Notably, female serum—whether from high-fat or exercise cohorts—more strongly suppressed oxidative stress and improved metabolic reprogramming, perhaps reflecting estrogen-mediated

antioxidant pathways or adipokine differences. This aligns with evidence that sex hormones modulate ALS progression and metabolic homeostasis(Tomas et al., 2021; Zamani et al., 2024).

In sum, systemic metabolic state clearly influences TDP-43–associated stress and may underlie the ALS paradox. Manipulating metabolism—via diet, drugs, or lifestyle—could buffer neuronal stress and alter disease course, but personalized, sex-specific approaches will be essential in future trials.

Summary

This study provides compelling evidence that TDP-43 dysfunction profoundly disrupts cellular energy metabolism, with distinct consequences across different cell types and systemic contexts. By integrating findings from in vitro models and metabolic stress analyses, this work advances our understanding of how TDP-43 dysfunction contributes to neurodegeneration in ALS and FTLD. The key findings are summarized as follows and in figure 10.1 below:

1. **TDP-43 Dysfunction and Motor Neuron Metabolism:** TDP-43 perturbation induces a metabolic breakdown in motor neurons, with TDP-43 knockdown triggering a hypermetabolic maladaptation and mutant TDP-43 (M337V) causing subtle yet progressive metabolic alterations. Knockdown-induced metabolic overdrive is marked by enhanced glycolysis, increased mitochondrial respiration, and excessive ATP production, leading to oxidative stress and redox imbalance. On the other hand, mutant TDP-43 elicits a progressive shift in metabolic flux, with upregulation of the pentose phosphate pathway, altered TCA cycle activity, and impaired ATP homeostasis, suggesting a delayed rather than immediate metabolic failure.

2. **Cell-Type-Specific Metabolic Adaptations:** TDP-43 dysfunction elicits distinct metabolic responses in different neural cell types, underscoring motor neurons' heightened metabolic vulnerability in ALS. While NSC34 motor neuron-like cells undergo energy-intensive metabolic reprogramming that drives oxidative stress, BV2 microglia exhibit a predominant glycolytic shift, maintaining mitochondrial function with minimal oxidative damage. In contrast, N2A neuroblastoma cells—representing non-motor neurons—demonstrate a marginal hypometabolic response. These findings reinforce the selective metabolic vulnerability of motor neurons, which may underpin their heightened susceptibility to TDP-43 pathology in ALS.

3. **Metabolic Sensing in TDP-43 Dysfunction:** A central regulator of metabolic homeostasis, AMPK, exhibits dysregulated activation dynamics in response to TDP-43 depletion and mutation. TDP-43 knockdown leads to dysregulated activation of AMPK that is not emanable to ATP abundance, while mutant TDP-43 sustains AMPK activation under stress conditions, potentially leading to chronic metabolic exhaustion. These findings suggest that AMPK dysregulation contributes to energy imbalance in ALS, further exacerbating neuronal vulnerability by disrupting the adaptive capacity to metabolic stress.

4. **Systemic Metabolic Influences on TDP-43 Dysfunction:** Beyond intrinsic cellular adaptations, systemic metabolic states modulate TDP-43-associated metabolic stress in a cell-type- and sex-dependent manner. Serum from high-fat diet (HFD)-fed mice suppressed glycolysis and mitochondrial respiration in TDP-43-deficient neurons, while voluntary exercise (VE)-derived serum had divergent effects depending on sex. These findings suggest that extrinsic metabolic factors influence the trajectory of TDP-43-driven metabolic dysregulation, providing a potential link between metabolic disorders and ALS progression.

Together, these findings highlight a previously underexplored role of metabolic dysregulation in diseases characterized by TDP-43 dysfunction. The convergence of metabolic dysfunction, AMPK dysregulation, and systemic metabolic influences suggests that targeting metabolic pathways may hold therapeutic potential for TDP-43 proteinopathies, such as ALS. These insights provide a foundation for refining disease models and therapeutic strategies, emphasizing the need for cell-type-specific and context-dependent approaches in the study of TDP-43-associated neurodegeneration.

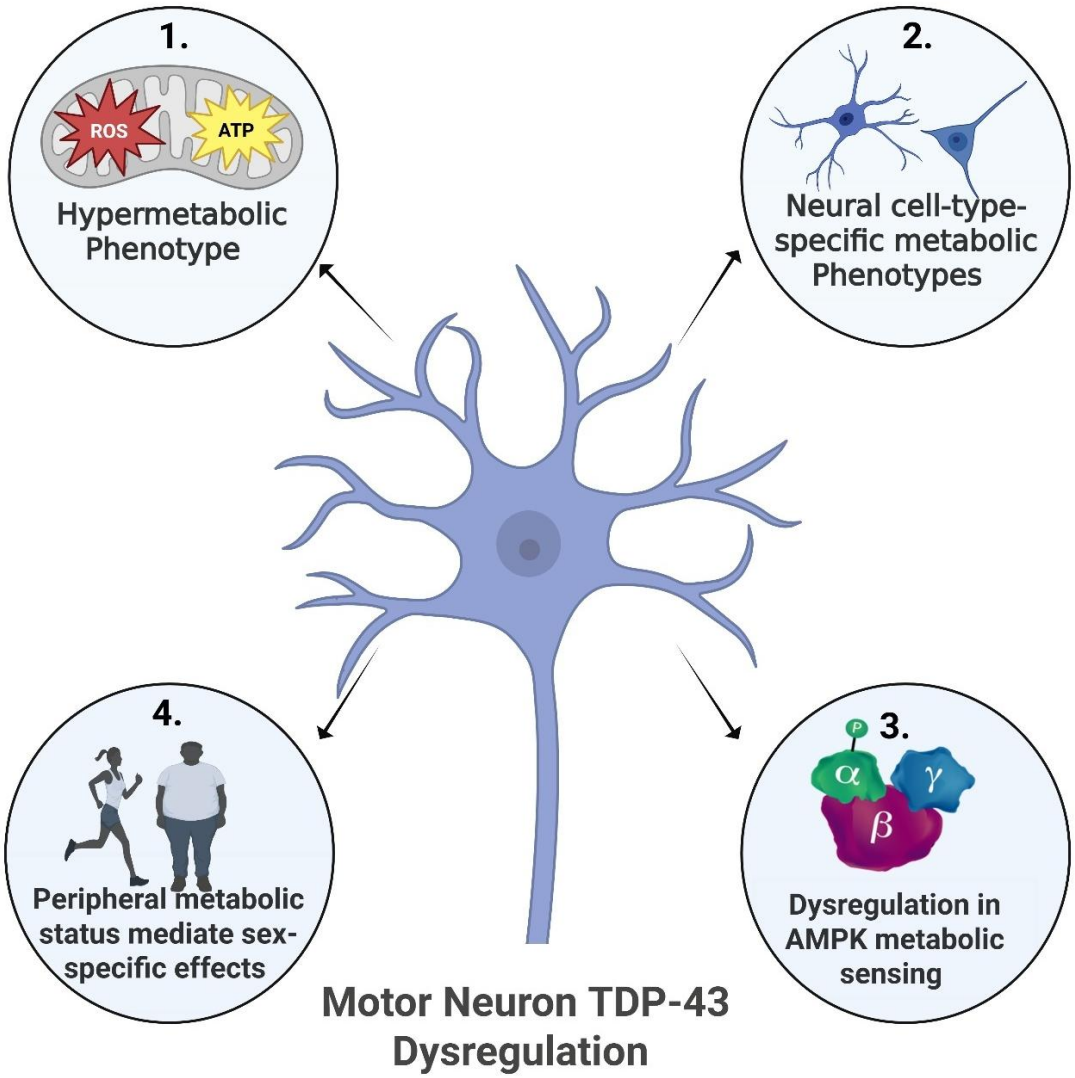

Figure 10.1 | TDP-43 dysregulation in motor neurons drives a composite metabolic signature comprising: (1) hyper-metabolism (↑glucose reliance, ATP from glycolysis + OxPhos, ↑ROS); (2) cell-type divergence—NSC-34 motor neurons undergo robust bioenergetic reprogramming, BV2 microglia shift to glycolysis, N2A neuroblastoma cells attenuate metabolism; (3) maladaptive AMPK signalling (persistent phosphorylation despite energy abundance); (4) sex-dependent systemic modulation—serum from voluntary-exercise or high-fat-diet mice alters TDP-43-deficient motor-neuron metabolism differently in male versus female pools. *Created in* https://BioRender.com

Study Limitations

While this study provides valuable insights into TDP-43-associated metabolic dysfunction, certain limitations must be acknowledged to contextualize the findings and guide future research. These limitations pertain to the use of in vitro models, the temporal nature of metabolic adaptations, sex-dependent metabolic effects, and constraints in patient-derived data.

1. **In Vitro Model Limitations:** The primary cellular models used in this study—NSC34 motor neuron-like cells, BV2 microglia, and N2A neuroblastoma cells—provide critical mechanistic insights into TDP-43-driven metabolic reprogramming. However, in vitro systems inherently lack the complex cellular interactions present in the in vivo nervous system, limiting their ability to fully recapitulate disease pathology. NSC34 motor neuron-like cells, while motor neuron-like, do not fully mimic mature motor neurons, potentially limiting the translation of findings to human ALS. Additionally, the absence of astrocytes, oligodendrocytes, and other glial components precludes an investigation into neuron-glia metabolic crosstalk, a key contributor to neurodegenerative processes in ALS and FTLD.

2. **Time-Dependent Nature of Metabolic Changes:** Metabolic alterations following TDP-43 perturbation exhibit a dynamic and evolving profile, yet this study primarily captures early-stage metabolic adaptations due to practical constraints in long-term in vitro experiments. While knockdown experiments highlight immediate hypermetabolic responses, and mutant TDP-43 expression reveals progressive metabolic reprogramming, the long-term consequences of these changes—particularly how they contribute to irreversible neuronal damage—remain unresolved. ALS is a progressive disease, and the time-dependent nature of metabolic adaptations warrants future studies employing longitudinal analyses or chronic TDP-43 perturbation models to assess cumulative metabolic stress and its role in disease progression.

3. **Sex-Specific Metabolic Effects:** This study identifies sex-dependent metabolic responses to systemic metabolic influences, particularly in the regulation of glycolysis and mitochondrial function following TDP-43 depletion. However, the underlying molecular mechanisms driving these sex differences remain unresolved. While findings suggest that hormonal, genetic, or immune-mediated factors may influence metabolic resilience in ALS, further investigations are needed to identify sex-specific metabolic regulators and determine whether they impact ALS progression or therapeutic responses. Additionally, the use of male and female mouse serum to model systemic metabolic effects does not fully capture human sex differences,

necessitating future studies incorporating patient-derived serum or sex-stratified transcriptomic analyses.

4. **Constraints in Patient-Derived Data (Only Two ALS Samples):** A key limitation of the transcriptomic comparisons in Part VII is the small sample size of ALS patient-derived RNA-seq data (n = 2). While FTLD transcriptomic analyses included five patient samples, the limited representation of ALS cases reduces statistical power and generalizability, potentially obscuring disease-specific transcriptional alterations. Furthermore, the heterogeneity of ALS and FTLD cases—including differences in disease stage, genetic background, and clinical presentation—introduces variability that cannot be fully accounted for in small datasets. Future studies should incorporate larger, well-stratified patient cohorts and integrate single-cell transcriptomic approaches to dissect cell-type-specific metabolic changes in ALS and FTLD more comprehensively.

Future Research Directions

Future research should focus on the following areas:

- **In Vivo and Advanced Model Validation of Findings:** While in vitro models provide mechanistic insights into TDP-43-associated metabolic dysfunction, their limitations necessitate in vivo validation to confirm the relevance of these findings within a physiological context. Future studies should employ TDP-43 transgenic or knockout animal models to assess metabolic alterations in a system that incorporates neuronal-glial interactions, systemic metabolic influences, and disease progression dynamics. Additionally, patient-derived models, such as induced pluripotent stem cell (iPSC)-derived motor neurons, offer a valuable platform for studying patient-specific metabolic dysregulation and therapeutic responses. Expanding to other neural cell types, including astrocytes, oligodendrocytes, and microglia, will provide a more comprehensive understanding of cell-type-specific vulnerabilities and their contribution to ALS and FTLD pathogenesis. Furthermore, organoid models, which more closely mimic the three-dimensional architecture of the brain and cellular interactions, could serve as a powerful tool for dissecting metabolic crosstalk in TDP-43 proteinopathies and for preclinical drug screening aimed at restoring metabolic balance in ALS and FTLD.
- **Metabolic interventions as potential therapeutic targets:** Investigating motor neuron-targeted metabolic therapies for ALS, particularly during the prodromal or presymptomatic stages, by exploring pharmacological modulation of AMPK, mitochondrial enhancers, and

dietary interventions (e.g., ketogenic or high-fat diets) to counteract early metabolic dysregulation and support neuronal resilience. In vivo validation of TDP-43 metabolic dysregulation: Employing TDP-43 transgenic/knockout models, longitudinal metabolic assessments, and multi-omics approaches to assess disease progression and potential therapeutic windows.

- **Expanding ALS/FTLD Transcriptomic Datasets for Precision Insights:** To enhance the robustness and translational value of transcriptomic analyses in ALS and FTLD, future research should prioritize increasing patient sample sizes, ensuring sufficient representation across diverse clinical subtypes and disease stages. Integrating clinical and metabolic profiling with transcriptomic data will help uncover potential correlations between metabolic dysfunction and disease progression, refining our understanding of patient-specific molecular vulnerabilities. Additionally, leveraging single-cell RNA sequencing (scRNA-seq) will allow for a more granular investigation of cell-type-specific transcriptomic changes, particularly in motor neurons, astrocytes, microglia, and oligodendrocytes. These efforts will improve the resolution of disease-specific molecular pathways, identify novel biomarkers, and facilitate the development of personalized therapeutic strategies tailored to distinct ALS and FTLD subpopulations..

- **Neuron-Glia Metabolic Interactions in TDP-43-Associated Neurodegeneration:** Future research should investigate the metabolic contributions of astrocytes, oligodendrocytes, and their interactions with motor neurons in the context of TDP-43 dysfunction. Astrocytes play a critical role in neuronal energy homeostasis by regulating glucose uptake, lactate shuttling, and redox balance, yet their metabolic response to TDP-43 pathology remains poorly understood. Similarly, oligodendrocytes are essential for lipid metabolism and axonal support, and disruptions in their metabolic function may contribute to ALS-related white matter degeneration. Understanding neuron-glia metabolic crosstalk—including how astrocytes buffer metabolic stress and how oligodendrocytes sustain neuronal energy supply—could provide key insights into the selective vulnerability of motor neurons in ALS. Future studies should explore how TDP-43 dysfunction alters astrocytic and oligodendrocyte metabolism, and whether targeting these pathways could offer neuroprotective therapeutic strategies.

- **Gut Microbiome and Metabolic Dysregulation in ALS and FTLD:** Given the established link between metabolic disorders and gut microbiome alterations, future research should

investigate how TDP-43 dysfunction influences gut microbiota composition and gut-brain axis communication in ALS and FTLD. The gut microbiome plays a crucial role in regulating systemic metabolism, immune function, and neuroinflammation, all of which are implicated in ALS pathology. Dysbiosis-induced metabolic imbalances may exacerbate neurodegeneration by altering short-chain fatty acid production, gut barrier integrity, and peripheral inflammation. Future studies should focus on longitudinal gut microbiome profiling in ALS and FTLD patients, assessing microbial shifts in relation to disease progression and metabolic dysfunction. Additionally, prebiotic, probiotic, or microbiome-targeted therapies should be explored as potential metabolic interventions to restore gut homeostasis and mitigate neuronal vulnerability in ALS. Understanding how gut-derived metabolites influence neuronal energy metabolism and TDP-43-driven pathology could open new avenues for therapeutic intervention.

Conclusion

What began as an epidemiological curiosity evolved into a scientific inquiry that uncovered complex links between TDP-43 dysfunction and cellular energy metabolism. This work set out to explore a paradox that challenges conventional understanding—that metabolic conditions typically viewed as detrimental may, under certain circumstances, offer resilience against ALS. Through a series of carefully controlled experiments, this thesis demonstrates that TDP-43 dysfunction—whether through loss-of-function or mutation—is a key driver of maladaptive metabolic reprogramming in motor neurons, marked by energy imbalance, impaired metabolic sensing, and oxidative vulnerability. Along the way, it became evident that this vulnerability is not uniform across cell types, nor immune to external influence—systemic metabolic states and sex-specific factors can significantly shape cellular responses. Collectively, these findings position metabolic dysfunction as a central feature of TDP-43 proteinopathy and reinforce the rationale for targeting metabolic pathways as potential therapeutic strategies.

Importantly, these insights offer a plausible biological lens through which to interpret the paradox outlined in the Preface. If TDP-43 dysfunction induces metabolic reprogramming in motor neurons, and if external metabolic states such as diabetes modulate this vulnerability, then the delayed ALS progression observed in metabolically compromised patients may reflect an adaptive shift in neuronal energy management. Conversely, the hypermetabolic state often found in physically fit individuals could exacerbate underlying vulnerabilities.

While these connections require further experimental validation, this work represents a foundational step toward understanding why two patients—alike in diagnosis but different in metabolic profile—may follow such divergent clinical trajectories. Future research should prioritize in vivo validation, patient-specific modeling, and mechanistic studies to more precisely define the role of TDP-43-driven metabolic dysfunction in ALS progression and to inform the development of targeted interventions.

References

1. Ahmed, R. M. (2021). Metabolism in frontotemporal dementia. Alzheimer's & Dementia, 17(S6), S492–S500.. https://doi.org/10.1002/alz.055309
2. Ahmed, R. M., Landin-Romero, R., Liang, C. T., Keogh, J. M., Henning, E., Strikwerda-Brown, C., Devenney, E. M., Hodges, J. R., Kiernan, M. C., Farooqi, I. S., & Piguet, O. (2019). Neural networks associated with body composition in frontotemporal dementia. Annals of Clinical and Translational Neurology, 6(9) 1–12. https://doi.org/10.1002/acn3.50869
3. Ahmed, R. M., MacMillan, M., Bartley, L., Halliday, G. M., Kiernan, M. C., Hodges, J. R., & Piguet, O. (2014). Systemic metabolism in frontotemporal dementia. Neurology, 83(20), 1812–1818. https://doi.org/10.1212/WNL.0000000000000993
4. Ahmed, R. M., Mioshi, E., Caga, J., Shibata, M., Zoing, M., Bartley, L., Piguet, O., Hodges, J. R., & Kiernan, M. C. (2014). Body mass index delineates ALS from FTD: implications for metabolic health. Journal of Neurology, 261(9), 1819–1826. https://doi.org/10.1007/s00415-014-7416-6
5. Appleby-Mallinder, C., Schaber, E., Kirby, J., Shaw, P. J., Cooper-Knock, J., Heath, P. R., & Highley, J. R. (2021). TDP43 proteinopathy is associated with aberrant DNA methylation in human amyotrophic lateral sclerosis. Neuropathology and Applied Neurobiology, 47(1), 61–72. https://doi.org/10.1111/nan.12625
6. Atkinson, R. A. K., Collins, J. M., Sreedharan, J., King, A. E., & Fernandez-Martos, C. M. (2024). Alterations to metabolic hormones in amyotrophic lateral sclerosis and frontotemporal dementia postmortem human tissue. Journal of Neuropathology & Experimental Neurology, 83(11), 907–916. https://doi.org/10.1093/JNEN/NLAE054
7. Bouteloup, C., Desport, J. C., Clavelou, P., Guy, N., Derumeaux-Burel, H., Ferrier, A., & Couratier, P. (2009). Hypermetabolism in ALS patients: An early and persistent phenomenon. Journal of Neurology, 256(8), 1236–1242. https://doi.org/10.1007/S00415-009-5100-Z/TABLES/3
8. Buratti, E. (2018). TDP-43 post-translational modifications in health and disease. Expert Opinion on Therapeutic Targets, 22(3), 279–293. https://doi.org/10.1080/14728222.2018.1439923
9. Carey, J. L., & Guo, L. (2022). Liquid-Liquid Phase Separation of TDP-43 and FUS in Physiology and Pathology of Neurodegenerative Diseases. Frontiers in Molecular Biosciences, 9, 826719. https://doi.org/10.3389/FMOLB.2022.826719/BIBTEX
10. Chalitsios, C. V., Ley, H., Gao, J., Turner, M. R., & Thompson, A. G. (2024). Apolipoproteins, lipids, lipid-lowering drugs and risk of amyotrophic lateral sclerosis and frontotemporal dementia: a meta-analysis and Mendelian randomisation study. Journal of Neurology, 271(10), 3456–3468. https://doi.org/10.1007/S00415-024-12665-X
11. Chou, C.-C., Zhang, Y., Umoh, M. E., Vaughan, S. W., Lorenzini, I., Liu, F., Sayegh, M., Donlin-Asp, P. G., Chen, Y. H., Duong, D. M., Seyfried, N. T., Powers, M. A., Kukar, T., Hales, C. M., Gearing, M., Cairns, N. J., Boylan, K. B., Dickson, D. W., Rademakers, R., … Rossoll, W. (2018). TDP-43 pathology disrupts nuclear pore complexes and nucleocytoplasmic transport in ALS/FTD. Nature Neuroscience 2017, 21(2), 228–239. https://doi.org/10.1038/s41593-017-0047-3
12. Conicella, A. E., Dignon, G. L., Zerze, G. H., Schmidt, H. B., D'Ordine, A. M., Kim, Y. C., Rohatgi, R., Ayala, Y. M., Mittal, J., & Fawzi, N. L. (2020). TDP-43 α-helical structure tunes liquid–liquid phase separation and function. Proceedings of the National Academy of Sciences of the United States of America, 117(11), 5881–5892. https://doi.org/10.1073/pnas.1912055117
13. Dardiotis, E., Siokas, V., Sokratous, M., Tsouris, Z., Aloizou, A. M., Florou, D., Dastamani, M., Mentis, A. F. A., & Brotis, A. G. (2018). Body mass index and survival from amyotrophic lateral sclerosis: A meta-analysis. In Neurology: Clinical Practice *8*(5), 412–419. https://doi.org/10.1212/CPJ.0000000000000521
14. De Boer, E. M. J., Orie, V. K., Williams, T., Baker, M. R., De Oliveira, H. M., Polvikoski, T., Silsby, M., Menon, P., Van Den Bos, M., Halliday, G. M., Van Den Berg, L. H., Van Den Bosch, L., Van Damme, P., Kiernan, M., Van Es, M. A., & Vucic, S. (2021). TDP-43 proteinopathies: A new wave of neurodegenerative diseases.

In Journal of Neurology, Neurosurgery and Psychiatry (Vol. 92, Issue 1, pp. 86–95). BMJ Publishing Group. https://doi.org/10.1136/jnnp-2020-322983

15. Dewey, C. M., Cenik, B., Sephton, C. F., Johnson, B. A., Herz, J., & Yu, G. (2012). TDP-43 Aggregation In Neurodegeneration: Are Stress Granules The Key? Brain Research, 1462, 16. https://doi.org/10.1016/J.BRAINRES.2012.02.032
16. Di Rita, A., & Strappazzon, F. (2020). Neuroblastoma and oxidative stress: From pathogenesis to in vitro models of neurodegeneration. Oxidative Stress and Dietary Antioxidants in Neurological Diseases, 67–79. https://doi.org/10.1016/B978-0-12-817780-8.00005-0
17. Dormann, D., & Haass, C. (2011a). TDP-43 and FUS: A nuclear affair. In Trends in Neurosciences, 34(7), 339–348. Elsevier Current Trends. https://doi.org/10.1016/j.tins.2011.05.002
18. D'Ovidio, F., D'Errico, A., Carnà, P., Calvo, A., Costa, G., & Chiò, A. (2018). The role of pre-morbid diabetes on developing amyotrophic lateral sclerosis. European Journal of Neurology, 25(1), 164–170. https://doi.org/10.1111/ene.13465
19. Dupuis, L., Corcia, P., Fergani, A., Gonzalez De Aguilar, J. L., Bonnefont-Rousselot, D., Bittar, R., Seilhean, D., Hauw, J. J., Lacomblez, L., Loeffler, J. P., & Meininger, V. (2008). Dyslipidemia is a protective factor in amyotrophic lateral sclerosis symbol. Neurology, 70(13), 1004–1009. https://doi.org/10.1212/01.wnl.0000285080.70324.27
20. El-Wahsh, S., Finger, E. C., Piguet, O., Mok, V., Rohrer, J. D., Kiernan, M. C., & Ahmed, R. M. (2021). Predictors of survival in frontotemporal lobar degeneration syndromes. In Journal of Neurology, Neurosurgery and Psychiatry *92*(4), 395–402. https://doi.org/10.1136/jnnp-2020-324349
21. Fang, M., Deibler, S. K., Nana, A. L., Vatsavayai, S. C., Banday, S., Zhou, Y., Almeida, S., Weiss, A., Brown, R. H., Seeley, W. W., Gao, F. B., & Green, M. R. (2023). Loss of TDP-43 function contributes to genomic instability in amyotrophic lateral sclerosis. Frontiers in Neuroscience, 17, 1251228. https://doi.org/10.3389/FNINS.2023.1251228/BIBTEX
22. Felemban, R. A., François-Moutal, L., Sayegh, M., Perez-Miller, S., Gokhale, V., Zarnescu, D. C., & Khanna, M. (2019). Remodeling the interactions between TDP43 and RNA for development of therapeutics for ALS. The FASEB Journal, 33(S1), 12-33. https://doi.org/10.1096/fasebj.2019.33.1_supplement.670.1
23. Feneberg, E., Gordon, D., Thompson, A. G., Finelli, M. J., Dafinca, R., Candalija, A., Charles, P. D., Mäger, I., Wood, M. J., Fischer, R., Kessler, B. M., Gray, E., Turner, M. R., & Talbot, K. (2020). An ALS-linked mutation in TDP-43 disrupts normal protein interactions in the motor neuron response to oxidative stress. Neurobiology of Disease, 144, 105-150. https://doi.org/10.1016/J.NBD.2020.105050
24. Gao, J., Wang, L., Huntley, M. L., Perry, G., & Wang, X. (2018). Pathomechanisms of TDP-43 in neurodegeneration. In Journal of Neurochemistry, 146(1), 7–20. Blackwell Publishing Ltd. https://doi.org/10.1111/jnc.14327
25. Garrett, L. R., & Niccoli, T. (2022). Frontotemporal Dementia and Glucose Metabolism. In Frontiers in Neuroscience 16(1), 109-121. https://doi.org/10.3389/fnins.2022.812222
26. Godoy-Corchuelo, J. M., Fernández-Beltrán, L. C., Ali, Z., Gil-Moreno, M. J., López-Carbonero, J. I., Guerrero-Sola, A., Larrad-Sainz, A., Matias-Guiu, J., Matias-Guiu, J. A., Cunningham, T. J., & Corrochano, S. (2022). Lipid Metabolic Alterations in the ALS–FTD Spectrum of Disorders. In Biomedicines, 10(5). MDPI. https://doi.org/10.3390/biomedicines10051105
27. Goutman, S. A., Boss, J., Iyer, G., Habra, H., Savelieff, M. G., Karnovsky, A., Mukherjee, B., & Feldman, E. L. (2023). Body mass index associates with amyotrophic lateral sclerosis survival and metabolomic profiles. Muscle and Nerve, 67(3), 208–216. https://doi.org/10.1002/mus.27744
28. Grossman, M., Seeley, W. W., Boxer, A. L., Hillis, A. E., Knopman, D. S., Ljubenov, P. A., Miller, B., Piguet, O., Rademakers, R., Whitwell, J. L., Zetterberg, H., & van Swieten, J. C. (2023). Frontotemporal lobar degeneration. Nature Reviews Disease Primers, 9(1), 78-86. https://doi.org/10.1038/s41572-023-00447-0
29. Guenther, E. L., Cao, Q., Trinh, H., Lu, J., Sawaya, M. R., Cascio, D., Boyer, D. R., Rodriguez, J. A., Hughes, M. P., & Eisenberg, D. S. (2018). Atomic structures of TDP-43 LCD segments and insights into reversible or pathogenic aggregation. Nature Structural and Molecular Biology, 25(6), 122-128. https://doi.org/10.1038/s41594-018-0064-2

30. Harrison, A. F., & Shorter, J. (2017). RNA-binding proteins with prion-like domains in health and disease. In Biochemical Journal *474*(8), 1417–1438. https://doi.org/10.1042/BCJ20160499
31. Hayes, L. R., & Kalab, P. (2022). Emerging Therapies and Novel Targets for TDP-43 Proteinopathy in ALS/FTD. Neurotherapeutics, 19(4), 1061–1084. https://doi.org/10.1007/S13311-022-01260-5
32. Huie, E. Z., Escudero, A., Saito, N., Harvey, D., Nguyen, M.-L., Lucot, K. L., LaGrande, J., Mungas, D., DeCarli, C., Lamar, M., Schneider, J. A., Kapasi, A., Rissman, R. A., Teich, A. F., & Dugger, B. N. (2023). TDP-43 Pathology in the Setting of Intermediate and High Alzheimer's Disease Neuropathologic Changes: A Preliminary Evaluation Across Ethnoracial Groups. Journal of Alzheimer's Disease, 1–11. https://doi.org/10.3233/JAD-220558
33. Huisman, M. H. B., Seelen, M., De Jong, S. W., Dorresteijn, K. R. I. S., Van Doormaal, P. T. C., Van Der Kooi, A. J., De Visser, M., Schelhaas, H. J., Van Den Berg, L. H., & Veldink, J. H. (2013). Lifetime physical activity and the risk of amyotrophic lateral sclerosis. Journal of Neurology, Neurosurgery and Psychiatry, 84(9). https://doi.org/10.1136/jnnp-2012-304724
34. Ingre, C., Chen, L., Zhan, Y., Termorshuizen, J., Yin, L., & Fang, F. (2020). Lipids, apolipoproteins, and prognosis of amyotrophic lateral sclerosis. Neurology, 94(17), E1835–E1844. https://doi.org/10.1212/WNL.0000000000009322
35. Jawaid, A., Khan, R., Polymenidou, M., & Schulz, P. E. (2018a). Disease-modifying effects of metabolic perturbations in ALS/FTLD. In Molecular Neurodegeneration (Vol. 13, Issue 1). BioMed Central Ltd. https://doi.org/10.1186/s13024-018-0294-0
36. Jawaid, A., Salamone, A. R., Strutt, A. M., Murthy, S. B., Wheaton, M., McDowell, E. J., Simpson, E., Appel, S. H., York, M. K., & Schulz, P. E. (2010). ALS disease onset may occur later in patients with pre-morbid diabetes mellitus. European Journal of Neurology, 17(5), 733–739. https://doi.org/10.1111/j.1468-1331.2009.02923.x
37. Jésus, P., Fayemendy, P., Nicol, M., Lautrette, G., Sourisseau, H., Preux, P. M., Desport, J. C., Marin, B., & Couratier, P. (2018). Hypermetabolism is a deleterious prognostic factor in patients with amyotrophic lateral sclerosis. European Journal of Neurology, 25(1), 97–104. https://doi.org/10.1111/ENE.13468
38. Jiang, L., & Ngo, S. T. (2022a). Altered TDP-43 Structure and Function: Key Insights into Aberrant RNA, Mitochondrial, and Cellular and Systemic Metabolism in Amyotrophic Lateral Sclerosis. In Metabolites, 12 (8), 34-41. https://doi.org/10.3390/metabo12080709
39. Julian, T. H., Glascow, N., Barry, A. D. F., Moll, T., Harvey, C., Klimentidis, Y. C., Newell, M., Zhang, S., Snyder, M. P., Cooper-Knock, J., & Shaw, P. J. (2021). Physical exercise is a risk factor for amyotrophic lateral sclerosis: Convergent evidence from Mendelian randomisation, transcriptomics and risk genotypes. EBioMedicine, 68(1), 54-66. https://doi.org/10.1016/J.EBIOM.2021.103397/ATTACHMENT/B472A4FF-4036-40BC-B63E-EAEDE747AA0B/MMC2.XLSX
40. Kakihana, T., Takahashi, M., Katsuragi, Y., Yamashita, S. I., Sango, J., Kanki, T., Onodera, O., & Fujii, M. (2021). The optineurin/TIA1 pathway inhibits aberrant stress granule formation and reduces ubiquitinated TDP-43. IScience, 24(7), 23-29. https://doi.org/10.1016/J.ISCI.2021.102733
41. Kalkonde, Y. V., Jawaid, A., Qureshi, S. U., Shirani, P., Wheaton, M., Pinto-Patarroyo, G. P., & Schulz, P. E. (2012). Medical and environmental risk factors associated with frontotemporal dementia: A case-control study in a veteran population. Alzheimer's and Dementia, 8(3), 204–210. https://doi.org/10.1016/j.jalz.2011.03.011
42. Kansal, K., Mareddy, M., Sloane, K. L., Minc, A. A., Rabins, P. V., McGready, J. B., & Onyike, C. U. (2016). Survival in Frontotemporal Dementia Phenotypes: A Meta-Analysis. In Dementia and Geriatric Cognitive Disorders *41*(1–2), 15–28. https://doi.org/10.1159/000443205
43. Keating, S. S., San Gil, R., Swanson, M. E. V., Scotter, E. L., & Walker, A. K. (2022). TDP-43 pathology: from noxious assembly to therapeutic removal. Progress in Neurobiology, January, 102229. https://doi.org/10.1016/j.pneurobio.2022.102229
44. Khalfallah, Y., Kuta, R., Grasmuck, C., Prat, A., Durham, H. D., & Vande Velde, C. (2018). TDP-43 regulation of stress granule dynamics in neurodegenerative disease-relevant cell types. Scientific Reports 2018 8:1, 8(1), 1–13. https://doi.org/10.1038/s41598-018-25767-0

45. Koza, P., Beroun, A., Konopka, A., Górkiewicz, T., Bijoch, L., Torres, J. C., Bulska, E., Knapska, E., Kaczmarek, L., & Konopka, W. (2019). Neuronal TDP-43 depletion affects activity-dependent plasticity. Neurobiology of Disease, 130, 104499. https://doi.org/10.1016/j.nbd.2019.104499
46. Kumar, S. T., Nazarov, S., Porta, S., Maharjan, N., Cendrowska, U., Kabani, M., Finamore, F., Xu, Y., Lee, V. M. Y., & Lashuel, H. A. (2023). Seeding the aggregation of TDP-43 requires post-fibrillization proteolytic cleavage. Nature Neuroscience 2023 26:6, 26(6), 983–996. https://doi.org/10.1038/s41593-023-01341-4
47. LePage, K. T., Dickey, R. W., Gerwick, W. H., Jester, E. L., & Murray, T. F. (2005). On the use of neuro-2a neuroblastoma cells versus intact neurons in primary culture for neurotoxicity studies. Critical Reviews in Neurobiology, 17(1), 27–50. https://doi.org/10.1615/CRITREVNEUROBIOL.V17.I1.20
48. Lepiarz-Raba, I., Gbadamosi, I., Florea, R., Paolicelli, R. C., & Jawaid, A. (2023). Metabolic regulation of microglial phagocytosis: Implications for Alzheimer's disease therapeutics. In Translational Neurodegeneration (Vol. 12, Issue 1), 1-13. https://doi.org/10.1186/s40035-023-00382-w
49. Li, Q., Yokoshi, M., Okada, H., & Kawahara, Y. (2015). The cleavage pattern of TDP-43 determines its rate of clearance and cytotoxicity. Nature Communications 2015 6:1, 6(1), 1–12. https://doi.org/10.1038/ncomms7183
50. Lim, M. A., Selak, M. A., Xiang, Z., Krainc, D., Neve, R. L., Kraemer, B. C., Watts, J. L., & Kalb, R. G. (2012). Reduced activity of AMP-activated protein kinase protects against genetic models of motor neuron disease. Journal of Neuroscience, 32(3), 1123–1141. https://doi.org/10.1523/JNEUROSCI.6554-10.2012
51. Liscic, R. M., Grinberg, L. T., Zidar, J., Gitcho, M. A., & Cairns, N. J. (2008). ALS and FTLD: Two faces of TDP-43 proteinopathy. In European Journal of Neurology (Vol. 15, Issue 8, pp. 772–780). John Wiley & Sons, Ltd. https://doi.org/10.1111/j.1468-1331.2008.02195.x
52. Loganathan, S., Wilson, B. A., Carey, S. B., Manzo, E., Joardar, A., Ugur, B., & Zarnescu, D. C. (2022). TDP-43 Proteinopathy Causes Broad Metabolic Alterations including TCA Cycle Intermediates and Dopamine Levels in Drosophila Models of ALS. Metabolites, 12(2), 101. https://doi.org/10.3390/METABO12020101/S1
53. Longstreth, W. T., McGuire, V., Koepsell, T. D., Wang, Y., & van Belle, G. (1998). Risk of Amyotrophic Lateral Sclerosis and History of Physical Activity. Archives of Neurology, 55(2), 17-25. https://doi.org/10.1001/archneur.55.2.201
54. Manzo, E., Lorenzini, I., Barrameda, D., O'Conner, A. G., Barrows, J. M., Starr, A., Kovalik, T., Rabichow, B. E., Lehmkuhl, E. M., Shreiner, D. D., Joardar, A., Liévens, J. C., Bowser, R., Sattler, R., & Zarnescu, D. C. (2019). Glycolysis upregulation is neuroprotective as a compensatory mechanism in ALS. ELife, 8. https://doi.org/10.7554/ELIFE.45114
55. Mariosa, D., Beard, J. D., Umbach, D. M., Bellocco, R., Keller, J., Peters, T. L., Allen, K. D., Ye, W., Sandler, D. P., Schmidt, S., Fang, F., & Kamel, F. (2017). Body mass index and amyotrophic lateral sclerosis: A study of US military veterans. American Journal of Epidemiology, 185(5), 81-88. https://doi.org/10.1093/aje/kww140
56. Mariosa, D., Kamel, F., Bellocco, R., Ye, W., & Fang, F. (2015). Association between diabetes and amyotrophic lateral sclerosis in Sweden. European Journal of Neurology : The Official Journal of the European Federation of Neurological Societies, 22(11), 1436. https://doi.org/10.1111/ENE.12632
57. Maugeri, G., & D'Agata, V. (2020). Effects of physical activity on amyotrophic lateral sclerosis. In Journal of Functional Morphology and Kinesiology (Vol. 5, Issue 2), 24-29. MDPI Multidisciplinary Digital Publishing Institute. https://doi.org/10.3390/jfmk5020029
58. McCrate, M. E., & Kaspar, B. K. (2008). Physical activity and neuroprotection in amyotrophic lateral sclerosis. In NeuroMolecular Medicine (Vol. 10, Issue 2, pp. 108–117). https://doi.org/10.1007/s12017-008-8030-5
59. Melamed, Z., López-Erauskin, J., Baughn, M. W., Zhang, O., Drenner, K., Sun, Y., Freyermuth, F., McMahon, M. A., Beccari, M. S., Artates, J. W., Ohkubo, T., Rodriguez, M., Lin, N., Wu, D., Bennett, C. F., Rigo, F., Da Cruz, S., Ravits, J., Lagier-Tourenne, C., & Cleveland, D. W. (2019). Premature polyadenylation-mediated

loss of stathmin-2 is a hallmark of TDP-43-dependent neurodegeneration. Nature Neuroscience 2019 22:2, 22(2), 180–190. https://doi.org/10.1038/s41593-018-0293-z
60. Mitra, J., & Hegde, M. L. (2019). A Commentary on TDP-43 and DNA Damage Response in Amyotrophic Lateral Sclerosis. Journal of Experimental Neuroscience, 13, 1179069519880166. https://doi.org/10.1177/1179069519880166
61. Mompeán, M., Romano, V., Pantoja-Uceda, D., Stuani, C., Baralle, F. E., Buratti, E., & Laurents, D. V. (2016a). The TDP-43 N-terminal domain structure at high resolution. The FEBS Journal, 283(7), 34-44. https://doi.org/10.1111/febs.13651
62. Moujalled, D., Grubman, A., Acevedo, K., Yang, S., Ke, Y. D., Moujalled, D. M., Duncan, C., Caragounis, A., Perera, N. D., Turner, B. J., Prudencio, M., Petrucelli, L., Blair, I., Ittner, L. M., Crouch, P. J., Liddell, J. R., & White, A. R. (2017). TDP-43 mutations causing amyotrophic lateral sclerosis are associated with altered expression of RNA-binding protein hnRNP K and affect the Nrf2 antioxidant pathway. Human Molecular Genetics, 26(9), 1732–1746. https://doi.org/10.1093/hmg/ddx093
63. Nemoto, M., Nemoto, K., Sasai, H., Higashi, S., Ota, M., & Arai, T. (2024). Long -term multimodal exercise intervention for patients with frontotemporal lobar degeneration: Feasibility and preliminary outcomes. Dementia and Geriatric Cognitive Disorders Extra, *14*(1), 35–58. https://doi.org/10.1159/000542994
64. Neumann, M., Kwong, L. K., Lee, E. B., Kremmer, E., Flatley, A., Xu, Y., Forman, M. S., Troost, D., Kretzschmar, H. A., Trojanowski, J. Q., & Lee, V. M. Y. (2009). Phosphorylation of S409/410 of TDP-43 is a consistent feature in all sporadic and familial forms of TDP-43 proteinopathies. Acta Neuropathologica, 117(2), 137-151. https://doi.org/10.1007/S00401-008-0477-9
65. Nijssen, J., Comley, L. H., & Hedlund, E. (2017). Motor neuron vulnerability and resistance in amyotrophic lateral sclerosis. Acta Neuropathologica 2017 133:6, 133(6), 863–885. https://doi.org/10.1007/S00401-017-1708-8
66. Ning, P., Yang, B., Li, S., Mu, X., Shen, Q., Hu, F., Tang, Y., Yang, X., & Xu, Y. (2019). Systematic review of the prognostic role of body mass index in amyotrophic lateral sclerosis. Amyotrophic Lateral Sclerosis and Frontotemporal Degeneration, 20(5–6), 356–367. https://doi.org/10.1080/21678421.2019.1587631
67. O'Reilly, É. J., Wang, H., Weisskopf, M. G., Fitzgerald, K. C., Falcone, G., McCullough, M. L., Thun, M., Park, Y., Kolonel, L. N., & Ascherio, A. (2013). Premorbid body mass index and risk of amyotrophic lateral sclerosis. Amyotrophic Lateral Sclerosis and Frontotemporal Degeneration, 14(3), 205–211. https://doi.org/10.3109/21678421.2012.735240
68. Paganoni, S., Deng, J., Jaffa, M., Cudkowicz, M. E., & Wills, A. M. (2011). BODY MASS INDEX, NOT DYSLIPIDEMIA, IS AN INDEPENDENT PREDICTOR OF SURVIVAL IN AMYOTROPHIC LATERAL SCLEROSIS. Muscle & Nerve, 44(1), 14-20. https://doi.org/10.1002/MUS.22114
69. Paolicelli, R., Jawaid, A., Henstridge, C. M., Spires-Jones, T., Schulz, P. E., Paolicelli, R. C., Valeri, A., Merlini, M., Robinson, J. L., Lee, E. B., Rose, J., Appel, S., M-Y Lee, V., Trojanowski, J. Q., & Rajendran, L. (2017). TDP-43 Depletion in Microglia Promotes Amyloid Clearance but Also Induces Synapse Loss Article TDP-43 Depletion in Microglia Promotes Amyloid Clearance but Also Induces Synapse Loss. Neuron, 95, 297-308.e6. https://doi.org/10.1016/j.neuron.2017.05.037
70. Perera, N. D., Sheean, R. K., Scott, J. W., Kemp, B. E., Horne, M. K., & Turner, B. J. (2014). Mutant TDP-43 Deregulates AMPK Activation by PP2A in ALS Models. PLOS ONE, 9(3), e90449. https://doi.org/10.1371/JOURNAL.PONE.0090449
71. Perera, N. D., & Turner, B. J. (2016). AMPK Signalling and Defective Energy Metabolism in Amyotrophic Lateral Sclerosis. Neurochemical Research, 41(3), 544–553. https://doi.org/10.1007/S11064-015-1665-3,
72. Rafiq, M. K., Lee, E., Bradburn, M., Mcdermott, C. J., & Shaw, P. J. (2015). Effect of lipid profile on prognosis in the patients with amyotrophic lateral sclerosis: Insights from the olesoxime clinical trial. Amyotrophic Lateral Sclerosis & Frontotemporal Degeneration, 16(7–8), 478–484. https://doi.org/10.3109/21678421.2015.1062517

73. Ryan, S., Rollinson, S., Hobbs, E., & Pickering-Brown, S. (2022). C9orf72 dipeptides disrupt the nucleocytoplasmic transport machinery and cause TDP-43 mislocalisation to the cytoplasm. Scientific Reports, 12(1), 47-59. https://doi.org/10.1038/S41598-022-08724-W
74. Schweingruber, C., Nijssen, J., Mechtersheimer, J., Reber, S., Lebœuf, M., O'Brien, N. L., Mei, I., Hedges, E., Keuper, M., Benitez, J. A., Radoi, V., Jastroch, M., Ruepp, M.-D., & Hedlund, E. (2025). Single-cell RNA-sequencing reveals early mitochondrial dysfunction unique to motor neurons shared across FUS- and TARDBP-ALS. Nature Communications 2025 16:1, 16(1), 1–22. https://doi.org/10.1038/s41467-025-59679-1
75. Scotter, E. L., Chen, H. J., & Shaw, C. E. (2015). TDP-43 Proteinopathy and ALS: Insights into Disease Mechanisms and Therapeutic Targets. Neurotherapeutics, 12(2), 352-355. https://doi.org/10.1007/S13311-015-0338-X
76. Sharma, K., Stockert, F., Shenoy, J., Berbon, M., Abdul-Shukkoor, M. B., Habenstein, B., Loquet, A., Schmidt, M., & Fändrich, M. (2024). Cryo-EM observation of the amyloid key structure of polymorphic TDP-43 amyloid fibrils. Nature Communications, 15(1), 78-84. https://doi.org/10.1038/s41467-023-44489-0
77. Shi, P., Gal, J., Kwinter, D. M., Liu, X., & Zhu, H. (2010). Mitochondrial dysfunction in amyotrophic lateral sclerosis. Biochimica et Biophysica Acta - Molecular Basis of Disease, 1802(1), 45–51. https://doi.org/10.1016/j.bbadis.2009.08.012
78. St. Martin, J. L., Wang, L., & Kaprielian, Z. (2020). Toxicity in ALS: TDP-43 modifiers and C9orf72. In Neuroscience Letters (Vol. 716). Elsevier Ireland Ltd. https://doi.org/10.1016/j.neulet.2019.134621
79. Steyn, F. J., Tefera, T., Loganathan, S., Wilson, B. A., Carey, S. B., Manzo, E., Joardar, A., Ugur, B., & Zarnescu, D. C. (2022). TDP-43 Proteinopathy Causes Broad Metabolic Alterations including TCA Cycle Intermediates and Dopamine Levels in Drosophila Models of ALS. https://doi.org/10.3390/metabo12020101
80. Streit, L., Kuhn, T., Vomhof, T., Bopp, V., Ludolph, A. C., Weishaupt, J. H., Gebhardt, J. C. M., Michaelis, J., & Danzer, K. M. (2022). Stress induced TDP-43 mobility loss independent of stress granules. Nature Communications, 13(1). https://doi.org/10.1038/s41467-022-32939-0
81. Suk, T. R., & Rousseaux, M. W. C. (2020). The role of TDP-43 mislocalization in amyotrophic lateral sclerosis. Molecular Neurodegeneration, 15(1), 1–16. https://doi.org/10.1186/S13024-020-00397-1/FIGURES/2
82. Tomas, D., McLeod, V. M., Chiam, M. D. F., Wanniarachchillage, N., Boon, W. C., & Turner, B. J. (2021). Dissociation of disease onset, progression and sex differences from androgen receptor levels in a mouse model of amyotrophic lateral sclerosis. Scientific Reports, 11(1), 1–13. https://doi.org/10.1038/S41598-021-88415-0
83. Tran, N. N., & Lee, B. H. (2022). Functional implication of ubiquitinating and deubiquitinating mechanisms in TDP-43 proteinopathies. Frontiers in Cell and Developmental Biology, 10, 931-968. https://doi.org/10.3389/FCELL.2022.931968/BIBTEX
84. Tremblay, R. G., Sikorska, M., Sandhu, J. K., Lanthier, P., Ribecco-Lutkiewicz, M., & Bani-Yaghoub, M. (2010). Differentiation of mouse Neuro 2A cells into dopamine neurons. Journal of Neuroscience Methods, 186(1), 60–67. https://doi.org/10.1016/J.JNEUMETH.2009.11.004
85. Tziortzouda, P., Van Den Bosch, L., & Hirth, F. (2021). Triad of TDP43 control in neurodegeneration: autoregulation, localization and aggregation. In Nature Reviews Neuroscience (Vol. 22, Issue 4). Nature Research. https://doi.org/10.1038/s41583-021-00431-1
86. Vaage, A. M., Meyer, H. E., Landgraff, I. K., Myrstad, M., Holmøy, T., & Nakken, O. (2024). Physical Activity, Fitness, and Long-Term Risk of Amyotrophic Lateral Sclerosis: A Prospective Cohort Study. Neurology, 103(2), 102–110. https://doi.org/10.1212/WNL.0000000000209575
87. van Es, M. A., Hardiman, O., Chio, A., Al-Chalabi, A., Pasterkamp, R. J., Veldink, J. H., & van den Berg, L. H. (2017). Amyotrophic lateral sclerosis. The Lancet, 390(10107), 2084–2098. https://doi.org/10.1016/S0140-6736(17)31287-4/ASSET/EED00479-89A5-43FE-8787-77065C23ECD2/MAIN.ASSETS/GR4.JPG

88. Vandoorne, T., De Bock, K., & Van Den Bosch, L. (2018). Energy metabolism in ALS: an underappreciated opportunity? Acta Neuropathologica, 135(4), 489-500. https://doi.org/10.1007/S00401-018-1835-X
89. Wang, P., Deng, J., Dong, J., Liu, J., Bigio, E. H., Mesulam, M., Wang, T., Sun, L., Wang, L., Lee, A. Y. L., McGee, W. A., Chen, X., Fushimi, K., Zhu, L., & Wu, J. Y. (2019). TDP-43 induces mitochondrial damage and activates the mitochondrial unfolded protein response. In PLoS Genetics (Vol. 15, Issue 5). https://doi.org/10.1371/journal.pgen.1007947
90. Wang, W., Wang, L., Lu, J., Siedlak, S. L., Fujioka, H., Liang, J., Jiang, S., Ma, X., Jiang, Z., Da Rocha, E. L., Sheng, M., Choi, H., Lerou, P. H., Li, H., & Wang, X. (2016). The inhibition of TDP-43 mitochondrial localization blocks its neuronal toxicity. Nature Medicine, 22(8), 869–878. https://doi.org/10.1038/nm.4130
91. Wannarong, T., & Ungprasert, P. (2020). Diabetes mellitus is associated with a lower risk of amyotrophic lateral sclerosis: A systematic review and meta-analysis. Clinical Neurology and Neurosurgery, 199. https://doi.org/10.1016/j.clineuro.2020.106248
92. Wood, A., Gurfinkel, Y., Polain, N., Lamont, W., & Lyn Rea, S. (2021). Molecular Mechanisms Underlying TDP-43 Pathology in Cellular and Animal Models of ALS and FTLD. International Journal of Molecular Sciences, 22(9), 45-49. https://doi.org/10.3390/IJMS22094705
93. Yang, J. W., Kim, S. M., Kim, H. J., Kim, J. E., Park, K. S., Kim, S. H., Lee, K. W., & Sung, J. J. (2013). Hypolipidemia in patients with amyotrophic lateral sclerosis: A possible gender difference? Journal of Clinical Neurology (Korea), 9(2), 8-12. https://doi.org/10.3988/jcn.2013.9.2.125
94. Zamani, A., Thomas, E., & Wright, D. K. (2024). Sex biology in amyotrophic lateral sclerosis. Ageing Research Reviews, 95, 102228. https://doi.org/10.1016/J.ARR.2024.102228
95. Zhang, L., Tang, L., Huang, T., & Fan, D. (2022). Association between type 2 diabetes and amyotrophic lateral sclerosis. Scientific Reports, 12(1), 34-40. https://doi.org/10.1038/s41598-022-06463-6
96. Zhang, Q., Terawaki, S., Oikawa, D., Okina, Y., Usuki, Y., Ito, H., & Tokunaga, F. (2022). Suppression of Linear Ubiquitination Ameliorates Cytoplasmic Aggregation of Truncated TDP-43. Cells, 11(15). https://doi.org/10.3390/CELLS11152398
97. Zhang, Y. J., Xu, Y. F., Cook, C., Gendron, T. F., Roettges, P., Link, C. D., Lin, W. L., Tong, J., Castanedes-Casey, M., Ash, P., Gass, J., Rangachari, V., Buratti, E., Baralle, F., Golde, T. E., Dickson, D. W., & Petrucelli, L. (2009). Aberrant cleavage of TDP-43 enhances aggregation and cellular toxicity. Proceedings of the National Academy of Sciences of the United States of America, 106(18), 7607–7612. https://doi.org/10.1073/PNAS.0900688106/SUPPL_FILE/0900688106SI.PDF
98. Zhao, W., Beers, D. R., Henkel, J. S., Zhang, W., Urushitani, M., Julien, J. P., & Appel, S. H. (2010). Extracellular mutant SOD1 induces microglial-mediated motoneuron injury. GLIA, 58(2), 231–243. https://doi.org/10.1002/GLIA.20919,
99. Zhu, Q., Zhou, J., Zhang, Y., Huang, H., Han, J., Cao, B., Xu, D., Zhao, Y., & Chen, G. (2023). Risk factors associated with amyotrophic lateral sclerosis based on the observational study: a systematic review and meta-analysis. In Frontiers in Neuroscience *474*(8), 1417–1438.Frontiers Media S.A. https://doi.org/10.3389/fnins.2023.1196722

Appendix 1

TDP-43 Sequences

Mouse TDP-43 ORF

GCGATCGCCATGTCTGAATATATTCGGGTAACAGAAGATGAGAACGATGAACCCATTGAAATACCATCAGAAGACGATGGGACGGT
GTTGCTGTCCACAGTTACAGCCCAGTTTCCAGGGGCATGCGGCCTGCGCTACCGGAATCCCGTGTCTCAGTGTATGAGAGGAGTCC
GACTGGTGGAAGGAATTCTGCATGCCCCAGATGCTGGCTGGGGCAATCTGGTATATGTTGTCAACTATCCCAAAGATAACAAAAGG
AAAATGGATGAGACAGATGCTTCCTCTGCAGTGAAAGTGAAAAGAGCAGTCCAGAAAACATCTGACCTCATAGTGTTGGGTCTCC
CCTGGAAAACAACTGAGCAGGATCTGAAAGACTATTTCAGTACTTTTGGAGAGGTTCTTATGGTTCAGGTCAAGAAAGATCTTAA
AACTGGTCACTCGAAAGGGTTTGGCTTTGTTCGATTTACAGAATATGAAACCCAAGTGAAAGTAATGTCACAACGACATATGATAG
ATGGGCGATGGTGTGACTGTAAACTTCCCAACTCTAAGCAAAGCCCAGACGAGCCTTTGAGAAGCAGAAAGGTGTTTGTTGGACG
TTGTACAGAGGACATGACTGCTGAAGAGCTTCAGCAGTTTTTCTGTCAGTATGGAGAAGTGGTAGATGTCTTCATTCCCAAACCAT
TCAGAGCTTTTGCCTTCGTCACCTTTGCAGATGATAAGGTTGCCCAGTCTCTTTGTGGAGAGGATTTGATCATTAAAGGAATCAG
CGTGCATATATCCAATGCTGAACCTAAGCATAATAGCAATAGACAGTTAGAAAGAAGTGGAAGATTTGGTGGTAATCCAGGTGGCT
TTGGGAATCAGGGTGGGTTTGGTAACAGTAGAGGGGGTGGAGCTGGCTTGGGAAATAACCAGGGTGGTAATATGGGTGGAGGGAT
GAACTTTGGTGCTTTTAGCATTAACCCAGCGATGATGGCTGCGGCTCAGGCAGCGTTGCAGAGCAGTTGGGGTATGATGGGCATG
TTAGCCAGCCAGCAGAACCAGTCGGGCCCATCTGGGAATAACCAAAGCCAGGGCAGCATGCAGAGGGAACCAAATCAGGCTTTTG
GTTCTGGAAATAATTCCTACAGTGGTTCTAATTCTGGTGCCCCCCTTGGTTGGGGGTCAGCATCAAATGCAGGATCGGGCAGTGGT
TTTAATGGGGGCTTTGGCTCGAGCATGGATTCTAAGTCTTCTGGCT

Wild Type TDP-43 ORF (WTT)

ATGTCTGAATATATTCGGGTAACCGAAGATGAGAACGATGAGCCCATTGAAATACCATCGGAAGACGATGGGACGGTGCTGCTCTC
CACGGTTACAGCCCAGTTTCCAGGGGCGTGTGGGCTTCGCTACAGGAATCCAGTGTCTCAGTGTATGAGAGGTGTCCGGCTGGTAG
AAGGAATTCTGCATGCCCCAGATGCTGGCTGGGGAAATCTGGTGTATGTTGTCAACTATCCAAAAGATAACAAAAGAAAAATGGA
TGAGACAGATGCTTCATCAGCAGTGAAAGTGAAAAGAGCAGTCCAGAAAACATCCGATTTAATAGTGTTGGGTCTCCCATGGAAA
ACAACCGAACAGGACCTGAAAGAGTATTTTAGTACCTTTGGAGAAGTTCTTATGGTGCAGGTCAAGAAAGATCTTAAGACTGGTC
ATTCAAAGGGGTTTGGCTTTGTTCGTTTTACGGAATATGAAACACAAGTGAAAGTAATGTCACAGCGACATATGATAGATGGACGA
TGGTGTGACTGCAAACTTCCTAATTCTAAGCAAAGCCAAGATGAGCCTTTGAGAAGCAGAAAAGTGTTTGTGGGGCGCTGTACAG
AGGACATGACTGAGGATGAGCTGCGGGAGTTCTTCTCTCAGTACGGGGATGTGATGGATGTCTTCATCCCCAAGCCATTCAGGGCC
TTTGCCTTTGTTACATTTGCAGATGATCAGATTGCGCAGTCTCTTTGTGGAGAGGACTTGATCATTAAAGGAATCAGCGTTCATAT
ATCCAATGCCGAACCTAAGCACAATAGCAATAGACAGTTAGAAAGAAGTGGAAGATTTGGTGGTAATCCAGGTGGCTTTGGGAATC
AGGGTGGATTTGGTAATAGCAGAGGGGGTGGAGCTGGTTTGGGAAACAATCAAGGTAGTAATATGGGTGGTGGGATGAACTTTGG
TGCGTTCAGCATTAATCCAGCCATGATGGCTGCCGCCCAGGCAGCACTACAGAGCAGTTGGGGTATGATGGGCATGTTAGCCAGCC
AGCAGAACCAGTCAGGCCCATCGGGTAATAACCAAAACCAAGGCAACATGCAGAGGGAGCCAAACCAGGCCTTCGGTTCTGGAAA
TAACTCTTATAGTGGCTCTAATTCTGGTGCAGCAATTGGTTGGGGATCAGCATCCAATGCAGGGTCGGGCAGTGGTTTTAATGGAG
GCTTTGGCTCAAGCATGGATTCTAAGTCTTCTGGCTGGGGAATGTAG

TDP-43 Q331K Glutamine 331 mutated to Lysine (QKT)

ATGTCTGAATATATTCGGGTAACCGAAGATGAGAACGATGAGCCCATTGAAATACCATCGGAAGACGATGGGACGGTGCTGCTCTC
CACGGTTACAGCCCAGTTTCCAGGGGCGTGTGGGCTTCGCTACAGGAATCCAGTGTCTCAGTGTATGAGAGGTGTCCGGCTGGTAG
AAGGAATTCTGCATGCCCCAGATGCTGGCTGGGGAAATCTGGTGTATGTTGTCAACTATCCAAAAGATAACAAAAGAAAAATGGA
TGAGACAGATGCTTCATCAGCAGTGAAAGTGAAAAGAGCAGTCCAGAAAACATCCGATTTAATAGTGTTGGGTCTCCCATGGAAA
ACAACCGAACAGGACCTGAAAGAGTATTTTAGTACCTTTGGAGAAGTTCTTATGGTGCAGGTCAAGAAAGATCTTAAGACTGGTC
ATTCAAAGGGGTTTGGCTTTGTTCGTTTTACGGAATATGAAACACAAGTGAAAGTAATGTCACAGCGACATATGATAGATGGACGA
TGGTGTGACTGCAAACTTCCTAATTCTAAGCAAAGCCAAGATGAGCCTTTGAGAAGCAGAAAAGTGTTTGTGGGGCGCTGTACAG
AGGACATGACTGAGGATGAGCTGCGGGAGTTCTTCTCTCAGTACGGGGATGTGATGGATGTCTTCATCCCCAAGCCATTCAGGGCC
TTTGCCTTTGTTACATTTGCAGATGATCAGATTGCGCAGTCTCTTTGTGGAGAGGACTTGATCATTAAAGGAATCAGCGTTCATAT
ATCCAATGCCGAACCTAAGCACAATAGCAATAGACAGTTAGAAAGAAGTGGAAGATTTGGTGGTAATCCAGGTGGCTTTGGGAATC
AGGGTGGATTTGGTAATAGCAGAGGGGGTGGAGCTGGTTTGGGAAACAATCAAGGTAGTAATATGGGTGGTGGGATGAACTTTGG
*TGCGTTCAGCATTAATCCAGCCATGATGGCTGCCGCCCAGGCAGCACTA**AAG**AGCAGTTGGGGTATGATGGGCATGTTAGCCAGCC*
AGCAGAACCAGTCAGGCCCATCGGGTAATAACCAAAACCAAGGCAACATGCAGAGGGAGCCAAACCAGGCCTTCGGTTCTGGAAA
TAACTCTTATAGTGGCTCTAATTCTGGTGCAGCAATTGGTTGGGGATCAGCATCCAATGCAGGGTCGGGCAGTGGTTTTAATGGAG
GCTTTGGCTCAAGCATGGATTCTAAGTCTTCTGGCTGGGGAATGTAG

TDP-43 G294A Glycine 294 mutated to Alanine (GAT)

ATGTCTGAATATATTCGGGTAACCGAAGATGAGAACGATGAGCCCATTGAAATACCATCGGAAGACGATGGGACGGTGCTGCTCTC
CACGGTTACAGCCCAGTTTCCAGGGGCGTGTGGGCTTCGCTACAGGAATCCAGTGTCTCAGTGTATGAGAGGTGTCCGGCTGGTAG
AAGGAATTCTGCATGCCCCAGATGCTGGCTGGGGAAATCTGGTGTATGTTGTCAACTATCCAAAAGATAACAAAAGAAAAATGGA
TGAGACAGATGCTTCATCAGCAGTGAAAGTGAAAAGAGCAGTCCAGAAAACATCCGATTTAATAGTGTTGGGTCTCCCATGGAAA
ACAACCGAACAGGACCTGAAAGAGTATTTTAGTACCTTTGGAGAAGTTCTTATGGTGCAGGTCAAGAAAGATCTTAAGACTGGTC
ATTCAAAGGGGTTTGGCTTTGTTCGTTTTACGGAATATGAAACACAAGTGAAAGTAATGTCACAGCGACATATGATAGATGGACGA
TGGTGTGACTGCAAACTTCCTAATTCTAAGCAAAGCCAAGATGAGCCTTTGAGAAGCAGAAAAGTGTTTGTGGGGCGCTGTACAG
AGGACATGACTGAGGATGAGCTGCGGGAGTTCTTCTCTCAGTACGGGGATGTGATGGATGTCTTCATCCCCAAGCCATTCAGGGCC
TTTGCCTTTGTTACATTTGCAGATGATCAGATTGCGCAGTCTCTTTGTGGAGAGGACTTGATCATTAAAGGAATCAGCGTTCATAT
ATCCAATGCCGAACCTAAGCACAATAGCAATAGACAGTTAGAAAGAAGTGGAAGATTTGGTGGTAATCCAGGTGGCTTTGGGAATC
*AGGGTGGATTTGGTAATAGCAGA**GCG**GGTGGAGCTGGTTTGGGAAACAATCAAGGTAGTAATATGGGTGGTGGGATGAACTTTGG*
*TGCGTTCAGCATTAATCCAGCCATGATGGCTGCCGCCCAGGCAGCACTA**CAG**A**GC**AGTTGGGGTATGATGGGCATGTTAGCCAGCC*
AGCAGAACCAGTCAGGCCCATCGGGTAATAACCAAAACCAAGGCAACATGCAGAGGGAGCCAAACCAGGCCTTCGGTTCTGGAAA
TAACTCTTATAGTGGCTCTAATTCTGGTGCAGCAATTGGTTGGGGATCAGCATCCAATGCAGGGTCGGGCAGTGGTTTTAATGGAG
GCTTTGGCTCAAGCATGGATTCTAAGTCTTCTGGCTGGGGAATGTAG

TDP-43 M337V Methionine 337 mutated to Valine (MVT)

ATGTCTGAATATATTCGGGTAACCGAAGATGAGAACGATGAGCCCATTGAAATACCATCGGAAGACGATGGGACGGTGCTGCTCTC
CACGGTTACAGCCCAGTTTCCAGGGGCGTGTGGGCTTCGCTACAGGAATCCAGTGTCTCAGTGTATGAGAGGTGTCCGGCTGGTAG
AAGGAATTCTGCATGCCCCAGATGCTGGCTGGGGAAATCTGGTGTATGTTGTCAACTATCCAAAAGATAACAAAAGAAAAATGGA
TGAGACAGATGCTTCATCAGCAGTGAAAGTGAAAAGAGCAGTCCAGAAAACATCCGATTTAATAGTGTTGGGTCTCCCATGGAAA
ACAACCGAACAGGACCTGAAAGAGTATTTTAGTACCTTTGGAGAAGTTCTTATGGTGCAGGTCAAGAAAGATCTTAAGACTGGTC
ATTCAAAGGGGTTTGGCTTTGTTCGTTTTACGGAATATGAAACACAAGTGAAAGTAATGTCACAGCGACATATGATAGATGGACGA
TGGTGTGACTGCAAACTTCCTAATTCTAAGCAAAGCCAAGATGAGCCTTTGAGAAGCAGAAAAGTGTTTGTGGGGCGCTGTACAG
AGGACATGACTGAGGATGAGCTGCGGGAGTTCTTCTCTCAGTACGGGGATGTGATGGATGTCTTCATCCCCAAGCCATTCAGGGCC
TTTGCCTTTGTTACATTTGCAGATGATCAGATTGCGCAGTCTCTTTGTGGAGAGGACTTGATCATTAAAGGAATCAGCGTTCATAT
ATCCAATGCCGAACCTAAGCACAATAGCAATAGACAGTTAGAAAGAAGTGGAAGATTTGGTGGTAATCCAGGTGGCTTTGGGAATC
AGGGTGGATTTGGTAATAGCAGAGGGGGTGGAGCTGGTTTGGGAAACAATCAAGGTAGTAATATGGGTGGTGGGATGAACTTTGG
*TGCGTTCAGCATTAATCCAGCCATGATGGCTGCCGCCCAGGCAGCACTACAGAGCAGTTGGGGTATG**GTG**GGCATGTTAGCCAGCC*
AGCAGAACCAGTCAGGCCCATCGGGTAATAACCAAAACCAAGGCAACATGCAGAGGGAGCCAAACCAGGCCTTCGGTTCTGGAAA
TAACTCTTATAGTGGCTCTAATTCTGGTGCAGCAATTGGTTGGGGATCAGCATCCAATGCAGGGTCGGGCAGTGGTTTTAATGGAG
GCTTTGGCTCAAGCATGGATTCTAAGTCTTCTGGCTGGGGAATGTAG

Appendix 2

qPCR Primer List

Symbol	Forward Primer	Reverse Primer
ACACB	CATGGCAAGAGAAAAGCGGC	GGGACGTAATGATCCGCCAT
ACTB	CATTGCTGACAGGATGCAGAAGG	TGCTGGAAGGTGGACAGTGAGG
Ak7	CTGGACACCTATAGCAGCGG	AGGGCCGGTATTTTTGCTGA
ALDO-B	CTGTGTTGAGGATTGCTGACCAG	TCAGGAAGCACCTCTGGCTCAA
Arhgef18	GGAGGACGTTTTCAGTGAGGCT	GCTGTTTCTCCAGAAGGCTCTG
Bnip3	GCTCCAAGAGTTCTCACTGTGAC	GTTTTTCTCGCCAAAGCTGTGGC
CAMKK1	TCTACAGGACCTGCCAGTCACA	GCAGCTTGTACTGGTTCAGTTGC
CAMKK2	CAACGTGGTGAAGCTGGTAGAG	TGGTCTTCGGACAGTGGCTTGA
Ceacam18	TGGTGAGGATGTCGGCGGTAAA	GGCACTGGTATTGGCTGAGATG
ChAT	TGAGTACTGGCTGAATGACATG	AGTACACCAGAGATGAGGCT
CRAT	TCGCAGATTCTGACAGGTGA	GATCTGATCCGCAGTGAGGG
CS	ATGCAGAGGGAATGAACCGAGC	GAGTCAATGGCTCCGATACTGC
Dpy19l1	CTGTGACTTCCAGGATCTTTGGC	CTCCATGAAGTCAAACTCGGCTG
Eif2ak2	AGGTGTCACCAAACAGGAGGCA	GCTGCTGGAAAAGCCACTGAATG
Epha3	AGGAGAAGCGCCTTCACTTTGG	TTGGTGGCATCCAACTCCTTCG
Foxn4	ACGAAAGGACCTCGCTGCCATA	TAGGCTCTCCTCGTTTTCCAGG
G6PD	CTGTTCCGTGAGGACCAGATCT	TGAAGGTGAGGATAACGCAGGC
GYS1	CCGCTATGAGTTCTCCAACAAGG	AGAAGGCAACCACTGTCTGCTC
IDH2	AGATGGCAGTGGTGTCAAGGAG	CTGGATGGCATACTGGAAGCAG
Ism1	CACCTGTGGAAATGGCAACCAG	GCAAGCAGACTCACTTCAGTGG
Jazf1	CGACATAGCAGTGGCAGCCTTA	TCTCTGTGGTCCAGGACTCATC
Lrch2	TGGTCCCTTTGGCTTGAAGCCT	GCTGCCTTATCTGTTCACGCTC
Olfr698	GCTGCTTCTAGTCATCACCATGG	TCCACAACAGCCTTGGGAGTGA
PDK1	CTACCAGCCATGTCAGAGGATG	AGGCTGGTTTCCACCGTAGACA
PDK2	CGCCTATGACATGGCTAAGCTC	ACAGGTGGGAAGGGACATAGAC
PDK3	CCGTCGCCACTGTCTATCAAAC	CTCTCATGGTGTTAGCCAGTCG
PDK4	GTCGAGCATCAAGAAAACCGTCC	GCGGTCAGTAATCCTCAGAGGA
PDP	GTAGAGCCATGCTAGGTGTGCA	GGTGTTCCAGTTTCAGACGCTC
PDP1	GTAGAGCCATGCTAGGTGTGCA	GGTGTTCCAGTTTCAGACGCTC
PFK	CTGTTCGCTCTACCGTGAGGAT	TTGGAACCACCTTGACCAGTCC
PFKM	GCTTCTAGCTCATGTCAGACCC	CCAATCCTCACAGTGGAGCGAA
PP2CA	TCTTCCTCTCACTGCCTTGGTG	GAGGAACTTCCTGTAGGCGATC
Prkaa1	GGTGTACGGAAGGCAAAATGGC	CAGGATTCTTCCTTCGTACACGC
Prkaa2	CTGAAGCCAGAGAATGTGCTGC	GAGATGACCTCAGGTGCTGCAT
Prkab1	CCAAAAGTGCTCCGATGTGTCTG	GGGCTTTGAACCTCTCTTCTGG
Prkab2	GACTTCGTTGCCATCCTGGATC	CCAAGCTGACTGGTAACCACAG
Prkag1	TCTCCGCCTTACCTGTAGTGGA	GCAGGGCTTTTGTCACAGACAC
Prkag3	AAGCGGCTACTCAAGTTCCTGC	CCAGAACTACAGCCAAATCTCGG
PYGB	CCAGACTGCTTCAAGGACATCG	GTTCCTGATGACCTTCTTGGTCC
RPL13a	ATGACAAGAAAAAGCGGATG	CTTTTCTGCCTGTTTCCGTA
Samsn1	TCAGCATCCCTGTCCACATTCC	GCACACAGACTTCACGCCAAGT
SLC16A1	GACCATTGTGGAATGCTGCCCT	CGATGATGAGGATCACGCCACA
Snx10	GAACAATCGCCAGCATGTCGAC	ATGTCCTCGGAGTTCAGATGGC
STK11	GCCTGGAATACCTACACAGCCA	GCAGGTGTCATCCACAGCGAAA
STK11ip	GACTGGAGAGTGATGAAGGCTG	CTGACTGCTCTTCCTGGTTCTG
Tas2r137	GTTTCCCTGGTTGCCTACCTTC	CTCAGCACTCTGATCTCTGGAG
TDP 43	GATGGACGATGGTGTGACTGCA	AAGAACTCCCGCAGCTCATCCT
Tmem255b	CGTTCTGCTGTGCCATAGTCGA	CGACCATTCAAAGAGTAGCAGGT
Vmn1r29	CTCCTGTCAACTGACCTTCGTTC	GCCTCTCATCACCCTGCTTATG
Zfp385c	TCATCTGCGGTTCAACTCAGCG	GTGAGGCTGAAGACACCACTGT

Appendix 3

List of Tables

List of Figures

Appendix 4

Scientific Contributions and Outputs

Publication Record

Experimental (Selected)

1. ***Gbadamosi I,*** Binias S, Gielniewski B, Magno R, Duarte I, & Jawaid, A. Coding and non-coding RNA expression in NSC34 cells following TDP-43 depletion and mutant TDP-43M337V expression. Scientific Data. (2025, in press). https://doi.org/10.1038/s41597-024-03297-7
2. ***Gbadamosi I***, Yawson EO, Akesinro J, Adeleke O, Tokunbo O, Bamisi O, Ibrahim-Abdulkareem R, Awoniran P, Gbadamosi R, Lambe E, Atoyebi A, Bayo-Olugbami AA, Abayomi TA, Arogundade TT. Vitamin D attenuates monosodium glutamate-induced behavioural anomalies, metabolic dysregulation, cholinergic impairment, oxidative stress, and astrogliosis in rats. Neurotoxicology. 2024 Jul;103:297-309. doi: 10.1016/j.neuro.2024.06.015. Epub 2024 Jul 3. PubMed PMID: 38964510.
3. Arogundade TT, ***Gbadamosi I***, Enaibe BU. Maternal diet supplemented with African walnuts enhances cortico-hippocampal gene expression and histomorphology in rat offspring. Nutr Neurosci. 2024 Feb;27(2):159-171. doi: 10.1080/1028415X.2023.2166804. Epub 2023 Jan 12. PubMed PMID: 36635992.
4. Omotoso GO, Olanrewaju RA, Amedu NO, Kolo RM, ***Gbadamosi IT***. Calcium Supplementation Ameliorates Cerebellar Oxidative Stress in Lactational Aluminum-induced Neurotoxicity in Rats. Basic Clin Neurosci. 2022 Nov-Dec;13(6):789-798. doi: 10.32598/bcn.2022.1347.2. Epub 2022 Nov 1. PubMed PMID: 37323952; PubMed Central PMCID: PMC10262293.
5. Olajide OJ, Alliy ZO, Ojo DO, Osinubi OO, Bello SO, Ibrahim FE, Adukwu FO, Abikoye TO, ***Gbadamosi IT***, Mutholib NY, Bamisi O, Ajiboye OJ, Okesina AA, Alli-Oluwafuyi A, Oyewole AL, Nafiu AB, Akinola O. Neurobehavioral, neurochemical and synaptic plasticity perturbations during postnatal life of rats exposed to chloroquine in-utero. Neurotoxicol Teratol. 2021 Jul-Aug;86:106982. doi: 10.1016/j.ntt.2021.106982. Epub 2021 Apr 16. PubMed PMID: 33845156.
6. Olajide OJ, ***Gbadamosi IT***, Yawson EO, Arogundade T, Lewu FS, Ogunrinola KY, Adigun OO, Bamisi O, Lambe E, Arietarhire LO, Oluyomi OO, Idowu OK, Kareem R, Asogwa NT, Adeniyi PA. Hippocampal Degeneration and Behavioral Impairment During Alzheimer-Like Pathogenesis Involves Glutamate Excitotoxicity. J Mol Neurosci. 2021 Jun;71(6):1205-1220. doi: 10.1007/s12031-020-01747-w. Epub 2021 Jan 8. PubMed PMID: 33420680.
7. Armah FA, Henneh IT, Alake J, Ahlidja W, Amoani B, Ofori EG, Asante-Kyei B, Temitayo GI, Adokoh CK. Allanblackia floribunda Seed Extract Attenuates the Ethanol-Induced Gastric Ulcer in Rats via the Inhibition of TNF-α and INF-γ Levels and Modulation in the Expression of Ki67 Protein. Biomed Res Int. 2021;2021:6694572. doi: 10.1155/2021/6694572. eCollection 2021. PubMed PMID: 33521129; PubMed Central PMCID: PMC7819754.
8. Omotoso G, Oloyede O, Lawal S, ***Gbadamosi I***, Mutholib N, Abdulsalam F, Bature A, Babalola A, Ayeni B, Amedu N. Permethrin exposure affects neurobehavior and cellular characterization in rats' brain. Environ Anal Health Toxicol. 2020 Dec;35(4):e2020022-0. doi: 10.5620/eaht.2020022. Epub 2020 Nov 24. PubMed PMID: 33434422; PubMed Central PMCID: PMC7829406.
9. ***Gbadamosi IT***, Olawande B, Emmanuel YO, Timothy AT, Kehinde O, Susan LF, Ezra L, Joseph OO. Inhibitory potentials of Cymbopogon citratus oil against aluminium-induced behavioral deficits and neuropathology in rats. Anat Cell Biol. 2020 Sep 30;53(3):342-354. doi: 10.5115/acb.20.099. PubMed PMID: 32839358; PubMed Central PMCID: PMC7527123.
10. Omotoso GO, Arietarhire LO, Ukwubile II, ***Gbadamosi IT***. The Protective Effect of Kolaviron on Molecular, Cellular, and Behavioral Characterization of Cerebellum in the Rat Model of Demyelinating Diseases. Basic Clin Neurosci. 2020 Sep-Oct;11(5):609-618. doi: 10.32598/bcn.9.10.300. Epub 2020 Sep 1. PubMed PMID: 33643554; PubMed Central PMCID: PMC7878059.
11. Omotoso GO, Ukwubile II, Arietarhire L, Sulaimon F, ***Gbadamosi IT***. Kolaviron protects the brain in cuprizone-induced model of experimental multiple sclerosis via enhancement of intrinsic antioxidant mechanisms: Possible therapeutic applications?. Pathophysiology. 2018 Dec;25(4):299-306. doi: 10.1016/j.pathophys.2018.04.004. Epub 2018 Apr 27. PubMed PMID: 29730092.
12. Olajide OJ, Fatoye JO, Idowu OF, Ilekoya D, ***Gbadamosi IT***, Gbadamosi MT, Asogwa NT. Reversal of behavioral decline and neuropathology by a complex vitamin supplement involves modulation of key neurochemical stressors. Environ Toxicol Pharmacol. 2018 Sep;62:120-131. doi: 10.1016/j.etap.2018.07.005. Epub 2018 Jul 7. PubMed PMID: 30005307.
13. Omotoso GO, ***Gbadamosi IT***, Afolabi TT, Abdulwahab AB, Akinlolu AA. Ameliorative effects of Moringa on cuprizone-induced memory decline in rat model of multiple sclerosis. Anat Cell Biol. 2018 Jun;51(2):119-127. doi: 10.5115/acb.2018.51.2.119. Epub 2018 Jun 27. PubMed PMID: 29984057; PubMed Central PMCID: PMC6026826.
14. Omotoso GO, Olajide OJ, ***Gbadamosi IT***, Rasheed MA, Izuogu CT. Kolaviron Protects the Prefrontal Cortex and Hippocampus against Histomorphological and Neurobehavioural Changes in Cuprizone Model of Multiple Sclerosis.

Malays J Med Sci. 2018 Mar;25(2):50-63. doi: 10.21315/mjms2018.25.2.6. Epub 2018 Apr 27. PubMed PMID: 30918455; PubMed Central PMCID: PMC6422579.

15. Omotoso GO, ***Gbadamosi IT***, Olajide OJ, Dada-Habeeb SO, Arogundade TT, Yawson EO. Moringa oleifera phytochemicals protect the brain against experimental nicotine-induced neurobehavioral disturbances and cerebellar degeneration. Pathophysiology. 2018 Mar;25(1):57-62. doi: 10.1016/j.pathophys.2017.12.003. Epub 2018 Jan 4. PubMed PMID: 29307662.
16. Olajide OJ, Ugbosanmi AT, Enaibe BU, Ogunrinola KY, Lewu SF, Asogwa NT, Akapa T, Imam A, Ibrahim A, ***Gbadamosi IT***, Yawson EO. Cerebellar Molecular and Cellular Characterization in Rat Models of Alzheimer's Disease: Neuroprotective Mechanisms of Garcinia Biflavonoid Complex. Ann Neurosci. 2017 May;24(1):32-45. doi: 10.1159/000464421. Epub 2017 Apr 21. PubMed PMID: 28827919; PubMed Central PMCID: PMC5551726.
17. Olajide OJ, Yawson EO, ***Gbadamosi IT***, Arogundade TT, Lambe E, Obasi K, Lawal IT, Ibrahim A, Ogunrinola KY. Ascorbic acid ameliorates behavioural deficits and neuropathological alterations in rat model of Alzheimer's disease. Environ Toxicol Pharmacol. 2017 Mar;50:200-211. doi: 10.1016/j.etap.2017.02.010. Epub 2017 Feb 6. PubMed PMID: 28192749.

Reviews and Book Chapter

1. Madrer N, Perera ND, Uccelli NA, Abbondanza A, Andersen JV, Carsana EV, Demmings MD, Fernandez RF, de Fragas MG**, *Gbadamosi IT***, Kulshrestha D, , … Fernández-Moncada I. Neural Metabolic Networks: Key Elements of Healthy Brain Function. J Neurochem. 2025;169(6). doi: 10.1111/JNC.70084.
2. Arogundade TT, Bayo-Olugbami AA, Akintoye OO, ***Gbadamosi IT***. Animal Assisted Therapy as Non-pharmacological Intervention for Dementia. In: Asuku AO, Ajagun EO, Ogungbangbe OO (eds.) Non-Pharmacological Interventions for Dementia. Taylor & Francis; 2025. Chapter 16.
3. Lepiarz-Raba I, ***Gbadamosi IT***, Florea R, Paolicelli RC, Jawaid A. Metabolic regulation of microglial phagocytosis: Implications for Alzheimer's disease therapeutics. Transl Neurodegener. 2023 Oct 31;12(1):48. doi: 10.1186/s40035-023-00382-w. Review. PubMed PMID: 37908010; PubMed Central PMCID:
4. ***Gbadamosi IT***, Henneh IT, Aluko OM, Yawson EO, Fokoua AR, Koomson A, Torbi J, Olorunnado SE, Lewu FS, Yusha'u Y, Keji-Taofik ST, Biney RP, Tagoe TA. Depression in Sub-Saharan Africa. IBRO Neurosci Rep. 2022 Jun;12:309-322. doi: 10.1016/j.ibneur.2022.03.005. eCollection 2022 Jun. PubMed PMID: 35746974; PubMed Central

Publicly Available Datasets

1. **Gbadamosi, I.**, Binias, S., Gielniewski, B., Magno, R., Duarte, I., & Jawaid, A**.** (2025). *Transcriptomics dataset of BV2 microglia cells following TDP-43 knockdown* [RNA-seq dataset].
   Figshare. https://doi.org/10.6084/m9.figshare.29256263
2. **Gbadamosi, I.,** Binias, S., Gielniewski, B., Magno, R., Duarte, I., & Jawaid, A. (2024). *Raw RNA-seq reads from NSC34 motor neurons following TDP-43 modulation* [RNA-seq raw FASTQ files].
   European Nucleotide Archive (ENA). https://www.ebi.ac.uk/ena/browser/view/PRJEB72199
3. **Gbadamosi, I.,** Binias, S., Gielniewski, B., Magno, R., Duarte, I., & Jawaid, A. (2024). *A dataset of NSC34 motor neuron coding and non-coding transcriptome following TDP-43 knockdown and mutant TDP-43 M337V expression* [RNA-seq dataset].
   Figshare. https://doi.org/10.6084/m9.figshare.25898785
4. **Gbadamosi, I.,** Binias, S., Gielniewski, B., Magno, R., Duarte, I., & Jawaid, A. (2024). *Comprehensive transcriptomic analysis of NSC34 motor neurons following TDP-43 modulation: Knockdown vs. Control and Wild Type vs. TDP-43 M337V mutation* [RNA-seq dataset].
   BioStudies (ArrayExpress). https://www.ebi.ac.uk/biostudies/arrayexpress/studies/E-MTAB-13738

Selected Conference Presentations (Selected)

1. **FENS Forum 2024**, Vienna, Austria – *Cell-specific regulation of glucose metabolism by TDP-43 protein* (June 2024).
2. **Neuronus Neuroscience Conference 2024**, Cracow, Poland – *Cell-Specific Regulation of Neuronal and Glial Glucose Metabolism by Neurodegeneration-Associated Protein, TDP-43* (April 2024).
3. **ISN-ESN Meeting 2023**, Porto, Portugal – *Depletion of Neurodegeneration-associated Protein 'TDP-43' Perturbs Energy Metabolism in Motor Neurons* (August 2023).
4. **IBRO World Congress 2023**, Granada, Spain – *Depletion of Neurodegeneration-associated protein TDP-43 perturbs cellular energy metabolism in motor neurons* (September 2023).
5. **Nencki Doctoral Conference 2023**, Warsaw, Poland – *Motor Neuron Energy Metabolic Reprogramming in TDP-43 Loss-of-Function: Implications for ALS and FTLD* (October 2023).
6. **Neurons in Action Conference 2023**, Poland – *TDP-43 and Energy Metabolism Interplay in Neurodegenerative Disorders* (June 2023).
7. **FENS Forum 2022** – *Role of Metabolism in TDP-43 Pathology and its Downstream Toxicity*.